IMPERIAL

Imperial College London
Department of Earth Science and Engineering

Ph.D. Thesis

Micromechanical Model for Hysteresis in Fluid-Saturated Porous Rocks under Hydrostatic Loading

Alvin Trévis Biyoghé

June 27, 2025

A thesis submitted in partial fulfillment of the requirements for the degree of Doctor of Philosophy of Imperial College London.

Declaration of Originality

I, author, declare that the work in this thesis is my own. The work of others has been appropriately referenced. A full list of references is given in the bibliography.

Copyright

The copyright of this thesis rests with the author. Unless otherwise indicated, its contents are licensed under a Creative Commons Attribution-NonCommercial 4.0 International Licence (CC BY-NC).

Under this licence, you may copy and redistribute the material in any medium or format. You may also create and distribute modified versions of the work. This is on the condition that: you credit the author and do not use it, or any derivative works, for a commercial purpose.

When reusing or sharing this work, ensure you make the licence terms clear to others by naming the licence and linking to the licence text. Where a work has been adapted, you should indicate that the work has been changed and describe those changes.

Please seek permission from the copyright holder for uses of this work that are not included in this licence or permitted under UK Copyright Law.

Abstract

This research aims to show that frictional microcracks cause the dependence of rocks' elastic properties on both the perturbation amplitude and the loading history. These relationships are essential for estimating wave velocities and, thus, for analysing laboratory experiments on fluid-saturated rocks under varying stress levels. The first step towards achieving this objective is to propose a microstructural prototype in which hydrostatic remote loading induces local deviatoric stress. This stress is essential for triggering the slip of microcracks once they are closed. The prototype's geometry is based on the classical spherical assemblage of Hashin (J. *Appl. Mech.*, 1962) and includes a fluid-filled central pore. Surrounding this pore is a spherical shell composed of a homogenised medium that is pervasively microcracked, according to the non-interactive model proposed by Kachanov (*Mech. Maters.*, 1982). The properties of the homogeneous material surrounding the central pore are determined by solving the boundary-value problem with the confining pressure applied to the outer boundary of the shell. The second step is to enhance this microstructural model by incorporating a distribution of crack aspect ratios within the spherical shell. We demonstrate how oscillations in loading, with decreasing amplitudes, enable the evaluation of dynamic elastic properties, ultimately leading to the determination of wave velocities. The third step complements these findings by providing experimentalists with a numerical tool to help them improve their methods for evaluating the arrival time of shear waves in tri-axial laboratory experiments. To achieve this, we propose a coupled numerical approach that captures the transformation of the voltage applied to a piezoelectric actuator into an S-wave. This approach also accounts for the propagation of the wave through the testing machine and specimen, as well as the generation of voltage at the receiver, where a complex wave pattern is detected.

Acknowledgements

I would like to extend my heartfelt appreciation to my supervisors, *Dr. Yves M. Leroy* and *Prof. Robert W. Zimmerman*, for their exceptional guidance and unwavering support at every stage of my PhD journey. Their insights and encouragement have been invaluable to my development as a researcher.

Special thanks to *Dr. Lucas Pimienta* from *Université de Lausanne* for his collaboration and scientific contributions. Our numerous discussions on experimental rock physics have undoubtedly enhanced the quality of this thesis.

I would like to thank *Dr. Ramin Nawab* and his Rock Physics and Poroelasticity team for their warm welcome and support during my research time at *TotalEnergies* in Pau, France.

I would like to thank *Prof. Christophe Barnes* from *CY Cergy Paris University*, and *Prof. Nicolas Triantafyllidis* from *École Polytechnique* in Palaiseau for helpful discussions on wave propagation and piezoelectricity.

I am very grateful to my colleagues at Imperial College for their support and companionship; without them, this journey would have felt particularly lonely. They helped foster an inspiring environment and cultivated grounds for academic excellence.

Finally, I thank my parents and siblings for their love and continuous moral support, even across distances.

Contents

1 Introduction **18**

1.1 Background . . . 18

1.1.1 Hysteresis in rocks . . . 19

1.1.2 Mechanics and waves . . . 19

1.2 Current state of research . . . 21

1.2.1 Influence of microcracks in uniaxial loading . . . 21

1.2.2 Influence of microcracks on wave propagation . . . 21

1.2.3 Implications of strain amplitude on static versus dynamic measurements . 21

1.3 Research gaps . . . 22

1.4 Focus and scope . . . 22

1.5 Questions and objectives . . . 23

1.6 Limitations . . . 24

1.7 Structure overview . . . 24

2 Frictional Microcrack Model with a Single Crack Family **26**

2.1 Introduction . . . 26

2.2 Problem description . . . 28

2.2.1 The shell material as a homogenized medium . . . 29

2.2.2 The fluid pressure . . . 32

2.2.3 Effective properties via the spherical assemblage . . . 35

2.3 Predictions of the model . . . 39

2.3.1 Effect of crack parameters on the bulk modulus, drained conditions . . . 39

2.3.2 Crack response around the cavity, drained conditions. . . . 42

2.3.3 Cyclic response with undrained conditions . . . 44

2.4 Application to hydrostatic compression of dry specimens . . . 46

2.5 Conclusion . . . 50

3 Frictional Microcrack Model with Cracks of Various Aspect Ratios **52**

3.1 Introduction . . . 53

3.2 Enhanced micromechanical model . . . 54

3.2.1 Crack aspect-ratio distribution . . . 55

3.2.2 Conventional crack inversion scheme . . . 56

3.2.3 Spherical assemblage . . . 57

3.3 Loading and Unloading simulation at large strain amplitude . . . 58
3.3.1 Preliminaries . . . 58
3.3.2 Model constraints and optimisation . . . 59
3.3.3 Results . . . 62
3.3.4 Correlation between modelled and measured porosity . . . 65
3.4 Forced oscillation simulation . . . 67
3.4.1 Estimation of compressibility and bulk modulus . . . 67
3.4.2 Strain amplitude dependence of bulk modulus . . . 68
3.4.3 Compressibility coefficients versus effective pressure . . . 70
3.5 Conclusion . . . 73

4 Simulations of Ultrasonic Wave Propagation 75
4.1 Introduction . . . 75
4.2 piezoelectric coupling . . . 77
4.2.1 3D governing equations . . . 77
4.2.2 Poling-induced anisotropy . . . 78
4.3 1D dynamics by the method of characteristics . . . 79
4.3.1 Analytical solution . . . 80
4.3.2 Application to the actuator . . . 82
4.3.3 Application to the receiver . . . 87
4.4 Validation and simplifications in 1D . . . 88
4.5 SFEM simulations for a simplified geometry . . . 92
4.5.1 P-wave generation and reception . . . 93
4.5.2 S-wave generation and reception . . . 94
4.6 SFEM simulations for validation with calibration specimen . . . 98
4.6.1 Wave propagation in steel sample and upper anvil . . . 99
4.7 Applications to rocks with contrasted velocity ratios and anisotropy . . . 102
4.8 Conclusion . . . 104

5 Conclusion 106
5.1 Summary . . . 106
5.2 Future research directions . . . 107
5.2.1 Amplification of local deviatoric stress . . . 108
5.2.2 Efficient crack closure scheme . . . 109
5.2.3 Enhanced wave propagation simulation . . . 109
5.2.4 Macrostructural scale . . . 110

References 111

Appendix A Experimental Study of Hysteresis in Hydrostatic Tests 117
A.1 Introduction . . . 117
A.2 Experimental setup and methods . . . 118
A.2.1 Data acquisition and processing . . . 118
A.3 Experimental results . . . 120

A.3.1 Hydrostatic loading of dry sample . . . 120
A.3.2 Hydrostatic loading of water-saturated sample . . . 123

Appendix B Microcrack Mechanics **127**
B.1 Elasticity solution . . . 127
B.2 Effective properties of an elastic medium with isotropic circular cracks . . . 128
B.3 Finite-element solution . . . 130
B.4 Numerical algorithm for cracks aperture update . . . 131
B.5 Numerical algorithm for frictional cracks update . . . 132
B.6 Kinematic hardening . . . 134
B.6.1 Kinematic hardening and fracture mechanics . . . 134
B.6.2 A single family with azimuthal symmetry . . . 135
B.7 Spherical Assembly effective properties for slipping cracks . . . 138
B.8 Elastic effective compressibility of composite sphere model . . . 142
B.9 Comparison with Biot-Gassmann . . . 142
B.10 Morlier's crack density inversion . . . 144
B.11 Influence of the sinusoidality of the loading path . . . 145

Appendix C Wave Propagation **147**
C.1 Bubnov-Galerkin method . . . 147
C.1.1 1D analysis . . . 148
C.1.2 2D analysis . . . 148
C.2 Impact of the backing material . . . 149
C.3 2D validation and first convergence analysis . . . 150
C.4 2D Convergence analysis . . . 151

List of Figures

Figure 1.1: PhD mind map. Colour code: *orange* = challenges, *gray* = PhD solutions, *green* = final objective. 25

Figure 2.1: The specimen's response includes two schemes: one for an isotropic crack distribution in a fluid-saturated elastic matrix, and another for pressure control when the tap is open. 29

Figure 2.2: A crack of the isotropic distribution, within the shell at the distance r from the pore centre, has the unit normal $\underline{n}$ oriented by the two polar angles β and β'. 30

Figure 2.3: Influence of crack density on the effective elastic properties of a cracked matrix (κ^*, G^*) and a spherical assembly $(\bar{\kappa}, \bar{G})$, based on analytical solutions assuming all cracks are open (see Christensen, 1990 for $\bar{G}$). . . 38

Figure 2.4: The influence of the crack density on the two effective Biot's coefficients (the REV α^* and the assemblage $\bar{\alpha}$) and on the assemblage Skempton's coefficient. 39

Figure 2.5: The cyclic evolution of the bulk modulus with the confining pressure, the reference simulation. 40

Figure 2.6: The cyclic evolution of the effective assemblage Biot's coefficient $\bar{\alpha}$ with the confining pressure. 41

Figure 2.7: The crack slipping regime and distribution as a function of the radial position at five loading stages. 43

Figure 2.8: Bulk modulus for undrained conditions with water or glycerin and comparison with drained and undrained conditions. 45

Figure 2.9: Volumetric strain versus confining pressure varying the crack density c, matrix elasticity modulus E, matrix Poisson's ratio ν, and friction angle φ. 46

Figure 2.10: Volumetric strain versus confining pressure for Chauvigny. The fitting parameters are: $c = 0.4$, $\varphi = 32°$, $\nu = 0.2$, $E = 61$ GPa, $\sigma_C = 1.0$ MPa and ϕ=16.2%. 48

Figure 2.11: The experimental data of the hydrostatic compression cycle for C-2 and C-3 carbonates versus the theoretical curves. 49

Figure 3.1: Schematics of the prototype's geometry. 57

Figure 3.2: The experimental data from Chapman *et al.* (2023) and the fit of the loading data based on eq. (3.12). 59
Figure 3.3: Flowchart of the modelling of the stress-strain curve during a hydrostatic compression simulation. 60
Figure 3.4: Volumetric strain versus confining pressure for different simulations (*fit 0*, *fit 1*, and *fit 2*), compared to data. 62
Figure 3.5: (a) Open crack density versus confining pressure and (b) Crack porosity distribution for each fit. 63
Figure 3.6: Volumetric strain versus confining pressure for different simulations *Fit 3* compared to data. 64
Figure 3.7: (a) Crack porosity distribution and (b) open crack density versus confining pressure for *Fit 3*. 65
Figure 3.8: Best fits of the stress-strain measurements done on various rocks of different natures. 66
Figure 3.9: The modelled versus measured porosity for the carbonate C-2, carbonate C-3, Chauvigny limestone, Bentheim sandstone, Mushan sandstone, and Sierra white granite. 67
Figure 3.10: Fourier transform on simulated data. 68
Figure 3.11: Simulated results of the forced oscillations using *Fit 1* and *Fit 2* are compared with measurements. 69
Figure 3.12: The simulated bulk compressibility values C_{bc} and C_{bp} for fits 0, 1, and 2 are compared to the measurements. 71
Figure 3.13: simulated C_{bp} and C_{bc} using an oscillating confining pressure of 0.1 MPa on *fit 1*, at different differential Terzaghi stress, during the loading and unloading phases. 73

Figure 4.1: The 1D bar is composed of a rock specimen in its central section and of two steel anvils at the two ends. The PZT actuator and receiver are to the right and left of the specimen. 79
Figure 4.2: Schematics of the method of characteristics in 1D. 80
Figure 4.3: Comparison of the analytical solution (red curve) with the numerical results (black curve). 89
Figure 4.4: The displacement at the boundary between the actuator and the porous specimen as a function of time. 90
Figure 4.5: The voltage at the receiver as a function of time. 91
Figure 4.6: Active material of P and S wave transducers. 93
Figure 4.7: P-Receiver voltage for the problem presented in Figure 4.6 following an electric pulse at the P-actuator. 94
Figure 4.8: S-Receiver voltage for the problem presented in Figure 4.6 following an electric pulse at the S-actuator. 95
Figure 4.9: The wave pattern at different times following the emission of the S wave. 96
Figure 4.10: Experimental set up. Two different top anvils are used in our experiments, a short (5 cm) and a long (7.1 cm). 99

Figure 4.11: Simulation mesh containing 1918 spectral elements (150049 nodes) for an average resolution of 1209 nodes per square centimetre. 100
Figure 4.12: Snapshots at three different times of the simulation of the propagation of waves inside a stainless steel sample and the upper anvil. 101
Figure 4.13: Waveform captured by the S-wave receiver, experimentally (red curve) and numerically (blue curve). 102
Figure 4.14: Numerical results of the propagation of an S wave inside various rocks . 103

Figure 5.1: Updated PhD mind map. Colour code: *orange* = challenges, *green* = completed objectives, *gray* = solutions that were not completed during the PhD. 108

Figure A.1: FFT processing of raw data to remove drifting effect for stress and strain. 118
Figure A.2: Schematic representation of the dissipated energy ΔE (area of the stress-strain loop) and the average stored energy V (area delimited in red). 119
Figure A.3: Stress-strain curve when oscillating the confining pressure by $\Delta P_c \sim 0.052$ MPa, at $P_c = 1, 3, 9$. 120
Figure A.4: The attenuation factor Q^{-1}, calculated via the FFT method **(a)**, and ellipse method **(b)**. 121
Figure A.5: Stress-strain curves at different oscillation amplitudes of confining pressure ΔP_c MPa. 122
Figure A.6: Bulk modulus (black curve) as a function of the amplitude of the oscillations of the confining pressure, and the corresponding Q^{-1} 123
Figure A.7: Stress-strain loops at $P_{eff} = 5$ MPa 124
Figure A.8: Bulk modulus as a function of the oscillation amplitude, and the corresponding Q^{-1}. 124
Figure A.9: Stress-strain loop and K values (slopes) at different stages. 125
Figure A.10: Stress-strain loop of the hydrostatic loading of the saturated sample in a semi-undrained regime. 125

Figure B.1: Evolution of the position of the elasticity domain in the stress space. . . 135
Figure B.2: Remote stress σ_H versus hoop strain ϵ_θ and volumetric strain ϵ_V. . . . 137
Figure B.3: Predictions with Biot-Gassmann of the undrained bulk modulus from the poral porosity and the drained modulus and comparison with the numerical undrained modulus. The elastic material composing the pore shell is purely elastic, setting $\alpha = 0$ (indicating the absence of microporosity). 143
Figure B.4: Predictions for the undrained bulk modulus when $\alpha = 0.8$ (indicating some microporosity within the matrix). 144
Figure B.5: Fourier transform on simulated data. 145
Figure B.6: Fourier transform on simulated data. 146

Figure C.1: The comparison of the shear stress in the lower anvil and actuator. . . . 149

Figure C.2: The 2D mesh, with two elements in each piezo-electric device highlighted in red, for the comparison with the exact 1D solution. 150
Figure C.3: Waveforms at the receiver for different mesh resolutions (number of elements in each piezo-electric device is provided) and comparison with the exact solution in (a). The difficulty of picking the arrival of the S wave is illustrated by zooming in on the waveform in (b). The vertical dashed segment marks the exact arrival time. 152
Figure C.4: Meshes of different resolutions used for convergence analysis on the simplified problem of section 4.5. 153
Figure C.5: Waveforms at the receiver for different mesh resolutions presented in Figure C.4. 154

List of Tables

Table 2.1: Best fitting parameters for the experimental data. 48

Table 3.1: List of parameters used in the hydrostatic loading and unloading simulations for *fit 0*, *fit 1*, and *fit 2*. 63

Table 4.1: The material parameter for PZT ceramics. 79
Table 4.2: Notation used to describe the trajectory and phase of waves. 95
Table 4.3: Properties of the steel materials used in the calibration experiment. . . . 99
Table 4.4: Properties of two sandstones proposed because of their different v_P/v_S ratio. 103

Nomenclature

MICROMECHANICAL MODEL

Lower Case Roman

$\underline{b}$	Displacement jump
$\underline{m}$	Unit vector defining the slip rate direction
$\underline{n}$	Unit normal vector to the crack surface
$\underline{p}$	Unit tangential vector to the crack surface
a	Crack aspect ratio
c	uniform crack density
l	Crack radius
n	Number of cracks in a representative volume element of the matrix
p_f	Fluid pressure
r	Radial position
s	Scalar equal to $\underline{m} \cdot \underline{p} = \pm 1$
u	radial displacement function
v_P	P-wave velocity
v_S	S-wave velocity

Upper Case Roman

$\bar{E}$	Young's modulus of the assemblage
$\bar{G}$	shear modulus of the assemblage
$\mathbb{C}$	Isotropic fourth-order compliance tensor
$\underline{\underline{B}}$	Crack compliance tensor
$\underline{T}$	Stress vector

A_1, A_2 Crack distribution parameters

E Young's modulus of the matrix

E^* Young's modulus of the matrix+cracks

G shear modulus of the matrix

G^* shear modulus of the matrix+cracks

P_c Confining pressure

R_P Pore radius

R_S Outer radius of the shell

R_{pM} Storage coefficient at constant strain

S Skempton's coefficient of the assemblage

V_A Assemblage volume

V_f Total fluid volume in assemblage

V_P Pore volume

V_S Shell volume

V_{fC} Fluid volume in cracks

V_{fS} Fluid volume in the shell

V_{SP} Sample volume

$\mathcal{V}_f$ Total fluid in rock and dead volume

Lower Case Greek

α Biot's coefficient of the matrix

α^* Biot's coefficient of the matrix+cracks

$\bar{\alpha}$ Effective Biot's coefficient of the assemblage

$\bar{\kappa}$ Bulk modulus of the assemblage

$\bar{\kappa}_i$ zero pressure bulk modulus of the assemblage

$\bar{\kappa}_u$ Undrained bulk modulus of the assemblage

$\bar{\kappa}_\infty$ high-pressure bulk modulus of the assemblage

$\bar{\nu}$ Poisson's ratio of the assemblage

$\bar{c}_{opi}$ Zero pressure open-crack density in the assemblage

$\bar{c}_{op}$ Open-crack density in the assemblage

β, β' Polar angles for crack orientation

γ Crack compliance scalar

κ Bulk modulus of the matrix

κ^* Bulk modulus of the matrix+cracks

κ_f Bulk modulus of the fluid

μ Friction coefficient

ν Poisson's ratio of the matrix

ν^* Poisson's ratio of the matrix+cracks

ϕ Porosity due to pore

ϕ_D Porosity equivalence of dead volume

ϕ_M matrix porosity

σ_c Crack closure stress

σ_H Remote hydrostatic stress

$\underline{\underline{\epsilon}}$ Strain tensor

$\underline{\underline{\epsilon}}^c$ strain tensor of crack contribution

$\underline{\underline{\sigma}}$ stress tensor

$\underline{\omega}$ Back stress in kinematic hardening criterion

$\underline{\tau}$ Resolved shear stress vector

θ Total assemblage's volumetric strain

θ^p Assemblage's plastic volumetric strain

φ friction angle

c_{cum} Cumulative crack density in a representative volume element in the shell

WAVE PROPAGATION

Lower Case Roman

$\underline{\underline{e}}$ Third order electromechanical coupling tensor

c Celerity

l Length of the piezoelectric ceramic

q Electric body charge

u Displacement

Upper Case Roman

$\mathbb{C}$ Fourth-order stiffness tensor of the piezoelectric ceramic

$\underline{D}$ Electric displacement vector

$\underline{E}$ Electric field vector

A Unknown function of time

B_1 Material constant

C stiffness in 1D

F Forward wave characteristics

G Backward wave characteristics

L Half the length of the sample

Q Prescribed electric potential

T Pulse period

V Prescribed voltage

$V(t)$ Voltage function

V_P P-wave velocity

V_S S-wave velocity

E Young's modulus

Lower Case Greek

κ Acoustic impedance

ν Poisson's ratio

ρ material density

$\underline{\underline{\epsilon}}$ Strain tensor of the piezoelectric ceramic

$\underline{\underline{\sigma}}$ Stress tensor of the piezoelectric ceramic

$\underline{\underline{\varepsilon}}$ Dielectric permittivity matrix

φ Electric field potential

Chapter 1

Introduction

1.1 Background

A wide range of underground activities, oil and gas exploitation, geothermal energy, or CO_2 sequestration, require periodic acquisition of three-dimensional (3D) seismic data (Landrø, 2015; Lumley, 2010; Vasquez *et al.*, 2019). These data, also known as 4D or time-lapse seismic data, are used to characterise the evolution of the underground target over time. For instance, in carbon sequestration projects, geophysicists use 4D seismic data to monitor the spreading of CO_2 plumes inside reservoirs.

Seismic data provide the velocity V_P of the P-waves and the fastest velocity V_S of the S-waves inside a rock formation. These velocity values, which depend on the local state of stress, the nature of the fluid inside the rock's pores, and the mechanical behaviour of the rock itself, are then used to estimate the average physical properties of the rock formation. Geophysicists possess the tools to account for the effects of the nature of the pore fluid on V_P and V_S. Still, they need to assess the impact of the non-linear and hysteretic effect of the stress path and the associated rock's internal deformation mechanics to determine the rock's properties accurately. Therefore, rock mechanics specialists are solicited to evaluate the dependence of the wave velocity measurements on the rock's structure and stress path.

For this purpose, different laboratory experiments are conducted on small rock samples. Some of these experiments, such as hydrostatic loading or fluid substitution tests (Vasquez *et al.*, 2019), are considered low-cost regarding time (a few hours) and cost. They nevertheless provide an estimate of the elastic moduli of the rock. On the other hand, some experiments are costly; reservoir stress path tests on fluid-saturated samples (*e.g.*, forced oscillation tests), using slow cycles of pore-fluid pressure and starting from initial stress conditions require a two-week procedure. Different experiments pose different challenges, and often come to disparate conclusions. These discrepancies in results are a significant issue for experimentalists, as numerous protracted experiments are usually necessary to study each physical phenomenon separately.

The inconsistency in results is partly due to the dependence of rocks' elastic properties on amplitude and frequency. Using geophysical methods in the laboratory, particularly ultrasonic

waves travelling through rock samples, provides valuable insights and raises new questions. When examining wave propagation within the medium, it is essential to consider the role of wavelength and its relationship with the volume being probed. The effects of scale and frequency are significant factors that need to be addressed, but are not yet fully understood.

At the same time, traditional rock mechanics methods raise significant questions. These methods are grounded in the principles of mechanics for homogeneous materials and usually involve applying large stress increments while measuring the strain in rocks. This approach rests on the assumption that rheological laws, such as Hooke's law, are applicable regardless of the amplitude of strain and the stress regime, whether loading or unloading. However, rocks are complex and often heterogeneous materials at the microscale. Most porous rocks exhibit hysteresis, which has not yet been theoretically explained under hydrostatic conditions.

1.1.1 Hysteresis in rocks

Hysteresis is a significant topic of discussion across various fields. In geoscience, in particular, understanding hysteresis in rocks helps predict rock behaviour under cyclic loading. Referring back to the earlier example of geological storage, in which the rock undergoes repeated compression and extension, the bulk modulus evolves due to hysteresis and fatigue. Therefore, exploring the hysteretic effects of microcracks in such settings would help assess the efficiency of the storage and monitor microstructural damage.

At the microscale, the presence of microcracks and other heterogeneities affects the sensitivity of rocks' elastic properties to pressure amplitude and frequency (Walsh, 1965; Pimienta *et al.*, 2015; Borgomano *et al.*, 2017). As explained by Walsh (1965) and Kachanov *et al.* (2005), the slipping of cracks due to pressure loading, particularly in uniaxial tests, results in energy dissipation at certain loading amplitudes and frequencies. This energy loss, inherent to anelastic deformation, complicates the accurate measuring of the rock's elastic properties. Several studies have examined the frequency effect by drawing parallels with visco-elasticity (Pimienta *et al.*, 2015; Borgomano *et al.*, 2017; David *et al.*, 2013; Lissa *et al.*, 2021; Sun *et al.*, 2020). However, the role of amplitude and stress regime has rarely been investigated, but may be as significant as that of frequency in natural rocks, as shown by the recent findings of Chapman *et al.* (2023).

1.1.2 Mechanics and waves

Understanding the microcrack response to propagating waves is crucial for accurately assessing rocks' mechanical properties and behaviour under various stress conditions. The following discussion introduces the complex interactions between pressure waves, pore structures, and strain amplitudes, highlighting key phenomena such as squirt flow and wave propagation at the laboratory scale.

The propagation of a pressure wave through a fluid-saturated rock generates a pressure gradient that induces, within the pore space, an interaction between the more compliant cracks and the stiffer pores, known as squirt flow. Moreover, squirt flow occurs at high wave frequencies and corresponds to an unrelaxed state characterised by a non-uniform pressure over the material's

representative elementary volume (REV). This phenomenon has been observed experimentally (Mavko *et al.*, 1979; O'Connell *et al.*, 1978), and simulated numerically (Lissa *et al.*, 2021). There is a transition below this high-frequency regime, for which the pores are locally undrained. There is no fluid exchange external to the REV, and the fluid pressure is uniform but modified by the wave propagation. At lower frequencies, there is a fluid exchange with the outside of the REV, which allows for fluid transport, and thus, the fluid pressure can be considered independent of wave propagation. The drained-undrained transition was shown to adhere to a viscoelastic-like behaviour with a unique transition zone (Nowick, 2012).

The influence of the strain amplitudes must be identified to reconcile static and dynamic measurements. Whereas wave strain amplitudes are typically in the range of 10^{-7} to 10^{-6}, loading tests instead measure strain amplitudes from 10^{-4} to 10^{-3}. Hence, a difference in strain amplitudes of at least three to four orders of magnitude occurs. Over such large magnitudes, linear elasticity was seldom shown to be appropriate for rocks. Microcrack theories were devised to investigate the physical parameters involved. However, further work is needed since, even though the dissipation due to crack-slipping has been evaluated analytically in dry uni-axial conditions (David *et al.*, 2012, among others), such a theoretical framework does not apply to the low-cost hydrostatic experiments described above because cracks cannot slip under local hydrostatic stress. Hence, it is of interest to further explore the influence of frictional cracks at different pressure amplitudes, fluid pressure regimes (drained or undrained), and loading conditions (hydrostatic, oedometric, triaxial tests), to propose a complete theory that would explain the amplitude dependence of elasticity measurements, based on microcracks mechanics. The main difficulty is to create a deviatoric stress state at the microscale from the remote hydrostatic loading. In doing so, we expect to reconcile some of the findings of the above low- and high-cost experiments.

Another challenge experimentalists encounter when characterising rock properties is interpreting and picking the first arrival time of S-waves in fluid-saturated samples. This evaluation of the S-wave velocity is essential for assessing the dynamic elastic properties of rocks. A numerical study on the propagation of an elastic wave, from the emission to the reception and the interaction with the acquisition device, is proposed to shed some light on the accuracy of these measurements. This numerical approach at a length scale that includes the whole specimen also provides an opportunity to study the role of heterogeneities on the variability of the velocity measurements. It should be mentioned that academic experimentalists often use quarry specimens which are as homogeneous as possible. In contrast, industrial testing is done on cores retrieved from wells containing a noticeable distribution of defects (vugs, heterogeneities, *etc.*). During summer placements, this work was done in collaboration with *TotalEnergies* at their research laboratories in Pau, France.

1.2 Current state of research

1.2.1 Influence of microcracks in uniaxial loading

The slipping of cracks has long been recognised as the primary cause of hysteresis in rocks subjected to static uniaxial loading (Walsh, 1965; Kachanov, 1982; David *et al.*, 2012). Walsh (1965) explained that the crack-sticking phase at the beginning of unloading creates hysteresis during the uniaxial elastic compression of rocks. This hysteresis occurs because, after the sliding of cracks during loading, twice as much stress is required to initiate the sliding of the same cracks in the opposite direction during unloading. Indeed, analytical models of frictional microcracks, as developed by David *et al.* (2012) and Aleshin *et al.* (2007), have built upon Walsh's seminal work, and have successfully reproduced hysteresis in uniaxial loading conditions. Nevertheless, hysteresis is also observed in dry rocks under macroscopic hydrostatic stress, as demonstrated by studies such as Chapman *et al.*, 2023; Wang *et al.*, 2021; Bakhorji *et al.*, 2010; Jizba *et al.*, 1990; Martin III *et al.*, 1994; and Jeng *et al.*, 2002. In these cases, the connection between hysteresis and frictional cracks is not evident, as there is no macroscopic shear stress to initiate crack slipping.

1.2.2 Influence of microcracks on wave propagation

Regarding the effect of cracks on rocks' dynamic and quasi-static elastic properties, it has been well studied, particularly regarding acoustic non-linearity caused by the interaction between cracks and propagating waves (Biwa *et al.*, 2004; Baltazar *et al.*, 2002; Solodov, 1998). Acoustic non-linearity appears when the amplitude of the propagating wave is large enough to mobilise cracks through mechanisms such as clapping (the opening and closing of cracks) or frictional sliding, leading to hysteresis. This phenomenon is understood in the field of ultrasonics, and has even been used to localise individual cracks by analysing the harmonics and new frequencies that they generate (Delrue *et al.*, 2017). The theory behind acoustic non-linearity is mathematically complex and challenging to implement in 3D. Most existing models are two-dimensional and typically involve superposing an elastic medium with a small finite number of cracks that have known geometries and positions (Aleshin *et al.*, 2018). Generally, the cracks studied in these numerical models are relatively large (10 mm – 20 mm) and exhibit a marked non-linear effect, as discussed by Delrue *et al.* (2018). However, these models, which require discretising each crack, are not well-suited for exploring the influence of microcracks on wave propagation in natural rock samples, which typically contain hundreds of randomly distributed microcracks of unknown shapes.

1.2.3 Implications of strain amplitude on static versus dynamic measurements

The strain amplitude also significantly influences the difference between static and dynamic measurements of bulk modulus. Research by Chapman *et al.* (2023) demonstrates that when static experiments are conducted at smaller strain amplitudes, the resulting measurements more closely align with dynamic properties. This was observed through slow forced oscillations that

induced strain amplitudes ranging from 10^{-6}, similar to the amplitude of ultrasonic waves, to 10^{-3}. The study revealed that a key mechanism behind the discrepancy between static and dynamic bulk modulus depends on strain amplitude, even in dry rocks. This finding, observed at low frequencies, appears to rule out fluid flow effects, making frictional dissipation the primary factor to consider at such frequencies. Frictional sliding is directly related to the amplitude of the strain; the larger the amplitude, the more significant the sliding effect. However, no theoretical model currently substantiates the idea that, under hydrostatic conditions, the sliding of frictional microcracks and contacts contributes to the discrepancy between static and dynamic bulk modulus measurements.

1.3 Research gaps

There is evidence for hysteresis in rocks under hydrostatic loading. However, no theoretical study has ever explored the causes of such hysteresis, to the author's knowledge. Under hydrostatic stress, no macroscopic phenomenon explains the hysteresis in volumetric strain. Many unchecked hypotheses gravitate around this topic. Some argue that the rock's relaxation rate could cause such hysteresis, doubting the true static nature of the experiments. Others point to a possible non-isotropic distribution of microcracks in certain rocks, which might lead to hysteresis.

Although the complexities of hysteresis in rocks under hydrostatic loading are still largely unexplored, there are also significant knowledge gaps regarding the practical challenges of ultrasonic wave propagation in rocks at the laboratory scale. Ultrasonic simulations at the laboratory scale are relatively rare and often rely on proxies, such as displacement, to replicate the input pulse and output signal (Huang *et al.*, 2021; Yurikov *et al.*, 2019). These approximations typically consider the displacement in only one direction, resulting in independent signals for longitudinal and transversal waves. Although the piezoelectric materials inside the captors have a poling direction, designed to generate/capture either P or S waves, some mechanical energy from the unwanted type of wave will always be converted into an electrical signal.

1.4 Focus and scope

The micromechanical model developed in this research simulates hysteresis in dry or saturated porous rocks under hydrostatic loading. It is specifically designed for homogeneous poroelastic sedimentary rocks, such as sandstones and carbonates. The model only utilises parameters with real physical significance, including crack density, rock porosity, and the elastic properties of the rock's mineral phase. This model is applicable to both drained and undrained experiments, with the assumption that fluid pressure remains homogeneous throughout the sample. It is tailored for experiments that apply a slow-progressing hydrostatic load within the specimen's elastic range, ensuring that no crack propagation or nucleation occurs. Additionally, it can simulate forced oscillation experiments by oscillating either the confining pressure or the fluid pressure, using oscillation amplitudes as small as 0.01 MPa. These small amplitudes correspond to strains on the order of 10^{-6} to 10^{-7}, similar to those induced by propagating ultrasonic waves.

The micromechanical model is developed as part of a numerical rock mechanics laboratory that simulates the rock's response to stress perturbations, such as loading and ultrasonic wave propagation tests, within a confining cell. While the thesis focuses on microstructural mechanics, it also examines issues at the machine scale, specifically regarding the accurate detection of S-waves in hydraulic press experiments. To achieve this, we have devised a method to simulate the propagation of waves from the source to the receiver while considering the interactions between the sensors, the rock sample, and the hydraulic press. This numerical tool can be configured for any shape of confining cell and any piezoelectric sensor, provided that its piezoelectric parameters are known, as well as for any acquisition geometry.

1.5 Questions and objectives

This research aims to answer four fundamental questions:

1. Are frictional microcracks responsible for the hysteresis observed in porous rocks during hydrostatic loading and unloading?
2. Is there a strain amplitude effect regarding the role of microcracks on hysteresis in hydrostatic conditions?
3. How do frictional microcracks contribute to the discrepancy between static and dynamic elastic properties, in particular the bulk modulus?
4. How can we improve dynamic measurements by increasing the accuracy of S-wave arrival detection in ultrasonic wave experiments, in the prospects of developing a numerical rock mechanics laboratory?

The first question will be addressed by developing a relatively simple micromechanical model incorporating randomly distributed, identical frictional microcracks, which generate hysteresis under hydrostatic loading. A more complex version of this micromechanical model, which includes a distribution of microcracks with various aspect ratios, will be proposed to explore the second and third questions. The potential influence of strain amplitude on the role of microcracks will be examined by simulating forced oscillation experiments with varying oscillation amplitudes.

Regarding the contribution of microcracks to the difference between the static and dynamic bulk modulus, small strain amplitudes (on the order of wave-induced strain, 10^{-6}) will be simulated both with and without frictional microcracks. If the two simulated results are identical, we will conclude that frictional microcracks do not affect the discrepancy between static and dynamic measurements. Conversely, if the results differ, we will be able to estimate the energy dissipation, caused by propagating waves, associated with frictional sliding. By quantifying this energy dissipation, we can correct the dynamic measurements for frictional effects.

The final question sets the foundation for developing a numerical rock mechanics laboratory that will, ultimately, incorporate the micromechanical model created in response to the previous question. Because most ultrasonic sensors used to measure the dynamic properties of rocks are

piezoelectric, and piezoelectric properties are essential for ensuring signal quality, we will address the last question by developing a spectral finite element tool that will solve the coupled electro-mechanical problem within the source, propagate the mechanical wave through the sample and apparatus, and convert the mechanical energy back into an electrical signal at the receiver. The simulated waveform at the receiver will provide insights into the noise surrounding the S-wave signal.

1.6 Limitations

The micromechanical model proposed in this thesis has some limitations that should be acknowledged for a comprehensive understanding of hysteresis under hydrostatic conditions.

First, the model is purely static, which means it does not take into account strain-rate effects or any other time-dependent mechanisms that may relate to frictional cracks. The friction coefficient used is consistently static, adhering to Coulomb's law. Similarly, no visco-elasticity is considered for fluid-saturated samples. In the model, fluids are defined only by their bulk modulus.

Second, the model assumes uniform slip across the surface of the crack without considering the possibility of partial slip at the outer edges of Hertzian contacts, as discussed in some previous studies (Mavko, 1979; Stewart *et al.*, 1983).

Lastly, the model neglects contact adhesion hysteresis, influenced by various surface forces such as Van der Waals attraction and electrostatic repulsion acting at the contacts (*e.g.*, Tutuncu *et al.*, 1992). This factor can be significant in some types of rocks.

1.7 Structure overview

The body of this research is organised into two parts. The first part focuses on developing a micromechanical model for hysteresis in porous rocks under hydrostatic loading. This section is divided into two chapters. The first chapter discusses a model featuring a single family of microcracks with identical shapes, published in the *Journal of the Mechanics and Physics of Solids* (Biyoghé *et al.*, 2024a). The second chapter, which has been submitted for publication, presents an enhanced version of that model by introducing a distribution of cracks with varying aspect ratios. Both models are applied to porous rocks of different types.

The third part introduces a numerical tool designed to assist experimentalists in identifying the S-wave during ultrasonic wave experiments, which has resulted in a publication in *Geophysics* (Biyoghé *et al.*, 2024b). This chapter provides a new analytical solution for the coupled electro-mechanical problem within piezoelectric transducers. The spectral finite element method is employed to simulate wave propagation from the source to the receiver within a confining cell. The simulated waveform is then analysed, clarifying the origin of the noise preceding the S-wave arrival and revealing the signature pattern of the S-wave.

Figure 1.1 provides a visual representation of the tentacular nature of this research, highlighting

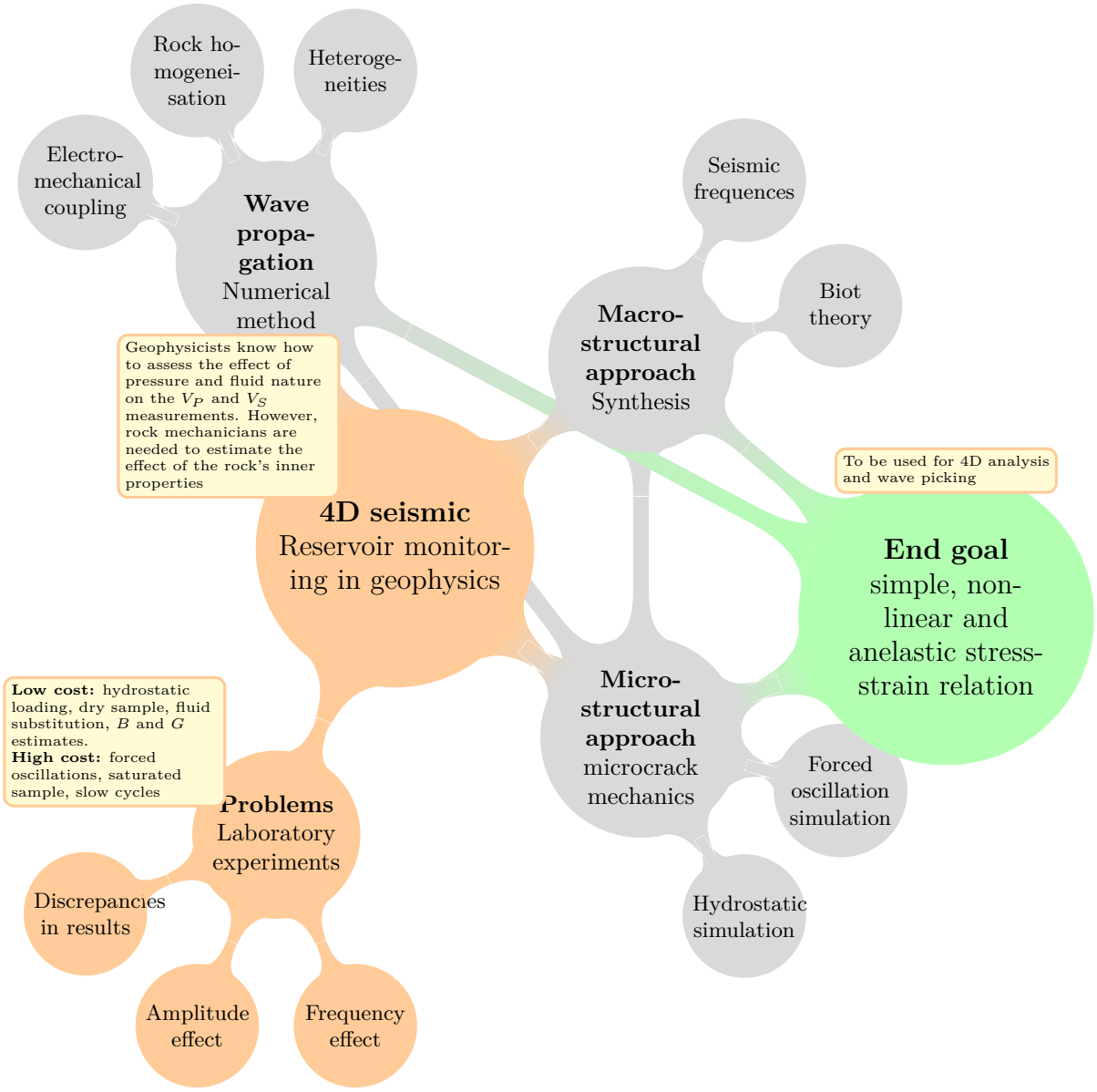


Figure (1.1) PhD mind map. Colour code: *orange* = challenges, *gray* = PhD solutions, *green* = final objective.

the connections between the main works of the thesis and showcasing the central themes of the research. The orange-coloured bubbles summarise the scientific questions, with the largest bubble representing the "client" who will hopefully utilise the final results of the thesis shown in the green bubble. The thesis work is illustrated through a series of grey bubbles grouped into three sections. At the bottom, we have the microstructural approach, which includes the hydrostatic experiment modelling that is currently under investigation. The group at the top of the figure pertains to numerical modelling at the scale of the specimen and the experimental device. The series of bubbles in the top right corresponds to the synthesis of all this work and suggests the possibility of proposing a simple, phenomenological theory for the end user. This phenomenological theory will be easier to apply while still preserving the essence of the micro-scale analyses.

Chapter 2

Frictional Microcrack Model with a Single Crack Family

Chapter Abstract

A micro-mechanical model is proposed to predict the stress-strain hysteresis during the cyclic hydrostatic loading of fluid-saturated rocks under drained or undrained conditions. A spherical pore is surrounded by a multi-cracked shell where local deviatoric stress develops despite the remote hydrostatic loading. The effective properties of the material composing the shell are constructed assuming an isotropic distribution of cracks with no interaction, and the overall properties thanks to the spherical assemblage approach. The fluid pressure in drained and undrained conditions is assumed to be uniform throughout the assemblage. A new analytical solution is proposed, assuming all cracks are closed and slipping either forwardly or reversely. It is shown with numerical simulations for drained conditions that this assumption is indeed respected for sufficiently small values of the crack friction angle. However, for reasonable values, the closed cracks during the unloading phase could slip in either direction: reversely close to the pore and still forwardly away from the pore. Moreover, at critical radii, the slip could occur in either direction depending on the crack orientation. A similar micro-structural response is observed for undrained conditions, although the remote confining stress required to close the cracks is much larger. The model's predictions compare favourably with recent experimental data on dry sandstones and carbonates, which were presented in a study on the influence of strain amplitude on the transition between static and dynamic properties. The crack density and matrix elasticity modulus are sufficient fitting parameters to accurately predict the hysteresis loops, especially for porosity levels above 10%.

2.1 Introduction

There are at least two motivations for conducting laboratory hydrostatic loading tests, both under dry and saturated conditions, to estimate the elastic properties of rocks. The first motivation stems from the simplicity of the procedure, which leads to low experiment costs, especially

under dry conditions. In the energy industry, such test results are used to connect wave velocity variations with fluid pressure changes, contributing to 4D seismic interpretations used for reservoir monitoring (Vasquez *et al.*, 2019). The second motivation stems from recent experimental advancements in the frequency and amplitude dependence of elastic properties to link the static and dynamic elastic properties (Pimienta *et al.*, 2015). However, the hydrostatic test presents some challenges. For instance, in static loading tests, different bulk modulus values are measured at various stages of the loading cycle. Moreover, the hysteresis between the loading and unloading stages is evidence of inelastic behaviour despite the lack of any macroscopic deviatoric stress (Chapman *et al.*, 2023; Wang *et al.*, 2021; Jizba *et al.*, 1990; Martin III *et al.*, 1994). Our interest in this chapter is to propose a micro-structural model justifying the cause of hysteresis and predicting the hysteresis loop in hydrostatic tests.

The presence of cracks has long been identified as the leading cause of hysteresis in compression tests (Walsh, 1965; Pimienta *et al.*, 2015; Borgomano *et al.*, 2017). The matching between experiments and theoretical predictions of this hysteresis for uni-axial loading is now established (*e.g.* David *et al.*, 2012) but remains open for hydrostatic loading. Local deviatoric stress is needed to cause the cracks to slip and trigger hysteresis. For this reason, the model problem of a spherical pore inside a spherical multi-cracked shell is proposed to generate the local deviatoric stress responsible for crack slip. The randomly distributed cracks, once closed and slipping, reduce the local shear modulus and thus affect the effective bulk modulus of the assemblage. Despite the absence of crack propagation or interaction, this influence results in a hysteretic evolution of the effective bulk modulus of the assemblage.

Several elements are necessary to construct this model problem and are now reviewed. A first homogenisation is considered to estimate the local effective properties within the multi-cracked shell, following the simple scheme for non-interactive penny-shaped cracks of Kachanov (1982). This first homogenisation supposes that the micro-cracks have the same dimensions, friction coefficient, and an isotropic distribution. In addition, the value of the crack density is purposely exaggerated to compensate for the lack of crack interaction. Using these same hypotheses, Aleshin *et al.* (2007) and David *et al.* (2012) have reproduced the hysteresis in Young's modulus of micro-cracked rocks under cyclic uniaxial loading. The quality of their results was a motivation for using Kachanov's scheme, among other micro-mechanics models (Christensen, 1990), to predict the hysteresis of rocks under hydrostatic cyclic loading.

A second homogenisation concerns the spherical multi-cracked shell and the fluid-filled pore interacting with the remote homogeneous medium. It follows the work of Hashin (1962) and is referred to as the spherical assemblage. This approach has garnered significant attention in the literature. For instance, it could be extended to an arbitrary number of layers (Hervé *et al.*, 1993), include interface conditions (Benveniste, 1985), and account for interaction via a Green's function approach (Kanaun *et al.*, 1986). Closer to our application, Pan *et al.* (1996) included a cracked layer in the spherical assemblage and used the dilute concentration method to estimate the effective properties. They only accounted for the effect of the crack's compliance to reproduce non-linear elasticity. No composite sphere assemblage model containing frictional cracks has been proposed so far, at least to the authors' knowledge. The proposed model

includes friction and accounts for the changes in the pore fluid pressure and volume (a dead fluid volume is also included) in drained or undrained conditions.

The contents of this chapter are as follows. Section 2.2 contains the presentation of the model problem, including the first homogenisation scheme to define the shell material properties, the evolution of the fluid pressure for undrained conditions, and the expected structure of the poro-elasto-plastic constitutive response at the assemblage scale. Rice (1977)'s argument (also discussed more recently in Viesca *et al.*, 2008) is invoked to suggest that the same Biot coefficient enters the relation between stress, strain, and fluid pressure changes as well as the relation between the pore volume fraction and the assemblage volume changes. The analytical solutions for drained and undrained conditions are also presented for open or closed and sticking cracks. A novel solution assuming all cracks slip is given in Appendix B.7. Since the assumptions behind these analytical solutions are not always valid, a numerical solution based on the finite-element method is also proposed (Appendix B.3). The numerical algorithms for open cracks and slipping cracks are discussed in Appendices B.4 and B.5, respectively. The difficulty of the second algorithm for a Coulomb criterion is that the stress path is via the tip of the cone (yield surface) at crack closure, as shown in Appendix B.6, which motivates the association between the fracture mechanics argument and the kinematic hardening plasticity model considered here. The hysteresis predicted by this model problem is presented in Section 2.3. The assemblage's response compares well with the new analytical solution for all slipping cracks, only for vanishing friction values. For reasonable values, it is shown that the crack activation is far from homogeneous during the loading cycle, which is the primary assumption of the analytical solution. The forward slip could still be activated within the shell material during the early unloading phase, concurrent with the reverse slip afterwards. Then, the impact of different crack parameters (crack closure stress, crack density, and friction) on the amount of hysteresis and the shape of the hysteresis loop is discussed. The predictions for undrained conditions are also presented. Section 2.4 proposes a set of numerical results matching the experimental data from Chapman *et al.* (2023) on the hydrostatic compression of different dry rock samples. The experimental hysteresis loops are well predicted while only using the crack density and the matrix elasticity modulus as fitting parameters.

2.2 Problem description

The model problem consists of a spherical assemblage subjected to hydrostatic loading, influenced by similar prototypes found in the literature since the early work of Hashin (1962). The geometry of the micro-structural prototype is presented in Figure 2.1. It includes a pore surrounded first by a shell and second by an infinite effective medium that sustains a homogeneous, hydrostatic stress state. The ratio of the pore to the external shell radii is set to represent the poral porosity of the effective medium: $\phi = (R_P/R_S)^3$, without taking into account the secondary porosity of the shell matrix. The shell material is an elastic and isotropic matrix with an isotropic distribution of initially open, penny-shaped cracks.

The constitutive relations are presented next in a rate form because of the non-linear evolution of

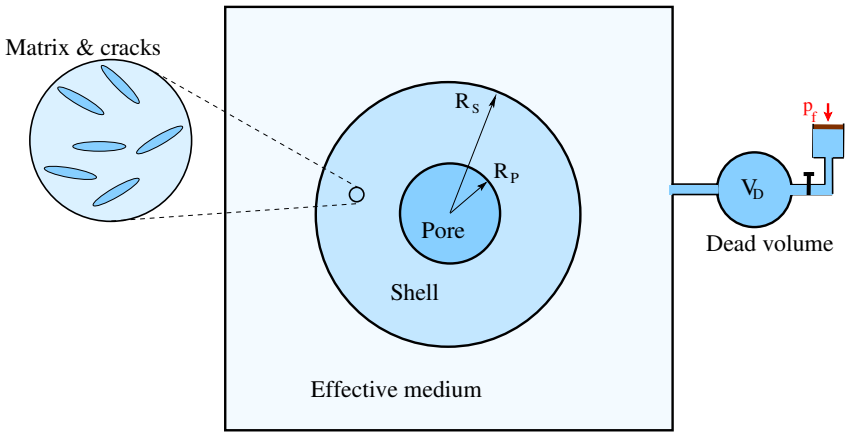


Figure (2.1) The specimen's response is described using two homogenisation schemes. The first scheme deals with an isotropic distribution of cracks within a porous, fluid-saturated elastic matrix. The second scheme covers the interaction between the spherical assemblage and the effective medium, maintaining a uniform stress state. The fluid pressure is uniform throughout the specimen and in the dead volume. The fluid mass remains constant if the tap is closed. If the tap is open, the experiment is pressure-controlled.

internal parameters. However, no physical time scales due to inertia or viscosity are introduced. The loading responsible for this evolution is initiated from hydrostatic conditions corresponding to the homogeneous stress state $-p_{f0}\underline{\underline{\delta}}$ within the assemblage and the fluid pressure p_{f0}. Note that a subscript of zero indicates the initial value of the highlighted quantity (except for the various porosities that will be introduced later). Also note that $\underline{\underline{\delta}}$ represents the second-order identity tensor, denoted with double underlines, which applies to all second-order tensors in the subsequent sections.

2.2.1 The shell material as a homogenized medium

The material composing the shell is a porous matrix with an isotropic distribution of cracks. The whole is described via a homogenisation scheme, disregarding any crack interaction. There is a separation of scales between the crack length and the micro-pore radius, with the latter being significantly smaller than the former. The objective is to summarise this homogenisation scheme presented by Kachanov (1982), to compute the fluid volume within the cracks, and to prepare the grounds for the interaction analysis with the pore.

Each material point within the shell is assumed to contain an isotropic distribution of penny-shaped micro-cracks with a dimensionless crack number nl^3/V in which n is the number of cracks of radius l contained in the REV of volume V. The strain rate over the representative elementary volume, denoted $\dot{\underline{\underline{\epsilon}}}$, is the sum of the strain rates due to the matrix and to the cracks,

$$\dot{\underline{\underline{\epsilon}}} = \mathbb{C} : (\dot{\underline{\underline{\sigma}}} + \alpha \dot{p}_f \underline{\underline{\delta}}) + \frac{c\pi}{2l} \int_{\mathcal{H}} \dot{\underline{b}}(\underline{n}) \otimes \underline{n} + \underline{n} \otimes \dot{\underline{b}}(\underline{n}) \, d\mathcal{H} \,, \tag{2.1}$$

in which $\mathbb{C}$ is the isotropic matrix compliance fourth-order tensor, $\dot{\underline{\underline{\sigma}}}$ is the stress rate tensor at the material point within the shell, and α is Biot's coefficient. The integral on the right-hand side of (2.1) is over the hemisphere $\mathcal{H}$ defining all possible orientations of the unit normal $\underline{n}$ of the micro-cracks, Figure 2.2. Note the two polar angles β and β' in this figure define the

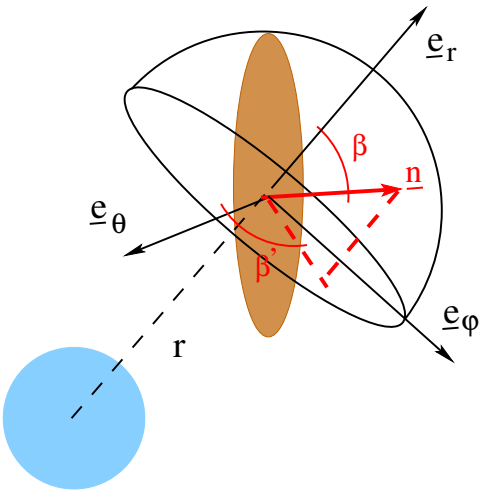


Figure (2.2) A crack of the isotropic distribution, within the shell at the distance r from the pore centre, has the unit normal $\underline{n}$ oriented by the two polar angles β and β'.

normal orientation and have the ranges $[0;\pi/2]$ and $[0,2\pi]$, respectively. The definition of $\mathcal{H}$ implies that the scalar c in (2.1) denotes the crack density spherical distribution $nl^3/(2\pi V)$ and is referred to as the crack density in what follows. For each crack orientation, there is an average displacement jump $\underline{b}$ across the crack surfaces, which contributes to the definition of the strain rate in eq. (2.1). The cracks are initially open, and the average displacement over the crack surfaces is then given by:

$$\dot{\underline{b}} = \underline{\underline{B}} \cdot (\dot{\underline{T}} + \dot{p}_f \underline{n}) \quad \text{with} \quad \underline{\underline{B}} = \gamma(\underline{\underline{\delta}} - \frac{\nu}{2} \underline{n} \otimes \underline{n}) \quad \text{and} \quad \gamma = \frac{32l}{3\pi E} \frac{1-\nu^2}{2-\nu}\,, \tag{2.2}$$

in terms of the second-order crack compliance tensor $\underline{\underline{B}}$, the stress vector $\underline{T}$ based on the stress at the material point within the shell and the crack compliance scalar γ function of E and ν, standing for the matrix elasticity modulus and Poisson's ratio, respectively. Note that the Terzaghi stress is used in (2.2), whereas Biot's effective stress is used for the elastic matrix response in (2.1). Note also that the displacement jump is decomposed into tangential and normal components:

$$\dot{\underline{b}} = \dot{\underline{b}}_t + \dot{\underline{b}}_n \quad \text{with} \quad \dot{\underline{b}}_n = \gamma(1-\frac{\nu}{2})\, \underline{n} \otimes \underline{n} \cdot (\dot{\underline{T}} + \dot{p}_f \underline{n}) \quad \text{and} \quad \dot{\underline{b}}_t = \gamma\, (\underline{\underline{\delta}} - \underline{n} \otimes \underline{n}) \cdot (\dot{\underline{T}} + \dot{p}_f \underline{n})\,, \tag{2.3}$$

these relations to the effective stress being deduced from (2.2).

Cracks are fluid-saturated, and their closure requires that the normal component of the effective stress vector to be larger in magnitude than the closing stress σ_C, a positive scalar. This condition reads, in terms of the total normal stress,

$$\sigma_n \leq -(\sigma_C + p_f) \quad \text{with} \quad \sigma_n = \underline{n} \otimes \underline{n} : \underline{\underline{\sigma}}\,. \tag{2.4}$$

Combine the normal displacement relation in (2.3) and this closing condition to estimate the initial aspect ratio of the circular cracks. This aspect ratio and its evolution during loading are essential to estimate the fluid volume contained in the cracks. In particular, the fluid volume

within the cracks is computed as follows for initial conditions. Consider a hydrostatic loading and use eq. (2.1) to determine the volume change for normal stress based on the closure criterion (2.4). The opposite value is the initial fluid volume in the cracks, which is referred to as the initial crack porosity:

$$\phi_C = \frac{32\pi}{3}\frac{\sigma_C}{E}(1-\nu^2)c\,. \tag{2.5}$$

Once a crack is closed, only its tangential component of the average displacement discontinuity continues to evolve because of slip, and its rate is controlled by a Coulomb condition f_n. Slip is prevented if

$$f_n \equiv |\underline{\tau} - \underline{\omega}_n| + \mu(\sigma_n + \sigma_C + p_f) < 0 \quad \text{with} \quad \underline{\tau} = (\underline{\underline{\delta}} - \underline{n}\otimes\underline{n})\cdot\underline{T}\,, \tag{2.6}$$

in which $\underline{\tau}$ is the resolved shear stress, μ a constant friction coefficient, and $\underline{\omega}$ is referred to as the back-stress. This last terminology is proposed because of the analogy between criterion (2.6) and the structure of the kinematic hardening of plasticity (Prager, 1955), as mentioned by Andrieux *et al.* (1986). The back-stress evolution is, however, different from what is constructed with a plasticity theory since it also evolves in the elastic range so that the criterion $f_n = 0$ at the transition between opening and closing (see Appendix B.6 for a complete discussion). The consequence of this evolution up to crack closure is that at first inspection of the stick condition in (2.6), the stress point is precisely at the tip of the Coulomb cone in the stress space spanned by the resolved shear and effective normal stresses. The back-stress in the elastic domain is thus simply equal to the resolved shear stress $\underline{\tau}$, which, given its definition in (2.6) and the structure of the crack compliance tensor in (2.2) and (2.3), is interpreted as the tangential displacement jump $\underline{b}_t$ divided by the compliance scalar γ: $\underline{\omega} = \underline{\tau} = (1/\gamma)\underline{b}_t$.

This relation between the tangential displacement jump and the back-stress is extended in a rate form if a slip occurs:

$$\dot{\underline{b}}_t = \gamma\,\dot{\underline{\omega}}\,. \tag{2.7}$$

The back-stress rate $\dot{\underline{\omega}}$ is zero if the stick condition corresponding to $f_n < 0$ or $f_n = 0$ and $\dot{f}_n < 0$ is respected. Slip occurs if $f_n = 0$ and $\dot{f}_n = 0$, and the latter equation is the consistency condition leading to the back-stress rate evaluation done in two steps. First define the direction of the back-stress rate $\dot{\underline{\omega}}$ with

$$\dot{\underline{\omega}} = \dot{\lambda}\underline{m} \quad \text{and} \quad \underline{m} = \frac{\underline{\tau} - \underline{\omega}}{|\underline{\tau} - \underline{\omega}|}\,, \tag{2.8}$$

in which $\underline{m}$ is a unit vector, and second, use the consistency condition to determine the rate of the yet unknown scalar $\dot{\lambda}$, where:

$$\dot{\lambda} = \underline{m}\cdot\dot{\underline{\tau}} + \mu(\dot{\sigma}_n + \dot{p}_f)\,. \tag{2.9}$$

A simple application of this framework to understand the response of a single crack family and to illustrate the definition of the back-stress is presented in Appendix B.6.

Further information is required to describe the fluid content at each material point composing the shell via what is classically called the pore volume fraction in the poro-mechanics literature (Rice *et al.*, 1976). In the present setting, this variable corresponds to the fluid volume within the elastic matrix and the cracks, normalised by the initial volume of the REV.

There is indeed a relation between the REV pore volume fraction rate of change $\dot{v}$ with first the fluid pressure and second the local matrix volume change, the latter being the difference between the REV rate $\dot{\epsilon}_v$ and the volume change of the cracks $\dot{\epsilon}_{vC}$. In this study, such a relation is proposed as if an energy potential was postulated (Rice, 1977), and consistently with eq. (2.1):

$$\dot{v} = \alpha(\dot{\epsilon}_v - \dot{\epsilon}_{vC}) + R_{pM}\dot{p}_f + \dot{\epsilon}_{vC}\,, \tag{2.10}$$
$$\text{with} \quad \dot{\epsilon}_{vC} = \frac{c\pi\gamma}{l}(1-\frac{\nu}{2})\int_{\mathcal{H}_O}(\dot{\sigma}_n + \dot{p}_f)\,d\mathcal{H} \;\text{ and }\; R_{pM} = \frac{(1-\alpha)(\alpha-\phi_M)}{\kappa}\,.$$

The additional material constant R_{pM} is the storage coefficient at constant volumetric strain defined here in terms of Biot's coefficient, the bulk modulus κ and the initial porosity ϕ_M of the elastic, isotropic matrix material composing the shell. Note that the integral in eq. (2.10) is restricted to the part of the hemisphere $\mathcal{H}_O$ corresponding to open cracks and that the integrand was obtained from the normal part of the crack displacement jump defined in eq. (2.3).

2.2.2 The fluid pressure

The fluid pressure during a test could either be controlled externally by a pump or vary because the total fluid mass is conserved. In Figure 2.1, the controlled pressure case corresponds to an open tap letting the fluid flow to or from a reservoir where the fluid level changes, ensuring the pressure is at the desired value. If the tap is closed, the pressure varies because the fluid mass within the specimen and the dead volume are conserved. In both cases, the specimen permeability is assumed to be large enough or equivalently, that the loading rate is slow enough, so that the fluid pressure change is homogeneous over the whole fluid system. Consequently, these two cases correspond to locally drained conditions with controlled pressure or constant fluid mass. Nevertheless, in what follows, they will be referred to as drained and undrained conditions, keeping in mind the macro-scale response. This section evaluates the pressure change during loading if the fluid mass is kept constant under undrained conditions.

The total fluid volume within the experimental system includes contributions from the pore, the shell volume due to its porosity and cracks, and the dead volume. The latter is constant in time, and the question is the evaluation of two earlier volume changes. First, consider the shell material and the pore volume fraction change of the REV, which is the integral through the loading of the expression in (2.10):

$$v = \frac{\alpha}{\kappa}[P + \alpha p_f + (1-\alpha)p_{f0}] + R_{pM}(p_f - p_{f0}) + \epsilon_{vC}\,, \tag{2.11}$$
$$\text{with} \quad \epsilon_{vC} = \frac{c\pi\gamma}{l}(1-\frac{\nu}{2})\left(\int_{\mathcal{H}_O}(\sigma_n + p_f)\,d\mathcal{H} - \int_{\mathcal{H}_C}\sigma_C\,d\mathcal{H}\right),$$

in terms of the hydrostatic stress $P = \mathrm{tr}(\underline{\underline{\sigma}})/3$, one-third of the stress tensor trace. This stress is introduced because the elastic part of the constitutive relation in (2.1) has been used to eliminate the elastic part of the REV strain rate in (2.10). The volume change due to the cracks ϵ_{vC} is defined in eq. (2.11)b with two integrals. The first integral is over $\mathcal{H}_O$, the part of the hemisphere corresponding to open cracks, and the second $\mathcal{H}_C$ over the complementary part where the cracks are closed. The second integrand is based on the closure criterion (2.4). The two quadratures over the hemisphere are now included following the techniques presented in Appendices B.2 and B.4:

$$\begin{aligned} \epsilon_{vC} \quad = \quad & \frac{c\pi^2\gamma}{3l}(2-\nu)((\sigma_r + p_f)(1-\cos^3\beta_c) + \\ & (\sigma_\theta + p_f)(2 - 3\cos\beta_c + \cos^3\beta_c) - 3\sigma_C\cos\beta_c\,)\,, \end{aligned} \tag{2.12}$$

with the introduction of β_c, the critical value of the first polar angle, which marks the limit of crack closure in the interval $[0;\pi/2]$ according to the condition (2.4).

The contribution of the REV to the shell material, equations (2.11) and (2.12), is now integrated over the shell domain to obtain the normalised shell fluid volume relative change

$$\begin{aligned} \frac{V_{fS} - V_{fS0}}{V_{S0}} = (R_{pM} + \frac{\alpha^2}{\kappa})(p_f - p_{f0}) + \frac{3\alpha}{\kappa(1-\phi)}\int_{\phi^{1/3}}^1 (P + p_{f0})\, r'^2 dr' + \\ \frac{c\pi^2\gamma}{l}\frac{2-\nu}{1-\phi}\int_{\phi^{1/3}}^1 [(\sigma_r + p_f)(1-\cos^3\beta_c) + \\ (\sigma_\theta + p_f)(2 - 3\cos\beta_c + \cos^3\beta_c) - 3\sigma_C\cos\beta_c\,]r'^2 dr \quad \text{with} \quad V_{fS0} = V_{S0}(\phi_M + \phi_C)\,, \end{aligned} \tag{2.13}$$

with the normalisation $r' = r/R_S$ and noting that the angle β_c is now a function of the radial position. The volume V_{S0} is the initial volume of the outer shell of the assembly $4\pi(R_S^3 - R_P^3)/3$ and V_{fS0} the initial shell fluid volume, which is due to its matrix porosity ϕ_M and to the initial crack porosity ϕ_C, the second defined in eq. (2.5)

The second contribution to the fluid volume of the spherical assembly is due to the pore:

$$V_P - V_{P0} = 3\frac{u(R_P)}{R_P}V_{P0} \quad \text{with} \quad V_{P0} = \frac{4\pi}{3}R_P^3\,, \tag{2.14}$$

expressed in terms of the radial displacement at the pore wall.

The current total fluid volume within the assemblage is then deduced from (2.13) times V_{S0} and (2.14). Divide this resulting scalar by the initial volume of the assemblage V_{A0}, multiply that by the initial volume of the specimen V_{SP0}, and add the volume of the dead volume V_D to obtain the total fluid content within the experimental system depicted in Figure 2.1. This global volume $\mathcal{V}_f$ is now presented normalized by the initial specimen volume:

$$\frac{\mathcal{V}_f}{V_{SP0}} \equiv (V_P + V_{fS})\frac{1}{V_{A0}} + \phi_D\,, \quad \text{with} \quad \phi_D = \frac{V_D}{V_{SP0}}\,, \tag{2.15}$$

introducing an apparent additional porosity ϕ_D defined as the dead volume divided by the initial

volume of the specimen. The initial value of the normalized global volume in (2.15) is:

$$\frac{\mathcal{V}_{f0}}{V_{SP0}} = \phi + (\phi_M + \phi_C)(1-\phi) + \phi_D \,, \tag{2.16}$$

having introduced the initial assemblage porosity ϕ, matrix porosity ϕ_M, and fracture porosity ϕ_C. The variation of the global fluid volume in eq. (2.15) is:

$$\frac{\Delta\mathcal{V}_f}{V_{SP0}} = \frac{\Delta V_P}{V_{P0}}\phi + \frac{\Delta V_{fS}}{V_{S0}}(1-\phi) \,, \tag{2.17}$$

since the dead volume is constant throughout the loading, and having introduced the symbol Δ to denote the variation of the various volumes from their initial conditions. This global fluid volume change, normalised by its initial value, is also related to the fluid pressure change and its bulk modulus κ_f so that, combining (2.16) and (2.17):

$$\frac{\Delta V_P}{V_{P0}}\phi + \frac{\Delta V_{fS}}{V_{S0}}(1-\phi) = -\frac{p_f - p_{f0}}{\kappa_f}[\phi + (\phi_M + \phi_C)(1-\phi) + \phi_D] \,. \tag{2.18}$$

The combination of the results in (2.18) with (2.14) and (2.13), after some simplifications, provide the equation for the fluid pressure:

$$Y_p(p_f - p_{f0}) = Y_H \quad \text{with} \tag{2.19}$$

$$Y_p = -\left(\frac{\phi_D + \phi}{\kappa_f} + (1-\phi)(R_{pM} + \frac{\alpha^2}{\kappa} + \frac{\phi_M + \phi_C}{\kappa_f}) + \frac{3c\pi^2\gamma}{l}(2-\nu)\int_{\phi^{1/3}}^{1}[1-\cos\beta_c]r'^2 dr'\right)$$

$$\text{and} \quad Y_H = 3\phi\frac{u(R_P)}{R_P} + \int_{\phi^{1/3}}^{1}\left[\frac{3\alpha}{\kappa}(P + p_{f0}) + \frac{c\pi^2\gamma}{l}(2-\nu)[(\sigma_r + p_{f0})(1-\cos^3\beta_c) + \right.$$

$$\left.(\sigma_\theta + p_{f0})(2 - 3\cos\beta_c + \cos^3\beta_c) - 3\sigma_C\cos\beta_c\right]r'^2 dr' \,.$$

Two special cases are of interest, the first corresponding to a matrix with open cracks ($\beta_c = \pi/2$ at every radius r' in eq. 2.19). The elasticity solution provided in Appendix B.1 is then used to find the following relation between the remote stress and the pressure change

$$p_f - p_{f0} = S\,(\sigma_H - p_{f0}) \quad \text{with} \quad S = \frac{Z_H}{Z_p} \,, \tag{2.20}$$

$$Z_p = \frac{1}{\kappa_f}[\phi_D + \phi + (\phi_M + \phi_C)(1-\phi)] + (R_{pM} + \frac{\alpha^2}{\kappa})(1-\phi) + \frac{c\pi^2\gamma}{l}(2-\nu)$$

$$+\frac{\alpha\phi}{\kappa} - \phi\frac{1-\alpha*}{\kappa^*} + \frac{3\phi}{1-\phi}(\frac{1}{3\kappa^*} + \frac{1}{4G^*}) \quad \text{and}$$

$$Z_H = \frac{3\phi}{1-\phi}(\frac{1}{3\kappa^*} + \frac{1}{4G^*}) + \frac{\alpha}{\kappa} + \frac{c\pi^2\gamma}{l}(2-\nu) \,,$$

the definition of the triplet, $(\alpha^*, \kappa^*, G^*)$ being found in eq. (B.16) in Appendix B.2. The second case of interest is if all cracks are closed, although eq. (2.20) should be applied to some reference stress conditions other than the initial ones. For this second special case the same triplet equals the solid matrix value (α, κ, G) and the crack density c is set to zero. In these two extreme cases, the relation in (2.20) is linear, as expected, showing that the loading through a pressure

change or the remote loading is proportional with a constant S, which could be interpreted as Skempton's coefficient. In all intermediate cases, including slipping cracks, the general formula (2.19) has to be used, and the results will be based on the numerical approach.

2.2.3 Effective properties via the spherical assemblage

The spherical assemblage presented in Figure 2.1 is now further discussed. Note that a second assumption of length scale separation has been introduced, where cracks are much smaller than the radius of the central pore. This assumption stems from the mathematics of the first homogenisation, which treats each crack as isolated within an infinite medium. In this first scheme, the length of the cracks does not affect the calculations since only the crack closure stress determines the shape of the cracks. Consequently, the difference in scale between the central pore and the REV requires that the cracks within the REV be significantly smaller than the pore itself. A one-to-ten ratio between the crack length and the pore radius is a reasonable assumption for physicists. That being said, the length of the crack remains an extrinsic parameter which does not appear when calculating the effective properties.

The compressive stress within the effective medium surrounding the sphere is isotropic with hydrostatic stress (one-third of the trace) equal to $-\sigma_H$. The interest is to determine the effective properties of the porous medium, ensuring stress continuity at the hollow sphere's external radius, either numerically or analytically. The structure of the constitutive relations expected at the assemblage level is first discussed before the analytical and numerical solutions are introduced.

Structure of the constitutive relations at the assemblage scale

For drained tests, following Rice (1977), the energy rate of change of the spherical assemblage should be described by:

$$\dot{\mathcal{E}} = -\dot{\theta}\sigma_H + p_f\dot{\bar{v}} - < F\dot{\xi} > , \tag{2.21}$$

in which θ and $\bar{v}$ are the volumetric deformation and the pore volume fraction of the assemblage, respectively. The scalar F stands for the collection of thermodynamic forces conjugate to the collection of internal variables ξ introduced in the section above to describe the crack response. The brackets $<>$ in eq. (2.21) denote the volume average over the assemblage. The thermodynamic forces are dependent on the local Terzaghi stress within the shell material, so it can be claimed that the volume average in eq. (2.21) is only a function of the effective stress $-\sigma_H + p_f$ and its rate. This dependence on Terzaghi stress developed by Rice (1977) leads to the equality between the irreversible volume change and the irreversible fluid fraction rate:

$$\dot{\theta}^p = \dot{\bar{v}}^p = -\mathbb{A}(\dot{\sigma}_H - \dot{p}_f) , \tag{2.22}$$

an equality which is further extended here by stating that these two rates must be proportional to the remote effective stress rate, introducing a non-linear function $\mathbb{A}$ of the remote effective stress and the collection of internal variables. This preliminary was necessary to introduce the

rate form of the assemblage response under drained conditions, which reads:

$$\begin{aligned} \dot{\sigma}_H &= -\bar{\kappa}^e(\dot{\theta} - \dot{\theta}^p) + \bar{\alpha}^e \dot{p}_f \,, \\ \dot{v} - \dot{v}^p &= \bar{\alpha}^e(\dot{\theta} - \dot{\theta}^p) + \bar{R}_p^e \dot{p}_f \,, \end{aligned} \tag{2.23}$$

in which $\bar{\kappa}^e$, $\bar{\alpha}^e$ and $\bar{R}_p^e$ are the elastic effective bulk modulus, the elastic Biot coefficient and the elastic storage coefficient at constant volume change of the assemblage. This elastic bulk modulus contributes partly to the P wave velocity, assuming a long wavelength compared to the radius of the assemblage. However, the interest here lies with the static estimate of the elastic properties with a sufficiently large strain increment so that the crack response is also involved. In other words, linearising the above non-linear properties should provide the relevant properties. These static properties are obtained by combining (2.22) and (2.23):

$$\begin{aligned} \dot{\sigma}_H &= -\bar{\kappa}\dot{\theta} + \bar{\alpha}\dot{p}_f \quad \text{with} \quad \bar{\kappa} = \frac{\bar{\kappa}^e}{1 + \bar{\kappa}^e \mathbb{A}} \quad \text{and} \quad \bar{\alpha} = \frac{\bar{\alpha}^e + \bar{\kappa}^e \mathbb{A}}{1 + \bar{\kappa}^e \mathbb{A}} \,, \\ \dot{v} &= \bar{\alpha}\dot{\theta} + \bar{R}_p \dot{p}_f \quad \text{with} \quad \bar{R}_p = \bar{R}_p^e + (1 - \bar{\alpha}^e)^2 \frac{\mathbb{A}\bar{\kappa}}{\bar{\kappa}^e} \,. \end{aligned} \tag{2.24}$$

The interesting result is that despite the dissipation mechanisms, there is symmetry in the above set of equations. The same Biot coefficient can be estimated by comparing the remote stress change and the fluid pressure change (at constant volume) or by relating fluid volume change and assemblage volume change (at constant fluid pressure). This finding is confirmed in Appendix B.7 for the case where all cracks in the assemblage shell are closed and slipping. This finding also justifies our estimate of the static Biot coefficient by using the second equation in (2.24) in what follows. This practice, convenient from the numerical point of view, is at odds with the laboratory procedure.

The structure of the constitutive relations at the assemblage scale for undrained tests is now discussed. The first of the two relations is between the remote stress rate $\dot{\sigma}_H$ and the volumetric strain rate, and the second is the definition of the evolution of the uniform pressure:

$$\dot{\sigma}_H = -\bar{\kappa}_u \, \dot{\theta} \quad \text{and} \quad p_f = p_{f0} + \frac{Y_H}{Y_p} \,. \tag{2.25}$$

The two functions Y_H and Y_p, defined in eq. (2.19), depend on the current value of the fluid pressure via the angle β_c and, more generally, on the state of stress within the assemblage. The bulk modulus is denoted $\bar{\kappa}_u$ as an undrained modulus since the fluid mass is conserved over the assemblage, including the dead volume.

Numerical solution

The solution for the model problem requires a numerical approach, which relies on the displacement-based finite-element method presented in Appendix B.3. The numerical algorithms to capture first the cracks's aperture evolution and second the frictional deformation are found in Appendix B.4 and B.5, respectively.

For the drained tests, two of the three effective properties, Biot's coefficient $\bar{\alpha}$, and the bulk

modulus, are deduced from the numerical solutions as follows. Time is discretised, and the volumetric deformation increment during the time increment Δt is $\Delta\theta = 3\Delta u(R_S)/R_S$ in terms of the radial displacement increment at the radius R_S. The effective bulk modulus $\bar{\kappa}$ during this increment for a constant fluid pressure test is then obtained by taking the ratio between the stress increment applied on the outer surface of the assemblage and the volumetric deformation increment. The fluid pressure being constant, Biot's coefficient $\bar{\alpha}$ is deduced from the second equation in (2.24) in which the pore volume fraction rate is interpreted as the fluid volume rate resulting from the contribution of the pore, the matrix, and the cracks, as defined in the previous section. The storage coefficient at constant volumetric strain is not computed but could be estimated with the following strategy: at any level of the applied load σ_H, first freeze the outer sphere radial displacement and thus the volumetric strain and second apply an incremental change in fluid pressure: the pore volume fraction of the assembly will then be modified providing the storage coefficient.

The numerical solution is coupled for the undrained tests since the fluid pressure changes over time. The solution strategy consists of a staggered scheme in which the fluid pressure is updated at the end of each time increment once a new equilibrium has been reached. The update is based on the solution of eq. (2.19), which is obtained with a fixed-point method. The effective bulk modulus is still determined as discussed above.

Analytical solutions for drained conditions

Analytical solutions have been derived for the effective properties of the assemblage in four different scenarios. In three scenarios, the Representative Elementary Volume (REV) within the shell material is characterised by three parameters $(\alpha^*, \kappa^*, G^*)$, similar to a poro-elastic, homogeneous material. This applies when the shell material has completely closed and sticking cracks at any radial position around the pore. In such cases, the set of moduli corresponds to the matrix properties. The second analytical solution holds if all cracks in the matrix are open at any radial position, and the corresponding moduli are found in eq. (B.16) in Appendix (B.2). The third scenario is when all cracks are closed and slipping with no friction, and the three moduli are defined by eq. (B.51), which is developed as a particular case in Appendix (B.7). The assembly response for these three cases is presented in Appendix (B.1), and the effective properties then read:

$$\bar{\kappa} = \kappa^* \frac{1-\phi}{1+\phi\frac{3\kappa^*}{4G^*}}, \quad \bar{\alpha} = 1-(1-\alpha^*)\frac{\bar{\kappa}}{\kappa^*}, \tag{2.26}$$

There is a fourth analytical solution for the effective properties if all cracks are closed and slipping with a non-zero friction coefficient in forward or reverse slip (Appendix B.7). The effective properties are found in eq. (B.50) and denoted $(\bar{\alpha}_s, \bar{\kappa}_s)$.

These analytical solutions are illustrated in Figure 2.3 constructed for a quartz matrix ($\kappa =$ 37 GPa, $\nu = 0.07$, $\alpha = 0$) and a pore porosity of 12.5%. The dotted, dashed and solid curves are the properties of the matrix, the REV (matrix+cracks) and the assemblage, respectively. The red and black curves are for the shear and bulk modulus. Note that the shear modulus

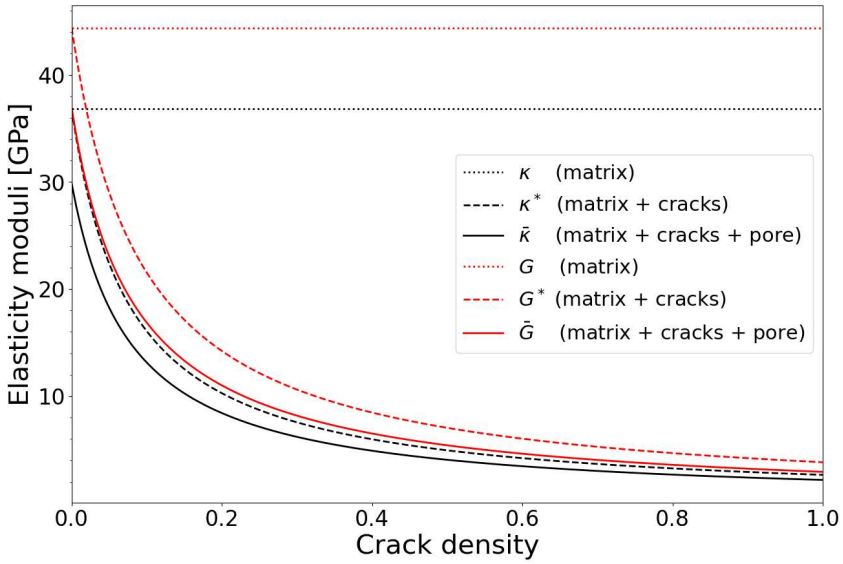


Figure (2.3) The influence of the crack density on the effective elastic properties of the matrix with cracks (κ^*, G^*) and of the spherical assembly $(\bar{\kappa}, \bar{G})$. Predictions are based on the analytical solutions, assuming that all cracks are open. The solution for the assemblage effective shear modulus $\bar{G}$ is found in Christensen (1990).

is based on the solution of Christensen *et al.* (1979) and presented in Christensen (1990). The assemblage properties for a zero density are smaller than the quartz values by 20% and 30% for the shear and the bulk modulus, respectively. A crack density of 0.20 is large enough for the drop to be a factor of four to five from the matrix properties. These results show that the presence of the pore provides a minor part of the drop in both the bulk and shear modulus, which is dominated by the influence of crack density. One could tentatively use these results to forecast the evolution of the assemblage bulk modulus during a hydrostatic loading leading to the closure of the cracks: the bulk modulus could be increased by a factor of four to five.

Analytical solution for undrained regime

For a linear material with either all open or all closed cracks at any radius of the spherical assemblage, the effective bulk modulus has the following expression (Zimmerman, 2000):

$$\bar{\kappa}_u = \frac{\bar{\kappa}}{1 - \bar{\alpha} S}\,, \tag{2.27}$$

having combined eq. (2.20) with (2.24a) and $\bar{\kappa}$ and $\bar{\alpha}$ given in (2.26). This scalar $\bar{\kappa}_u$ is interpreted as the undrained bulk modulus of the spherical assemblage.

The analytical solutions presented deserve further discussion, which will significantly help explain the non-linear solutions presented next. Biot's coefficient and Skempton's coefficient, defined in eq. (2.20), are presented in Figure 2.4 as a function of the crack density. The dotted horizontal line corresponds to the matrix Biot's coefficient. The black dashed and solid curves depict the effective Biot's coefficient of the REV and the assemblage, respectively. It agrees with the matrix value for a zero crack density and increases by up to 20% with increasing crack density. The three red curves correspond to the variation of Skempton's coefficient with the

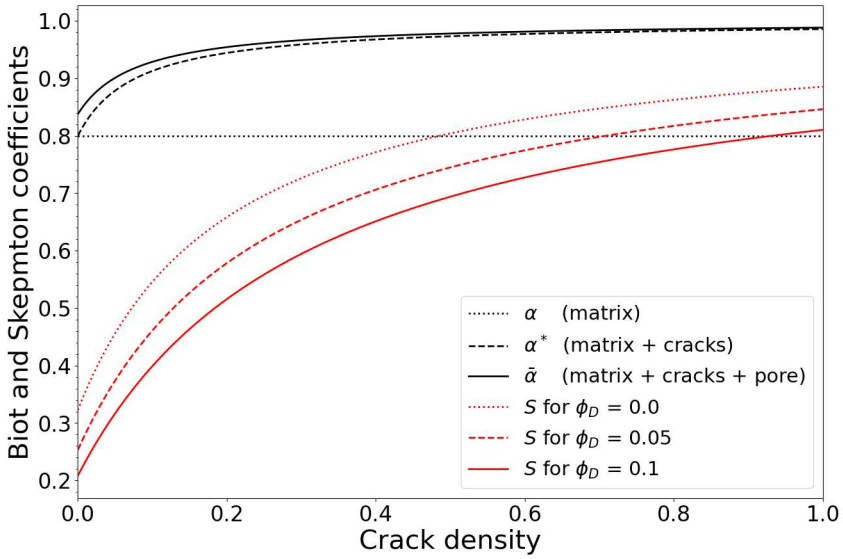


Figure (2.4) The influence of the crack density on the two effective Biot's coefficients (the REV α^* and the assemblage $\bar{\alpha}$) and on the assemblage Skempton's coefficient, for three values of the dead volume equivalent porosity. Predictions are based on the analytical solutions, assuming all cracks are open.

crack density for three values of the void porosity (ϕ_D is the volume of the dead volume divided by the specimen volume). There is a variation of roughly four as the crack density is increased to unity. The presence of the dead volume leads to an underestimate of the true Skempton coefficient.

2.3 Predictions of the model

The influence of different crack parameters on the macroscopic bulk modulus during a cyclic hydrostatic test is first presented, followed by an analysis of the cracks' behaviour at the micro-scale. The pore fluid pressure ($p_f = 0.1$ MPa) is kept constant for drained simulations, and the porosity is set to $\phi = 12.5\%$. The confining pressure (σ_H) is increased from 0.1 MPa to 30 MPa (drained simulations) or 70 MPa (undrained simulations) and then decreased back to the initial value. The numerical predictions are compared with the analytical solutions if all cracks are closed and sticking or open (eq. (2.26) and Appendix B.2) and if all cracks are slipping in forward or reverse mode (Appendix B.7).

2.3.1 Effect of crack parameters on the bulk modulus, drained conditions

The impact of the three crack parameters (μ, σ_C, and c) is now considered: each parameter is varied individually, while the other two and the pore fluid pressure are kept constant.

Figure 2.5a shows the evolution during a loading cycle of the bulk modulus as a function of confining pressure, with $\mu = 0.6$, $c = 0.6$, and $\sigma_C = 5$ MPa (orange curve). Two values bound the bulk modulus. The lower bound (lower dotted black line) at $\kappa = 3.27$ GPa is the bulk modulus of the assemblage for open cracks. The upper bound (upper dotted line) is the bulk modulus, assuming all cracks are closed and sticking at $\kappa = 28.8$ GPa. The numerical predictions matching perfectly the lower bound is logical, as all cracks are initially open. During loading,

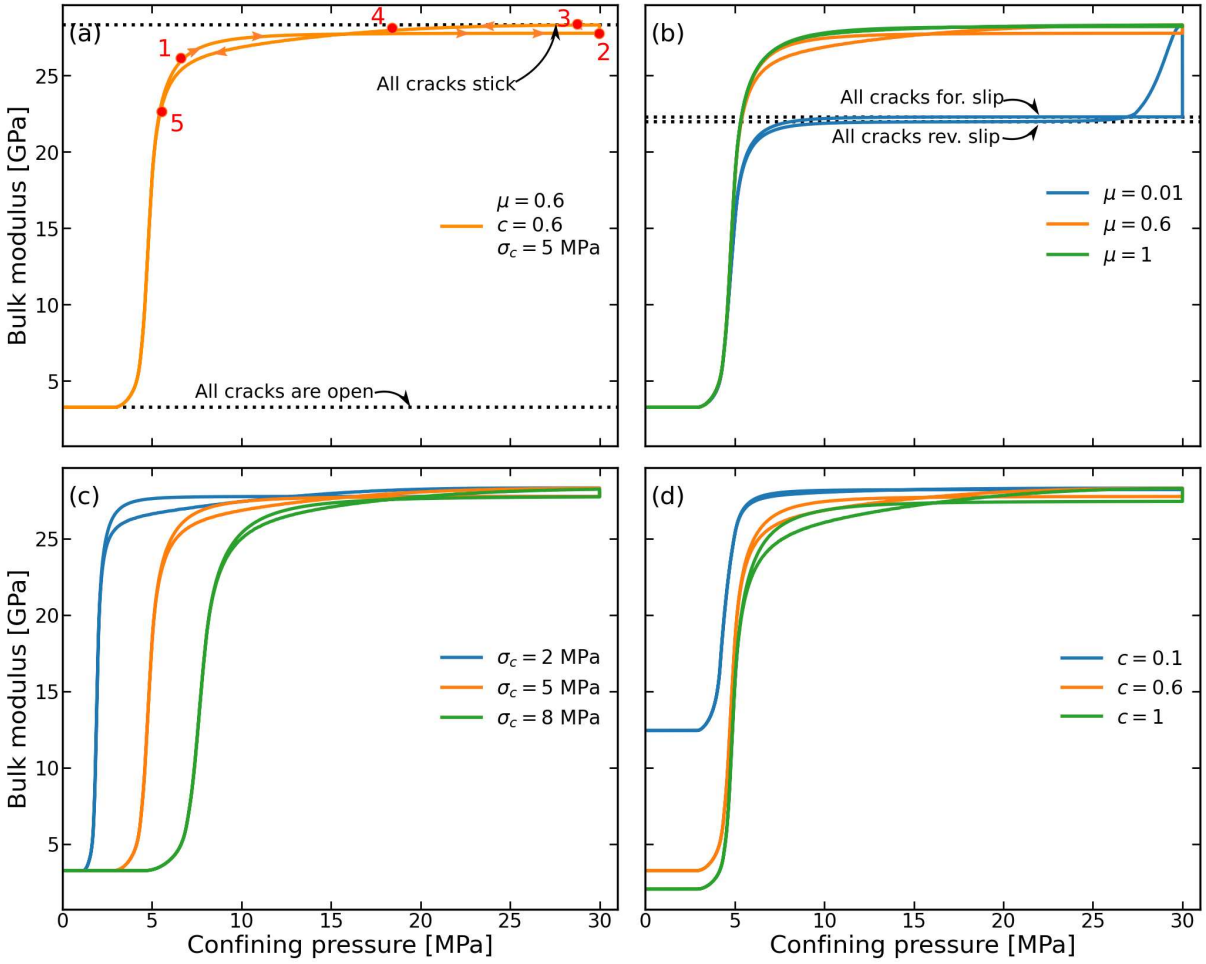


Figure (2.5) The cyclic evolution of the bulk modulus with the confining pressure, the reference simulation in (a). Influence of the friction coefficient, the closure stress, and the crack concentration in (b), (c), and (d), respectively. Dotted lines are analytical solutions for open or closed cracks, sticking or sliding in reverse or forward modes.

cracks start closing slightly before the closure stress of 5 MPa. At a compression of 10 MPa, the bulk modulus is increased by approximately nine times, reaching an asymptote somewhat lower than the analytical solution for all cracks closed and sticking. Upon unloading, the prediction plateaus just below the upper bound before decreasing back to the initial value of the bulk modulus, revealing the hysteresis effect and the crack dissipation. Figure 2.5a does not show the asymptotic solutions that assume all cracks slip in forward or reverse modes. These two asymptotes at 33.3 MPa and 14.3 MPa, not shown in the Figure, are off numerical predictions, indicating that some assumptions made for their derivations are invalid in this particular case.

Interestingly, this discrepancy disappears if the value of the crack friction coefficient is lowered close to zero (see the two dotted horizontal lines in Figure 2.5b). The numerical predictions match at the end of loading and after the early unloading stage. Also, the friction coefficient doesn't affect the early phase of loading and the final phase of unloading as the loading approaches the crack closure stress. Note the negligible hysteresis for a friction coefficient equal to one (green curve).

Figure 2.5c illustrates the impact of the closure stress. As it decreases, the closed loops shift

towards the left. However, the minimum and maximum predictions are unaffected by this parameter. Figure 2.5d shows these two values to be highly sensitive to the crack concentration. Nevertheless, the crack concentration has little effect on the transition. The evolution of Biot's

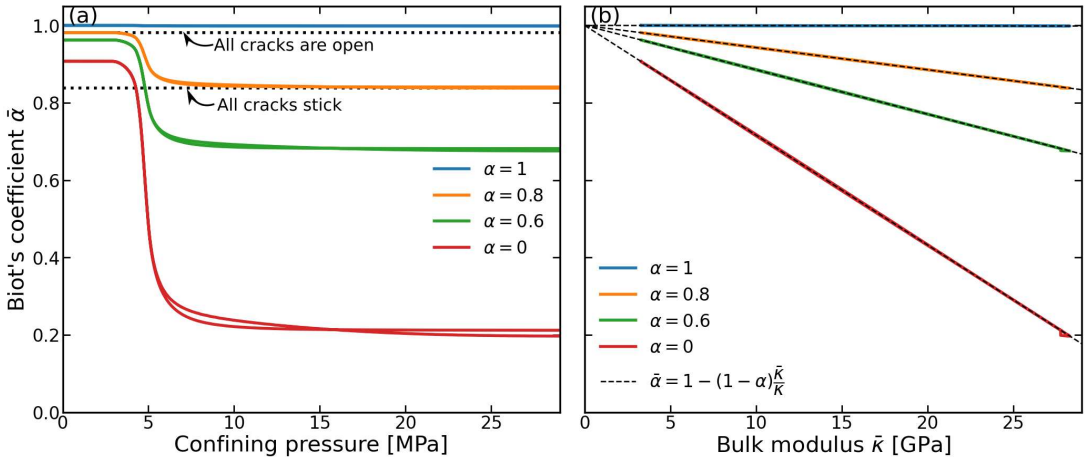


Figure (2.6) The cyclic evolution of the effective assemblage Biot's coefficient $\bar{\alpha}$ with the confining pressure for different values of matrix Biot's coefficient in a). The relation between the effective Biot's coefficient and bulk modulus is linear (eq. 2.28) as shown with the dashed lines, b).

coefficient is presented in Figure 2.6a to conclude the discussion on the effective properties of the assemblage. The data are precisely those considered for the reference curve in Figure 2.5 with a crack friction coefficient set to 0.6 and matrix Biot's coefficient equal to 0.8 (orange curve). The cyclic response aligns with the results presented in Figure 2.4, with a value close to 0.98 for low confining pressure as all cracks are open and around 0.84 for the most significant values of the confining pressure, resulting in the closure of most cracks. The exact asymptotic values are illustrated with the dotted lines. The blue and green curves are obtained for a larger and a smaller matrix Biot's coefficient compared to the reference value. The variation of this coefficient does not influence the transition but controls the asymptotic value for considerable confining pressures. Note that there is a slight hysteresis during the cycle, which is more visible for the zero value of the matrix Biot's coefficient. Moreover, the butterfly structure of this hysteresis is very analogous to the one observed for the bulk modulus in Figure 2.5 with a cross-over of the loading and unloading paths at approximately the confining pressure of 5 MPa. This analogy prompted the authors to plot Biot's coefficient as a function of the bulk modulus, Figure 2.5b. The variation is linear and given, up to numerical accuracy, by:

$$\bar{\alpha} = 1 - (1 - \alpha)\frac{\bar{\kappa}}{\kappa}. \tag{2.28}$$

This linear response is, of course, a surprise, although it has been seen four times in this chapter while discussing analytical solutions. Consider first the case of all cracks closed and slipping in either forward or reverse mode, eq. (B.50) in Appendix B.7. The three other cases correspond to a homogeneous response within the shell with either all open cracks, all closed and sticking cracks or all closed and slipping with zero friction. For these homogeneous responses, combine the shell effective Biot's coefficient in eq. (B.5) of Appendix B.1 with eq. (2.26) and obtain indeed the result in (2.28). The surprise comes from the fact that (2.28) also holds for any crack

activation pattern encountered during the cyclic loading. Proof of this statement[1], which is not given here, would require showing that the displacement field for complex crack response has the structure found in eq. (B.46).

The discussion above has highlighted the significant difference between the numerical predictions and the analytical solution for all cracks slipping in forward or reverse mode, especially for sensible values of the friction coefficient. To resolve this discrepancy, the cracks' response must be analysed at a finer scale. The analysis is presented in the following section.

2.3.2 Crack response around the cavity, drained conditions.

Figure 2.7 is proposed to analyse the response of the populations of cracks around the cavity. The two columns on the left illustrate the results for the two values of the friction coefficient of 0.01 and 0.6, respectively. The five rows of three graphs correspond to different values of the confining pressure, numbered from 1 to 5 (1 and 2 during loading and 3 to 5 during unloading) as defined in Figure 2.5a. Each graph in these two left columns presents the angle β_c, which marks the limit of open and closed cracks (dashed blue curve and values read on the right axis), as well as the proportion of cracks sliding in forward or reverse mode (red and black curve and values read on the left vertical axis). The column of graphs on the right of Figure 2.7 compares the crack's response for the two values (green and purple colours) of the friction coefficient at a specific distance of the pore centre set to $0.628R_S$. The crack distribution (first polar angle β) ranges from zero to 90 degrees, and the cracks are shown as either open, sticking, or slipping in forward or reverse mode.

The first point of comparison between the results for the two values of the friction coefficient is at the confining pressure of 6 MPa, the top row of Figures 2.7. The crack closure curve is similar for the two values. The crack orientations above the curves are closed and are open below. Cracks at a radius larger than approximately $0.77R_S$ are all closed. As the radius is decreased below this $0.77R_S$, the population of open cracks increases. It is impossible to close all cracks since the normal stress for $\beta = 0$ is the radial stress, which is equal to the initial pore pressure at the pore wall. Among the closed cracks, the red curve indicates that for $\mu = 0.01$, 70% to 100 % of cracks slip as one moves away from the pore wall. For $\mu = 0.6$, less than 20% of cracks slip. Surprisingly, the cracks closest to the pore (i.e., between $r = 0.5R_S$ and $0.6R_S$) are activated. The right plot confirms this interpretation. At $r = 0.628R_S$, the same cracks are open, but the closed cracks slip for the low friction and stick for the large friction.

The second comparison is at the maximum loading for $\sigma_H = 30$ MPa and corresponds to the second row in Figures 2.7. All cracks are closed for a radius greater than $0.53R_S$, approximately. Only a few cracks near the pore remain open. If the friction is low, almost all the closed cracks

[1] A simple tentative argument could be proposed, similar to the one followed, to relate Biot's coefficient to the ratio of the effective bulk modulus to the skeleton bulk modulus. Consider eq. (2.24)a to describe the response of a comparison solid, meaning that it is valid for any fluid and remote pressure rates. Choose then $\dot{\sigma}_H = \dot{p}_f$ and conclude that $-(1-\bar{\alpha})\dot{p}_f/\bar{\kappa} = \dot{\theta}$. This assemblage volumetric deformation rate can be estimated from a micro-scale point of view. The matrix sustains on its boundary a purely normal loading set to $\dot{p}_f$ and thus develops a stress rate purely hydrostatic. Its volumetric rate is thus $(\alpha-1)\dot{p}_f/\kappa$. The fluid in the open cracks must sustain the same volumetric rate if still open. The deformation is thus the same, homogeneous, for the matrix and fluid phases, and thus equal to the assemblage $\dot{\theta}$. Combine these two results to obtain eq. 2.28.

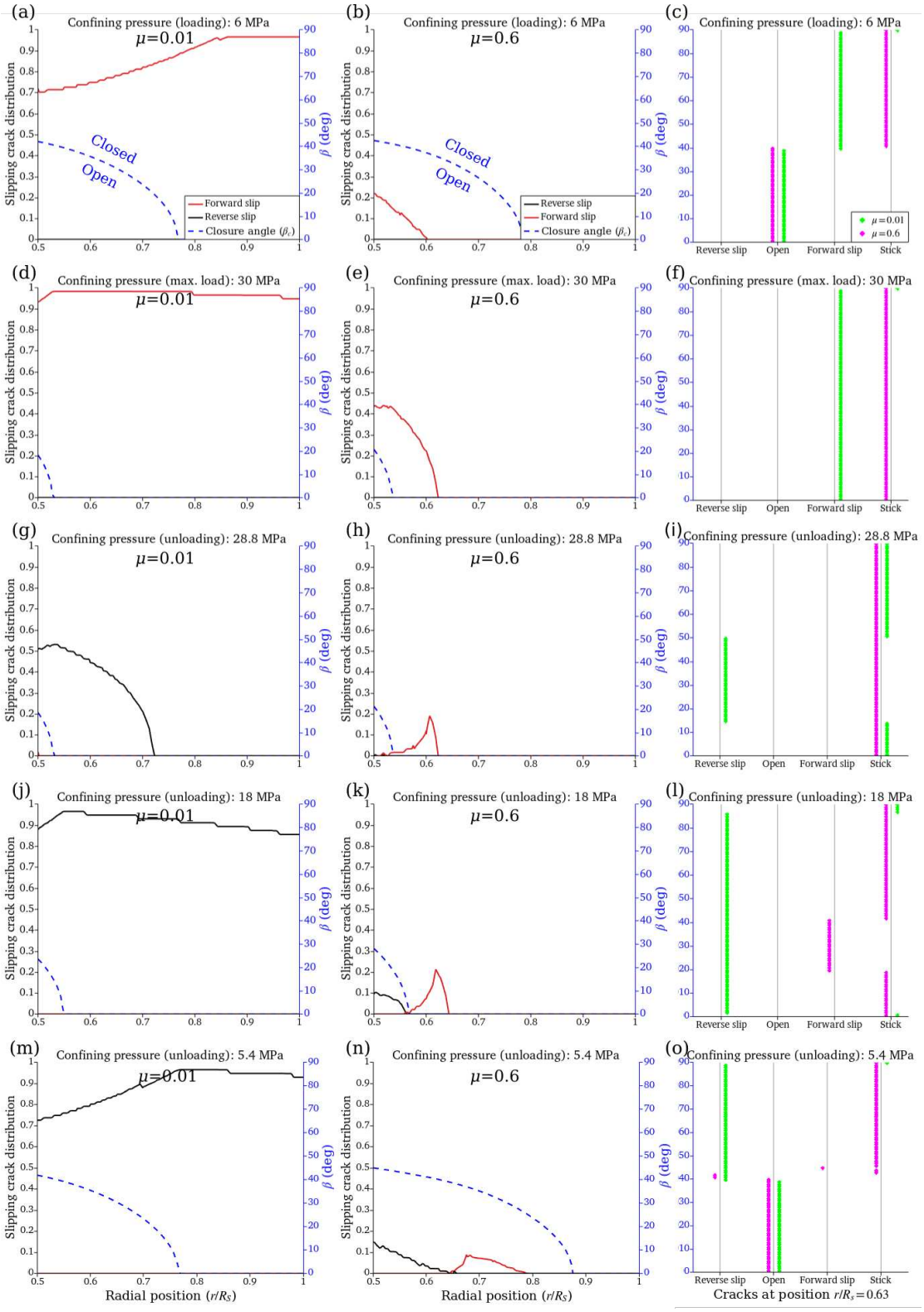


Figure (2.7) The crack slipping regime and proportion of slipping cracks as a function of the radial position at five stages of the loading cycle defined in Figure 2.5. The left and central columns of plots for friction coefficient values of 0.01 and 0.6, respectively. The dashed blue curve in each plot represents the crack closure polar angle β_c (right vertical axis). Above this angle, all cracks are closed, and below it, they are open. The red and black curves are the proportion of cracks slipping in forward or reverse mode (left vertical axis). The right column of plots shows the crack regime at a specific radius (r/R_s) for the first polar angle β.

slip; however, with large friction, only a tiny fraction of the cracks closest to the pore slip. The proportion is around 40% and decreases to zero for a radius close to $0.62R_S$. The plot to the right confirms the difference with all cracks sticking or slipping for the large and low friction, respectively, at $r = 0.628R_S$.

The three other comparisons are done during the unloading phase. During the initial stage (σ_H equals 28.8 MPa and third row in Figure 2.7), the black curve indicates that the cracks experience an almost instantaneous reverse slip in the case of low friction. The proportion of reverse slipping cracks decreases with the radius. At the pore wall, approximately half of the cracks show reverse slipping. This proportion increases during further unloading and then decreases because of the cracks reopening, as seen from Figure 2.7j and m. However, for the large friction (Figure 2.7h, k and n), the response is very different with a continuous forward slip of a population of cracks despite the overall unloading. Many cracks around $r = 0.6R_s$ continue to forward slip. This group of sliding cracks is getting translated towards the external part of the shell as unloading is pursued while the population of cracks reverse slipping increases away from the pore. The other surprise is the observation at $r = 0.628R_S$, during the last phase of unloading, Figure 2.7o: there are at the same radius cracks slipping in either reverse or forward slip for an orientation close to 40 and 45 degrees, respectively.

2.3.3 Cyclic response with undrained conditions

Attention is now focused on undrained conditions. The first graph in Figure 2.8a compares the drained (dry) response to the undrained response for glycerin ($\kappa_f = 4.5$ GPa) and water ($\kappa_f = 2.2$ GPa). This comparison assumes a matrix Biot coefficient of 0.8, and no dead volume. All other parameters are the same as those used in the earlier reference simulation. The assemblage bulk modulus significantly differs from the drained case when all cracks are open or when most are closed and sticking. The limiting cases of all open and all closed and sticking are represented by the dotted lines in the graph for the water-saturated case, and the numerical predictions match them well. The other difference with the drained case is the transition between the two limits, which is delayed because of the fluid contribution to the overall bulk modulus and the variation in fluid pressure. The delay becomes more significant as the fluid bulk modulus increases. Note also that increasing the fluid bulk modulus reduces the hysteresis effect.

The variation in fluid pressure is presented in Figure 2.8b for the case of water (solid curve). The variation is approximately bi-linear, starting from an initial value of 0.1 MPa and ending at slightly less than 40 MPa. The analytical expressions for the Skempton coefficient found in eq. (2.20) work well for both all open and closed and sticking cracks, and they provide the slopes of the dotted and dashed lines starting either from the initial or the final fluid pressure, as seen in Figure 2.8b. The sudden change from ”all cracks are open” to ”all cracks stick” occurs approximately at a confining pressure of 30 MPa, which is also the pressure at which the bulk modulus sees a rapid transition from low to high values in Figure 2.8a. Although not visible on the graph, there is a slight hysteresis in the fluid pressure variation. If the cracks are active, there is a maximum difference of 0.07 MPa in fluid pressure between loading and unloading.

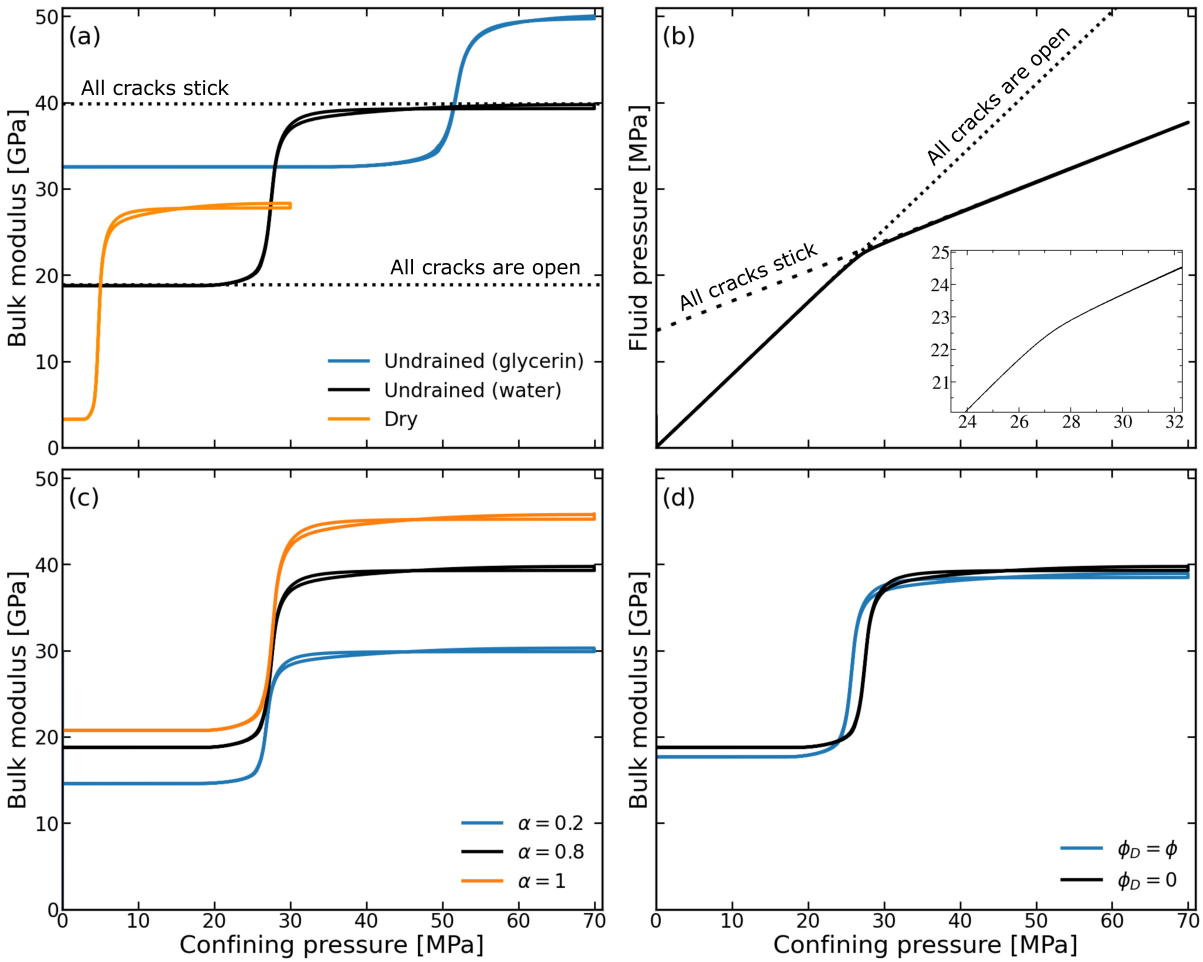


Figure (2.8) Bulk modulus for undrained conditions with water or glycerin and comparison with drained (dry) conditions in (a). Evolution of the pressure during a cycle with water in (b) (units MPa but gradation identical to vertical axis in a). Influence of the matrix Biot's coefficient in (c) and of the dead volume in (d) in the case of water.

Figure 2.8c and 2.8d present two additional plots investigating the impact of the matrix Biot coefficient and dead volume on the assemblage bulk modulus. The black reference curve corresponds to water and a matrix Biot coefficient of 0.8. The two limiting values, for low and large confining pressure, are influenced by the matrix Biot coefficient. The larger the Biot coefficient, the larger these limits are. However, this coefficient does not affect the transition nor the closing of the cracks. Figure 2.8d shows the impact of dead volume. Increasing ϕ_D results in a slight reduction in bulk modulus and a decrease in the confining pressure required to transition between the two limiting values.

A surprising result is observed in Figure 2.8a, which deserves further discussion. The bulk modulus at the end of the loading phase is close to 40 GPa and 50 GPa for water and glycerin, respectively. These values are much larger than the matrix bulk modulus, approximately 35 GPa. It is classically observed in rocks that the undrained bulk modulus does not exceed the dominant mineral bulk modulus. This difference is very sensitive to the matrix Biot coefficient, as can be seen from Figure 2.8c for the water: the critical value of α beyond which the assemblage modulus is greater than the matrix bulk modulus is between 0.2 and 0.8. If one assumes that all

cracks are closed and sticking at the end of loading, then this critical value of α at which the two moduli are equal is found analytically and is 0.47 and 0.78 for water and glycerin. This finding reveals some applicability limits of the proposed prototype to classical rocks. The matrix Biot coefficient is set to zero in the next section, and the results do not suffer from this limitation.

In addition, a detailed comparison between the current model's predictions for the undrained bulk modulus and Biot-Gassmann's relation is provided in Appendix B.9.

2.4 Application to hydrostatic compression of dry specimens

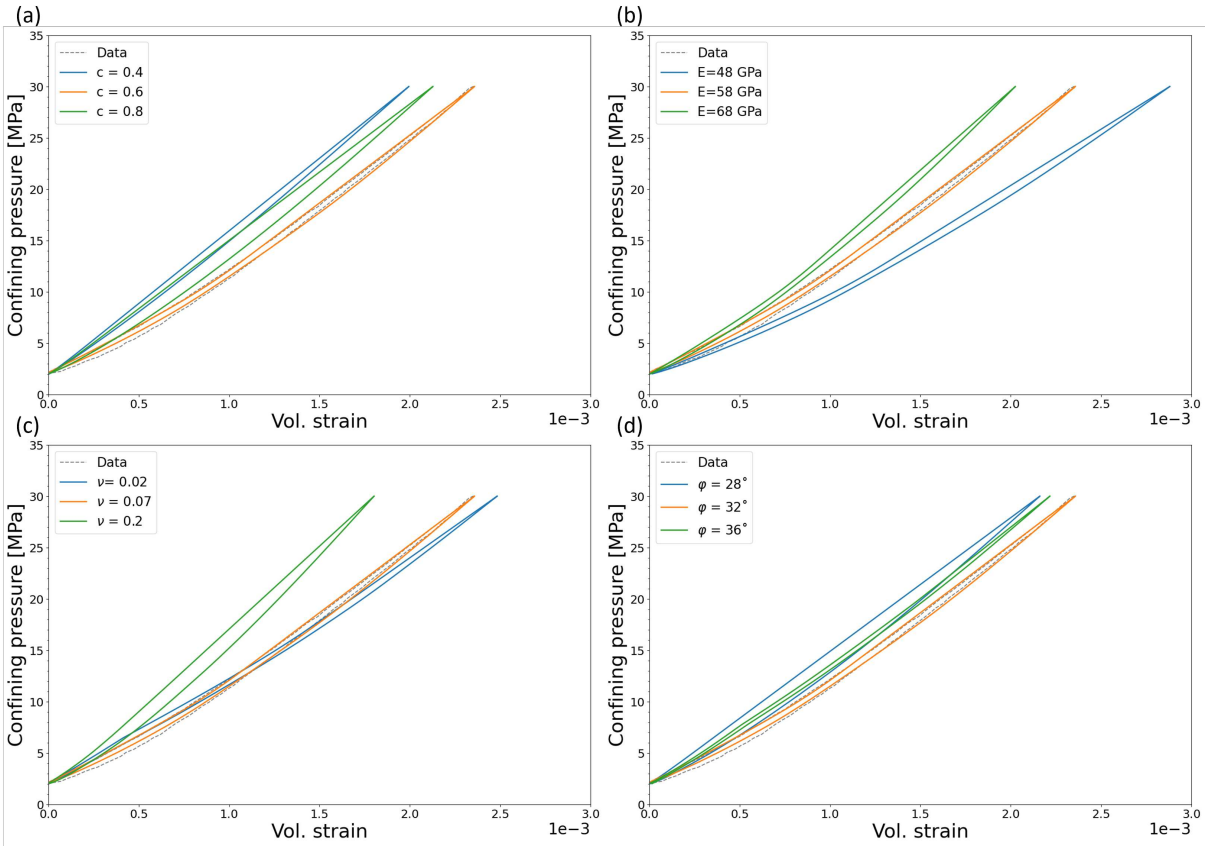


Figure (2.9) Volumetric strain versus confining pressure varying the crack density c, matrix elasticity modulus E, matrix Poisson's ratio ν, and friction angle φ in a to d. The best fit for Bentheim is obtained for $c = 0.6$, $\varphi = 32°$, $\nu = 0.07$ and $E = 58$ GPa (orange curve). Note that the porosity is the same for all simulations and is equal to the real sample's porosity ϕ=22.2% and that $\sigma_C = 2$ MPa.

The stress-strain curves from hydrostatic compression tests on dry samples are now simulated. The experimental data come from Chapman *et al.* (2023) and showcase four rock samples. The clean Bentheim sandstone (95% quartz) has a 22% porosity and a grain size between 18 and 500 μm. The Chauvigny limestone has a 16.2% porosity and is entirely composed of calcite. The two carbonates, C-2 and C-3, have a porosity of 17.1% and 14.7%, respectively. C-2 is granular and is mainly composed of calcite ($\geq$ 95%), whereas C-3 has a shrub facies and contains a mix of calcite (45.5%), quartz (38.3%) and dolomite (15.2%).

In dry conditions, the numerical model takes six parameters as input: c, φ, ν, E, ϕ, and σ_C, which are now discussed. The porosity related to the central pore is set to the experimentally

measured value, as crack porosity is negligible (less than 0.05%). The crack closure stress used in the model corresponds to the confining pressure at which the hysteresis loop would close at the end of the loading cycle. It is inferred from the stress-strain curve. The Poisson's ratio of the matrix is fixed at 0.07 for sandstones and 0.2 for carbonates, while the friction angle is set between $\varphi = 32°$ and $\varphi = 41°$. However, given that the value range of the elasticity modulus is quite large for common minerals (90-100 MPa for quartz and 90-150 MPa for calcite), E is used as a fitting parameter. Also, information about the crack density is not assessed experimentally and is thus a fitting parameter. A first analysis of the Bentheim sandstone is proposed below to understand the impact of all the parameters that are not strictly measured (E, c, φ, ν).

Figure 2.9 shows the influence of the matrix properties on the hysteresis loop for Bentheim at fixed $\sigma_C = 2$ MPa, and $\phi = 22.2\%$. In Figure 2.9a (with $E = 58$ GPa, $\varphi = 32°$, $\nu = 0.07$), increasing c from 0.4 to 0.8 leads to a smaller slope and a more considerable hysteresis. In Figure 2.9b (with $c = 0.6$, $\varphi = 32°$, $\nu = 0.07$), the increase of E leads to the rise of the average slope and the decrease of the dissipated energy ΔE_n (loop area). Note that E has a more significant impact on the slope than on ΔE_n. From Figure 2.9 (with $E = 58$ GPa, $c = 0.6$, $\varphi = 32°$), observe that the increase in ν from 0.02 to 0.2 results in both a more significant slope and ΔE_n. Figure 2.9d (with $E = 58$ GPa, $c = 0.6$, $\nu = 0.07$) shows that the increase in φ from 28° to 36° results in the decrease in hysteresis, as well as the more concave curve. The best fit for the data, provided by the least square method with E and c as fitting parameters (at fixed $\varphi = 32°$ and $\nu = 0.07$), is obtained at $E = 58\tilde{\text{G}}\text{Pa}$ and $c = 0.6$ as shown by the orange curve. The predicted elasticity modulus is thus notably smaller than that of quartz.

The fitting considers the amount of hysteresis, a proxy for the energy dissipated by the sample, and is conventionally represented by the attenuation factor Q^{-1}. This attenuation factor is the ratio of the area of the hysteresis loop to the average energy stored in the sample (O'Connell *et al.*, 1978). It stems from the direct definition of the attenuation factor as the ratio of the dissipated energy ΔE_n to the average energy V_n stored by the rock:

$$Q^{-1} = \frac{\Delta E_n}{4\pi V_n} , \tag{2.29}$$

a definition found in Borgomano *et al.* (2017), and that differs by a factor of two from similar definitions in classical contributions such as Knopoff (1964) and Jaeger *et al.* (2009). In practical terms, ΔE_n is the area of the hysteresis loop, and V_n is the area below the loop; both areas were computed incrementally, following Tisato *et al.* (2012). The value retrieved from the reported data of Bentheim is $Q^{-1}_{exp} = 1.03 \times 10^{-2}$ and that of the numerical hysteresis is $Q^{-1}_{num} = 1.05 \times 10^{-2}$. This is a good match, considering the model's simplicity, and the difference is certainly below the experimental accuracy.

In addition to Bentheim, the numerical results for Chauvigny show a very good fit with $Q^{-1}_{exp} = 1.47 \times 10^{-2}$ and $Q^{-1}_{num} = 1.46 \times 10^{-2}$. Figure 2.10 displays the data and numerical volumetric strain versus confining pressure for Chauvigny. The numerical result corresponds to : $c = 0.4$, $\varphi = 32°$, $\nu = 0.2$, $E = 61$ GPa, $\sigma_C = 1.0$ MPa, ϕ=16.2%. Again, only c and E are fitting parameters since ϕ and σ_C are inferred from the data, and ν and φ are fixed for simplicity.

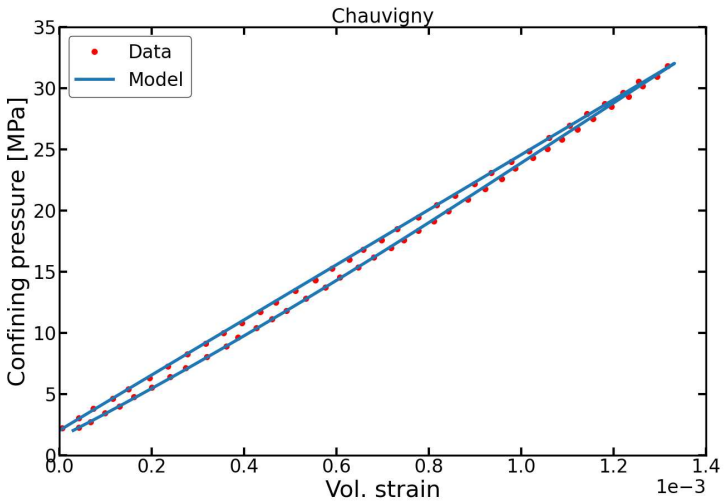


Figure (2.10) Volumetric strain versus confining pressure for Chauvigny. The fitting parameters are: $c = 0.4$, $\varphi = 32°$, $\nu = 0.2$, $E = 61$ GPa, $\sigma_C = 1.0$ MPa and ϕ=16.2%.

Note that the experimental curve for Chauvigny is quite linear and symmetrical: convex in loading and concave in unloading. This effect is achieved first by reducing the closure stress to a fraction of the initial stress state so that some of the cracks are already closed under these initial conditions, and secondly by assuming a low crack density.

Table (2.1) Best fitting parameters for the experimental data.

Parameter	Bentheim	Chauvigny	C-2	C-3
E [GPa]	57	61	80	68
ν	0.07	0.20	0.20	0.20
φ [°]	32	32	41	30
c	0.60	0.40	0.8	0.5
σ_C [MPa]	2	1	3	5
ϕ [%]	22.2	16.2	43.0	28

Regarding the other two carbonates, C-2 and C-3, the stress-strain curves are neither symmetrical nor quasi-linear. This makes using E and c as the only fitting parameters more difficult. Figure 2.11c and 2.11b show the best fit using two fitting parameters (E and c) for C-2 and C-3, respectively. Note that although the amount of hysteresis is closely matched, the slopes are very different. Several factors can explain the curvier aspects of the C-2 and C-3 loops, notably the grain and pore shapes and the nature of the grain contacts. Unfortunately, no analysis of the pore shape is available for these samples. A micro-porosity within the matrix could be included in the model fits; however, this would indicate a smaller central pore and result in even less deviatoric stress, thereby worsening the match to the data. The curved shape of the experimental loop suggests increased activation of cracks, necessitating a higher deviatoric stress. Yet, the proposed prototype in this chapter uses a spherical pore to generate deviatoric stress, which is thus controlled entirely by porosity. The measured porosities for C-2 and C-3 are too small to reproduce the data using this simple prototype. Notably, carbonates have complex microstructures with varying grain shapes and microporosities of different types that are not accounted for. Additionally, when closely examining the curves for C-2 and C-3

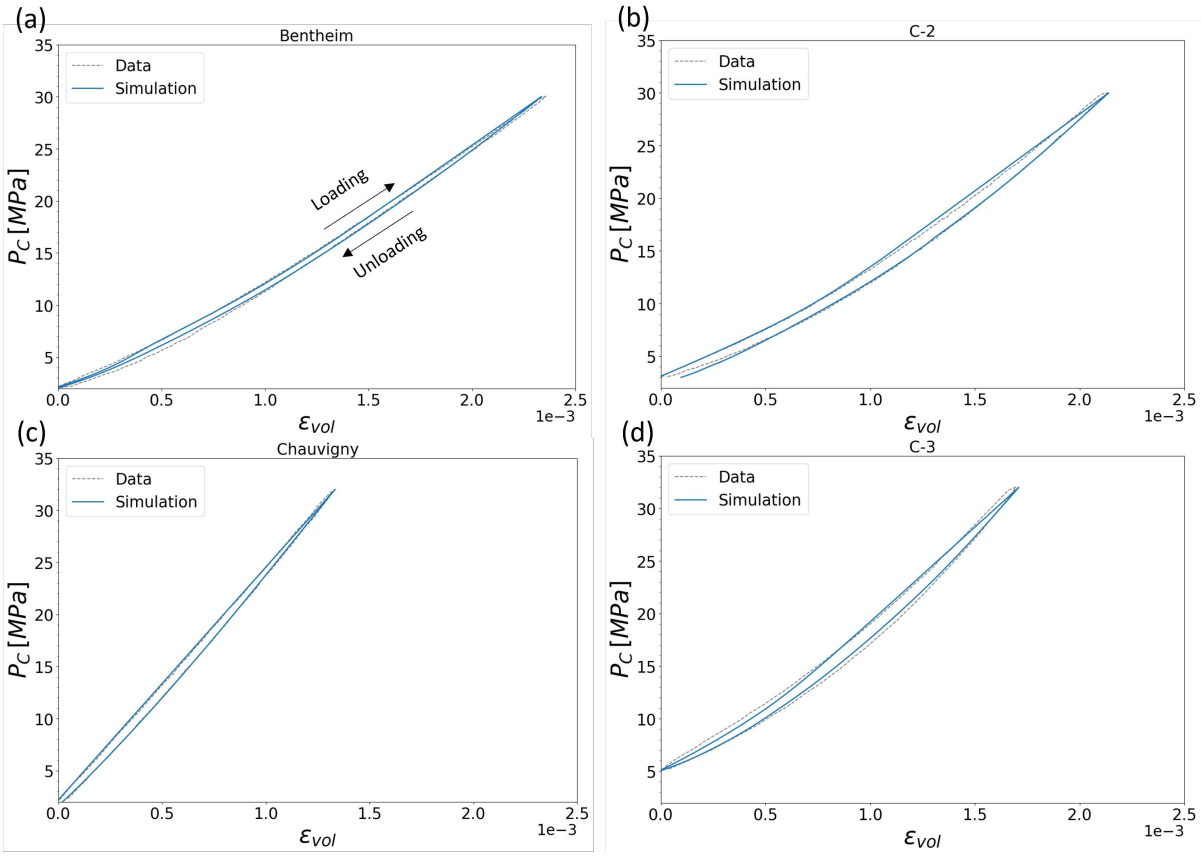


Figure (2.11) The experimental data of the hydrostatic compression cycle for C-2 and C-3 carbonates versus the theoretical curves. In a and b, the best fit is when using only E and c as fitting parameters. In c and d, the best fit is when using E, c, ϕ, μ and ν as fitting parameters.

(Figure 3e and 3f of Chapman *et al.*, 2023) at higher confining pressures, it is evident that there is an evolving strain at a constant pressure of 30 MPa, which resembles creep-like behaviours. These behaviours are not observed in the other rocks and could be due to minerals' plasticity, which is not accounted for. To address this limitation, one can either increase the porosity in the model or flatten the central pore. The former solution was adopted to fit the data, since further development would be needed to try the latter. Figure 2.11c and 2.11d show the best fits for C-2 and C-3 by optimising E, c, ϕ, μ and ν. For C-2, the optimal crack density is larger, $c = 0.8$. This may indicate an overcompensation from using a single crack aspect ratio. The pronounced nonlinearity of the hysteresis loop suggests that the progressive closing of cracks with varying aspect ratios instead of that of identical cracks positioned at different distances from the pore. Hence, to accurately simulate the effect of a distribution of cracks with different aspect ratios, a greater number of identical cracks is needed. The overcompensation in crack density may also relate to the absence of crack-to-crack interaction at the REV scale. Such interaction could enhance crack slipping, thereby decreasing the number of cracks needed to induce both nonlinearity and hysteresis.

The best-fitting parameters are summarised in Table 2.1.

2.5 Conclusion

A model problem to capture the hysteresis in hydrostatic compression tests has been proposed. It is built with two homogenisation schemes, the first at the REV scale within the shell material and the second for the assemblage composed of the pore, the shell and the homogeneous effective medium. It considers uniform pore-fluid pressure at the assemblage length scale for either drained or undrained conditions, the fluid mass within the specimen, and the additional dead volume constant in the latter case.

The hysteresis is analysed by plotting the bulk modulus versus the remote compressive stress during the loading cycle. Four stages labelled (i) to (iv) are observed during a typical cycle. Stage (i) applies during the early phase of compression and during the late stage of unloading since all cracks are open. Stage (ii) corresponds to the end of loading when the crack population is closed and the slipping cracks are stabilised. Stage (iii) signals the beginning of unloading, and most of the closed cracks stick. Stage (iv) marks a stage closer to the initial conditions with the reopening of cracks and slipping of the closed cracks. Four analytical solutions are proposed for open cracks (stage i), all closed-sticking cracks and closed-slipping in either forward or reverse mode. The two latter solutions were expected to capture stages (ii) and (iv). The finite-element solution enables the capture of the transitions between these various stages and the assessment of the validity of the assumptions behind the analytical solutions.

The finite-element solution in stages (i) and (iii) matches the analytical solution. The analytical values are functions of the matrix elasticity and the crack properties for the drained case, as well as the fluid bulk modulus and matrix Biot coefficient for undrained conditions. Surprisingly, the new analytical solution for all slipping cracks is only reasonably matched for low values of the friction angle. Two of the assumptions considered for the analytical development are invalid. First, in all cases, there is always a small shell around the pore where cracks do not close because they are oriented such that their normal stress is close to the radial stress and thus controlled by the pore pressure. The second reason is that not all cracks do not stick at the reversal of the assemblage confining pressure. There is indeed a zone where forward slip is pursued during the early phase of unloading. This zone extent is shifted towards the assembly's outer radius as reverse slip is initiated closer to the pore during the unloading. Moreover, it is observed that at critical radii, the population of cracks could be in the four states: open, closed and sticking, closed and slipping forwardly or reversely, depending on their orientation.

The finite-element solution for the assemblage Biot coefficient is proposed for drained conditions and thus constant fluid pressure. It is based on the ratio of the fluid volume rate of change (pore volume fraction rate) to the assemblage volume. This Biot coefficient is found to be an affine function of the assemblage bulk modulus. This same relation was indeed derived for the four analytical solutions, but not shown to prevail for general crack states.

The finite-element predictions also reveal the key parameters controlling the transition between stages (i) and stages (ii) and (iii), which marks the crack closure. The main parameter is the crack closure stress, although the crack concentration also has a minor influence. The fluid bulk modulus becomes a key parameter for undrained conditions, while the matrix Biot coefficient

and dead volume have a minor impact.

The fitting of experimental data from the hydrostatic compression of dry sandstones and carbonates presented by Chapman *et al.* (2023) is done in two optimisations using the least square method on the stress-strain data. The first optimisation uses only the matrix elasticity modulus and the crack density. In contrast, the second optimisation makes use of all six parameters (assemblage porosity, crack stress closure, crack friction, Biot coefficient, the elasticity modulus and Poisson's ratio of the matrix). The hysteresis loops of Bentheim sandstone and Chauvigny limestone are well predicted using the first optimisation. The quality of the fit of the transitional phase between (i) and (ii) depends on the deviatoric stress generated by the central pore. A larger central pore leads to a more extended transition. However, the specimen porosity due to the central pore does not cause enough deviatoric stress to match the data from the C-2 and C-3 carbonates. For these two samples, the second optimisation (including a considerable increase in the porosity) results in a good fit. The model seems to perfectly predict the hysteresis loop of porous samples ($\phi \geq 10\%$).

The application of this model problem could be extended in different directions, and two are now briefly discussed. The first direction is due to the inability of this micro-structural model to match the experimental results for low porosity rock, as observed for the granite and two of the carbonates tested by Chapman *et al.* (2023). One could wonder if visco-plasticity could explain the issue for the latter. For the former, it is clear that another source of deviatoric stress, such as the interaction of an isotropic distribution of frictional cracks, should replace the spherical pore. This micro-structural model is now validated for porous rocks and should be applied to capture the strain amplitude dependence of the quasi-static elastic properties at low differential stress (Pimienta *et al.*, 2017). These cyclic straining, with amplitude as small as 10^{-6} and at a constant mean differential stress, generate a hysteresis due to the closure and the slip of a distribution of cracks in terms of aspect ratio, which has not been accounted for here. Introducing this distribution and selecting the appropriate crack density parameter will then become a central issue (Kachanov, 1993) to enhance the applicability of our model problem.

Chapter 3

Frictional Microcrack Model with Cracks of Various Aspect Ratios

Chapter Abstract

The slipping of microcracks and frictional contacts has previously been shown to explain the hysteresis in rocks' response under hydrostatic loading. This mechanism may also explain the discrepancy between dry rocks' static and dynamic elastic properties. This chapter extends the previously proposed micromechanical model by incorporating a distribution of microcracks with varying aspect ratios to simulate real-world conditions better. The model is applied to the Bentheim sandstone through three series of simulations. First, hydrostatic loading and unloading, for a strain amplitude of 2×10^{-3}, predict hysteresis, elastic properties, and crack distribution. Second, based on this first information and at various stages of the first loading, hydrostatic forced oscillations with strain amplitudes from 10^{-6} to 10^{-4} are shown to link dynamic and static properties. Lastly, simulations of confining pressure and pore fluid pressure oscillations assess microcrack contributions to bulk compressibility parameters C_{bp} and C_{bc}. In the first series, the hysteretic volumetric strain response between the loading and unloading phases is well predicted if porosity is roughly twice the measured value. A linear relationship between modelled and measured porosity across diverse rock types facilitates hysteresis and crack density predictions. In the second series, the transition from static to dynamic bulk modulus is well captured and closely aligns with experimental results. It does reveal that the behaviour of microcracks - closing, slipping, and sticking due to slight pressure changes - affects the bulk modulus' amplitude dependence. In the third series, microcracks respond differently to C_{bc} and C_{bp} oscillations, with more cracks activated during confining pressure oscillations than during pore fluid pressure oscillations. This has significant implications for field-scale cyclic fluid injection and extraction, and in particular for the interpretation of the geophysical monitoring.

3.1 Introduction

Subsurface work, such as underground fluid storage, changes the stress state within the host rock (Kim *et al.*, 2021). The loading path in stress space dictates the non-linear elastic response of the rock, and there is often a discrepancy between loading and unloading behaviour. This hysteresis between the loading and unloading stages hampers the prediction of the rock's behaviour during cyclic loading. The slipping of microcracks has been deemed responsible for such hysteresis if there is remote deviatoric stress (Walsh, 1965; David *et al.*, 2012). However, hysteresis is also observed in dry rocks under macroscopic hydrostatic loading, as evidenced by Chapman *et al.* (2023), Wang *et al.* (2021), Bakhorji *et al.* (2010), Jizba *et al.* (1990), Martin III *et al.* (1994), Ma *et al.* (2018), and Jeng *et al.* (2002), among others. In that case, the link between hysteresis and frictional cracks is not obvious, since there is no macroscopic deviatoric stress to trigger crack-slipping. That is why we developed a micromechanical model that simulates hysteresis under remote hydrostatic stress, presented in the previous chapter and published in Biyoghé *et al.*, 2024a. The model considers the classical spherical assemblage (Hashin, 1962) with a spherical pore inside a matrix shell containing isotropically distributed microcracks (Kachanov, 1992) and the whole immersed in a homogeneous medium. We found that the stress concentration around the pore created enough deviatoric stress to activate the cracks and cause hysteresis. However, those results were primarily qualitative, proving that cracks are indeed the main driver for hysteresis under remote hydrostatic stress, but they were unable to predict the amount of hysteresis based only on the loading stage measurements. This limitation is partly due to the use of a single aspect ratio for all cracks. The present study adds further complexity by considering a distribution of various crack aspect ratios to enhance our quantitative and predictive capabilities. In practice, we intend to predict hysteresis based on the loading stage measurements.

In addition to hysteresis, the proposed microcrack mechanics may also explain the discrepancy between static and dynamic elastic properties, specifically the bulk modulus, in dry specimens, as suggested by Chapman *et al.* (2023). We hypothesise that at larger strain amplitudes, on the order of 10^{-4}, which correspond to static measurements, a significant number of cracks are mobilised, especially at low confining pressure (less than 20 MPa). As a result, the static bulk modulus is lower than the dynamic one. The dynamic bulk modulus is associated with strains on the order of 10^{-6} induced by propagating waves, which activate only a tiny fraction of the cracks, leading to a significantly larger bulk modulus. The strain amplitude transition from static to dynamic elastic properties is investigated by simulating forced hydrostatic oscillations to induce strains from 10^{-6} to 10^{-4}.

Forced oscillation (FO) simulations also provide valuable insights into compressibility measurements. In their experiments, Pimienta *et al.* (2017) utilised FO ($\pm$0.1 MPa) of confining and pore fluid pressure to examine how the bulk compressibility, either C_{bc} or C_{bp}, as defined by Zimmerman (1990), changes with increasing differential pressure; a similar study is presented in Appendix A. By simulating this experiment, we aim to predict not only the evolution of C_{bc} and C_{bp} but also the apparent compressibility of the rock's skeleton (unjacketed), C_s, which is defined as $C_{bc} - C_{bp}$. Theoretically, C_s is expected to remain constant within the rock's elastic

domain. However, experiments have shown that it sometimes fluctuates and tends to be larger at low effective pressures (Tarokh *et al.*, 2019). This observation implies that C_{bc} and C_{bp} do not behave similarly under low effective pressures. Specifically, more microcracks become activated during oscillations of confining pressure (C_{bc}) than during oscillations of pore fluid pressure (C_{bp}). This hypothesis will be tested using our enhanced micromechanical model.

The enhanced microcrack model is applied to a 22% porosity Bentheim sandstone in two types of simulations to achieve the following three tasks: predict the loading versus unloading hysteresis based on the loading measurements, predict the strain amplitude transition from static to dynamic properties, and reveal the contribution of microcracks to C_{bc}, C_{bp}, and the difference $C_{bc} - C_{bp}$.

The first series of simulations consists of the loading and unloading hydrostatic cycle based on experimental data from Chapman *et al.* (2023). We aim to predict the rock's hysteretic strain path in the unloading based on the model fit of the loading stress-strain curve. The model fit of the loading data is first constrained by the measured porosity, low-pressure bulk modulus (at 1 MPa) and high-pressure bulk modulus (at 25 MPa). The optimisation of the modelled parameters to the loading data will infer the best crack distribution function accounting for slip. If, in that configuration, the model does not predict the expected hysteresis because of insufficiently induced local deviatoric stress, we then solve the inverse problem by fitting the entire hysteresis loop to find both the crack distribution and the optimal modelled porosity. This latter scenario instigates examining the relationship between modelled and measured porosity. To achieve this, additional results are modelled using rocks of various types and porosities. Measurements from one Bentheim sandstone (Wang *et al.*, 2021), three carbonates (Chauvigny, C-2, and C-3) (Chapman *et al.*, 2023), the Mushan sandstone (Jeng *et al.*, 2002), and Sierra white granite (Martin III *et al.*, 1994) are used for this purpose.

The second series of simulations deals with forced oscillations. Confining pressure oscillations of various amplitudes are used to assess the strain amplitude dependence of the bulk modulus. The third series of simulations examines forced oscillations of a fixed small amplitude ($\pm$ 0.1 MPa) of the confining or pore pressure. These oscillations are simulated for increasing average differential pressures to estimate C_{bc} and C_{bp}. The behaviour of microcracks caused by slight pressure changes in the second and third series of simulations is analysed using the best model fits from the first series on loading and unloading.

3.2 Enhanced micromechanical model

The constitutive relations rely on a double homogenisation scheme. The first homogenisation is for a representative volume element containing a fluid-saturated poro-elastic matrix with an isotropic distributions of penny-shaped cracks, as in Kachanov, 1982, with the introduction of various aspect ratios. The second homogenisation considers a spherical assemblage (Hashin, 1962) with a fluid-filled pore, a shell material responding according to the predictions of the first homogenisation scheme, both embedded in a homogeneous medium (Figure 3.1).

In this section, we first define the crack aspect-ratio distribution function within the matrix. Next, we establish the constitutive relations at the assemblage level. Finally, we outline the model constraints, including the measured low-pressure bulk modulus at 1 MPa, the high-pressure bulk modulus at 25 MPa, and the initial porosity, along with the optimisation workflow for these parameters.

3.2.1 Crack aspect-ratio distribution

The objective is to extend the prototype of the previous chapter to account for a distribution of cracks of different aspect ratios. The previous chapter does not explicitly utilise the crack aspect ratio a. Instead, the crack geometry is defined using the crack closure stress, denoted by σ_c. This stress represents the minimum normal stress required to close the crack. Since we use the non-interactive effective medium theory, the initial aspect ratio and closure stress are directly proportional to each other. The following relation describes the relationship between these two parameters for penny-shaped cracks (Kachanov, 1982):

$$a = \gamma\sigma_c(1-\nu/2) \quad \text{with} \quad \gamma = \frac{32}{3\pi E}\frac{1-\nu^2}{2-\nu}\,, \tag{3.1}$$

in which E and ν are the Young's modulus and Poisson's ratio of the rock's mineral phase. The crack porosity distribution function ϕ_c is described in terms of the crack closure stress instead of the crack aspect ratio, and the following parametrization is proposed:

$$\phi_c(\frac{\sigma_c}{E}) = A_1\frac{\sigma_c}{E}\exp\left(-A_2\frac{\sigma_c}{E}\right), \tag{3.2}$$

introducing the two scalars A_1 and A_2. The relation between the crack porosity and crack density can also be constructed from a fracture mechanics argument:

$$\phi_c(\frac{\sigma_c}{E}) = \frac{32\pi}{3}\frac{\sigma_C}{E}(1-\nu^2)c(\frac{\sigma_c}{E})\,, \tag{3.3}$$

in which c is the unknown crack density, a function of the closure stress.

Compare now the parametrisation in eq.(3.2) and the theory in eq.(3.3) to deduce the crack density function and the cumulative crack density $c_{cum}(\sigma_c/E)$:

$$c\left(\frac{\sigma_c}{E}\right) = \frac{3A_1}{32\pi(1-\nu^2)}\exp\left(-A_2\frac{\sigma_c}{E}\right) \quad \text{and} \tag{3.4}$$

$$c_{cum}\left(\frac{\sigma_c}{E}\right) \equiv \int_0^{\sigma_c/E} c\left(\frac{\sigma_c'}{E}\right)\,d\frac{\sigma_c'}{E} = \frac{3A_1}{32\pi A_2(1-\nu^2)}\left[1-\exp\left(-A_2\frac{\sigma_c}{E}\right)\right]. \tag{3.5}$$

This crack density distribution is now considered in the following constitutive relations for the REV expressed in a rate form. The elastic strain rate, the difference between the total strain rate $\dot{\underline{\underline{\epsilon}}}$ and the strain rate due to the cracks $\dot{\underline{\underline{\epsilon}}}^c$ is given by

$$\dot{\underline{\underline{\epsilon}}} - \dot{\underline{\underline{\epsilon}}}^c = \mathbb{C}\colon(\dot{\underline{\underline{\sigma}}} + \alpha\dot{p}_f\underline{\underline{\delta}})\,, \tag{3.6}$$

in terms of the Cauchy stress rate $\dot{\underline{\underline{\sigma}}}$ and the fluid pressure rate $\dot{p}_f$. The material parameters introduced in eq. (3.6) are Biot's coefficient α, and the matrix's bulk modulus κ and shear modulus G incorporated in the isotropic elasticity fourth-order tensor $\mathbb{C}$. Note that $\underline{\underline{\delta}}$ is the identity tensor, and other second-order tensors are double-underlined. The definition of the deformation rate due to the cracks is based on the non-interactive scheme of Kachanov (1982):

$$\dot{\underline{\underline{\epsilon}}}^c = \frac{\pi}{2} \int_0^{\sigma_c^{max}/E} c\left(\frac{\sigma_c}{E}\right) \int_{\mathcal{H}_c} \dot{\underline{b}}(\underline{n}) \otimes \underline{n} + \underline{n} \otimes \dot{\underline{b}}(\underline{n})\, d\mathcal{H}_c\, d\frac{\sigma_c}{E}\,. \tag{3.7}$$

This definition involves two integrals. The inner integral is calculated over the hemisphere $\mathcal{H}_c$, which represents the double integral of the two orientation angles, β and $beta'$ of the unit normal to the crack surface. The angle β ranges from 0 to π, while β' ranges from 0 to $\frac{\pi}{2}$, as illustrated in Figure 3.1. This setup corresponds to an isotropic distribution of cracks with uniform aspect ratios. The vector $\dot{\underline{b}}$ denotes the average displacement jump rate for each crack orientation, considering both normal and tangential directions. This inner integral is a function of the closure stress σ_c, hence the necessity of the outer integral.

The outer integral sums the contributions from various potential aspect ratios, using the crack density function as a weight. It ranges from 0 to σ_c^{max}, thus establishing a cut-off point for the possible aspect ratios. In addition, the appendix B discusses the numerical quadrature for the inner integral in detail. We propose using the classical Gaussian quadrature to evaluate the outer integral. We consider a total of eighty distinct crack families, each with its own aspect ratio, to ensure convergence and high definition. This includes forty families that close at normal stress levels between 0 and $\sigma_c^{max}/5$. Additionally, there are forty families that close at normal stress levels ranging from $\sigma_c^{max}/5$ to σ_c^{max}.

The crack distribution utilised in our model is a novel approach accounting for frictional sliding. For this reason, in the next section, we will present the conventional crack density inversion technique, which only considers the incremental closing of the cracks. We will compare the results from these two methods later in the study.

3.2.2 Conventional crack inversion scheme

The crack density of open cracks can be approximated from the stress-strain curve of the hydrostatic compression test using Morlier's scheme (Morlier, 1971). Morlier's crack inversion method assumes that the non-linearity of the stress-strain curve during the loading phase is due to the progressive closing of cracks of different aspect ratios. This method also assumes that there are no crack-to-crack interactions. To simplify calculations, we consider that all cracks are ellipsoidal, since it has been shown that the crack shape has little influence on crack density estimations (Walsh, 1965; Zimmerman, 1990). The expression of the evolution of the open-crack density $\bar{c}_{op}$ with confining pressure is detailed in Appendix B.10 and reads

$$\bar{c}_{op} = \frac{9}{16}\left(\frac{\bar{\kappa}_\infty}{\bar{\kappa}} - 1\right)\left(\frac{1-2\bar{\nu}_\infty}{1-\bar{\nu}_\infty^2}\right), \tag{3.8}$$

where $\bar{\kappa}$ is the measured bulk modulus of the sample at different confining pressures, while $\bar{\kappa}_\infty$ and $\bar{\nu}_\infty$ are the effective bulk modulus and Poisson's ratio of the "minerals + non-closable pores" measured at high pressure. Note that in Zimmerman, 1990, $\bar{\kappa}_\infty$ and $\bar{\nu}_\infty$ are taken to be the moduli of the pure mineral phase of the rock, but it is more realistic to interpret them as the properties of the homogenised rock that contains only non-closable pores.

3.2.3 Spherical assemblage

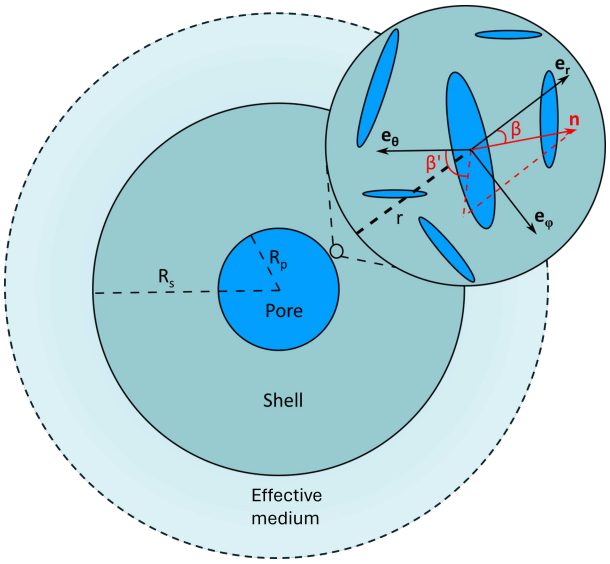


Figure (3.1) The specimen response is constructed with two homogenisation schemes. The first scheme is for an isotropic distribution of cracks, oriented by their unit normal $\underline{n}$ via the two polar angles β and β', as represented symbolically in the inset, within a porous, fluid-saturated elastic matrix. The resulting material composes the shell of a spherical assemblage with a fluid-filled pore. The second homogenisation scheme is for the interaction between the spherical assemblage and the effective medium, sustaining a homogeneous stress state.

The REV relationships described above pertain to the material points located within the shell of the spherical assemblage illustrated in Figure 3.1. The fluid-filled pore (radius R_p) generates the deviatoric stress in the shell (outer radius R_s) and is essential for the slipping of the frictional, closed crack within the REV. The second homogenisation follows the original proposal by Hashin (1962): the material surrounding the spherical assembly experiences a hydrostatic stress state ($-P_c\underline{\underline{\delta}}$), which serves as the homogenised solution and defines the loading on the external boundary of the shell. This solution is derived by solving the boundary value problem, ensuring continuity of radial stress and displacement at the external radius, while applying a specified fluid pressure within the cavity.

The crack density has been defined above in eq. (3.4) at the scale of the REV within the shell surrounding the pore. In this contribution, we will need to compare this crack density with the density of open cracks within the whole assemblage which is denoted $\bar{c}_o$. This macro-scale function is obtained as follows. First, consider the REV at any radial position in the shell and estimate the density of open cracks with

$$\int_0^{\sigma_c^{max}/E} c(\frac{\sigma_c}{E}) \int_{\mathcal{H}_c} H(\sigma_n + \sigma_C + p_f)\, d\mathcal{H}_c\, d\frac{\sigma_c}{E}\,, \tag{3.9}$$

in which $H(\sigma_n + \sigma_C + p_f)$ is the Heaviside function. It equals zero as long as $\sigma_n + \sigma_C + p_f < 0$, which is the closing criterion for any fracture sustaining the normal stress σ_n. Second, integrate eq. (3.9) along the radial direction of the spherical assemblage to get the macro-scale crack density:

$$\bar{c}_{op} = 3\int_{R_p/R_s}^1 \int_0^{\sigma_c^{max}/E} c(\frac{\sigma_c}{E}) \int_{\mathcal{H}_c} H(\sigma_n + \sigma_C + p_f)\, d\mathcal{H}_c\, d\frac{\sigma_c}{E}\, r'^2 dr'\,, \tag{3.10}$$

in which $r' = r/R_s$. The factor of three introduced before the first integral ensures that $\bar{c}_o p$ properly accounts for the porosity. Consequently, if all cracks were open, and since the same distribution is found at all radii around the pore, the limiting value of the macro-scale crack density is $(1-\phi)c_{cum}(\sigma_c^{max}/E)$, the cumulative crack density being defined in eq. (3.4) and ϕ being the porosity due to the central pore, $(R_p/R_s)^3$. Consequently, the initial open crack density is given by

$$\bar{c}_{opi} = \frac{3A_1(1-\phi)}{32\pi A_2(1-\nu^2)}\,, \tag{3.11}$$

with the addition of i in the subscript to indicate that the crack density is at its initial value. Note that a superposed bar on a variable, as in (3.11), signals a property defined at the assemblage scale after the second homogenisation. Similarly, a star in the superscript denotes a quantity evaluated at the REV within the shell material after the first homogenisation.

3.3 Loading and Unloading simulation at large strain amplitude

Here, we examine the experimental results, specifically the stress-strain curve, obtained from the slow hydrostatic loading and unloading of the dry Bentheim sandstone. These results are then compared with our model's predictions, which consider a distribution of crack aspect ratios and frictional sliding. We will derive parameters associated with the rock's solid phase and microcracks by optimising the modelled parameters to match the experimental stress-strain curve.

3.3.1 Preliminaries

The Bentheim sandstone used in this study is a clean sandstone consisting of 95% quartz with a porosity of 22% and a grain size ranging between 18 and 500 microns. The hydrostatic test conducted by Chapman *et al.* (2023) involved slowly loading the sample from an initial confining pressure of 2 MPa to a maximum pressure of 30 MPa (within the elastic range of the rock), and then slowly unloading it back to 2 MPa. This procedure was repeated three times to eliminate all inelastic artefacts and recover identical loops.

The grey curve in Figure 3.2 represents the experimental stress-strain curve, showing both non-linearity and hysteresis between the loading and unloading phases. At low pressure ($P_c = 5$ MPa), the average bulk modulus was 9.4 MPa during loading, and 9.1 MPa during unloading.

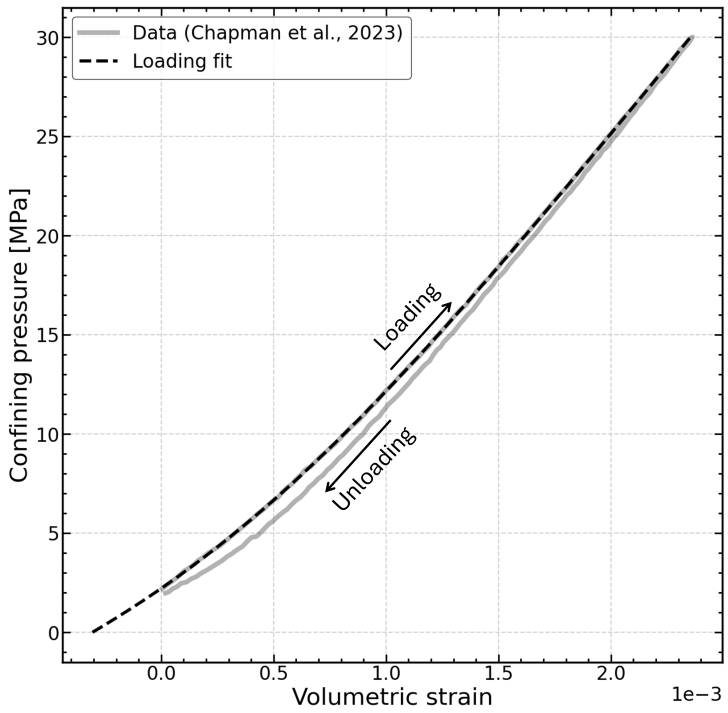


Figure (3.2) The experimental data from Chapman *et al.* (2023) and the fit of the loading data based on eq. (3.12).

At high pressure ($P_c = 25$ MPa), the values were 12.7 MPa during loading and 14.6 MPa during unloading, as stated in Table 3 of Chapman *et al.* (2023). It is worth noting that the data at zero pressure cannot be directly obtained from the measurements. However, we can fit the data with a curve in the form of eq.(5.8) of Zimmerman (1990):

$$\epsilon_{vol} = CP_c - De^{-P_c/\hat{P}_c} + F\,. \tag{3.12}$$

For the loading phase, the fitting parameters were $C = 0.072\ Pa^{-1}$, $D = 0.197{\times}10^{-3}$, $\hat{P}_c = 0.490$ Pa, $F = 6.33{\times}10^{-3}$. The dashed black line represents this fit. We now read an initial ($P_c = 1$ MPa) bulk modulus of $\bar{\kappa}_i = 7.4$ MPa. From Figure 2 and Table 1 of Chapman *et al.* (2023), we find that the high-pressure limits of the elastic wave speeds for the dry rock are $V_p = 3700$ m/s and $V_s = 2250$ m/s, and the density is 2036 kg/m^3. From these values, we can infer that the effective bulk and shear moduli of "minerals + non-closable pores" are $\bar{\kappa}_\infty = 14.1$ GPa, and $\bar{G}_\infty = 10.3$ GPa. This dynamic bulk modulus is very close to the static value at the high-pressure end of the loading curve, which Table 3 of Chapman *et al.* (2023) reports as 13.9 GPa. These values of $\bar{\kappa}_\infty$ and $\bar{G}_\infty$ lead to a Poisson's ratio of $\bar{\nu}_\infty = 0.206$. Now, the low-pressure and high-pressure limits can be used to constrain the parametrisation of the model for data fitting and compute the crack density function in eq. (3.8).

3.3.2 Model constraints and optimisation

From the loading stress-strain curve, we read the initial low-pressure bulk modulus $\bar{\kappa}_i$ and the maximum high-pressure bulk modulus $\bar{\kappa}_\infty$. The rock's porosity ϕ is also measured experimentally. Using these three parameters, we can derive the solid phase parameters E and ν in terms

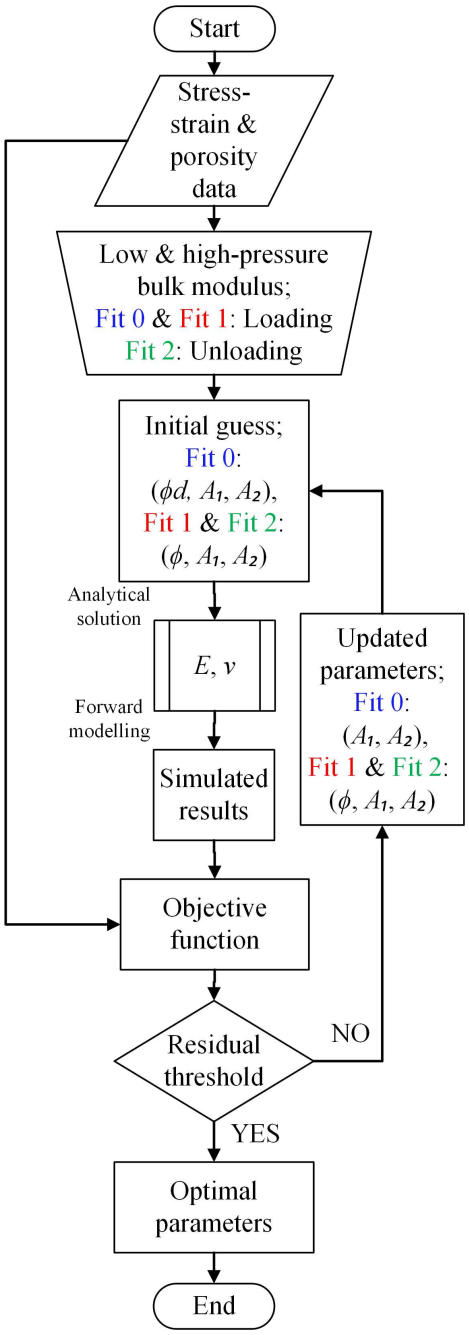


Figure (3.3) Flowchart of the modelling of the stress-strain curve during a hydrostatic compression simulation.

of the initial open-crack density. The following provides a step-by-step explanation of how this is done.

Based on the elasticity solutions presented in the previous chapter, we know that the effective bulk modulus κ^* and shear modulus G^* of a matrix containing a population of open microcracks of density c are given by

$$\frac{1}{\kappa^*} = \frac{1}{\kappa} + c\pi^2\gamma(2-\nu) \quad \text{, and} \quad \frac{1}{2G^*} = \frac{1}{2G} + 2c\pi^2\gamma(1-\frac{\nu}{5}), \tag{3.13}$$

where κ and G are the elastic parameters of the rock's solid phase. We then write the effective bulk modulus of the spherical assemblage as

$$\bar{\kappa} = \kappa^* \frac{1-\phi}{1+\phi\frac{3\kappa^*}{4G^*}}. \tag{3.14}$$

After substituting κ^* and G^* by their expressions in eq. (3.13), we obtain

$$\bar{\kappa} = \frac{\kappa(1-\phi)}{1+\kappa c\pi^2\gamma(2-\nu)+\frac{\phi\kappa}{4G}[3+4Gc\pi^2\gamma(1-\nu/5)]}, \tag{3.15}$$

and then solve for c:

$$c = \left[\frac{1}{\pi^2\gamma[2-\nu+\phi(1-\nu/5)]}\right]\left[\frac{1-\phi}{\bar{\kappa}} - \frac{1}{\kappa} - \frac{3\phi}{4G}\right]. \tag{3.16}$$

Low-pressure condition: At zero confining pressure, all cracks remain open, and using the initial crack density in eq.(3.11), eq.(3.16) provides

$$\frac{A_1}{A_2} = \frac{2-\nu}{(1-\phi)[2-\nu+\phi(1-\nu/5)]}\left[\frac{E(1-\phi)}{\bar{\kappa}_i} - 3(1-2\nu) - \frac{3\phi(1+\nu)}{2}\right], \tag{3.17}$$

having replace κ and G by their expressions in terms of E and ν.

High-pressure condition: At high pressure, we assume that all cracks are closed, even though there is a small fraction of cracks closest to the pore that never close. We write $\bar{\kappa} = \bar{\kappa}_\infty$, $\kappa^* = \kappa$, $G^* = G$, and $c = 0$. Using the elasticity elasticity solution in eqn (3.14), we solve for E:

$$E = \frac{3\bar{\kappa}_\infty[1-2\nu+\phi(\frac{1+\nu}{2})]}{1-\phi}. \tag{3.18}$$

Thanks to the low- and high-pressure limiting values, we obtain a system of two equations, eq.(3.17) and eq. (3.18), with two unknowns E and ν to be used as input parameters in the model for a given set of crack parameters A_1 and A_2.

We will conduct simulations with porosity (ϕ) treated either as a constraint or a fitting parameter. First, we will evaluate whether the measured porosity can accurately predict the observed hysteresis. If it does not, we will determine the optimal value of ϕ. Additionally, the only other parameters that will be optimised are the crack distribution scalars, A_1 and A_2. The complete modelling flowchart is illustrated in Figure 3.3.

3.3.3 Results

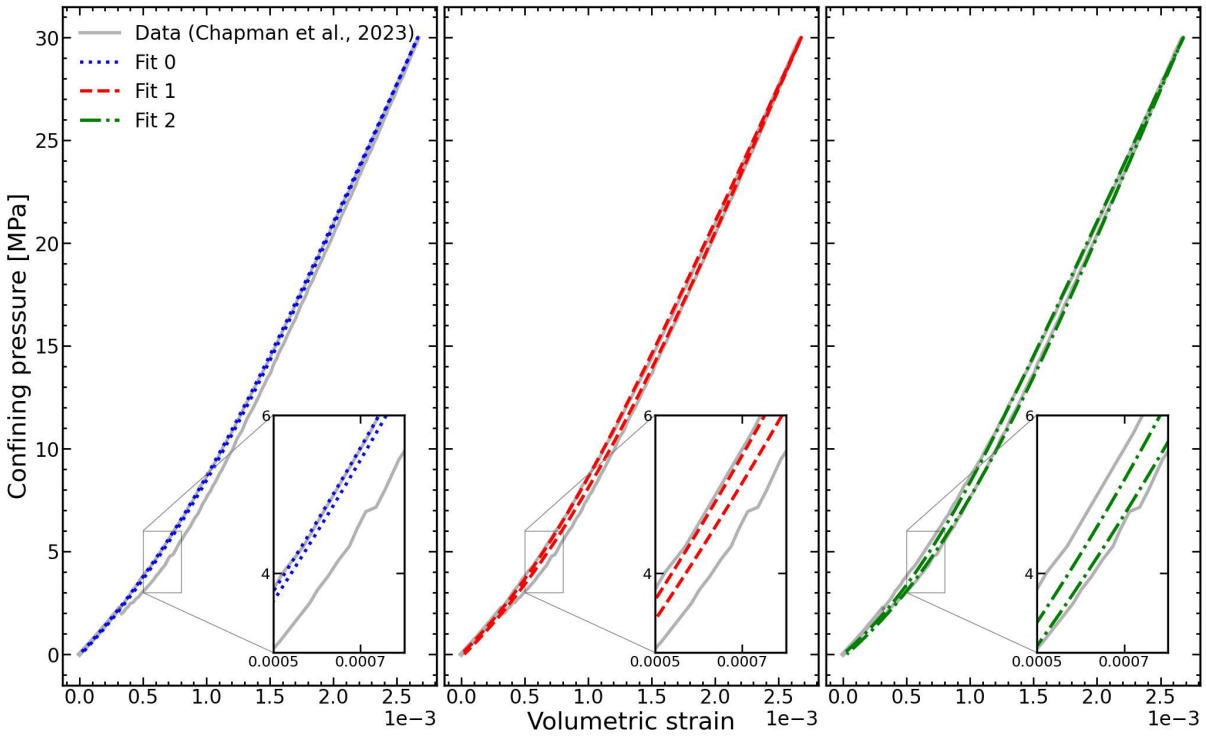


Figure (3.4) The relationship between the volumetric strain and confining pressure is evaluated for different simulations (*fit 0*, *fit 1*, and *fit 2*) and compared to the experimental data from Chapman *et al.* (2023). *Fit 0* is based on a measured porosity of 0.222 and utilises data from the loading curve. In contrast, *fit 1* does not constrain porosity, treating it as a fitting parameter. For *fit 3*, rather than using the loading phase data as constraints, it relies on the unloading phase to predict the strain response during the loading phase.

The relationship between the volumetric strain and confining pressure is evaluated for the three fits and compared to the experimental data in Figure 3.4. *Fit 0* is based on a measured porosity of 0.222, and utilises data from the loading curve. In contrast, *Fit 1* does not constrain porosity, treating it as a fitting parameter. For *Fit 3*, the porosity is also optimised, but rather than using the loading phase data as constraints, it relies on the unloading phase to predict the strain response during the loading phase.

Fit 0 achieves an excellent fit for the loading phase; however, the model predicts only a small amount of hysteresis between the loading and unloading phases. This means that a porosity of 0.222 is too small to generate the appropriate amount of frictional sliding and hysteresis, considering our spherical pore geometry. *Fit 1* also shows a good match with the measurements, although it predicts slightly less hysteresis than what was observed. It fits the unloading phase better at confining pressures above 10 MPa than those below. Additionally, *Fit 1* predicts larger bulk modulus values at low pressures and shows a smoother transition between the high-pressure and low-pressure bulk modulus values. This suggests a more gradual reopening of the cracks during the simulated unloading process. The evolution of the gradient of the unloading data curve indicates either a more abrupt reopening of the cracks at low pressure or a different crack distribution compared to the loading phase. This latter aspect prompted us to run the simulation *Fit 2*, which aims to predict the loading response based on unloading measurements,

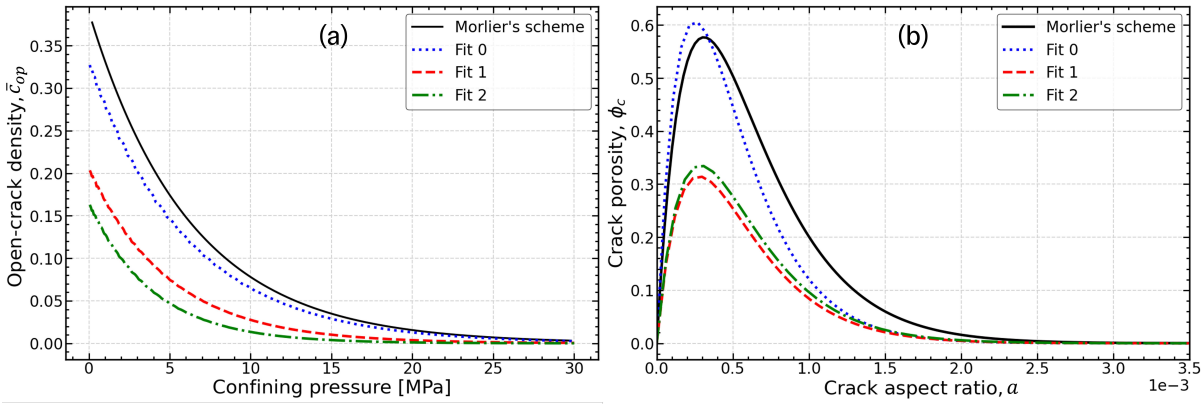


Figure (3.5) (a) Open crack density versus confining pressure and (b) Crack porosity distribution for each fit, compared to estimates derived from Morlier's scheme (Morlier, 1971) applied to the loading data. The total crack porosity is the area below the curve.

as opposed to predicting unloading from loading measurements. *Fit 2* shares similarities with *Fit 1*, but it is tailored to provide a more accurate representation of the unloading data rather than the loading data. Notably, both fits yield an optimal porosity value of 0.45.

In addition to the stress-strain hysteresis loop, the simulations also provide insights into the distribution of crack aspect ratios and the evolution of open-crack density with varying confining pressure. Figure 3.5 illustrates the evolution of open-crack density and crack distribution for each fit, taking into account frictional sliding, as well as estimates derived from Morlier's scheme (Morlier, 1971) for comparison purposes.

In Figure 3.5a, Morlier's inversion reveals an initial crack density of 0.37, with complete crack closure occurring at 30 MPa. *Fit 0* exhibits crack characteristics that are very similar to those from Morlier's inversion. In contrast, *Fit 1* and *Fit 2* predict initial crack density values of 0.20 and 0.16, respectively, with complete crack closure occurring at a confining pressure of approximately 20 MPa. This indicates that for *Fit 1* and *Fit 2*, the non-linearity observed in the stress-strain curve above 20 MPa is solely attributable to frictional sliding.

Furthermore, Figure 3.5b demonstrates that, although the amplitudes differ, all fits yield similar crack aspect ratio distributions, with a peak crack porosity of approximately $a = 0.3 \times 10^{-3}$.

Table (3.1) List of parameters used in the hydrostatic loading and unloading simulations for *fit 0*, *fit 1*, and *fit 2*. The data-constrained parameters include $\bar{\kappa}_i$, $\bar{\kappa}_\infty$, and ϕ (only for *fit 0*). The parameters A_1 and A_2 (as well as ϕ for *fit 1* and *fit 2*) are optimised to fit the data. Additionally, E and ν are calculated analytically using equations (3.18) and (3.17). Note that the internal friction coefficient μ was not measured; therefore, a value of 0.28 was used for quartz, as referenced in the literature (Senetakis *et al.*, 2013).

Fit	**Assemblage**			**Matrix**		**Cracks**		
	$\bar{\kappa}_i$ [GPa]	$\bar{\kappa}_\infty$ [GPa]	ϕ	E [GPa]	ν	A_1	A_2	μ
Fit 0	7.4	14.1	0.22	37.5	0.22	8480	3950	0.28
Fit 1	7.4	14.1	0.45	41.7	0.38	5900	3500	0.28
Fit 2	7.0	14.1	0.45	32.8	0.45	5800	3500	0.28

All the parameters used in the three simulations are listed in Table 3.1. The data-constrained

parameters include $\bar{\kappa}_i$, $\bar{\kappa}_\infty$, and ϕ (only for *Fit 0*). The parameters A_1 and A_2 (as well as ϕ for *Fit 1* and *Fit 2*) are optimised to fit the data. Additionally, E and ν are calculated analytically using equations (3.18) and (3.17). We remark that the values of Poisson's ratio for *Fit 1* and *Fit 2* are relatively high, at 0.38 and 0.45, respectively. In fact, an increase in Poisson's ratio is expected for *Fit 2*, given the constraints of the simulation. *Fit 2* was performed to better match the unloading curve. Since the average bulk modulus during unloading is larger than during loading, and recognising that bulk modulus is inversely related to $1 - 2\nu$, an increase in bulk modulus corresponds to an increase in Poisson's ratio. However, the value of ν and the overall quality of the fits may be significantly influenced by the initial bulk modulus, $\bar{\kappa}_i$, which was approximated in the preliminary analysis using equation (3.12). To investigate this further, a brief sensitivity analysis is now proposed to assess how variations in the initial bulk modulus affect the prediction.

Let us consider a *Fit 3* similar to *Fit 0*, meaning that the porosity is constrained to the measured porosity of 0.222, with the exception that $\bar{\kappa}_i$ is now optimised. Figure 3.6 shows the hysteresis loop for *Fit 3*. The predicted parameters are $\bar{\kappa}_i = 4.5$ GPa, $E = 31.6$ GPa, $\nu = 0.31$, $A_1 = 20000$, $A_2 = 6000$, and $\mu = 0.28$. *Fit 3* not only predicts a smaller value of Poisson's ratio, but it also yields hysteresis despite using the measured porosity. However, the predicted crack parameters are very different from the other fits, as shown in Figure 3.7, with an initial crack density close to 0.5 and a narrower distribution of crack aspect ratios.

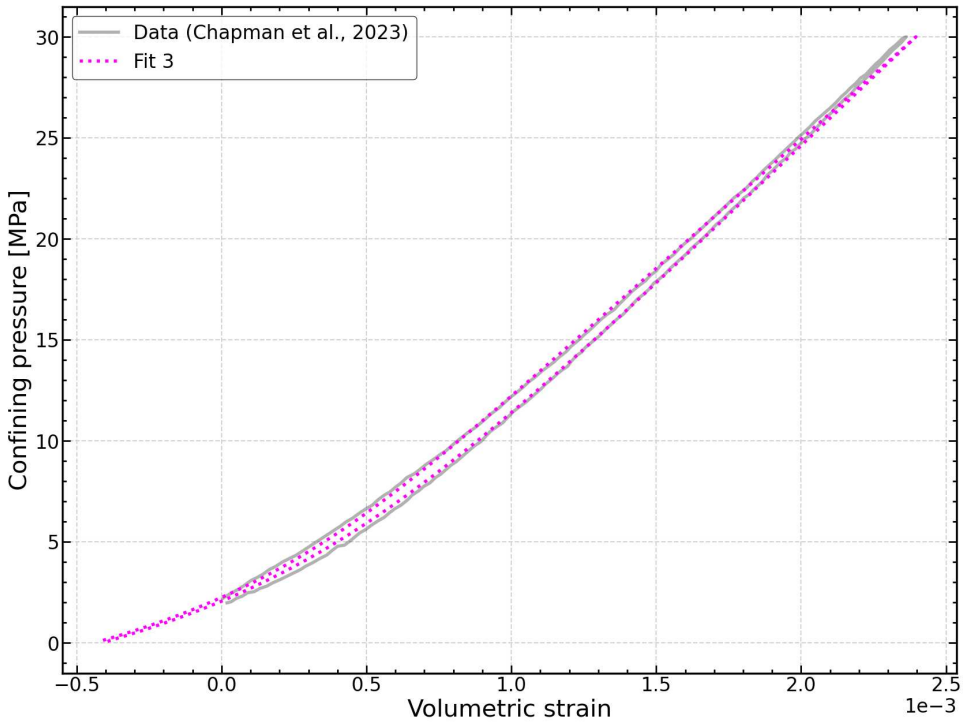


Figure (3.6) The relationship between the volumetric strain and confining pressure is evaluated for *Fit 3* and compared to the experimental data from Chapman *et al.* (2023). *Fit 0* is based on a measured porosity of 0.222 and utilises $\bar{\kappa}_\infty$= 14.1 GPa from the data but optimises $\bar{\kappa}_i$, along with the crack parameters, to match the data.

These results demonstrate that the value of the initial/zero-pressure bulk modulus, which is not systematically measured by experimentalists, has a significant impact on the model's pre-

dictions. Still, the approximation presented in equation (3.12) has proven to be quite effective (Zimmerman, 1990), and it may be worthwhile to prioritise it over calculating the initial bulk modulus using the current model, which is why *Fit 3* will not be used in the rest of the chapter (forced oscillations). However, optimising the initial bulk modulus provides a fresh perspective on crack distribution, which significantly differs from Morlier's approach (Figure 3.7).

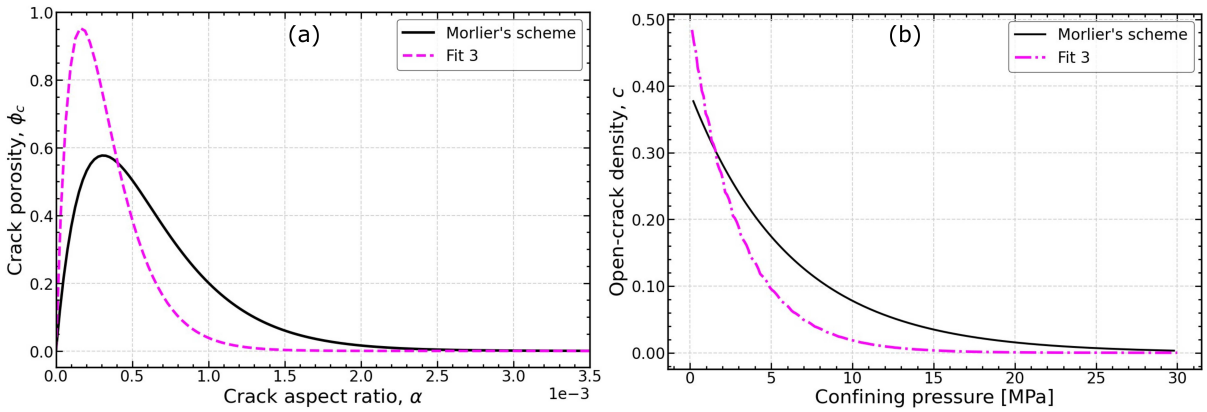


Figure (3.7) (a) Crack porosity distribution and open-crack density versus confining pressure for *Fit 3*, compared to estimates derived from Morlier's scheme (Morlier, 1971) applied to the loading data. The total crack porosity is the area below the curve.

3.3.4 Correlation between modelled and measured porosity

The results showed that to predict the unloading stress-strain curve of the Bentheim sandstone based on the loading measurements, the modelled porosity needed to be doubled. This means that the simplified shape (spherical central pore) based on the measured porosity is not sufficient to create the appropriate level of deviatoric stress felt by the surrounding microcracks and necessary for slip. Hence, we need to systematically increase the size of the central pore to simulate the amount of local deviatoric stress that occurs experimentally. Finding a relation between the modelled and measured porosities is necessary to unlock the model's predictive power.

To decipher a trend between the modelled and measured porosity, a series of simulations were conducted on six additional rocks of various natures (two sandstones, four limestones, and one granite). Figure 3.8 shows the best fits for a – carbonate C-2, b – carbonate C-3, c – Chauvigny limestone, d – Bentheim sandstone (Wang *et al.*, 2021), e – Mushan sandstone (Jeng *et al.*, 2002), and f – Sierra white granite (Martin III *et al.*, 1994). For some samples (Bentheim sandstone, Mushan sandstone, and Sierra white granite), the experimental data show a residual strain at zero pressure during unloading, possibly due to the relaxation rate and other phenomena unrelated to microcrack sliding. Because the model is not strain-rate sensitive, we do not expect it to capture such residual strain.

All the best fits required an increase in porosity. By plotting the modelled porosity against the measured porosity for each sample, we observe a linear trend, as shown in Figure 3.9. The modelled porosity is given by $y = 1.46x + 0.12$, where x is the measured porosity. This indicates that for a given measured porosity, we can estimate the optimal porosity based on this linear

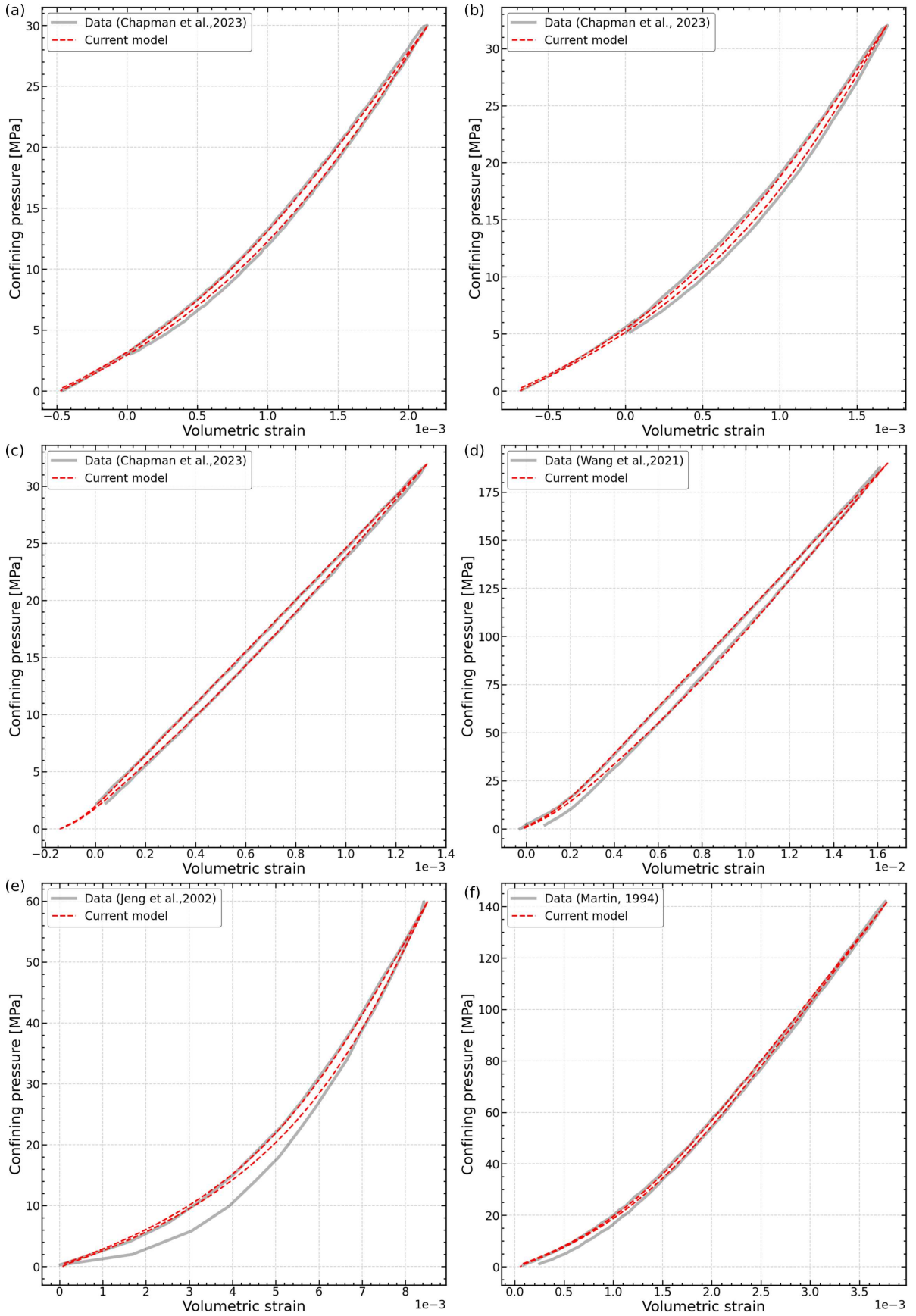


Figure (3.8) Best fits of the stress-strain measurements done on various rocks of different natures; a– carbonate C-2, b– carbonate C-3, c– Chauvigny limestone, d– Bentheim sandstone, e– Mushan sandstone, and f– Sierra white granite.

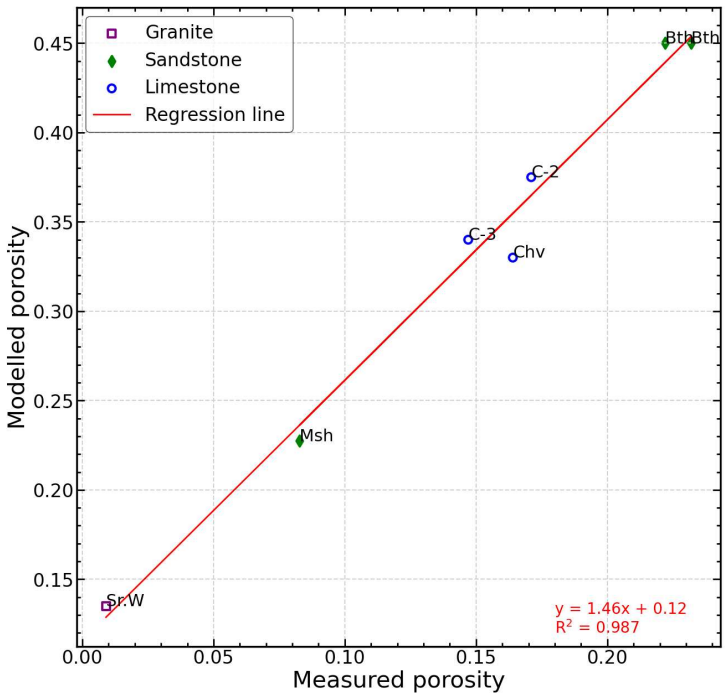


Figure (3.9) The modelled versus measured porosity for the carbonate C-2, carbonate C-3, Chauvigny limestone, Bentheim sandstone, Mushan sandstone, and Sierra white granite.

trend. We can then use this optimal porosity in the forward model to predict hysteresis.

3.4 Forced oscillation simulation

In this section, we first analyse the strain amplitude dependence of the bulk modulus through FO simulations for (*Fit 1* and *Fit 2*) of various amplitudes for increasing effective pressure. The purpose is to bridge the gap between static and dynamic bulk modulus measurements.

Second, we compare the compressibility measurements obtained through small amplitude oscillations from the study conducted by Pimienta *et al.* (2017) with the simulations *Fit 0*, *Fit 1* and *Fit 2*. We will also simulate the difference between FO in the loading versus unloading phase. The objective is to reveal the crack contribution to different bulk compressibility values to better understand experimental measurements, which sometimes deviate from theoretical poroelastic behaviour.

3.4.1 Estimation of compressibility and bulk modulus

In each FO simulation, six saw-tooth pressure cycles are applied, as illustrated in Figure 3.10a. We then perform a Fourier transform on the stress and strain oscillations to obtain the signal amplitudes, as shown in Figure 3.10b. The bulk modulus is calculated from the ratio of the maximum peak amplitudes in the stress and strain spectra. This Fourier transform method is the standard approach used by experimentalists for analysing forced oscillations (Pimienta *et al.*, 2015; Pimienta *et al.*, 2017; Borgomano *et al.*, 2017; Chapman *et al.*, 2023). This method is slightly sensitive to the sinusoidal nature of these oscillations. A brief analysis of this sensitivity

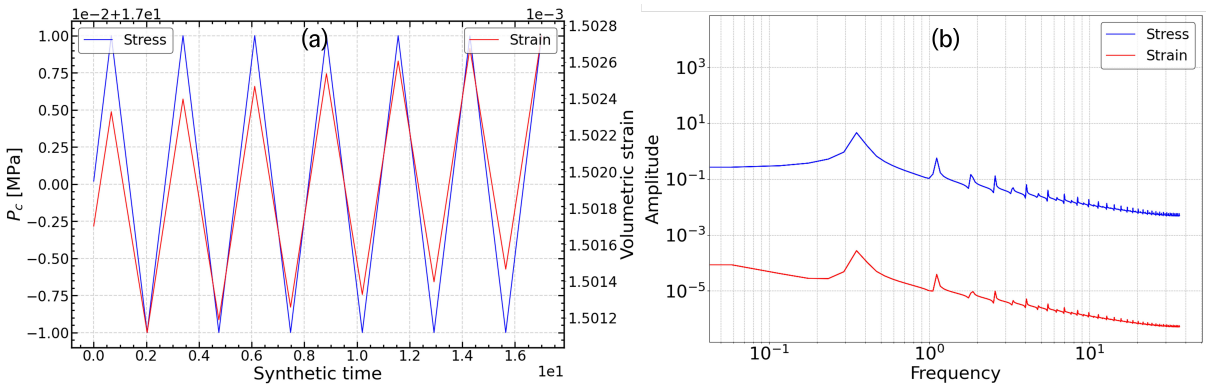


Figure (3.10) The Fourier transform is performed on the simulated stress and strain signals from (a) to (b). Then the bulk modulus is calculated from the ratio of the maximum peak amplitudes in the stress and strain spectra.

is presented in Appendix B.11, comparing two types of oscillation signals: a triangular function and a step function.

3.4.2 Strain amplitude dependence of bulk modulus

Figure (3.11) illustrates the bulk modulus as a function of strain amplitude, where the volumetric strain is divided by three to approximate the uniaxial strain (on the order of 10^{-6}) induced by propagating waves. This data is associated with different oscillation amplitudes at specific effective pressures of 5, 7.5, 15, and 25 MPa. The graph shows the results of *Fit 1* and *Fit 2*, along with dynamic, FO (referred to as quasi-static in Chapman *et al.*, 2023), and static experimental data (see section 3.3).

At an effective pressure of 5 MPa, both *Fit 1* and *Fit 2* align closely with the static data at large strain amplitudes (approximately 2×10^{-4}). However, they predict a small-strain bulk modulus between 9.5 and 10 GPa, which is about 10% lower than the dynamic measurement. This indicates the model does not produce sufficient crack effects to explain the 15% discrepancy observed between the static and dynamic measurements.

At an effective pressure of 7.5 MPa, only dynamic and static data were available, revealing a discrepancy of 12% between the two measurements. In *Fit 1*, there is a 5% difference between the small strains (ranging from 10^{-7} to 10^{-6}, which are associated with dynamic properties) and the large strain amplitudes (around 2×10^{-4}, which are tied to static measurements). The transition occurs between strain amplitudes of approximately 3×10^{-7} and 3×10^{-5}. *Fit 2* shows a similar trend, but the discrepancy between the simulated smallest and largest strains is more pronounced, reaching 9.5%.

At an effective pressure of 15 MPa, both *Fit 1* and *Fit 2* predict a dynamic bulk modulus that is 4.5% and 4.2% greater than the static bulk modulus, respectively. *Fit 2* consistently lies above *Fit 1*, although both curves exhibit the same trend of decreasing bulk modulus as the strain amplitude increases. Furthermore, these fits closely follow and bound the experimental quasi-static data.

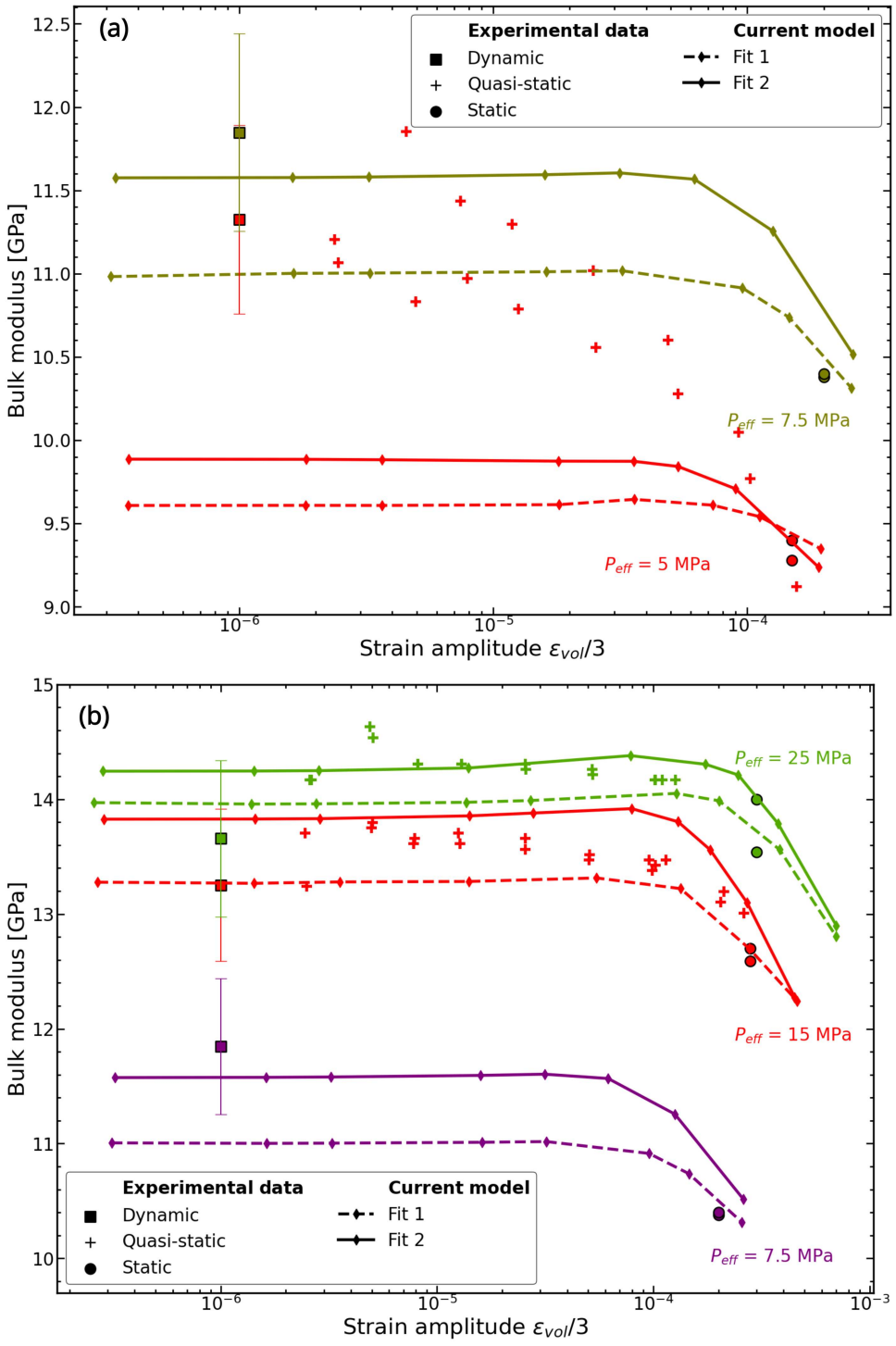


Figure (3.11) The simulated results of the forced oscillations using *Fit 1* and *Fit 2* are compared with the forced-oscillation (quasi-static), static, and dynamic measurements obtained by Chapman *et al.* (2023). It is important to note that whereas the data reflect measurements taken during both the loading and unloading phases, the FO simulations were conducted only during the loading phase. This is because there is minimal difference in the simulated results of forced oscillations between the loading and unloading phases for a given fit.

At an effective pressure of 25 MPa, the two fits are closer to each other, showing minimal discrepancy between the dynamic and static bulk modulus, which aligns with the measurements. Notably, the transition zone appears at larger strain amplitudes, near 3×10^{-4}.

Overall, the simulated results match the experimental observations regarding how the bulk modulus depends on strain amplitude. They also highlight a transition zone between dynamic and static measurements. The findings confirm that in dry sandstones, the differences observed between static and dynamic measurements primarily stem from frictional contacts and microcracks, which react differently based on the applied stress amplitude. The model can be effectively used to predict the dynamic strain response using static data.

3.4.3 Compressibility coefficients versus effective pressure

Definitions of compressibilities

The compressibility of a rock is a parameter that defines how its volume changes in response to a change in confining pressure. In porous rocks, volume changes can also occur due to changes in pore pressure, regardless of the confining pressure. This means that the pore pressure P_p, felt by all cracks, can vary independently from the confining pressure P_c and the pore volume V_p can be independent of the bulk volume V_b. Based on these four independent variables, Zimmerman *et al.* (1986) introduced four different compressibilities that relate changes in either V_b or V_c to changes in P_c or P_p, at constant temperature. Pore compressibility can be measured by a change in confining pressure at constant fluid pressure (C_{pc}) or by a change in pore pressure at constant confining pressure (C_{pp}). Similarly, bulk compressibility can be measured by a change in confining pressure at constant fluid pressure (C_{bc}) or by a change in pore pressure at constant confining pressure (C_{bp}):

$$C_{bc} = -\frac{1}{V_b^i}\left(\frac{\partial V_b}{\partial P_c}\right)_{P_p}, \quad C_{bp} = \frac{1}{V_b^i}\left(\frac{\partial V_b}{\partial P_p}\right)_{P_c}, \tag{3.19}$$

$$C_{pc} = -\frac{1}{V_p^i}\left(\frac{\partial V_p}{\partial P_c}\right)_{P_p}, \quad C_{pp} = \frac{1}{V_p^i}\left(\frac{\partial V_p}{\partial P_p}\right)_{P_c}. \tag{3.20}$$

This study will concentrate on the bulk compressibilities C_{bp} and C_{bc}.

Analytical solutions for C_{bp} and C_{bc} can be derived in two scenarios: when all cracks are open and when all cracks are closed and sticking. The solutions are directly inferred from the previous chapter, and their construction is also detailed in appendix B.8:

$$C_{bc} = \frac{1}{\bar{\kappa}}\,, \text{and} \quad C_{bp} = C_{bc} - \frac{(1-a)}{\kappa}\,. \tag{3.21}$$

Compressibility predictions

We simulated small amplitude oscillations (± 0.1 MPa) in both the confining and pore fluid pressure to assess the bulk compressibility parameters, C_{bc} and C_{bp}, derived from the model fits *fit 0*, *fit 1*, and *fit 2*. The results are illustrated in Figure 3.12, where we juxtapose the simulated

bulk compressibility values for C_{bc} and C_{bp} against the experimental measurements obtained by Pimienta *et al.* (2017) on Bentheim sandstone, which was sourced from the same geological block investigated by Chapman *et al.* (2023). The two sets of measurements are consistent with each other in terms of bulk modulus and compressibility C_{bc}, within the error margins presented by Pimienta *et al.* (2017).

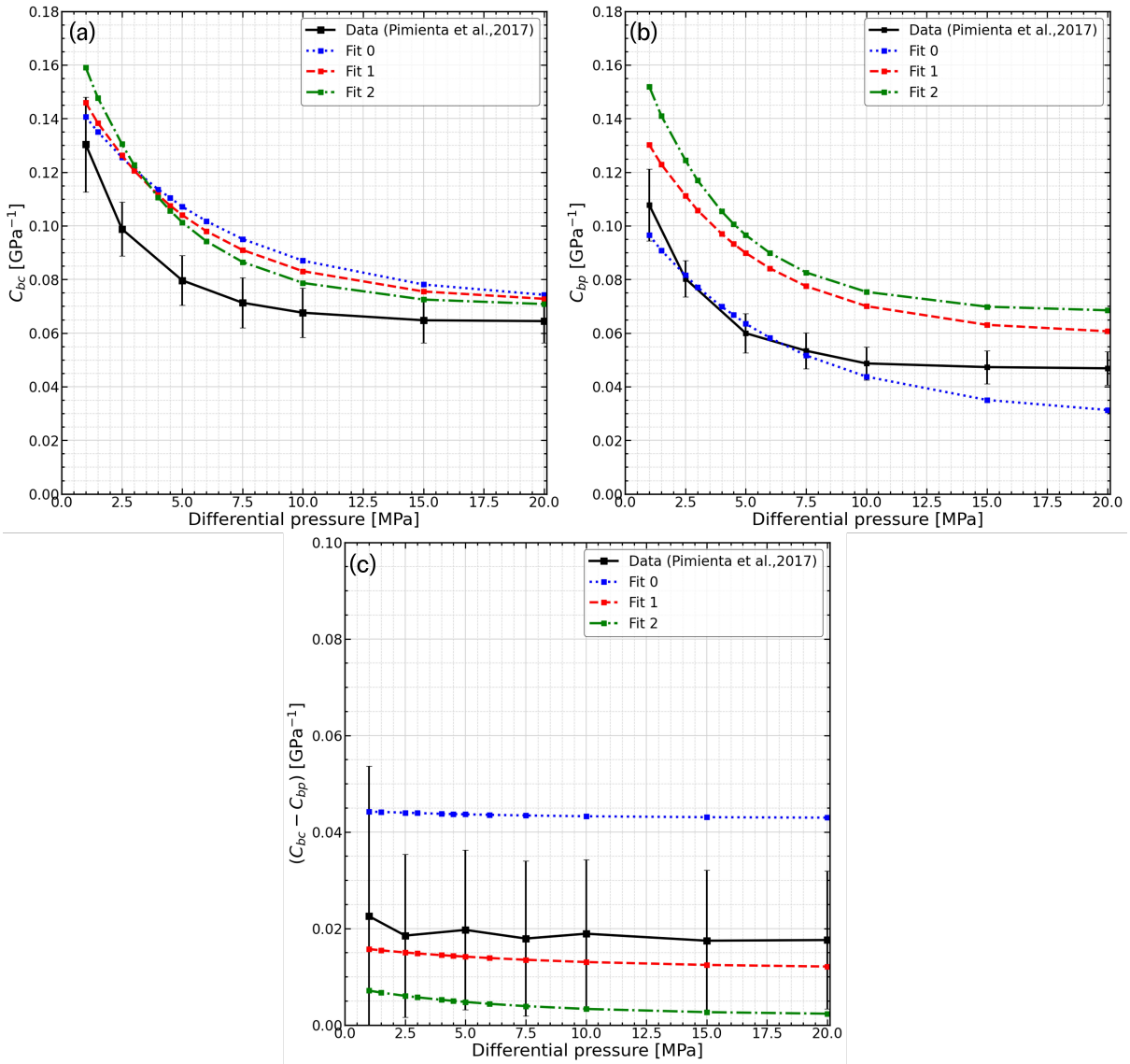


Figure (3.12) The simulated bulk compressibility values C_{bc} and C_{bp} for fits 0, 1, and 2 are compared to the measurements reported by Pimienta *et al.* (2017) on a Bentheim sandstone, which was cored from the same block as that studied by Chapman *et al.* (2023). The results show how C_{bc} and C_{bp} evolve with increasing differential pressure, as well as the apparent compressibility of the rock's skeleton $(C_{bc} - C_{bp})$. It is expected that the compressibility of the skeleton will approach 0.02 GPa^{-}1 at high pressure for clean sandstones composed of 99% quartz.

In the case of C_{bc}, all three fitting models reveal a strikingly similar trend: a gradual decline in values from an initial peak of 0.14–0.16 GPa^{-1} down to a minimum value of 0.07 GPa^{-1}. Remarkably, the predictions for C_{bc} tend to be, on average, 7% to 10% higher than the empirical measurements but ultimately converge at the same lower threshold of 0.07 GPa^{-1}, suggesting a mutual trend in compressibility as pressure increases.

Conversely, C_{bp} shows a different dynamic. *fit 1* and *fit 2* are closely aligned, exhibiting comparable trends to the experimental data. However, these two fittings consistently produce values that are greater than the observed data. In contrast, *fit 0* diverges significantly from its counterparts, initially aligning well with the data at differential pressures below 10 MPa. Yet, as the pressure keeps rising, *fit 0* starts to deviate, ultimately reaching a minimum value of 0.03 GPa^{-1} at a differential pressure of 20 MPa. In comparison, the actual measurements converge towards 0.05 GPa^{-1}. This divergence underscores the complex nature of bulk compressibility under varying pressure conditions.

The differences in physical properties, particularly the crack parameters and hysteresis discussed in previous sections, have a smaller impact on C_{bc} compared to C_{bp}. This is supported by the fact that the fits yield similar results for C_{bc} but show considerable variation for C_{bp}. This distinction is evident in Figure 3.12, which depicts the difference $C_{bc} - C_{bp}$. This difference represents the apparent compressibility of the rock's skeleton and, in theory, should remain independent of pressure. However, the results indicate that it varies under differential pressures below 15 MPa for *fit 1*, *fit 2*, and the experimental data, while it remains nearly constant for *fit 0*.

The main reason for this variation is the influence of Biot's coefficient within REV, which includes both the matrix and cracks. While the Biot coefficient is zero in the matrix, the presence of cracks introduces a non-zero Biot coefficient, as explained in Appendix B. Consequently, fluctuations in confining pressure and pore pressure lead to different local stress distributions. This results in microcracks responding differently to oscillations of confining pressure and pore fluid pressure, especially under low differential pressures. More cracks are activated during C_{bc} simulations than during C_{bp} simulations. This finding has significant implications for projects involving cyclic fluid injection and extraction, highlighting the need to monitor the rock's skeleton strength carefully.

Loading versus unloading

In the monotonic loading experiment, hysteresis was observed. It raises the natural query about the potential disparity between the results of the FO experiment during unloading and those during the loading phase described above. Due to the complexity of the procedure and time limitations, Pimienta *et al.* (2017) solely undertook the experiment during the loading phase, resulting in the absence of data for the unloading phase. Nevertheless, it is feasible to numerically simulate both scenarios, conduct a comparative analysis, and evaluate the necessity of performing both the loading and unloading experiments in the laboratory.

In Figure 3.13, the modelled evolution of C_{bp} and C_{bc} is shown during both the loading and unloading phases. A very small difference exists between the loading and unloading phases for both C_{bp} and C_{bc}. The greatest variances occur at larger differential pressures of 15 MPa and 20 MPa, corresponding to the middle section of the hysteresis loop from *fit 1*. It is safe to say that the difference between the loading and unloading results is too small to necessitate both experiments to be systematically conducted in the laboratory.

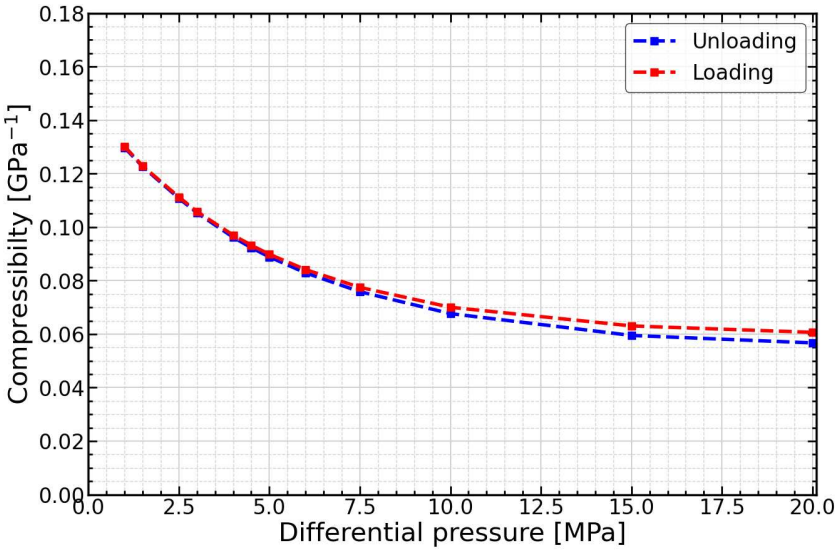


Figure (3.13) simulated C_{bp} and C_{bc} using an oscillating confining pressure of 0.1 MPa on *fit 1*, at different differential Terzaghi stress, during the loading and unloading phases.

3.5 Conclusion

This study has extended our previous microcrack model (Biyoghé *et al.*, 2024a) to predict hysteresis in rocks subjected to hydrostatic compression by incorporating a distribution of microcracks with varying aspect ratios. The application of this model to Bentheim sandstone revealed that the predicted porosity must be approximately twice the measured porosity to simulate the observed hysteresis accurately. Coupled with additional measurements on other rocks, we found a linear relationship between modelled and measured porosity, facilitating the prediction of hysteresis and crack density distribution across different rock types.

The FO simulations using the enhanced micromechanical model predicted the strain amplitude transition from static to dynamic bulk modulus. The results closely matched the experimental observations and showed that the complex mobilization (closing, slip, and stick) of microcracks near the pore due to slight pressure changes leads to amplitude dependence of the bulk modulus.

Similarly, additional FO simulations demonstrated that the sliding of microcracks significantly influences the bulk compressibility parameters C_{bp} and C_{bc} of the Bentheim sandstone, particularly at low differential pressures. The model's ability to replicate the experimental trends in compressibility values indicates its efficacy in representing the micromechanical processes occurring during forced oscillations. We found that the microcracks respond differently to confining pressure (C_{bc}) and pore fluid pressure C_{bp} oscillations. The variation arises from Biot's coefficient in the REV, which accounts for both the matrix and cracks. While the matrix has a Biot coefficient of zero, the cracks introduce a non-zero value. Consequently, changes in confining and pore pressure result in different local stress distributions.

Since our model can effectively predict the dynamic strain response using static data, future work should focus on predicting static properties based on dynamic measurements. This challenge is significant for geophysicists, who often have access to dynamic measurements but lack

corresponding static data. Simulations of the wave propagation test for dynamic measurements can assist in mapping the transition from dynamic to static elastic properties. A second development direction is for modelling purposes at a larger scale, such as the reservoir scale. In that instance, and because of the spatial discretisation, a simplified constitutive relation with a limited number of internal variables to replace our complex crack distribution will be required.

Chapter 4

Simulations of Ultrasonic Wave Propagation

Chapter Abstract

Accurately determining the emitted S-wave arrival time at the piezoelectric receiver of laboratory triaxial cells is challenging due to the complex preceding P and S wave patterns. To analyse this pattern and decipher the proper arrival time of the emitted S-wave, we simulate wave propagation from the actuator to the receiver. The piezoelectric response is accounted for, and the electromechanical coupling is solved using either the spectral finite-element method or two simplifications: a linear spatial variation of the electric potential over the actuator and a simplified Bubnov-Galerkin approach to capture the same field over the receiver. The fully-coupled algorithms are validated with 1-D simulations and compared with an exact solution constructed with the method of characteristics. Simulations for a 2D simplified experimental system show the validity of the two simplifications and their advantage in terms of CPU times. The comparison of simulation results through a section of the triaxial cell with laboratory calibration data for a steel specimen validates our choice of a damping material proxy within the actuator. A final series of simulations for two orthotropic shales with different anisotropy axis orientations with respect to the cell and two Fontainebleau sandstones having very contrasted V_P/V_S ratios is presented. These differences have little impact on the wave pattern at and just after the arrival of the main S wave. The pattern is more influenced by the experimental setup geometry and the actuator's internal structure than by the nature of the specimen.

4.1 Introduction

Laboratory techniques play a crucial role in investigating the properties of rocks, and one widely used is the ultrasonic propagation technique (UPT). Since its popularisation at the end of the 1960s (Birch, 1960; Nur *et al.*, 1969), UPT has become a standard method for evaluating the elastic properties of rocks (Krautkrämer *et al.*, 2013; Prassianakis *et al.*, 2004). The rock's dynamic elastic moduli can be inferred by propagating high-frequency (MHz) waves through

rock specimens, and analysing the travel times of these waves. The P-wave velocity is easily deduced from the first wave arrival time. However, accurately determining the S-wave velocity is more challenging due to superimposed surface waves and early reflections defining the wave pattern (Liu *et al.*, 2009). This chapter aims to predict both the S-wave arrival time and its signature pattern applied to a triaxial press setting numerically.

To overcome these challenges, numerical simulations can be used to guide experimentalists. Numerical methods have been extensively utilised in large-scale, low-frequency seismic investigations, aiding in the interpretation of seismic profiles (Komatitsch *et al.*, 1999; Komatitsch *et al.*, 2000). Nevertheless, when it comes to ultrasonic simulations at the laboratory scale, they are relatively rare and often rely on proxies, such as displacement, to replicate the input pulse and output signal (Huang *et al.*, 2021; Yurikov *et al.*, 2019). These approximations typically isolate vertical and horizontal displacements, resulting in independent signals for longitudinal and transversal waves. Although the piezoelectric materials inside the captors have a poling direction, they are designed to generate/capture either P or S waves, and some mechanical energy from the unwanted type of wave will always be converted into electricity. Therefore, it becomes crucial to consider the characteristics of the PZT used as actuators and receivers in UPT (Kwun *et al.*, 1988). Note that the abbreviation PZT (lead, zirconate, titanate) will be used as a general term to designate any type of piezoelectric ceramic.

Numerical methods have been extensively utilised in large-scale, low-frequency seismic investigations, aiding in the interpretation of seismic profiles (Komatitsch *et al.*, 1999; Komatitsch *et al.*, 2000). Nevertheless, ultrasonic simulations at the laboratory scale are relatively rare and often rely on proxies, such as displacement, to replicate the input pulse and output signal (Huang *et al.*, 2021; Yurikov *et al.*, 2019). These approximations typically consider the displacement in only one direction, resulting in independent signals for longitudinal and transversal waves. Although the piezoelectric materials inside the captors have a poling direction (designed to generate/capture either P or S waves), some mechanical energy from the unwanted type of wave will always be converted into an electrical signal.

This chapter presents a novel approach to UPT simulations by solving the electromechanical problem at the transducers via the spectral finite element method (SFEM) to correctly predict the S-wave arrival time and signature pattern. A review of numerical methods for modelling mechanical wave propagation was done by Seriani *et al.* (2020). Among other numerical methods, such as discontinuous Galerkin and finite volume methods, SFEM is well suited for wave propagation problems at high frequencies, as demonstrated by Komatitsch *et al.* (2000), Luo *et al.* (2010), Hennings *et al.* (2013), and is one method in which we have experience (Leroy, 2011). Whereas there exists a substantial literature on numerical simulations of the piezoelectric effect to enhance transducer design (Zhou *et al.*, 2015; Yaghmaie *et al.*, 2018; Nguyen-Van *et al.*, 2008), such simulations have not, to our knowledge, been performed for UPT measurements in a triaxial press or other geophysical settings. Our goal is to predict the electronic output signal at the arrival of the S-wave, using SFEM for spatial discretisation and the explicit central difference scheme for time integration. In this process, a 1 MHz voltage pulse is applied between the actuator electrodes, which generates a series of S and P waves propagating through

the confining cell, sample, and sensors. The wave-induced deformation pulse is converted into an electrical signal at the receiver electrodes, ultimately leading to a measurable voltage signal. We show how the voltage waveform at the receiver depends on the piezoelectric properties of the PZT (lead, zirconate, titanate) transducers that are used as actuators and receivers in UPT and on the geometry of the triaxial press. Note that the abbreviation PZT will be used as a general term to designate any piezoelectric ceramic.

The rock specimens under investigation are homogeneous and either isotropic or anisotropic. We provide a visual representation of the UPT experiment by showcasing the propagation of waves and their interactions with the apparatus, receiver, and each other. A mix of quantitative and qualitative analyses is conducted to identify noise in the waveform before the arrival of the emitted S-wave by comparing the wave phases and pattern arriving at the receiver with the experimental results.

We first present the piezoelectric governing equations. We then provide the analytical solution to the coupled problem for a 1D steel bar, where an actuator and receiver are inserted on either side of the rock specimen. The weak form of the coupled problem and the central difference scheme for its solution are given in Benjeddou, 2000. The validity of our numerical method is assessed through comparisons with the analytical solution. Furthermore, we explore simplifications of the coupled problem to reduce computational time and propose numerical proxies for the 2D actuator and receivers. Finally, we compare our 2D simulations with laboratory results, focusing on a calibration test conducted with an inox steel specimen with additional information on the effect of the PZT's backing material in Appendix C.2. We also discuss the influence of Poisson's ratio and rock anisotropy on the waveform by comparing predictions on different rock types, including Fontainebleau sandstones and orthotropic shales. It turns out that the waveform is more influenced by the experimental setup's geometry and the PZT actuator's internal structure than by the nature of the specimen.

4.2 piezoelectric coupling

4.2.1 3D governing equations

The governing equations for the PZT can be found in numerous publications, and the formulation given in the monograph of Yang (2018) is used in what follows. Most of the literature assumes a linear relationship between stress, strain, and electrical field, which is valid under two conditions. Firstly, one has to check that the components of the strain tensor are much less than unity. Secondly, the stress changes due to the electric field should be smaller than the changes due to deformation. The linear coupled constitutive relations for the PZT material are

$$\begin{aligned} \underline{\underline{\sigma}} &= \mathbb{C} : \underline{\underline{\epsilon}} - {}^{t}\underline{\underline{\underline{e}}} \cdot \underline{E}, \\ \underline{D} &= \underline{\underline{\underline{e}}} : \underline{\underline{\epsilon}} + \underline{\underline{\varepsilon}} \cdot \underline{E}, \end{aligned} \tag{4.1}$$

in which the mechanical unknowns are $\underline{\underline{\sigma}}$ and $\underline{\underline{\epsilon}}$, the Cauchy stress tensor and the linearised strain tensor, while the electric unknowns are $\underline{E}$ and $\underline{D}$, the electric field and the electric displacement

vector, respectively. The material's parameters introduced in (4.1) are the fourth-order tensor $\mathbb{C}$ for the elasticity stiffness, the third-order coupling tensor $\underline{\underline{\underline{e}}}$ for the piezoelectric properties, and the second-order tensor $\underline{\underline{\varepsilon}}$ corresponding to the dielectric permittivity properties.

The governing equations include the classical equation of motion as well as Gauss's law

$$\nabla \cdot \underline{D} = q\,, \quad \forall \underline{x} \in \Omega_t\,, \tag{4.2}$$

at any point $\underline{x}$ of the domain Ω_t occupied by the PZT and in which q is the electric body charge. Furthermore, the electrical field is derived from a potential

$$\underline{E} = -\underline{\nabla \varphi}\,, \quad \forall \underline{x} \in \Omega_t\,, \tag{4.3}$$

where φ is the electric field potential (Maxwell's law). The boundary conditions to solve the coupled problem include the classical boundary conditions in terms of force density and displacement, complemented by the following essential and natural boundary conditions for the electric variables (Zhang *et al.*, 2003):

$$\varphi = V\,, \quad \forall \underline{x} \in \partial\Omega_t^V \quad \text{and} \quad \underline{D} \cdot \underline{n} = -Q\,, \quad \forall \underline{x} \in \partial\Omega_t^Q\,, \tag{4.4}$$

in which V and Q are the imposed electric potential and surface charge, respectively. These two quantities are defined on the complementing parts of the domain boundary $\partial\Omega_t^Q \cup \partial\Omega_t^V = \partial\Omega_t$ of externally pointing unitary normal $\underline{n}$. Initial conditions should be provided to complete the coupled problem's definition.

4.2.2 Poling-induced anisotropy

The PZT is polarised: the temperature is raised above the Curie temperature, and then an electric current is applied in the poling direction and maintained until the temperature decreases below the threshold (Karaki *et al.*, 2007). This poling exercise results in a material having an anisotropy, typically a transverse isotropic structure for the PZT ceramic considered in our modelling.

Matrix notation is used in what follows with the Voigt convention: the order is σ_{11}, σ_{22}, σ_{33}, σ_{32}, σ_{13}, σ_{12}, taking the stress tensor as an example. Note that the strain tensor's fourth to sixth components contain a factor two: ${}^t\{\epsilon\} = (\epsilon_{11}, \epsilon_{22}, \epsilon_{33}, 2\epsilon_{32}, 2\epsilon_{13}, 2\epsilon_{12})$. Consider now the poling direction to be the third direction of our coordinate system, so that the material tensors introduced in eq. (4.1) are written in matrix notation as

Table (4.1) The material parameter for PZT ceramics of material density $\rho = 7600$ kg/m^3 following Yang (2018). The constant ε_0 is the free-space electric permittivity equal to 8.854×10^{-12}F/m.

Stiffness GPa	piezoelectric C/m^2	Permittivity F/m
$C_{11} = 135$	$e_{31} = -1.9$	$\varepsilon_{11} = 504\varepsilon_0$
$C_{12} = 67.9$	$e_{33} = 9.0$	$\varepsilon_{33} = 260\varepsilon_0$
$C_{13} = 68.1$	$e_{24} = 9.8$	
$C_{33} = 113$		
$C_{44} = 22.2$		

$$
[\mathbb{C}] = \begin{bmatrix} C_{11} & C_{12} & C_{13} & 0 & 0 & 0 \\ & C_{11} & C_{13} & 0 & 0 & 0 \\ & & C_{33} & 0 & 0 & 0 \\ & & & C_{44} & 0 & 0 \\ & & & & C_{44} & 0 \\ & & & & & \dfrac{C_{11}-C_{12}}{2} \end{bmatrix}, \tag{4.5}
$$

$$
[\underline{\underline{e}}] = \begin{bmatrix} 0 & 0 & 0 & 0 & e_{24} & 0 \\ 0 & 0 & 0 & e_{24} & 0 & 0 \\ e_{31} & e_{31} & e_{33} & 0 & 0 & 0 \end{bmatrix}, \quad [\underline{\underline{\varepsilon}}] = \begin{bmatrix} \varepsilon_{11} & 0 & 0 \\ & \varepsilon_{11} & 0 \\ & & \varepsilon_{33} \end{bmatrix},
$$

the lower part of the elasticity stiffness, and permittivity being deduced by symmetry. The values of the ten material parameters introduced in (4.5) are presented in Table 4.1.

4.3 1D dynamics by the method of characteristics

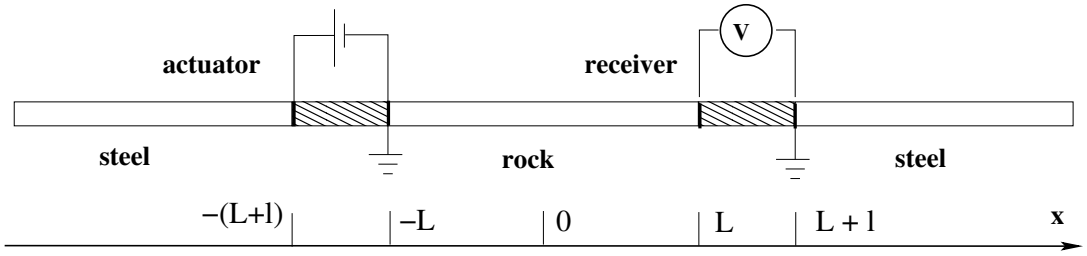


Figure (4.1) The 1D bar is composed of a rock specimen in its central section and of two steel anvils at the two ends. The PZT actuator and receiver are to the right and left of the specimen.

The problem presented in this section is proposed for two reasons. The first one is to have an exact solution to validate the numerical simulations in 1D, but also in 2D and 3D. The second reason is the need to understand the time dependence of the voltage at the receiver for a simple actuator source. The domain consists of a 1D bar, composed on the left and right of steel sections and in the middle by a rock specimen of length $2L$. The PZT actuator and receiver, of length l, are on the left and right of the sample, Figure 4.1. The steel sections are sufficiently long to avoid any reflection at the remote boundaries within the duration of the experiment.

4.3.1 Analytical solution

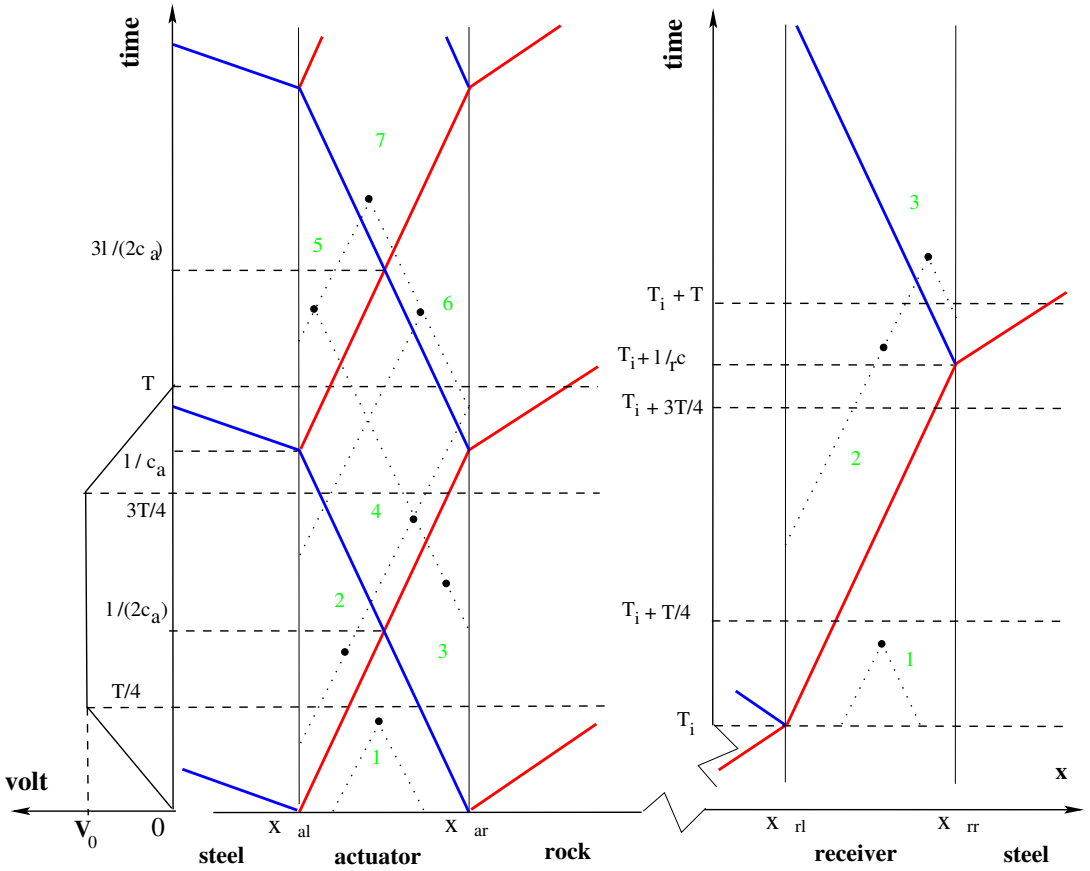


Figure (4.2) The method of characteristics is applied to the piezoelectric actuator and receiver to construct the displacement, strain, stress, and electric field in the 1D bar illustrated in Figure 4.1. The voltage applied to the left of the actuator is a simple pulse, and its graph, which is a function of time, is presented on the left. The dotted segments are characteristics passing through one typical point of every domain (solid dot) and are proposed to illustrate the solution in terms of displacement. The arrival time of the emitted wave on the receiver is T_i.

The material response presented in equation (4.1) simplifies in this 1D setting to

$$\sigma = C_i\,\epsilon \quad \text{with} \quad i = s \text{ or } p\,, \tag{4.6}$$

within the porous rock (subscript p) and the steel (subscript s). The coupled response in the PZT actuator (a) and the receiver (r) reads

$$\begin{aligned} \sigma &= C_i^*\,\epsilon - e_i E \quad \text{with} \quad i = a \text{ or } r\,, \\ D &= e_i\epsilon + \varepsilon_i E\,. \end{aligned} \tag{4.7}$$

Gauss's law in equation (4.2) simplifies to the gradient of the electric displacement being equal to zero in the absence of any volume charge. The electric displacement is thus a function of time only and not space: it is uniform over the receiver and the actuator, two scalars denoted

as $D_i(t)$. These scalars are used in equation (4.7) which now reads

$$\begin{aligned} \sigma(x,t) &= C_i\,\epsilon(x,t) - \frac{e_i}{\varepsilon_i} D_i(t) \quad \text{with} \quad C_i = C_i^* + \frac{e_i^2}{\varepsilon_i}\,, \\ E(x,t) &= -\frac{e_i}{\varepsilon_i}\epsilon(x,t) + \frac{1}{\varepsilon_i} D_i(t)\,, \end{aligned} \tag{4.8}$$

where each variable's spatial and/or time dependence has been identified. Note that the electric field is in this context a scalar and is noted E, not to be confused with Young's modulus introduced further down. The electric field is minus the gradient of the potential $E(x,t) = -\varphi_{,x}(x,t)$ and is now expressed in terms of the strain and displacement thanks to the second equation in (4.8):

$$\varphi(x,t) = \frac{e_i}{\varepsilon_i} u(x,t) - \frac{1}{\varepsilon_i} D_i(t) x + A(t)\,, \tag{4.9}$$

up to a function of time only $A(t)$. This function will be found from the continuity condition for the potential discussed in what follows. Note that this potential is imposed at the two electrodes of the actuator and one of the receivers:

$$\begin{aligned} &\text{Actuator}: \quad \varphi(-L-l,t) = V(t)\,, \quad \varphi(-L,t) = 0 \quad \forall\, t\,, \\ &\text{Receiver}: \qquad\qquad \varphi(L+l,t) = 0\,, \quad \forall\, t\,. \end{aligned} \tag{4.10}$$

in which $V(t)$ is the imposed potential on the left electrode of the actuator. The potential $\varphi(L,t)$ at the receiver left electrode, also denoted $v(t)$, is the problem unknown. The boundary condition there thus corresponds to a flux type according to (4.4) and in the absence of any charge, it implies that the electric displacement flux is zero. Since this electric displacement is uniform over the receiver, the conclusion is that it must be zero at any time: $D_r(t) = 0$, $\forall t$.

The d'Alembert decomposition is considered, so the displacement is the sum of two functions

$$u(x,t) = F(x - c_i t) + G(x + c_i t) \quad \text{with} \quad c_i = \sqrt{\frac{C_i}{\rho_i}}\,, \tag{4.11}$$

introducing the celerity c_i for every material ($i = s, a, p, r$, with s for steel, a for actuator, p for porous rock, and r for receiver). The functions F and G are constant along the lines $x = c_i t + \alpha$ and $x = -c_i t + \beta$, respectively, which are the characteristics. They correspond to a forward- and a backward-propagating wave. The advantage of using d'Alembert's decomposition is that the equation of motion is automatically satisfied, and we are left with having to determine the functions F and G from the initial and boundary values, knowing that they are constant along the two characteristics.

Figure 4.2 illustrates the methodology. The voltage applied to the left electrode of the actuator is presented as a function of time on the left. It consists of a pulse with a rise time $T/4$, a constant plateau at V_0 during half the pulse duration, and a linear decrease to zero during the last quarter of the pulse. The two plots to the right of this function represent the waves travelling through the actuator and receiver, respectively, in a space spanned by the position and time. The red and blue segmented lines are the forward and backward waves. These segments

are defining subdomains, numbered in green, over which the solution is uniform if there is no coupling. The instantaneous propagation of the electric information adds complexity to these fields, which are determined in what follows.

4.3.2 Application to the actuator

Consider the triangular subdomain (1) associated with times less than $l/(2c_r)$ corresponding to the time necessary for the forward wave emanating from the left and the backward wave coming from the right electrode to cross each other. No wave has reached any point in this area, as illustrated by the two dotted segments coming from the horizontal axis and getting to the solid dot. The displacement and strain are thus zero. However, the propagation of the information due to the electric quasi-static problem is instantaneous (speed of light !), and the stress and the electric field are non-zero and homogeneous. Both are functions of the first remaining unknown, the electric displacement $D_a(t)$. The second unknown is the constant introduced while integrating the electric field to obtain the potential. To summarise:

$$\begin{aligned} \text{Subdomain (1)}: \qquad & u(x,t)=0\,, \quad \epsilon(x,t)=0\,, \quad \sigma(x,t)=-e_a E(t)\,, \\ & E(x,t)=\tfrac{1}{\varepsilon_a}D_a(t) \quad \varphi(x,t)=-\tfrac{1}{\varepsilon_a}D_a(t)x+A_{12}(t)\,, \end{aligned} \tag{4.12}$$

for the two unknown functions $D_a(t)$ and $A_{12}(t)$. The two subscripts for the second function indicate that it will be determined by the continuity of the potential between subdomains (1) and (2).

Points in the triangular subdomain (2) are defined for a time less than l/c_a. They receive a forward wave $F_a(x-c_at)$ emitted from the left electrode. The backward wave emanating from the initial conditions axis is zero. Note that the emission of the forward wave from the left electrode is also accompanied by the emission of a backward wave through the steel section $G_s(x+c_st)$. The displacement and the stress at the electrode ($x_{al}=-L-l$) are continuous through time providing two conditions

$$\begin{aligned} G_s(x_{al}+c_st) &= F_a(x_{al}-c_at)\,, \\ C_sG_s'(x_{al}+c_st) &= C_aF_a'(x_{al}-c_at)-\frac{e_a}{\varepsilon_a}D_a(t)\,, \end{aligned} \tag{4.13}$$

valid for any time in $[0, l/c_a]$. The second equation in this system is now integrated in time

$$\kappa_sG_s(x_{al}+c_st)=-\kappa_aF_a(x_{al}-c_at)-\frac{e_a}{\varepsilon_a}\int_0^t D_a(t')dt'\,, \quad \text{with} \quad \kappa_i=c_i\rho_i\,, \tag{4.14}$$

having set to zero the constant of integration based on the initial conditions and introduced the acoustic impedance κ_i for every material. The first equation in (4.13) and (4.14) yield the solution

$$G_s(x_{al}+c_st)=F_a(x_{al}-c_at)=-\frac{e_a}{\varepsilon_a}\frac{1}{\kappa_a+\kappa_s}\int_0^t D_a(t')dt'\,. \tag{4.15}$$

The displacement at any point of subdomain (2) is then obtained by following the characteristic

back to the left electrode:

$$\text{Subdomain (2)}: \quad F_a(x - c_a t) = -\frac{e_a}{\varepsilon_a}\frac{1}{\kappa_a + \kappa_s}\int_0^{t-(x-x_{al})/c_a} D_a(t')dt' . \tag{4.16}$$

The strain is deduced from this displacement as well as the stress and the electric field thanks to (4.8) and according to (4.9). Further integration of minus the electric field, from the left electrode at x_{al} to the current point x, provides the potential which reads

$$\text{Subdomain (2)}: \varphi(x,t) = V(t) - \frac{1}{\varepsilon_a} D_a(t)(x - x_{al}) + \frac{(e_a/\varepsilon_a)^2}{\kappa_a + \kappa_s}\int_{t-(x-x_{al})/c_a}^{t} D_a(t')dt' . \tag{4.17}$$

This potential is continuous with the expression given in (4.12) for subdomain (1) along the characteristic $x = x_{al} + c_a t$ providing the unknown function:

$$A_{12}(t) = V(t) + \frac{1}{\varepsilon_a} D_a(t) x_{al} + \frac{(e_a/\varepsilon_a)^2}{\kappa_a + \kappa_s}\int_0^{t} D_a(t')dt' . \tag{4.18}$$

Similar reasoning is applied to a subdomain (3) which is symmetric to subdomain (2) with respect to a vertical axis through the centre of the actuator. Any point there sees only a backward wave $G_a(x + c_a t)$ emitted from the right electrode at $x_{ar} = -L$. This emission is coupled with the production of a forward wave through the porous rock $F_p(x - c_p t)$. The continuity at the left electrode of the displacement and of the stress at an arbitrary time in $[0; t/c_r]$, after integration in time of the latter condition, provides the displacement

$$G_a(x_{ar} + c_a t) = F_p(x_{ar} - c_p t) = \frac{e_a/\varepsilon_a}{\kappa_p + \kappa_a}\int_0^{t} D_a(t')dt' . \tag{4.19}$$

The displacement at an arbitrary point of subdomain (3) is deduced by following the characteristic linked to the left electrode. The potential at this point is then found from the difference in displacement at x and the associated point along the characteristic at the right electrode. These two results read

$$\begin{aligned} \text{Subdomain (3)}: \qquad u(x,t) = G_a(x + c_a t) &= \frac{e_a/\varepsilon_a}{\kappa_p + \kappa_a}\int_0^{t-(x_{ar}-x)/c_a} D_a(t')dt' , \\ \varphi(x,t) &= -\frac{(e_a/\varepsilon_a)^2}{\kappa_p + \kappa_a}\int_{t-(x_{ar}-x)/c_a}^{t} D_a(t')dt' - \frac{1}{\varepsilon_a} D_a(t)(x - x_{ar}) . \end{aligned} \tag{4.20}$$

The solution for the potential in subdomains (1), (2), and (3) is given in equations (4.12), (4.17), and (4.18), respectively up to the electric displacement $D_a(t)$, which remains so far unknown. The continuity of the potential between subdomains (1) and (2) led to the estimation of the function $A_{12}(t)$ now given in equation (4.18). The missing link is between subdomains (1) and (3) and the continuity of the potential along the characteristic $x = x_{ar} - c_a t$, which defines their common boundary. This continuity condition provides

$$D_a(t) - B_1\int_0^{t} D_a(t')dt' = \frac{\varepsilon_a V(t)}{l} \quad \text{with} \quad B_1 = \frac{e_a^2}{\varepsilon_a l}\frac{\kappa_p + 2\kappa_a + \kappa_s}{(\kappa_p + \kappa_a)(\kappa_s + \kappa_a)} . \tag{4.21}$$

The general solution reads

$$D_a(t) = \frac{\varepsilon_a}{l} \exp(B_1 t) \int_0^t V'(t') \exp(-B_1 t') dt' \,. \tag{4.22}$$

This general solution takes the following particular expression for the pulse presented on the left of Figure 4.2, considering the rise time of $T/4$ and up to $t = l/(2c_a)$

$$\begin{aligned} t \le T/4 : \qquad & D_a(t) = \frac{\varepsilon_a 4V_0}{lTB_1} [\exp(B_1 t) - 1] \,, \\ T/4 \le t \le l/(2c_a) : \quad & D_a(t) = \frac{\varepsilon_a 4V_0}{lTB_1} \exp(B_1 t) \left[1 - \exp(-B_1 T/4)\right] . \end{aligned} \tag{4.23}$$

The application of the method of characteristics to subdomains (4) to (7) in Figure 4.2 does not offer any new difficulties, and the essential elements are now summarised. Points in subdomain (4) see the superposition of the forward wave $F_a(x - c_a t)$ and the backward wave $G_a(x + c_a t)$ defined in subdomains (2) and (3), respectively. The potential is given by a relation of the same type as in (4.9) with a function $A_4(t)$ resulting from the time integration. To summarise:

$$\begin{aligned} \text{Subdomain (4)} : \quad u(x,t) &= F_a\left(x_{al} - c_a(t - \frac{x - x_{al}}{c_a})\right) + G_a\left(x_{ar} + c_a(t - \frac{x_{ar} - x}{c_a}\right) \\ &= -\frac{e_a/\varepsilon_a}{\kappa_a + \kappa_s} \int_0^{t-(x-x_{al})/c_a} D_a(t') dt' + \frac{e_a/\varepsilon_a}{\kappa_p + \kappa_a} \int_0^{t-(x_{ar}-x)/c_a} D_a(t') dt' \,, \\ \varphi(x,t) &= \frac{e_a}{\varepsilon_a} u(x,t) - \frac{1}{\varepsilon_a} D_a(t) x + A_4(t) \,. \end{aligned} \tag{4.24}$$

The function $A_4(t)$ is also designated by $A_{42}(t)$ and $A_{45}(t)$ if evaluated by continuity between subdomains (4) and (2) and between (4) and (5) for time in $[l/2c_a; l/c_a]$ and $[l/c_a; 3l/2c_a]$, respectively. The first of these two functions can already be estimated since we know the potential in subdomain (2) up to time l/c_a thanks to equations (4.17) and (4.18). The continuity between subdomains (4) and (2) along the characteristic $x = x_{ar} - t/c_a)$ provides:

$$A_{42}(t) = V(t) + D_a(t) \frac{x_{al}}{\varepsilon_a} - \frac{(e_a/\varepsilon_a)^2}{\kappa_a + \kappa_s} \int_0^{t'} D_a(t') dt' \,. \tag{4.25}$$

The continuity in potential between subdomain (4) and (3) is now also enforced along the characteristic $x = x_{al} + t c_a$, providing the same condition as in (4.21). The electric displacement is thus

$$\begin{aligned} l/(2c_a) \le t \le 3T/4 : \qquad & D_a(t) = \frac{\varepsilon_a 4V_0}{lTB_1} \exp(B_1 t) \left[1 - \exp(-B_1 T/4)\right] , \\ 3T/4 \le t \le l/c_a : \quad & D_a(t) = \tfrac{\varepsilon_a 4V_0}{lTB_1} \exp(B_1 t)[1 - \exp(-B_1 T/4) + \exp(-B_1 t) \\ & \qquad - \exp(-3B_1 T/4)] \,. \end{aligned} \tag{4.26}$$

Subdomain (5) has the left electrode on its boundary, and the displacement and stress there are due to a backward and a forward wave within the actuator and a backward wave in the steel section. The two continuity conditions provide the expression for the forward wave at any point in this subdomain after a time integration from l/c_a to the time of interest t. The

displacement within subdomain (5) is due to the forward wave coming from the left electrode and the backward wave emanating from the right electrode. The displacement and potential are summarised by:

$$\text{Subdomain (5) :} \tag{4.27}$$
$$u(x,t) = -\frac{e_a/\varepsilon_a}{\kappa_a+\kappa_s}\int_0^{t-(x-x_{al})/c_a} D_a(t')dt' + \frac{e_a/\varepsilon_a}{\kappa_p+\kappa_a}\left\{\frac{\kappa_a-\kappa_s}{\kappa_a+\kappa_s}\int_0^{t-(x-x_{al}+l)/c_a} D_a(t')dt' + \int_0^{t-(x_{ar}-x)/c_a} D_a(t')dt'\right\},$$
$$\varphi(x,t) = V(t) + \frac{e_a}{\varepsilon_a}\left(u(x,t)-u(x_{al},t)\right) - \frac{1}{\varepsilon_a}D_a(t)(x-x_{al})\,.$$

Having the potential in subdomains (4) and (5), equations (4.24) and (4.27), respectively, the continuity between the two domains ($x = x_{al} + c_a(t - l/c_a)$) is enforced up to time $3l/(2c_a)$ yielding the yet unknown function:

$$A_{45}(t) = V(t) + \frac{D_a(t)}{\varepsilon_a}x_{al} + \frac{(e_a/\varepsilon_a)^2}{\kappa_a+\kappa_s}\left\{\int_0^t D_a(t')dt' - \frac{2\kappa_a}{\kappa_a+\kappa_p}\int_0^{t-l/c_a} D_a(t')dt'\right\}. \tag{4.28}$$

The solution for subdomain (6) is constructed similarly. The displacement is first determined on the right electrode and then extended to internal points with the addition of the forward wave from sub-domain (2). The solutions for the displacement and the potential are:

$$\text{Subdomain (6) :} \tag{4.29}$$
$$u(x,t) = -\frac{e_a/\varepsilon_a}{\kappa_a+\kappa_s}\int_0^{t-(x-x_{al})/c_a} D_a(t')dt' + \frac{e_a/\varepsilon_a}{\kappa_a+\kappa_p}\left\{\int_0^{t-(x_{ar}-x)/c_a} D_a(t')dt' - \frac{\kappa_a-\kappa_p}{\kappa_a+\kappa_s}\int_0^{t-(x_{ar}-x+l)/c_a} D_a(t')dt'\right\},$$
$$\varphi(x,t) = \frac{e_a}{\varepsilon_a}\left(u(x,t)-u(x_{ar},t)\right) - \frac{1}{\varepsilon_a}D_a(t)(x-x_{ar})\,.$$

The next step of the study of the actuator is the continuity condition between the subdomains (6) and (4) along the characteristic $x = x_{ar} - c_a(t - l/c_a)$ for time $t \in [l/c_a; 3l/(2c_a)]$. The expressions for the potential are found in equations (4.27) and (4.24) with (4.25) for the function $A_{45}(t)$ for the two subdomains, respectively. The continuity condition reads

$$D_a(t) - B_1\int_{t-l/c_a}^t D_a(t')dt' = \frac{\varepsilon_a}{l}V(t) - B_2\int_0^{t-l/c_a} D_a(t')dt' \quad \text{with} \quad B_2 = \frac{-\kappa_s+2\kappa_a-\kappa_p}{(\kappa_a+\kappa_s)(\kappa_a+\kappa_p)}\frac{e_a^2}{\varepsilon_a l}\,. \tag{4.30}$$

Note that the right-hand side of eq. (4.30) is known since the electric displacement has been determined up to time l/c_a as seen from eq. (4.26). The general solution for a time less than $3l/(2c_a)$ is then

$$D_a(t) = \exp(B_1 t)\left\{d_a + \int_{l/c_a}^t \exp(-B_1 t')\left[\frac{\varepsilon_a}{l}V'(t')' - (B_1+B_2)D_a(t'-\frac{l}{c_a})\right]dt'\right\} \tag{4.31}$$
$$\text{with} \quad d_a = \frac{\varepsilon_a 4V_0}{lTB_1}\left[1-\exp(-\frac{B_1T}{4})+\exp(-\frac{B_1 l}{c_a})-\exp(-\frac{3B_1T}{4})\right]$$

the constant d_a being found by continuity at time l/c_a. For the particular shape of the voltage pulse and accounting for the solution at previous times given in (4.23) and (4.26), this solution

reads

$$
\begin{aligned}
& & D_a(t) &= d_a \exp(B_1 t) + \tfrac{\varepsilon_a 4V_0}{lTB_1} Z(t) \qquad (4.32)\\
\frac{l}{c_a} \le t \le \mathrm{T}: & & Z(t) &= [1 - \exp(B_1(t - \tfrac{l}{c_a}))] + \tfrac{B_1+B_2}{B_1}[(1 - B_1(t - \tfrac{l}{c_a}))\\
& & & \quad \times \exp(B_1(t - \tfrac{l}{c_a})) - 1]\,,\\
T \le t \le \frac{l}{c_a} + \frac{T}{4}: & & Z(t) &= \exp(B_1(t-T)) - \exp(B_1(t - \tfrac{l}{c_a})) +\\
& & & \quad \tfrac{B_1+B_2}{B_1}\left[(1 - B_1(t - \tfrac{l}{c_a}))\exp(B_1(t - \tfrac{l}{c_a})) - 1\right]\,,\\
\frac{l}{c_a} + \frac{T}{4} \le t \le \frac{3l}{2c_a}: & & Z(t) &= -\exp(B_1(t - \tfrac{l}{c_a})) + \tfrac{B_1+B_2}{B_1}\left\{\left(\exp(\tfrac{B_1 T}{4})(1 - B_1\tfrac{T}{4}) - 1\right)\right.\\
& & & \quad \times \exp(B_1(t - \tfrac{T}{4} - \tfrac{l}{c_a})) - B_1(t - \tfrac{T}{4} - \tfrac{l}{c_a})\exp(B_1(t - \tfrac{l}{c_a})\\
& & & \quad \left.[1 - \exp(-\tfrac{B_1 T}{4})]\right\} + \exp(B_1(t-T))\ .
\end{aligned}
$$

The last studied subdomain is number (7) up to time $2l/c_a$. The displacement results from the sum of the forward wave coming from the electrode on the boundary of domain 5 and the backward wave from the right electrode on the boundary of domain 6. The potential is determined up to the new unknown function $A_{75}(t)$:

$$
\begin{aligned}
& \text{Subdomain (7)}: \qquad (4.33)\\
u(x,t) &= -\frac{e_a/\varepsilon_a}{\kappa_a + \kappa_s}\left\{\int_0^{t-(x-x_{al})/c_a} D_a(t')dt' - \frac{\kappa_a - \kappa_s}{\kappa_a + \kappa_p}\int_0^{t-(x-x_{al}+l)/c_a} D_a(t')dt'\right\}\\
&\quad + \frac{e_a/\varepsilon_a}{\kappa_a + \kappa_p}\left\{\int_0^{t-(x_{ar}-x)/c_a} D_a(t')dt' - \frac{\kappa_a - \kappa_p}{\kappa_a + \kappa_s}\int_0^{t-(x_{ar}-x+l)/c_a} D_a(t')dt'\right\},\\
\varphi(x,t) &= \frac{e_a}{\varepsilon_a}u(x,t) - \frac{1}{\varepsilon_a}D_a(t)x + A_{75}(t)\,.
\end{aligned}
$$

The function $A_{75}(t)$ is found by continuity of the potential along the characteristic $x = x_{al} - c_a(t - 2l/c_a)$, which is forming the boundary between subdomains (7) and (5):

$$
\begin{aligned}
A_{75}(t) = \frac{D_a(t)}{\varepsilon_a}x_{al} + V(t) - \frac{(e_a/\varepsilon_a)^2}{\kappa_a + \kappa_s}\left\{-\int_0^t D_a(t')dt' + \frac{\kappa_a - \kappa_s}{\kappa_a + \kappa_p}\int_0^{t-l/c_a} D_a(t')dt'\right\} \qquad (4.34)\\
+ \frac{(e_a/\varepsilon_a)^2}{\kappa_a + \kappa_p}\int_{t-l/c_a}^0 D_a(t')dt'\,.
\end{aligned}
$$

Further continuity condition between subdomains (7) and (6) along the characteristic $x = x_{ar} + c_a(t - 2l/c_a)$ leads to the same ordinary differential equation as in equation (4.30). For the pulse of interest and times within $[3l/2c_a; 2l/c_a]$, the voltage is zero so the solution reads

$$D_a(t) = D_a(\frac{3l}{2c_a})\exp(B_1(t-\frac{3l}{2c_a})) - \frac{B_1+B_2}{B_1}\frac{\varepsilon_a 4V_0}{lTB_1}W(t) \quad (4.35)$$

, with

$$\frac{3l}{2c_a} \le t \le \frac{l}{c_a}+\frac{3T}{4}: \quad W(t) = B_1(t-\frac{3l}{2c_a})\exp(B_1(t-\frac{l}{c_a}))[1-\exp(-\frac{B_1T}{4})]\,,$$

$$\frac{l}{c_a}+\frac{3T}{4} \le t \le \frac{2l}{c_a}: \quad W(t) = \exp(B_1(t-\frac{l}{c_a})\Big\{[1-\exp(-\frac{B_1T}{4})]B_1(\frac{3T}{4}-\frac{l}{2c_a})$$
$$+\exp(-\frac{3B_1T}{4}) + [1-\exp(-\frac{B_1T}{4})-\exp(-\frac{3B_1T}{4})]$$
$$\times B_1(t-\frac{3T}{4}-\frac{l}{c_a}) - \exp(-B_1(t-\frac{l}{c_a}))\Big\}\,,$$

in which $D_a(\frac{3l}{2c_a})$ is found from equation (4.32).

4.3.3 Application to the receiver

The second objective of this 1D study is to understand the wave impinging on the receiver and the potential to be measured between its two electrodes positioned at $x_{rl} = L$ and $x_{rr} = L + l$, Figure 4.1. The wave crossing the porous rock arrives at $T_i = 2L/c_p$ on the left electrode at x_{rl}, so the time interval to be studied is $[T_i; T_i + 2l/c_r]$. The forward wave arriving on the left electrode $F_p(x_{rl} - c_p t)$ is equal to the reflected wave in the actuator at the position x_{ar} at times $t - T_i$ and is thus the function $G_a[x_{ar} + c_a(t - T_i)]$ defined in equation (4.20) for times in $[T_i; T_i + l/c_r]$. For larger times, the impinging wave has a displacement corresponding to the displacement defined in equation (4.29) for subdomain (6) of the actuator setting $x = x_{ar}$ and the time to $t - T_i$.

This wave impinging on the left electrode triggers a transmission within the receiver $F_r(x_{rl} - c_r t)$ and also a reflection within the porous rock $G_p(x_{rl} + c_p t)$. These three waves are seen on the characteristic plot presented on the right-hand side of Figure 4.2. Note that the arrival of the emitted wave at T_i does not induce a zero electric displacement $D_r(t)$ because of the boundary condition on the left electrode as discussed above. This analysis is now documented in more detail for the three subdomains (1) to (3):

$$\text{Subdomain (1)}: \quad u(x,t) = 0\,, \quad \epsilon(x,t) = 0\,, \quad \sigma(x,t) = 0\,, \quad E(t) = 0\,, \quad \varphi(t) = 0\,. \quad (4.36)$$

The potential, which has to be uniform, is inferred from the zero voltage boundary condition at the right electrode.

Subdomain (2) is studied using the classical approach: continuity of displacement and stress at the left electrode is first studied to estimate the forward wave propagating within the receiver, and the displacement is then generalised to the whole subdomain. The results are

$$\text{Subdomain (2)}: \quad u(x,t) = F_r(x - c_r t) = \frac{2\kappa_p}{\kappa_r + \kappa_p} F_p\left(x_{rl} - c_p(t - \frac{x - x_{rl}}{c_r})\right), \quad (4.37)$$
$$\varphi(x,t) = v(t) + \frac{e_r}{\varepsilon_r}\left(u(x,t) - u(x_{rl},t)\right),$$

in which $v(t)$ is the voltage unknown at the left electrode.

Points in subdomain (3) see the forward waves as in subdomain (2) and are also affected by the backward wave from the right electrode, where the voltage is set to zero. The results after having developed the continuity arguments at the right electrode read

$$\text{Subdomain (3)}: \quad u(x,t) = F_r\left(x - c_r t\right) + \frac{\kappa_r - \kappa_s}{\kappa_r + \kappa_s} F_r\left(x_{rr} - c_r(t - \frac{x_{rr} - x}{c_r})\right), \tag{4.38}$$
$$\varphi(x,t) = \frac{e_r}{\varepsilon_r}\left\{F_r(x - c_r t) + \frac{\kappa_r - \kappa_s}{\kappa_r + \kappa_s} F_r(x_{rr} - c_r(t - \frac{x_{rr} - x}{c_r})) - \frac{2\kappa_r}{\kappa_r + \kappa_s} F_r(x_{rr} - c_r t)\right\}.$$

The last effort concerns the electric potential continuities between subdomains (2) and (1) and (2) and (3) along the characteristic $x = x_{rl} + (t - T_i)c_r$ and $x = x_{rr} - c_r(t - T_i - l/c_r)$, respectively. These two conditions provide the measured potential

$$T_i \le t \le T_i + \frac{l}{c_r}: \qquad v(t) = \frac{e_r}{\varepsilon_r}\frac{2\kappa_p}{\kappa_p + \kappa_r} F_p(x_{rl} - c_p t), \tag{4.39}$$
$$T_i + \frac{l}{c_r} \le t \le T_i + \frac{2l}{c_r}: \quad v(t) = \frac{e_r}{\varepsilon_r}\frac{2\kappa_p}{\kappa_p + \kappa_r}\left[F_p(x_{rl} - c_p t) - \frac{2\kappa_r}{\kappa_r + \kappa_s} F_p(x_{rl} - c_p(t - \frac{l}{c_r}))\right].$$

This solution in terms of voltage and displacement will be used in section 4.4 to validate the numerical prediction. It will be seen that this voltage in eq. (4.39) takes off smoothly from the horizontal time axis, so picking the arrival time is fundamentally difficult. This observation, which is also made from the 2D results, raises the question of how to capture the main S wave arrival time. To back up this observation, it is proposed to construct the asymptotic development of the receiver voltage from eq. (4.39). The voltage is proportional to the emitted pulse, which is equal to the reflected wave in the actuator at the position x_{ar} at times $t - T_i$. This function $G_a[x_{ar} + c_a(t - T_i)]$ in eq. (4.20) is proportional to the integral in time of the electric displacement, which is defined for the early times in eq. (4.23). Combining this information, one obtains the Taylor expansion

$$v(t) \simeq \frac{e_a e_r}{\varepsilon_r}\frac{2\kappa_p}{(\kappa_p + \kappa_r)(\kappa_p + \kappa_a)}\frac{4V_0}{lT}\left(\frac{1}{2!}(t - T_i)^2 + \frac{1}{3!}B_1(t - T_i)^3 + ...\right), \tag{4.40}$$

providing the leading term, which is indeed quadratic.

4.4 Validation and simplifications in 1D

The objectives are now first to validate the numerical schemes with the help of the analytical solution to the 1D problem presented in section 4.3 and second to test two simplifications of the coupled problem.

The central difference scheme is used for time-stepping, whereas spectral finite elements (SFEM) are used for spatial discretisation. The computation of the electric field occurs subsequent to the update of the displacement field. Only the piezoelectric devices are discretised in the computation of this electric field, assuming they are completely isolated from the rest of the experimental machine. The model problem is seen in Figure 4.1, and the specimen and transducer's lengths

($2L$ and l) are set to 80 mm and 3 mm, respectively. The voltage pulse occurs over the time T with a maximum voltage V_0, these two quantities being set here to 0.8 µs and 100 V, respectively. The numerical solution is obtained with a mesh of 722 spectral elements, each having seven nodes and a time step of $10^{-4}\mu s$, which is 100 times smaller than the Courant limit (based on the minimum distance between two consecutive nodes).

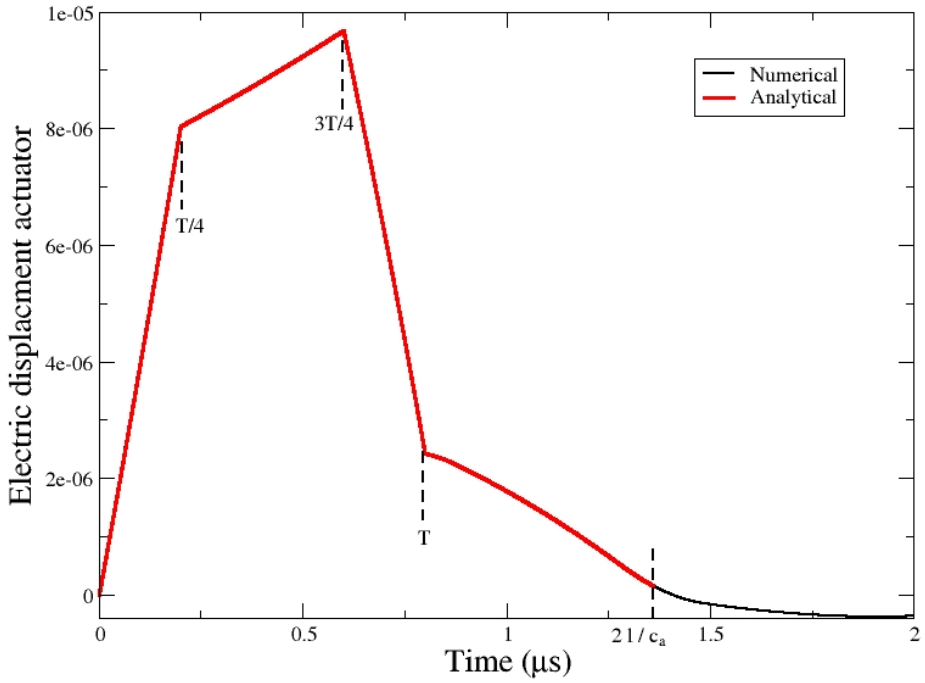


Figure (4.3) The electric displacement, uniform over the actuator as a function of time: comparison of the analytical solution (red curve) with the numerical results (black curve). The applied voltage is defined in Figure 4.2 and varies from time zero to T. The analytical solution was derived up to time $2l/c_a$ corresponding to twice the travelling time of the wave through the actuator.

The piezoelectric properties are those found in the poling direction and proposed in Table 4.1, and they are chosen identically for the actuator and the receiver. The elastic properties and density of the porous rock specimen and the steel section are set to (200 GPa, 7900 kg/m^3) and (10 GPa, 2400 kg/m^3), respectively.

The first element of the validation is presented in Figure 4.3 and corresponds to the electric displacement, which is uniform in the actuator. The exact solution, red curve, is presented up to the time $2l/c_a$ corresponding to the time for a wave to travel forward and backward through the piezoelectric. This analytical solution is based on equations (4.23, 4.26, 4.32) and (4.35). The exact solution is approximately piece-wise linear during the pulse duration up to time T. The value of the scalar B_1 defined in (4.21) is 0.145 $C^2F^{-1}kg^{-1}\mu s^{-1}$so that the relation (4.23) up to $T/4$ is indeed close to being proportional to time with an approximate value of $\varepsilon_a V_0/l = 7.7 \times 10^{-6}$ VF/mm^2 at this limiting time. The non-linear effects are observed once the voltage is set to zero at the actuator's left electrode. There is then an internal electric field responsible for the non-zero electric displacement. The numerical solution matches perfectly the exact solution, providing a first element of validation. The numerical solution also reveals

that the electric displacement is oscillating around zero for times larger than T, with a decaying amplitude due to the gradual loss of energy within the confines of the actuator.

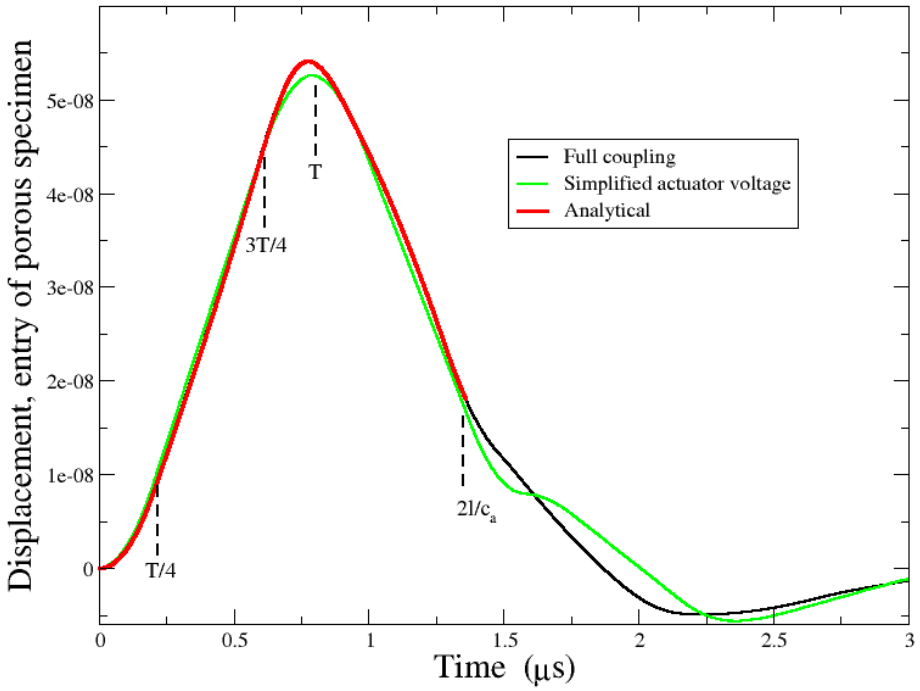


Figure (4.4) The displacement at the boundary between the actuator and the porous specimen as a function of time. Comparison of the analytical solution (red curve, constructed up to time $2l/c_a$) with the numerical solutions for a fully coupled simulation (black curve) and a simplification consisting of a linearly varying voltage within the actuator (green curve).

The second element of validation is the mechanical displacement at the boundary between the actuator and the porous rock, which is presented in Figure 4.4. This displacement is important since it is the pulse that will travel through the porous rock and will be detected by the receiver. The analytical solution corresponds again to the red curve and is constructed from equations (4.20) and (4.29). The displacement is non-linear, reaches a maximum prior to the end of the electric pulse at time T, and then decays. The complete oscillations in displacement occur over a period of the order of $2l/c_a$, which is longer than the voltage pulse duration T. The numerical solution, the black curve, catches perfectly the exact solution and then oscillates around zero due to the gradual decrease of internal energy.

There is an additional curve in green in Figure 4.4 which is obtained with a first simplification of the coupled problem suggested in the literature (*e.g.* Shiyekar *et al.*, 2011): the electric field is considered to vary linearly between the two electrodes as a first approximation during the electric pulse generation (for time $t < T$) and then set to zero. With the electric field and thus its gradient being postulated, there is no need to solve the electromechanical problem at the actuator, limiting the solution algorithm to the receiver only. The approximate solution matches rather well the exact solution during the duration of the electric pulse ($t < T$), and the difference is only felt afterward. Since our primary interest is the picking of the arrival time of the mechanical wave at the receiver, this first approximation is worth further study in

multi-dimensional problems.

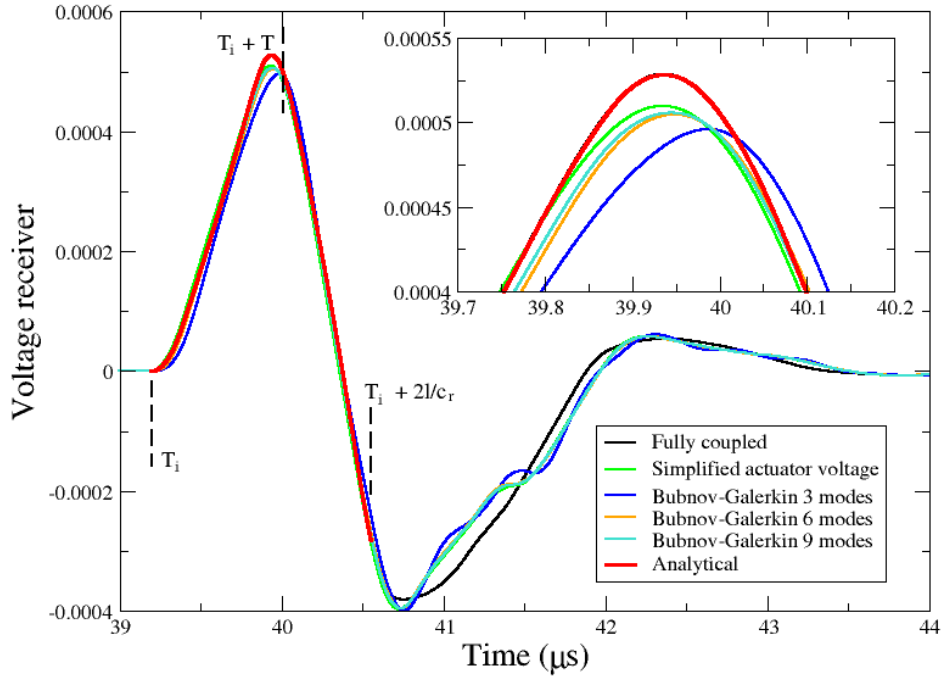


Figure (4.5) The voltage at the receiver as a function of time with T_i, T and $2l/c_r$, the arrival time of the emitted wave, the pulse duration and twice the travel time through the receiver, respectively. Comparison of the exact solution (red curve) with a fully coupled simulation (black curve), simplified approaches consisting first of a linearly varying voltage over the actuator (green curve) and second with Bubnov-Galerkin analysis of the receiver (3, 6, and 9 modes).

The last element of validation concerns the voltage detected at the receiver, once the wave has travelled through the porous rock. This voltage is presented in Figure 4.5 where the red curve is again the analytical solution, which is based on eq. (4.39). Note that the maximum voltage is approximately $5 \times 10^{-2} V_0$. An analysis of this voltage is now proposed, not at the maximum value but during the first part of the evolution of the voltage from the arrival time $T_i = 39.2\,\mu s$ to $T_i + T/4$. Equation (4.40), keeping the quadratic term only, indicates that the receiver voltage is proportional to the actuator maximum voltage times the dimensionless scalar 1.73×10^{-3} in the early arrival times. This ratio is less than that at the maximum but eq. (4.40) does reveal its dependence on the material properties of the piezoelectric devices and of the porous rock specimen.

Consider now the black curve in Figure 4.5 corresponding to the numerical solution with a full coupling. It does match the exact solution perfectly. The two curves cannot be differentiated in the inset despite the high resolution. The black curve is oscillating with a period of the order of $4l/c_r$, which is approximately four times longer than the duration of the signal at the actuator.

Additional curves are presented in Figure 4.5, which are now discussed. The green curve corresponds to the fully coupled solution within the receiver, while the first approximation proposed above, a linear electric field in the actuator, is considered. The arrival time and the initial variation of the voltage are not affected by this first approximation. The fully coupled and the

first approximation differ at the maximum voltage, as can be seen within the inset, with little consequence for our primary objective on wave picking. The other curves in the same Figure are obtained with the Bubnov-Galerkin approach presented in Appendix C.1. The main idea is to reduce the CPU time from the one needed for the fully-coupled solution via the spectral-element method using a trigonometric modal decomposition of the electric field, accounting for the boundary conditions at the electrodes. This second simplification is presented in Figure 4.5 for three, six, and nine modes. The simplified problem requires the solution of a system of equations with a diagonal matrix. The number of unknowns, from three to nine, corresponds to the mode amplitudes. These numbers should be compared to the sixty nodal unknowns for the electric field with the finite-element mesh. The matching of the Bubnov-Galerkin solutions with the approximate solution with a linear actuator voltage (green curve) requires at least nine modes. The difference between the two vanishes with an increasing number of modes. There is still indeed a small difference at the maximum potential with only nine modes (see inset), but the difference at the arrival times is minor, with no consequences for wave picking. The gain in CPU time, between the Bubnov-Galerkin approach and the Finite-Element method, is not of great concern in this 1D setting, but this favourable comparison encourages us to pursue this line of work for 2D and 3D problems.

In summary, we have proposed three elements to validate our numerical developments: the electric displacement through the actuator, the pulse propagating through the specimen, and the voltage measured at the receiver. The numerical solution matches the exact solution perfectly. Two simplifications to reduce the CPU time have been proposed and compared with the exact solutions. The first consists of postulating a linear electric field between the actuator electrodes, and the second captures the electric field in the receiver via a Bubnov-Galerkin approach. Note that the second simplification is not an approximation in the sense that it converges to the exact solution as the number of modes is increased. Another finding is that the oscillating pulse period at the receiver is four times the travelling time of the wave through the receiver.

4.5 SFEM simulations for a simplified geometry

The objective is now to test two proxies for the 2D actuators and receivers for P and S waves. Note that prior to this, the 2D numerical predictions for a P wave have been compared to the exact 1D solutions presented above by considering a bar of finite thickness. The results of this validation are not reported here for the sake of conciseness but can be found in Appendix C.3.

The details of the internal structure of the actuator and receiver are unknown, and the available information is the dimensions of the casing and active material (PZT ceramic). One of the reasons why numerical proxies are proposed in this section is that these proxies select the poling direction and the position of the electrodes. The proposed 2D actuator and receiver for S and P waves are presented in Figure 4.6a and 4.6b and correspond to blocks of size 10 mm $\times$ 3 mm. The poling direction is along the x_2-axis in the two cases, as illustrated by the dashed lines. The material properties are found in Table 4.1. The P and S proxies differ by the position of the electrodes, which are parallel to the 1- and 2-axis for P and S-devices, respectively. One

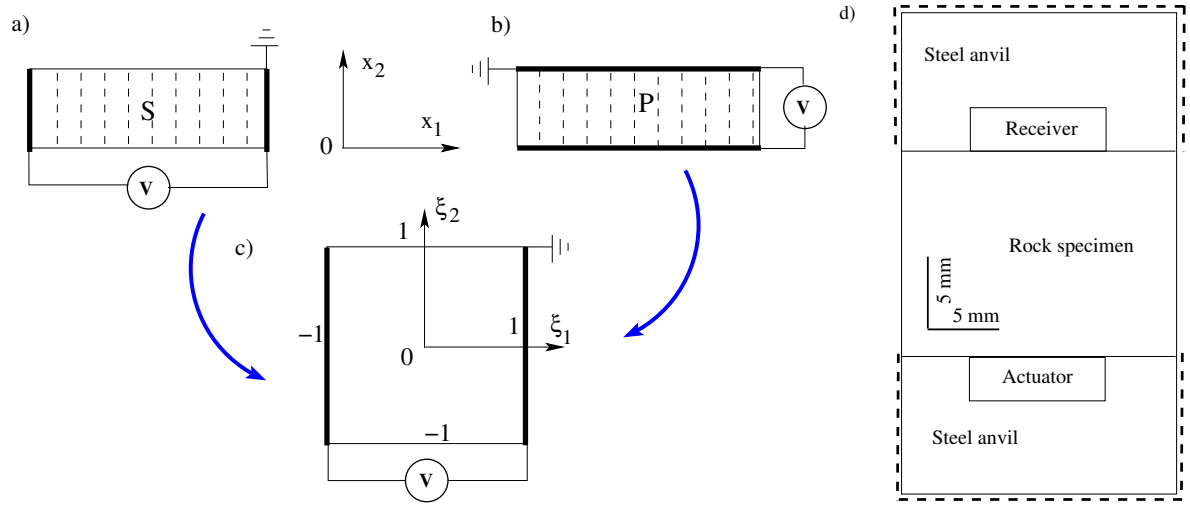


Figure (4.6) The piezoelectric for S and P-waves have the same poling direction (dashed lines) and differ by the position of the electrode in a) and b). The mapping to the computational domain for the application of the Bubnov-Galerkin method (see Appendix C.1) is presented in c). In d), the simple domain is proposed for testing the proxies for the actuator and receiver. The dashed lines show where absorbing boundary conditions are applied.

of the electrodes' voltages is set to zero. The two electrodes are linked either by a voltmeter for the receiver as illustrated in this Figure or by a generator for the actuator. The condition of a non-zero, uniform voltage at the receiver – the problem's unknown – is enforced by a penalty approach.

These proxies are tested in a simple domain geometry presented in Figure 4.6d. Two steel anvils of size 20 mm × 10 mm are bounding a rock specimen of size 20 mm × 14 mm. The piezoelectric devices are embedded in the anvil and are in perfect contact with the rock specimen. The steel anvils' external boundaries are covered with absorbing boundary conditions (dashed segments) based on the so-called first paraxial approximation of the wave propagation proposed by Clayton *et al.* (1977). The right and left specimen boundaries are stress-free. The steel anvils have properties: E = 200 GPa, ν= 0.3 and ρ= 7900 kg/m^3, and those of the porous rock are set to E = 13 GPa, ν=0.2 and ρ= 2300 kg/m^3.

The domain is discretised with a regular grid of 12×28 spectral elements, each having 49 nodes. For all simulations reported in this section, the time step is set to 2.5×10^{-4} µs, which is 100 times smaller than the Courant limit. A mesh sensitivity analysis is proposed in Appendix C.4.

4.5.1 P-wave generation and reception

The first set of results concerns the emission and the reception of P waves. Although our primary interest lies with S-waves, the influence of P-waves will always be felt and needs to be analysed. The results are presented in Figure 4.7. The voltage pulse at the actuator, scaled by a factor of 100, the dashed curve, is plotted at the time of arrival of the P wave, which is 5.59 µs. The receiver voltage based on the fully coupled approach, the black curve, rises after this latency time in a quadratic manner, as was observed in 1D. The pulse passes through a maximum and a minimum, the latter being larger than the former in absolute value. This fluctuation occurs

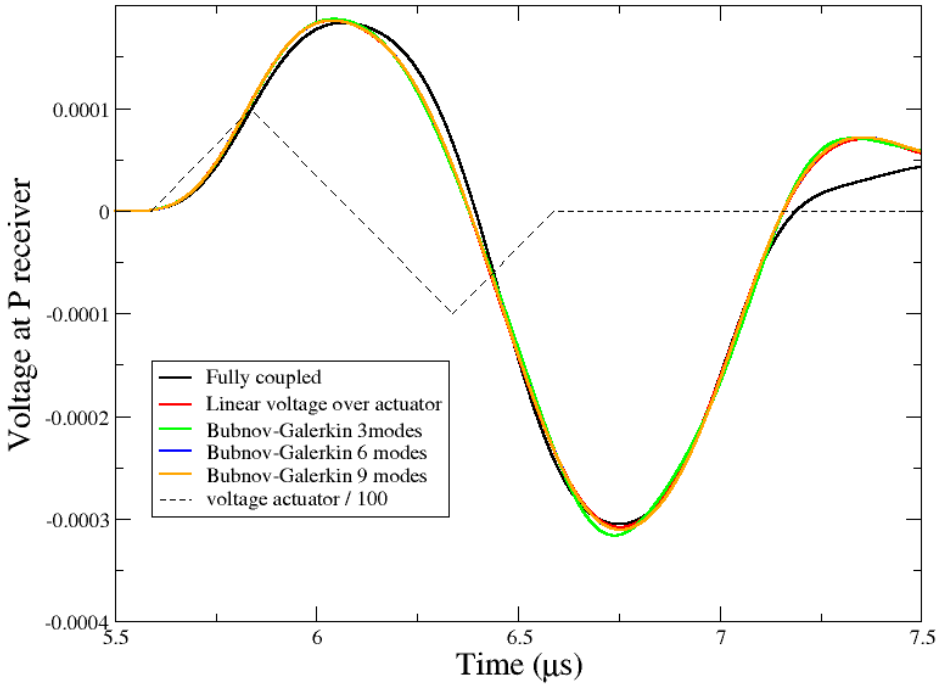


Figure (4.7) P-Receiver voltage for the problem presented in Figure 4.6 following an electric pulse at the P-actuator. The fully coupled solution is compared with the approximation for the actuator and also for the Bubnov-Galerkin approaches with different modes. The voltage at the actuator scaled by 1/100, dashed curve, is also superposed on the exact arrival time of 5.59 μs.

over approximately 1.6 μs, which is twice as long as the actuator pulse. This time is also close to $2l/c_{3p} = 1.36\,\mu s$ in which l is the receiver thickness and c_{3p} the P-wave velocity within the receiver. The arrival time of the P wave from the receiver voltage is not masked by any noise, but note again the initial quadratic type of response, which was observed in a 1D setting and predicted with equation (4.40), which renders the picking of the arrival time rather challenging,

A final note on Figure 4.7 concerns the red, green, blue, and orange curves. The first corresponds to the first simplification proposed in section 4.4: the electric potential within the actuator is assumed to vary linearly between the two electrodes. The three other curves were obtained with, in addition, the Bubnov-Galerkin scheme discussed in Appendix C.1 for the receiver voltage. Each mode corresponds to four functions as seen in eq. (C.7) and thus to four independent amplitudes. It is found that the Bubnov-Galerkin approach converges to the fully coupled solution as expected. The simulations with the simplification at the actuator and the Bubnov-Galerkin scheme are thus very close to the results for the fully coupled problem with the spectral elements. The gain in CPU time remains, nevertheless, minor in this 2D setting since the dynamics take most of the computational time.

4.5.2 S-wave generation and reception

The second set of results concerns the emission and the reception of an S-wave for a similar setup. The receiver voltage is presented in Figure 4.8, and the complexity of this signal compared to the P-voltage just discussed is quite complex. There is a parasitic P wave arriving at 5.75 μs,

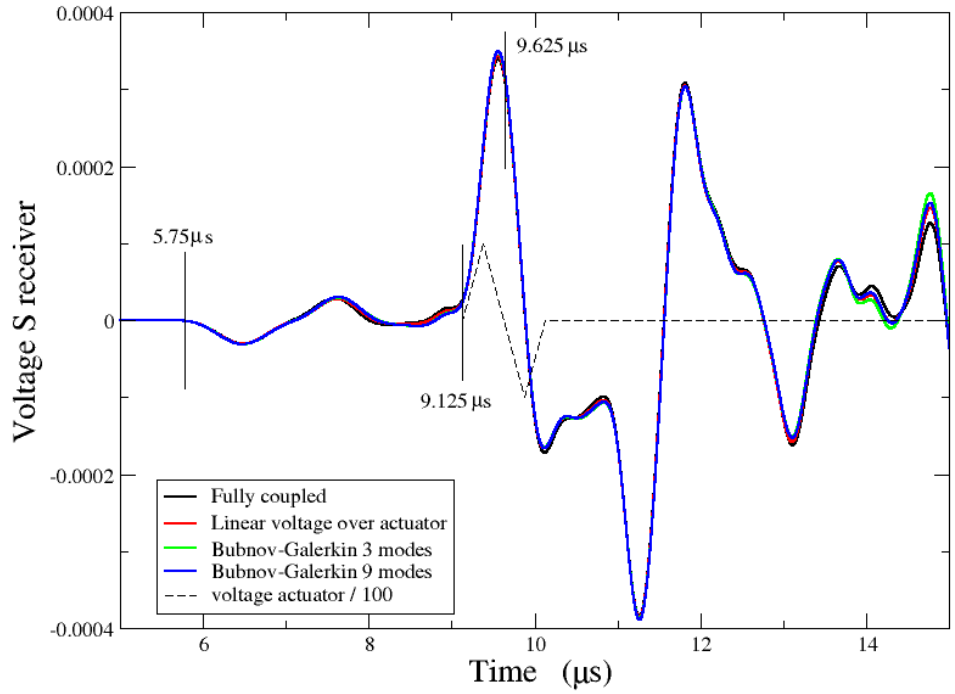


Figure (4.8) S-Receiver voltage for the problem presented in Figure 4.6 following an electric pulse at the S-actuator. The fully coupled solution is compared with the linear approximation for the actuator and the Bubnov-Galerkin approach with three and nine modes. The voltage at the actuator, scaled by 1/100, dashed curve, is also superposed on the arrival time of the S wave.

followed by a series of perturbations prior to the arrival time of the expected S wave at 9.125 µs, which is marked by a sharp rise in the voltage and a first maximum. The time from the arrival to the maximum is larger than half the period of the actuator source. This first peak is followed by a complex series of peaks with a negative potential. The signals last for a time much longer than the duration of the actuator source.

The main objective of this work is to analyse the wave pattern created by the actuator and transmitted to the receiver which is responsible for the complex voltage just briefly described. This wave pattern is presented in Figure 4.9.

The scalar used in the colour map to differentiate compressional and shear waves is defined as

Table (4.2) Notation used to describe the trajectory and phase of waves. A combination of letters is used to represent the wave phase. For example, P'_+s is a compressional wave that begins travelling upward but is then reflected at a critical angle as a shear head-wave.

Notation	Definition
P, S	Compressional or shear wave that travels upward
P′, S′	Compressional or shear wave that travels downward
p, s	Compressional or shear head wave
+	Symbol used to identify a wave that is generated at the top of the PZT
-	Symbol used to identify a wave that is generated at the bottom of the PZT
*	Symbol used to identify a wave that is generated on either side of the PZT

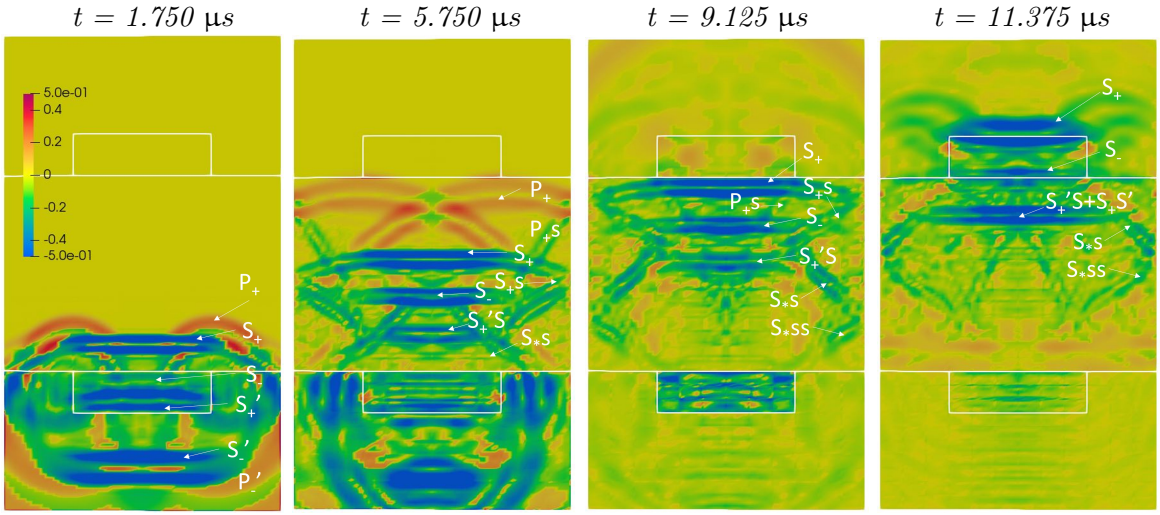


Figure (4.9) The wave pattern at different times following the emission of the S wave from the actuator for the model problem is presented in Figure 4.6. The plot to the left illustrates the wave pattern just after the end of the S-wave emission, which lasts 1 μs. The positive and negative values of the plotted scalar indicate where the P wave and the S wave are dominant, respectively. Times 5.750 and 9.125 correspond to the arrival times of the P-wave and the S-wave, respectively. The voltage picked up at the last three times is illustrated in Figure 4.8.

follows. In every material region, the nodal strain is decomposed into a spherical part and a deviatoric part. Two positive scalars are then computed: the absolute value of the trace of the spherical part, which is the absolute value of the volumetric change, and the second invariant of the deviatoric part, a measure of the equivalent shear strain. The two sets of scalars are then normalised by the maximum value of the two over each material. The final step consists of deciding if the wave is dominantly P or S. If the first scalar is larger than the second, it is the quantity to be plotted. If it is otherwise, the scalar to be plotted is minus the normalised equivalent shear strain. It is the distribution of this scalar which is plotted in Figure 4.9 selecting the range $[-0.5; 0.5]$ to provide a clear pattern. Red regions are P-wave-dominated, and green and blue regions are S-dominated. The yellow regions have not yet been reached by the travelling waves, or the deformation there is small compared to the maximum value. This scalar will be referred to as the wave factor in what follows.

Furthermore, a specific notation is introduced in Table 4.2 to identify the different wavefronts and phases. The waves generated from the two horizontal top and bottom boundaries are designated by the subscripts plus and minus, respectively. The waves due to the vertical lateral boundary are identified with an asterisk in subscript. Each horizontal boundary generates two waves, one propagating upward and one downward, as has been shown in the 1D setting. The latter is referred to with a prime. Lowercase letters are for head waves, and a combination of letters is used to represent the wave phase. For example, a S'_+S is an S wave generated from the actuator top boundary, propagating downward through the actuator and reflected upward at the lower interface. Another example is P_+s, which is a compressional wave generated from one of the two top corners of the PZT, which begins travelling upward but is then reflected at a critical angle as a shear wave at the specimen stress-free boundary. Note that transmitted waves through an interface keep the same name as the emitted waves. Having been through

these preliminaries, we are now in a position to provide an interpretation of Figure 4.9.

The plot to the left of Figure 4.9 characterises the emission and is taken at t=1.75 µs, so 0.75 µs after the end of the genesis of the S pulse from the actuator. The S_+ wave on top of the actuator has two parallel fronts oriented along the 1-axis and starting to propagate in the porous rock. These two fronts mark the maximum and minimum voltage separated by 0.5 µs. On top of these two parallel fronts, there are on both sides of the actuator, two circular P_+ wave arcs. They were emitted from the two top corners of the actuator, which are points of strain concentration. The emission also occurs at the bottom of the actuator, and S_- is about to arrive at the top boundary. Below but still within the actuator confine, two parallel S fronts are travelling upwards after a reflection on the lower interface (S'_+S). Within the lower anvil, two parallel fronts S'_- are travelling downwards and are preceded by the P'_- emitted from the lower corners. The lower fronts S'_- are travelling faster in the steel than the S_+ in the rock specimen and will be absorbed in the lower boundary of the anvil.

The second plot in Figure 4.9 is taken at $t = 5.750\,\mu s$ at the time of arrival of the P wave on the receiver. By then, the two circular P_+ arcs had intersected, where there was a green spot just on the vertical axis through the half-width of the structure. This region is of low activity in terms of volume change because one P wave arc leads to dilation while the other leads to compression of the same amount, but there is a slight shear effect. The two circulars have also reached the porous rock's left and right lateral, stress-free boundaries. The P-waves impinging on these boundaries have generated S-waves, which are green and labelled P_+s. They are interacting with the principal S waves (S_+, S_- and S'_+S) which are travelling behind the P arcs. Note the head wave S'_+s with a different orientation from the first head wave discussed above. There is a third head wave complementing this pattern S_*s due to the lateral propagation of the generated S waves.

The third plot at time $t = 9.125\,\mu s$ corresponds to the arrival time of the main S_+ wave at the receiver. The P-waves have already been partly transmitted through the upper anvil and absorbed by the boundary. The wave pattern in the rock is now S-dominated with the series of three successive pulses S_+, S_- and S'_+S with double fronts. The first front of the first pulse S has arrived at the receiver. Compared to the previous plot, note the addition of the S_*ss, which results from the interaction of the initially lateral wave with the vertical rock boundary. The last plot on the right of Figure 4.9 at time $t = 11.375\,\mu s$ is taken when the S_+ pulse reaches the receiver's top boundary and gets partly transmitted to the upper anvil. One can estimate that the three main S waves arrive within 3 µs.

We now use these last three plots to understand the voltage recorded by the receiver presented in Figure 4.8. The first fluctuation at $t = 5.75\,\mu s$ is the arrival of the P-wave front. It is felt during nearly 2 µs because it propagates through the receiver as observed for the P waves in a 1D setting as discussed in section 4.5.1. The first front of the first S pulse arrives at $t = 9.125\,\mu s$ and a large peak is reached at the arrival of the second front of the same pulse 0.5 µs later. The period of the voltage between two pulses is of the order of 2.2 µs (time from first positive peak to next positive peak). This time is very much in line with the arrival of the second pulse S_-

seen on the wave pattern at $t = 11.375\,\mu s$. The fluctuation of the receiver voltage is thus due to two effects: first, the complex and rather long S-wave pattern due to the three pulses with double fronts generated by the actuator, and second, the reflection of the first S-pulse within the receiver. Note that the characteristic time for an S-wave to travel through the receiver is $2l/c_{3s} = 3.5\mu s$ in which l is the receiver thickness and c_{3s} the S-wave velocity.

A final note on Figure 4.8 concerns the red, green, and blue curves. The first curve corresponds to the solution for an actuator voltage varying linearly between the two electrodes. The two other curves were obtained with, in addition, the Bubnov-Galerkin scheme discussed above and presented in Appendix C.1. These results compare very favourably with the solution for the fully coupled problem, but the gain in CPU times remains marginal as for the 2D P-wave simulations.

To summarise, two simple proxies for the S and P-wave PZTs have been proposed, and a methodology based on the analysis of the wave pattern crossing the porous rock and impinging on the receiver has been used to understand the arrival time of the main S wave and waveform. It is shown that the voltage response is due first to the P-wave and its associated S waves, and second to the arrival of a succession of three double S fronts due to the emissions from the two boundaries of the actuator and the reflections within the actuator. The voltage is further influenced by the reflection of the S pulses within the receiver confines. The next step consists of applying the same workflow to a section through the tri-axial testing machine of interest and showing how to control these multiple reflections within the actuator.

4.6 SFEM simulations for validation with calibration specimen

The section through the tri-axial cell is presented in Figure 4.10. The bottom and top anvils are composed of two pieces: one fixed to the rest of the machine and the other detachable. The upper detachable part can either be identical or 2.1 cm longer than the bottom equivalent. They are identical for longer specimens, as in this validation test. The transducers are inserted in cylindrical holes in the fixed parts with a spring pushing them into contact with the detachable part. These springs are not accounted for, and the contacts between the piezoelectric and the rest of the machine are assumed to be perfect (no displacement jump). Absorbing boundary conditions are imposed on all the external boundaries of the fixed parts, except, of course, with the detachable parts, as shown with the red segments in Figure 4.10. The S and P devices have a PZT part as in the previous section, but also an additional region called the backing. For the backing, we use a proxy that has the same elastic properties as the PZT, but without the piezoelectric effect. This proxy reduces the wave reflection and improves the matching with the experimental result, as discussed in Appendix C.2. The P devices, on the left of the S devices, have the same properties, but they are passive (no electric coupling) and were introduced only to account for their potential perturbation of the wave pattern. The sample is composed of inox steel, which is used to validate the experimental setup. These laboratory data are considered here for the selection of the backing material properties. A rock specimen will replace the inox specimen in the next section. The properties of the inox specimen and the anvil material are

given in Table 4.3. The finite-element mesh is composed of approximately 2000 elements, each having 100 nodes, as displayed in Figure 4.11. For all simulations hereafter, the time step is set to $5 \times 10^{-4}\mu s$, a lot smaller than Courant's limit.

Table (4.3) Properties of the steel materials used in the calibration experiment.

Variable	Symbol	Unit	Steel sample	Steel anvil
Density	ρ	kg/m^3	7,800	7,800
Young's modulus	E	GPa	198	185
Poisson's ratio	ν	N/A	0.30	0.27
P-wave velocity	V_P	m/s	5845.6	5444.0
S-wave velocity	V_S	m/s	3124.6	3055.8

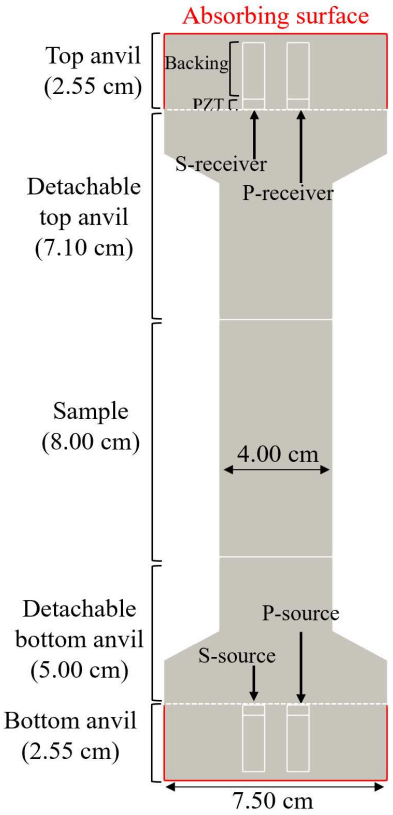


Figure (4.10) Experimental set up. Two different top anvils are used in our experiments, a short (5 cm) and a long (7.1 cm).

4.6.1 Wave propagation in steel sample and upper anvil

We have observed in Section 4.5.2 and Appendix C.2 the propagation within the actuator and lower anvil. For validation, we now concentrate on the upper part of the machine, including the inox steel specimen. The results of this simulation are then compared to the experimental data to guide our interpretation and validate the selection of backing material proposed in Appendix C.2.

Figure 4.12 presents the wave factor defined in section 4.5.1 and shows the situation inside the upper part of the system at three key moments: the first P-wave arrival (a), the arrival of P_+sp (b), and the arrival of the S_+ wave (c). In addition, Figure 4.13 displays a side-by-side comparison of the simulated (blue curve) and experimental (red curve) waveforms.

The first P wave arrives at $t = 32.05\,\mu s$ (Figure 4.12a) and is directly followed by a series of P_+s waves. At this moment, S_+ is propagating inside the sample and is being trailed by its reflections off the free surface S_+s, as well as S_- and its identifiable derivatives S_-s and S_-ss. Another major wave inside the sample that has not yet been discussed is P_+sp. It travels faster than S_+ because it is linked to P_+ and its interaction with the specimen's stress-free boundaries.

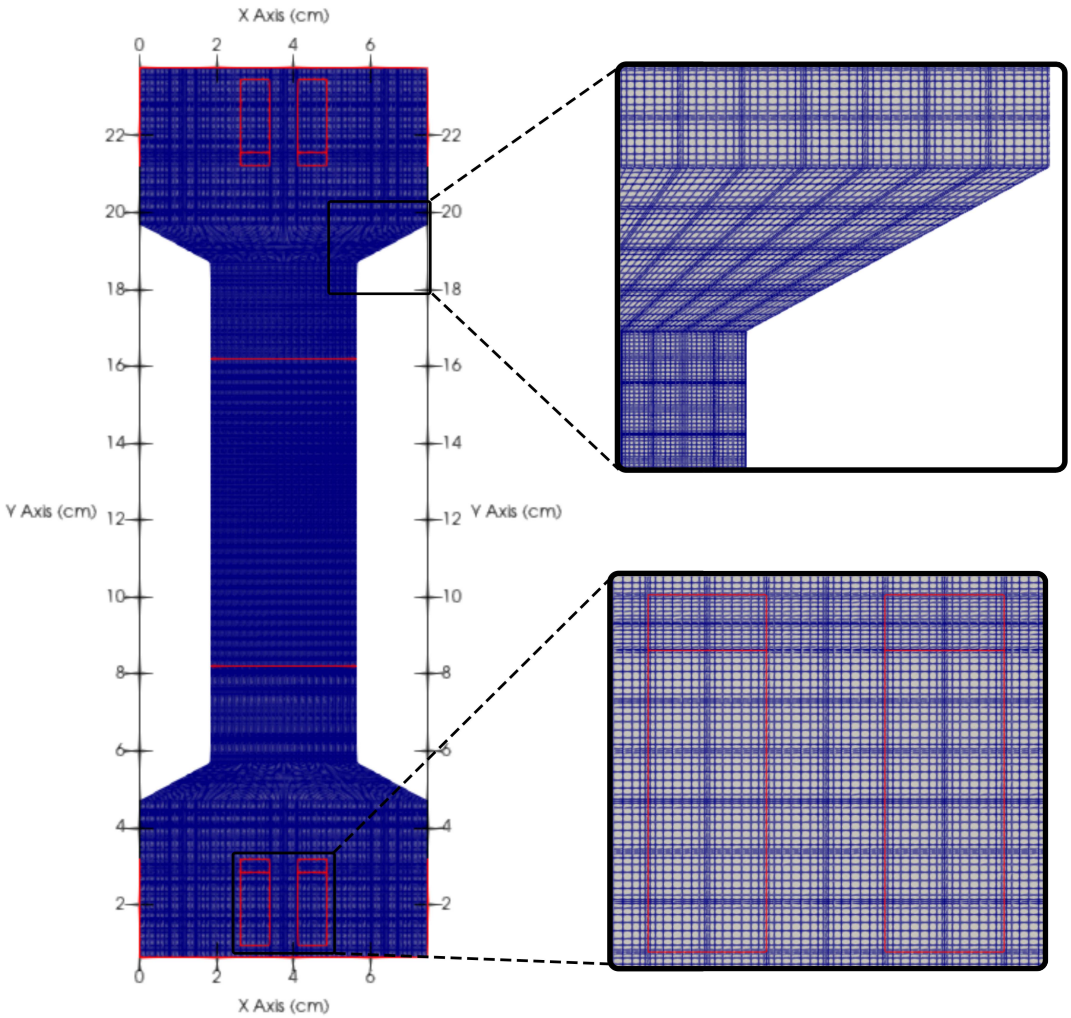


Figure (4.11) Simulation mesh containing 1918 spectral elements (150049 nodes) for an average resolution of 1209 nodes per square centimetre.

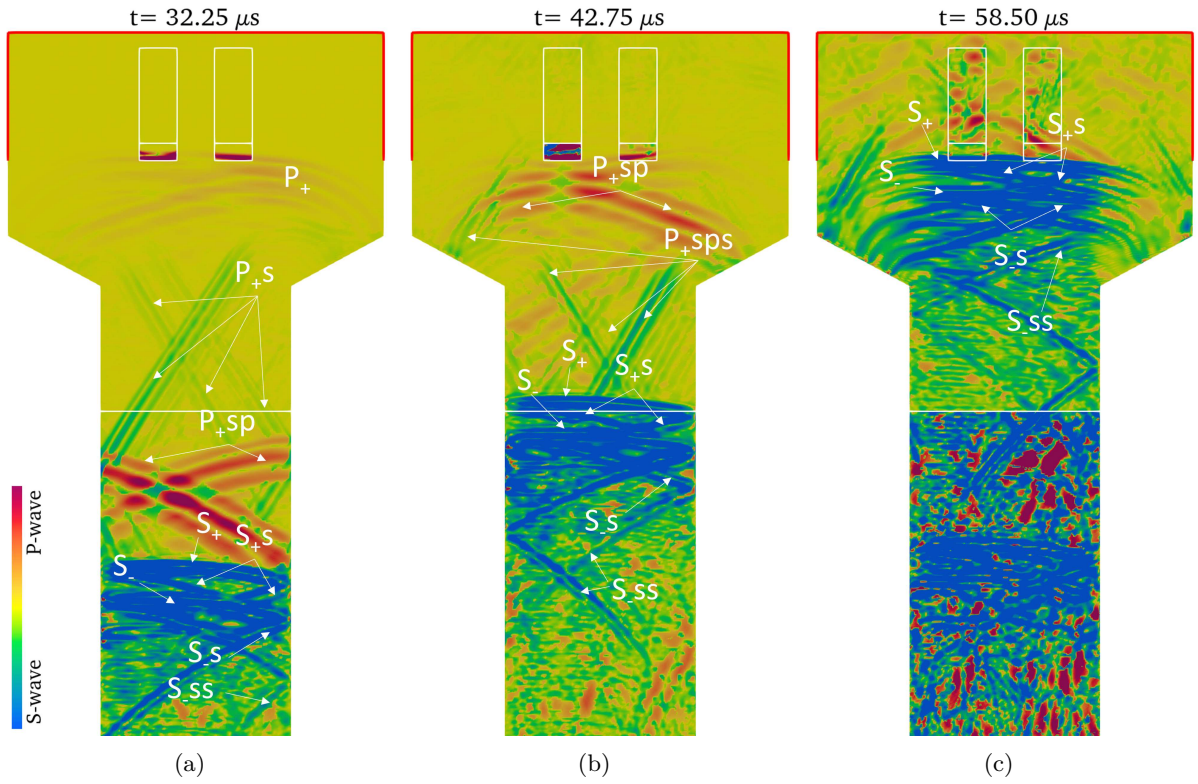


Figure (4.12) Snapshots at three different times of the simulation of the propagation of waves inside a stainless steel sample and the upper anvil, using an S-wave source. The first and last times correspond to the arrival of the first P and S waves, respectively.

Thus, it will disturb the waveform before the arrival of S_+.

Figure 4.12b shows the situation at $t = 42.75\,\mu s$, when P_+sp arrives at the receiver. It is closely followed by P_+sps waves, while S_+ is entering the top anvil. At this instant, the series of shear waves trailing S_+ remains the same as at $t = 32.05\,\mu s$. Note that inside the receiver's PZT material, waves are being reflected as others arrive at the base. These two simultaneous effects determine the voltage waveform at that time.

Figure 4.12c shows the situation at $t = 58.50\,\mu s$, when S_+ reaches the receiver. S_+ is directly followed first by S_+s and second by the superposition of S_- and S_+s. The last to arrive will be S_-ss. It is this series of S waves that determines the interesting part of the waveform.

Figure 4.13 displays the waveforms (arbitrary voltage) over time captured by the top left receiver experimentally (red curve) and numerically (blue curve). This arbitrary voltage was selected such that the amplitude of the superposition S_- plus S_+s matches the experimental result and thus facilitates our comparison. The arrival times of the main waves, based on Figure 4.12, are also reported on the waveform. On one hand, it shows that the first P wave arrives earlier in the simulation ($t = 32.05\,\mu s$) compared to the experiment ($t = 33.10\,\mu s$). This corresponds to a 3% error, which can be attributed to the fact that the precise physical properties of the anvils are unknown. Our choice of material properties favours matching the arrival of the S wave with that of the P wave. Furthermore, the first P-wave is closely followed by a series of pulses with

decreasing amplitudes. These pulses were identified as P_+s waves. We also observe that the voltage amplitudes of this first series of waves are significantly smaller in the simulation than in the experiment, even after normalisation. Indeed, this difference in magnitude holds true for all the waves that arrive before the S-wave. On the other hand, both the arrival time and the signal pattern of the S-wave in the simulation match the experimental data. The wave S_+ arrives at $t = 58.32\,\mu s$ within the error margin of the experimental result. The series of pulses that directly follow the arrival of S_+ is also clearly observed in the numerical waveform and matches the experimental results.

Overall, the results show that the numerical simulation accurately captures the arrival time of the S-wave. Moreover, the pattern of the groups of waves that follow the S-wave is also reproduced in the simulation. These results validate our design of numerical proxies for the piezoelectric material and enable us to consider rock specimens next.

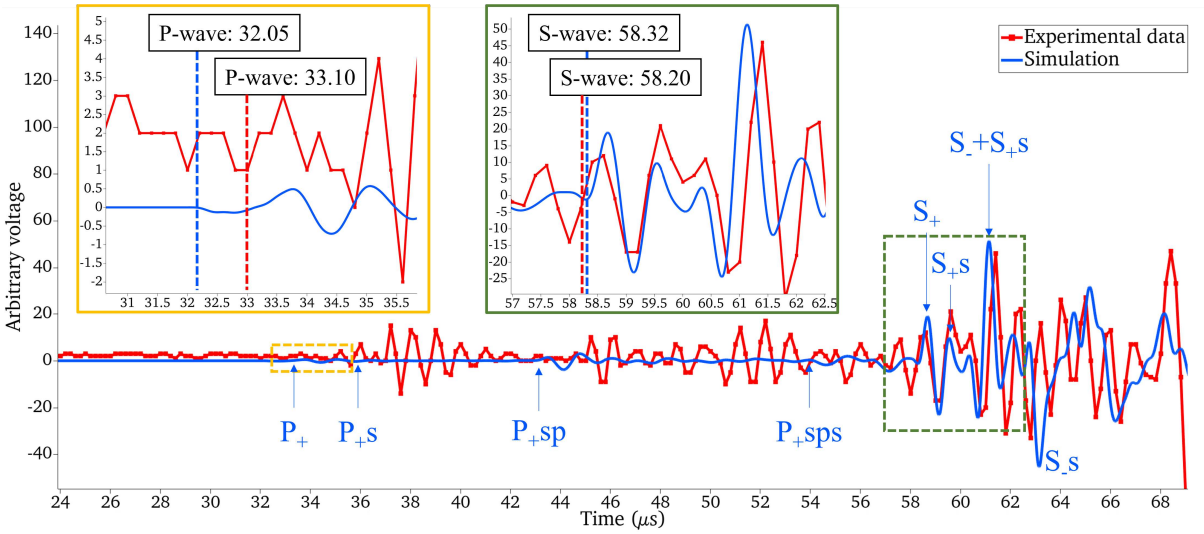


Figure (4.13) Waveform captured by the S-wave receiver, experimentally (red curve) and numerically (blue curve). The close-up of the P-wave and S-wave arrivals is shown inside the yellow and green frames, respectively. The arrivals of the various waves pointed by blue arrows are based on Figure 4.12.

4.7 Applications to rocks with contrasted velocity ratios and anisotropy

The V_P/V_S ratio of a rock, which is often provided by field measurements (sonic and seismic data), is a crucial parameter in the UPT since it can be used to guide the picking of the S-wave. It is of interest to know how the value of the V_P/V_S ratio of rock influences the waveform. For this purpose, we ran simulations on two identical rock specimens, but with different Poisson's ratios. We simulated in 2D the S-wave UPT on two clean (100% quartz), 3% porosity, Fontainebleau sandstones. One of the samples (Fo3B) underwent thermal microcracking, which increased its crack density to roughly 3%, while the other one (Fo3A) was left intact. These samples were experimentally studied by Pimienta *et al.* (2018) in their investigation of the influence of fractures on the V_P/V_S ratio of rocks in subduction zones. The laboratory experiments, done to capture Poisson's ratio (ν), consisted of small oscillations of the confining stress on both dry

and undrained saturated samples (Borgomano *et al.*, 2017). In their study, the authors disclose the ν values and their associated V_P/V_S ratio for Fo3A and Fo3B. The rocks' physical properties used in the simulations are listed in Table 4.4 and come from Pimienta *et al.* (2018). The goal of our simulations is to numerically check the impact that the difference in the V_P/V_S ratio may have on the waveform.

Moreover, we investigated the impact of anisotropy, another important parameter known to affect the elastic moduli, on waveforms. For this purpose, we simulated the S-wave propagation inside two wet shales with different orientations of their respective transverse isotropic axis. The elastic properties (Table 4.4) used for these shales are based on UPT measurements of Sarout *et al.* (2008), and the estimation of the anisotropic stiffness tensor is detailed in Sarout, 2006. One of the samples has a horizontal axis of isotropy (Sh1) and the other has a vertical one (Sh2), but they are otherwise identical. In their study, the authors showed, experimentally, the impact of anisotropy on the arrival times of different S-wave phases but did not discuss the dissimilarities of waveforms.

Table (4.4) The dynamic material properties of two sandstones proposed because of their different v_P/v_S ratio to capture the possible variation in wave pattern arriving at the receiver (data from Pimienta *et al.*, 2018), and two wet shales with different anisotropy (data from Table 3 of Sarout *et al.*, 2008).

Property	Units	Fontainebleau sandstone (Fo3A)	Fontainebleau sandstone (Fo3B)	Wet shale (Sh1)	Wet shale (Sh2)
P velocity	km/s	6.2	3.1	4.3	3.6
S velocity	km/s	3.3	2.0	2.3	1.9
v_P/v_S ratio		1.88	1.55	1.82	1.83
Density	kg/m^3	2300	2300	2450	2450

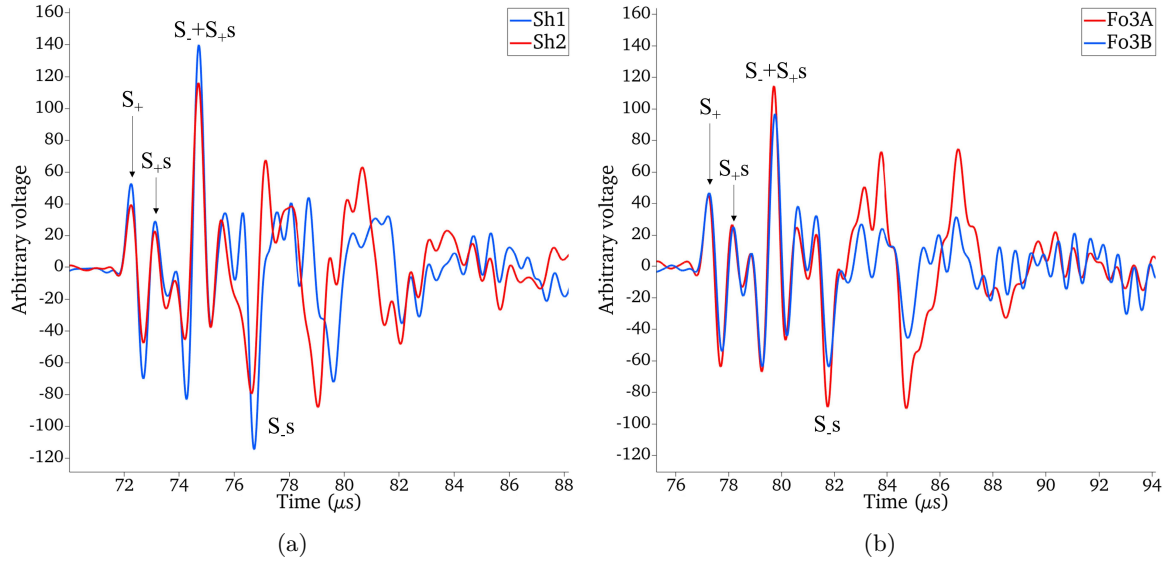


Figure (4.14) Numerical results of the propagation of an S wave inside two anisotropic shales with different isotropy axes **(a)** and two Fontainebleau sandstones with different Poisson's ratios **(b)**. A time shift was applied to fit the two arrival times of S_+ and to compare the two wave patterns.

The geometry used for the simulations is presented in Figure 4.10 with the longer version of the top anvil. The material properties of the apparatus are provided in Table 4.3. The mesh is

composed again of approximately 2000 elements, each with 49 nodes. The time step is set to $5 \times 10^{-4}\mu s$ for all simulations.

Figure 4.14 showcases the signal near the arrival of the S_+ wave in both simulations. The interpretation of the wave pattern within the surroundings of the receiver, following the workflow proposed in the previous section, has permitted us to identify the various waves impacting the waveform. The details of this construction are not presented because of their strong similarity with the results of the previous section. A timeshift was applied on the waveforms in Figure 4.14 to fit the two arrival times of S_+ and facilitate their comparison. The results of the simulations on the anisotropic shales show a difference in the amplitudes of S_+, S_+s, $S_- + S_+s$ and S_-s. In terms of pattern, there is a good overlap of the two waveforms until S_-s arrives (4.14a). The last part of the signal differs significantly in both amplitude and pattern. When it comes to the results of the simulations on the sandstones, similar observations are made, except that the difference in amplitudes is smaller and that there is a good fit of the two patterns even after the arrival of S_-s (Figure 4.14b).

Overall, it seems that the pattern of the waveform near the arrival of the S_+ wave is not greatly influenced by the rock's properties. It mainly depends on the details of the piezoelectric and the geometry of the experimental setup.

4.8 Conclusion

We have proposed a numerical workflow for accurately determining the arrival time of the S-wave in a triaxial cell, detected by PZT receivers. By conducting a series of 2D numerical simulations using the SFEM, we have analysed the propagation pattern of the emitted P and S waves through the experimental apparatus, porous specimen, and receiver, then predicted the receiver voltage as a function of time.

The fully coupled algorithm, considering both displacement and electric field, has been successfully validated in both 1D and 2D scenarios by comparing the numerical results with an analytical solution for a 1D bar with an actuator and receiver, via the method of characteristics. The instantaneous propagation of electric information has posed difficulties, as regions can interact before the superposition of forward and backward waves. Our findings demonstrate that, for a simple multi-linear voltage applied to the actuator electrode, the displacement pulse travelling through the specimen and the detected voltage at the receiver can be approximated as a quadratic function of time. This parabolic relationship makes it challenging to determine the exact arrival time at the receiver. We have observed that the magnitude ratio between the received and applied voltage is minimal, of the order of 5×10^{-2}, in a 1D setting. Various factors, including the properties of the PZT, the acoustic impedance of the porous rock, the duration of the voltage pulse, and the thickness of the PZT device, influence this ratio. Furthermore, we have identified that the received voltage manifests as an oscillating signal with a period larger than the duration of the input voltage. This period is associated with the time required for two to four reflections to occur within the receiver.

Because the exact internal structure of the PZT is unknown, we have proposed simple numerical proxies for the actuator in a 2D geometry. A backing material made of the same material as the PZT, but without the piezoelectric effect, was incorporated into the numerical proxies. The backing effectively reduced reflections within the PZT and achieved better agreement between numerical simulations and laboratory measurements for a calibration specimen made of stainless steel. We reproduced the complex wave pattern preceding the main S-wave arrival at the receiver, which arises from multiple P-waves and associated S-waves generated by the actuator hitting the specimen's boundaries. Indeed, our 2D simulations on porous rock specimens with varying properties demonstrated that the wave pattern near the S-wave arrival is predominantly influenced by the properties of the PZT and the experimental setup's geometry. On the contrary, variations in the rock's properties had a minor impact on that wave pattern. In other words, for a given experimental setup and piezoelectric material, we are able to capture the S-wave's arrival pattern for any homogeneous specimen. Furthermore, to improve computational efficiency, we proposed simplifications in the fully coupled algorithm, including a linear electric field assumption and the utilisation of the Bubnov-Galerkin method.

This line of work could be extended in various ways, and four of them are now briefly discussed. Firstly, the numerical simulations should be extended to 3D to closer mimic the laboratory experiments. The workflow proposed here already applies to 3D, and only an efficient, parallelised code version is necessary to proceed. Secondly, the proxies proposed for the actuator and receiver are certainly over-simplified. The piezoelectric material is layered, and the backing region does not respond elastically but visco-elastically. Such developments are certainly possible, and would enable the use of an actuator with a transfer function closer to the manufacturer's specifications. Thirdly, the specimens used in industrial laboratories are often extracted from cores and are rarely homogeneous, as revealed by X-ray tomography. Simulations such as the ones presented here could be conducted by accounting for the exact defect distribution and also its potential statistical distribution. The former would provide the wave velocities matching the experimental data, and the latter would provide uncertainties that cannot be obtained from the laboratory. Fourthly, the S wave waveform, which is controlled by the machine and piezoelectric properties, has been identified and could now be used to train an automatic workflow to pick the S wave's arrival time in the laboratory.

Chapter 5

Conclusion

5.1 Summary

This thesis was divided into five chapters. The first chapter was dedicated to the context of the project, including the central problem of determining the proper elastic properties of rocks when there is hysteresis between the loading and unloading phases. This central problem has implications for reservoir monitoring and 4D-seismics, since the prediction and interpretation of the response of the reservoir to stress variations cannot be done without an *a priori* estimation of its elastic properties. We emphasised that although hysteresis in rocks under remote deviatoric stress has been extensively studied and is now attributed to the presence of cracks, hysteresis under hydrostatic stress has never been modelled theoretically. We have highlighted evidence in the literature that hysteresis was indeed observed under remote hydrostatic stress and that it hinders the accurate measurement of the bulk modulus and other types of compressibility parameters. This led to many questions regarding the origin of that hysteresis. Inspired by previous studies, we hypothesised that frictional microcracks were the cause of hysteresis in rocks under remote hydrostatic stress by suggesting that local deviatoric stress is felt at the microscopic scale and triggers slip on the frictional microcracks. A micromechanical model capable of generating local deviatoric stress and hysteresis under remote hydrostatic stress was therefore proposed. It is composed of a central pore surrounded by a spheroidal shell containing isotropically distributed penny-shaped cracks.

The construction of this model was presented in the second chapter, detailing the entire research process. This included the application of a first homogenisation scheme to estimate the effective properties of a mineral shell containing microcracks, following the work of Kachanov (1982). Then, the effective hysteretic properties of the composite sphere assemblage were computed via a second homogenisation of the microcracked shell and central pore, according to the scheme of Hashin (1962). The application of the model to a set of porous rocks, including sandstones and limestones, resulted in hysteretic stress-strain curves that closely matched the experimental data. These primarily qualitative results provided strong evidence that microcracks are indeed the principal cause of hysteresis in hydrostatic loading experiments. Moreover, the modelled results matched the experimental hysteresis measurements for sensible parametric values of

friction and mineral phase elasticity.

In the third chapter, the micromechanical model was extended to enhance its quantitative predictions. Instead of considering a single family of identical cracks, a distribution of crack families of various aspect ratios was utilised to mimic natural rocks more closely. This finer version of the model was used to estimate the strain amplitude dependence of the bulk modulus through a series of simulations of hydrostatic forced oscillation experiments. It was found that the microcrack activity, proportional to the oscillation amplitude, is responsible for the discrepancy between static (strain amplitudes of 10^{-4}) and dynamic measurements (strain amplitudes of 10^{-6}) of the bulk modulus. Experimental measurements on the Bentheim sandstone supported this theoretical finding. The enhanced model also provided insights into the crack distribution inside rock specimens while accounting for frictional slip. The model yielded crack densities that were roughly half of those predicted by conventional crack density inversion schemes, which do not consider slip. When it came to the modelled porosity, it still had to be increased substantially to generate the appropriate amount of hysteresis. However, a linear relationship was found between the modelled and measured porosity, allowing for quantitative predictions of hysteresis based on the loading phase data.

Finally, the fourth chapter addressed the S-wave picking challenge that experimentalists often encounter during dynamic experiments. This was achieved through the forward modelling of the wave propagation test from the piezoelectric source to the receiver, using spectral finite elements. The fully coupled electromechanical problem was solved both numerically and analytically. A distinct S-wave signature pattern was identified in the waveform. Importantly, this signature was found to be influenced mainly by the geometry of acquisition and piezoelectric properties of the transducers, rather than the nature of the rock specimen. This understanding can significantly enhance the accuracy and reliability of S-wave picking in future experiments.

Many objectives were cleared, and the final goal of finding a non-linear and anelastic stress-strain relation that predicts hysteresis in hydrostatic conditions has been reached. For a visual representation, the PhD mind map presented in the introduction (Figure 1.1) has been updated with the completed objectives in Figure 5.1. The updated version now highlights in green how this research, conducted at the micromechanical scale through forced oscillation and hydrostatic loading simulations, combined with wave propagation simulations involving piezoelectricity on homogeneous samples, contributed to achieving the end goal. Overall, this thesis has advanced our understanding of the hysteresis phenomena in the hydrostatic loading of rocks and proposed a new numerical approach to wave propagation problems in a rock physics context. It now opens the door to new questions and possibilities, which are presented in the next section.

5.2 Future research directions

Four main future directions are proposed below. The first recommendation focuses on increasing the local deviatoric stress caused by the cavity without enlarging its size. The second suggestion explores a more efficient crack closure criterion that does not require the integration of numerous crack families with varying aspect ratios. The third idea addresses ways to improve wave

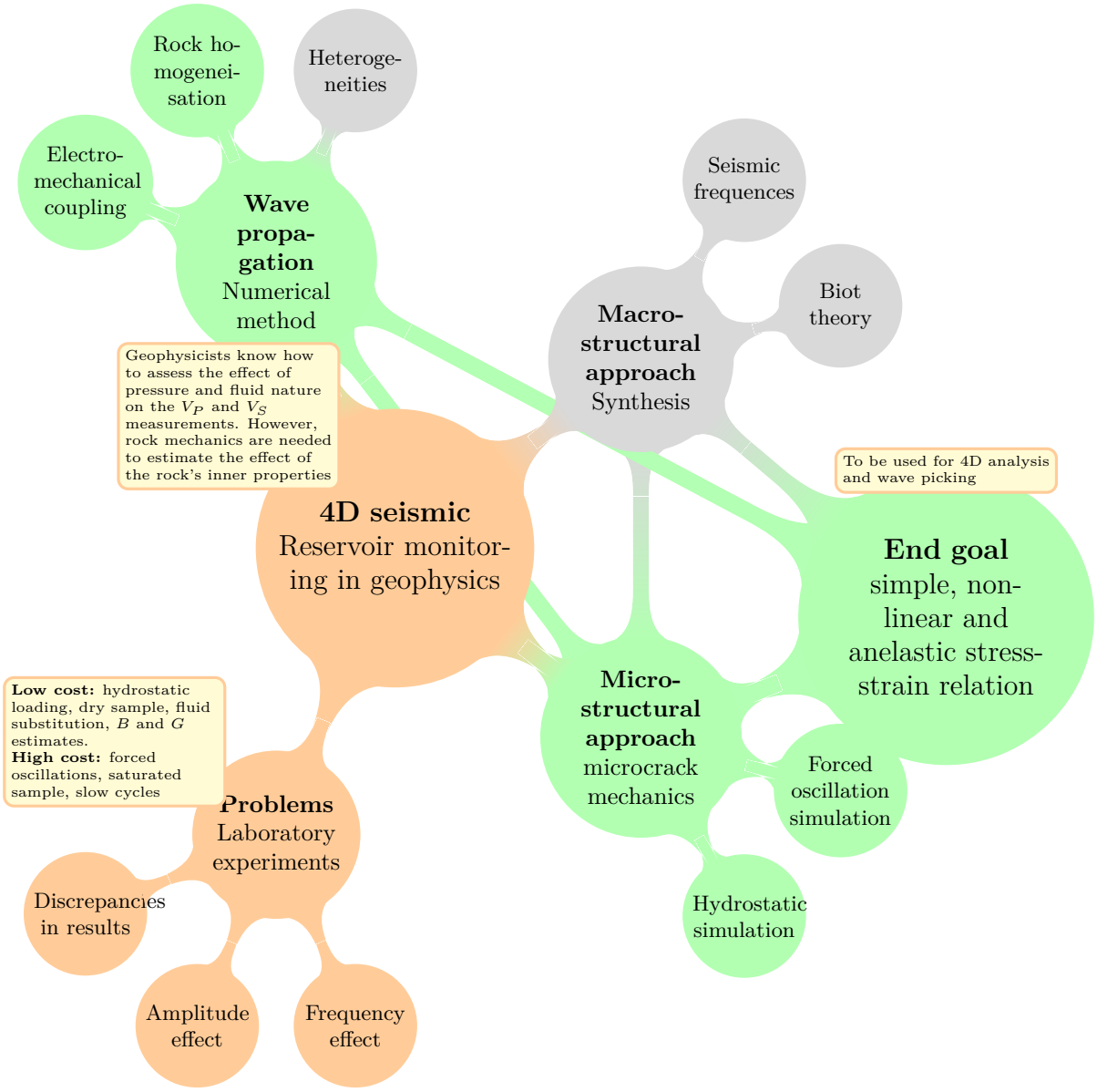


Figure (5.1) Updated PhD mind map. Colour code: *orange* = challenges, *green* = completed objectives, *gray* = solutions that were not completed during the PhD.

propagation simulations by incorporating three-dimensional heterogeneities in rock specimens. Finally, the last direction emphasises the potential for upscaling the micromechanical model.

5.2.1 Amplification of local deviatoric stress

Future research could investigate an efficient method for amplifying local deviatoric stress without increasing porosity, the size of the central pore. One potential approach is to change the shape of the central pore from a sphere to an ellipsoid. Depending on its aspect ratio, an ellipsoidal pore with the same volume could exhibit a stress concentration factor at its tips that is twice as high as that of a spherical cavity (Eshelby, 1957). However, a significant challenge of this approach is the loss of symmetry in three dimensions, which would necessitate extensive development to derive new analytical solutions and propose a numerical solving method.

In addition to changing the aspect ratio of the cavity, the nature of the inclusion filling can be modified. Instead of using a pore inclusion filled with fluid, a solid inclusion can be considered. This is especially relevant to low-porosity metamorphic rocks, which often contain mineral inclusions stiffer than the matrix. A stiffer inclusion in a softer matrix creates higher stress concentrations (Zhou *et al.*, 2022). This option maintains the spherical symmetry of the model, and the only further development would be to add an elastic rheology law to the inclusion.

Besides directly amplifying the local deviatoric stress induced by the inclusion, another direction of research is incorporating crack-to-crack interaction at the REV scale in the matrix. This would increase microcrack activity, similar to what a higher deviatoric stress would do. Kachanov (1993) proposes different crack interaction schemes for various crack configurations, including intersecting cracks, within an elastic medium. However, the development required to implement crack interaction into the micromechanical model could be significant. Nevertheless, there are already advanced fracture mechanics codes available that, while often applied to macroscale objects, account for crack interactions and other effects, as developed by Paluszny *et al.* (2018), Nejati *et al.* (2016), and Mohammadpour *et al.* (2025).

5.2.2 Efficient crack closure scheme

Currently, the crack closure criterion is directly proportional to the aspect ratio of the cracks. This indicates that each family of cracks is associated with a specific closure stress. Increasing the number of crack families raises the number of internal variables significantly. The numerical method developed in this thesis took into account forty crack families, which were sufficient to achieve convergence towards the same solution for the tested rock samples. However, some rocks may contain many more than forty crack families, so a more efficient approach than Gauss' integration for each crack family could be considered to minimise time complexity.

5.2.3 Enhanced wave propagation simulation

In this thesis, simulations of forward wave propagation were conducted on homogeneous materials. However, natural rocks used in industry often contain various defects and exhibit heterogeneity. It is beneficial to consider spatial heterogeneity in 3D. 3D X-ray computed tomography (CT) can be utilised to assess the uneven distribution of minerals and cracks at the laboratory scale. The CT images enable the mapping of pore space and permeability within the materials. This mapping allows for simulations of the effect of wave frequency on squirt flow and its influence on wave velocities, as well as the noise-to-signal ratio of the waveform. The primary efforts required to achieve this include the development of 3D spectral finite elements with piezoelectricity and the implementation of a method to generate a mesh with material phase identification from the CT images (Dai, 2011; Otsu *et al.*, 1975; Garboczi *et al.*, 2015). Repeated numerical simulations, once calibrated on the experimental observation, for various distributions of defects, would complement the laboratory measurements with uncertainty estimates.

5.2.4 Macrostructural scale

The final key direction for future research involves upscaling the micromechanical model to the field scale. This step is essential for 4D seismic and reservoir monitoring.

Currently, the model employs microcrack mechanics to predict the hysteretic strain response of rocks during hydrostatic loading cycles. It can also estimate the dynamic bulk modulus based on static measurements in dry rocks. However, reservoir monitoring relies on dynamic field data, specifically 4D seismic data, to infer rock properties from velocity maps. Therefore, upscaling the micromechanical model necessitates the ability to convert dynamic elastic properties into static properties. One approach is to reverse-engineer the mapping of static to dynamic elastic properties described in Chapter 3. In other words, the inverse problem should be solved starting with dynamic measurements taken at various confining pressures and then matching these measurements with the appropriate distribution of crack aspect ratios and porosity. Note that the rock's skeletal properties are derived from wave velocities at high pressures. Once the modelled porosity, crack aspect ratio distribution, and rock skeleton properties are established, these parameters can then be used to model the static hysteresis stress-strain loop.

References

Aleshin, V. and Van Den Abeele, K. (2007). "Microcontact-based theory for acoustics in microdamaged materials". *Journal of the Mechanics and Physics of Solids* 55.2, pp. 366–390.

Aleshin, V., Delrue, S., Trifonov, A., Matar, O. B., and Van Den Abeele, K. (2018). "Two dimensional modeling of elastic wave propagation in solids containing cracks with rough surfaces and friction–Part I: Theoretical background". *Ultrasonics* 82, pp. 11–18.

Andrieux, S., Bamberger, Y., and Marigo, J.-J. (1986). "A model of micro-cracked material for concretes and rocks". *Journal de Mécanique Théorique et Appliquée* 5.3, pp. 471–513.

Bakhorji, A. and Schmitt, D. R. (2010). "Laboratory measurements of static and dynamic bulk moduli in carbonate". *ARMA US Rock Mechanics/Geomechanics Symposium*. ARMA, ARMA–10.

Baltazar, A., Rokhlin, S. I., and Pecorari, C. (2002). "On the relationship between ultrasonic and micromechanical properties of contacting rough surfaces". *Journal of the Mechanics and Physics of Solids* 50.7, pp. 1397–1416.

Benjeddou, A. (2000). "Advances in piezoelectric finite element modeling of adaptive structural elements: a survey". *Computers & Structures* 76.1-3, pp. 347–363.

Benveniste, Y. (1985). "The effective mechanical behaviour of composite materials with imperfect contact between the constituents". *Mechanics of Materials* 4.2, pp. 197–208.

Birch, F. (1960). "The velocity of compressional waves in rocks to 10 kilobars, Part 1." *Journal of Geophysical Research* 65.4, pp. 1083–1102.

Biwa, S., Nakajima, S., and Ohno, N. (2004). "On the acoustic nonlinearity of solid-solid contact with pressure-dependent interface stiffness". *J. Appl. Mech.* 71.4, pp. 508–515.

Biyoghé, A. T., Leroy, Y. M., Pimienta, L., and Zimmerman, R. W. (2024a). "Stress–strain hysteresis during hydrostatic loading of porous rocks". *Journal of the Mechanics and Physics of Solids* 193.

Biyoghé, A. T., Leroy, Y. M., and Zimmerman, R. W. (2024b). "Simulations of S waves from the piezoelectric source to the receiver to assist in laboratory measurements of rock properties". *Geophysics* 89.3, MR91–MR106.

Borgomano, J. V. M., Pimienta, L., Fortin, J., and Guéguen, Y. (2017). "Dispersion and attenuation measurements of the elastic moduli of a dual-porosity limestone". *Journal of Geophysical Research: Solid Earth* 122.4, pp. 2690–2711.

Chapman, S., Fortin, J., Gallagher, A., and Borgomano, J. V. (2023). "Strain Amplitude Dependent Transition from Dynamic to Static Bulk Modulus in Rocks with and Without Preexisting Cracks". *Rock Mechanics and Rock Engineering*, pp. 1–18.

Christensen, R. and Lo, K. (1979). "Solutions for effective shear properties in three phase sphere and cylinder models". *Journal of the Mechanics and Physics of Solids* 27.4, pp. 315–330.

Christensen, R. M. (1990). "A critical evaluation for a class of micro-mechanics models". *Journal of the Mechanics and Physics of Solids* 38.3, pp. 379–404.

Clayton, R. and Engquist, B. (1977). "Absorbing boundary conditions for acoustic and elastic wave equations". *Bulletin of the Seismological Society of America* 67.6, pp. 1529–1540.

Dai, Q. (2011). "Two-and three-dimensional micromechanical viscoelastic finite element modeling of stone-based materials with X-ray computed tomography images". *Construction and building materials* 25.2, pp. 1102–1114.

David, E., Brantut, N., Schubnel, A., and Zimmerman, R. (2012). "Sliding crack model for nonlinearity and hysteresis in the uniaxial stress–strain curve of rock". *International Journal of Rock Mechanics and Mining Sciences* 52, pp. 9–17.

David, E. C. and Zimmerman, R. W. (2013). "Model for frequency-dependence of elastic wave velocities in porous rocks". *Poromechanics V: Proceedings of the Fifth Biot Conference on Poromechanics*, pp. 2431–2440.

Delrue, S., Aleshin, V., Sørensen, M., and De Lathauwer, L. (2017). "Simulation study of the localization of a near-surface crack using an air-coupled ultrasonic sensor array". *Sensors* 17.4, p. 930.

Delrue, S., Aleshin, V., Truyaert, K., Matar, O. B., and Van Den Abeele, K. (2018). "Two dimensional modeling of elastic wave propagation in solids containing cracks with rough surfaces and friction–Part II: Numerical implementation". *Ultrasonics* 82, pp. 19–30.

Eshelby, J. D. (1957). "The determination of the elastic field of an ellipsoidal inclusion, and related problems". *Proceedings of the royal society of London. Series A. Mathematical and physical sciences* 241.1226, pp. 376–396.

Garboczi, E. and Kushch, V. (2015). "Computing elastic moduli on 3-D X-ray computed tomography image stacks". *Journal of the Mechanics and Physics of Solids* 76, pp. 84–97.

Hashin, Z. (1962). "The Elastic Moduli of Heterogeneous Materials". *Journal of Applied Mechanics* 29, pp. 143–150.

Hennings, B., Lammering, R., and Gabbert, U. (2013). "Numerical simulation of wave propagation using spectral finite elements". *CEAS Aeronautical Journal* 4, pp. 3–10.

Hervé, E. and Zaoui, A. (1993). "n-Layered inclusion-based micromechanical modelling". *International Journal of Engineering Science* 31.1, pp. 1–10.

Huang, X., Di, B., Wei, J., Shuai, D., and He, L. (2021). "Finite-Element Analysis of Noise Preceding the Arrival of S-Wave in Ultrasonic Measurements of Rock Velocities". *IEEE Transactions on Ultrasonics, Ferroelectrics, and Frequency Control* 68.3, pp. 742–752.

Jaeger, J. C., Cook, N. G., and Zimmerman, R. W. (2009). *Fundamentals of rock mechanics*. John Wiley & Sons.

Jeng, F.-S., Weng, M.-C., Huang, T.-H., and Lin, M.-L. (2002). "Deformational characteristics of weak sandstone and impact to tunnel deformation". *Tunnelling and Underground Space Technology* 17.3, pp. 263–274.

Jizba, D. and Nur, A. (1990). "Static and dynamic properties of sandstones". *EAGE/SEG Research Workshop 1990*. European Association of Geoscientists & Engineers, pp. 326–332.

Kachanov, M. (1993). “Elastic solids with many cracks and related problems”. *Advances in applied mechanics* 30, pp. 259–445.

Kachanov, M. and Sevostianov, I. (2005). “On quantitative characterization of microstructures and effective properties”. eng. *International journal of solids and structures* 42.2, pp. 309–336.

Kachanov, M. L. (1982). “A microcrack model of rock inelasticity part I: Frictional sliding on microcracks”. *Mechanics of Materials* 1.1, pp. 19–27.

– (1992). “Effective Elastic Properties of Cracked Solids: Critical Review of Some Basic Concepts”. *Applied Mechanics Reviews* 45.8, pp. 304–335.

Kanaun, S. and Kudryavtseva, L. (1986). “Spherically layered inclusions in a homogeneous elastic medium”. *Journal of Applied Mathematics and Mechanics* 50.4, pp. 483–491.

Karaki, T., Yan, K., Miyamoto, T., and Adachi, M. (2007). “Lead-free piezoelectric ceramics with large dielectric and piezoelectric constants manufactured from BaTiO3 nano-powder”. *Japanese Journal of Applied Physics* 46.2L, p. L97.

Kim, K. and Makhnenko, R. (2021). “Changes in rock matrix compressibility during deep CO2 storage”. *Greenhouse Gases: Science and Technology*.

Knopoff, L. (1964). “Q”. *Reviews of Geophysics* 2.4, pp. 625–660.

Komatitsch, D., Barnes, C., and Tromp, J. (2000). “Simulation of anisotropic wave propagation based upon a spectral element method”. *Geophysics* 65.4, pp. 1251–1260.

Komatitsch, D., Vilotte, J.-P., Vai, R., Castillo-Covarrubias, J. M., and Sãnchez-Sesma, F. J. (1999). “The spectral element method for elastic wave equations – application to 2-D and 3-D seismic problems”. *International Journal for Numerical Methods in Engineering* 45.9, pp. 1139–1164.

Krautkrämer, J. and Krautkrämer, H. (2013). *Ultrasonic testing of materials*. Springer Science & Business Media.

Kwun, H., Jolly, W., Light, G., and Wheeler, E. (1988). “Effects of variations in design parameters of ultrasonic transducers on performance characteristics”. *Ultrasonics* 26.2, pp. 65–72.

Landrø, M. (2015). “4D Seismic”. en. *Petroleum Geoscience: From Sedimentary Environments to Rock Physics*. Ed. by K. Bjørlykke. Berlin, Heidelberg, pp. 489–514.

Leroy, Y. M. (2011). “Introduction to the finite-element method for elastic and elasto-plastic solids”. *Mechanics of Crustal Rocks*. Springer, pp. 157–239.

Lissa, S., Ruf, M., Steeb, H., and Quintal, B. (2021). “Digital rock physics applied to squirt flow”. *GEOPHYSICS* 86.4, MR235–MR245.

Liu, X. L. and Li, Y. J. (2009). “Ultrasonic waveform analysis for rock mechanical properties”. *International Journal of Rock Mechanics and Mining Sciences* 46, pp. 637–646.

Lumley, D. (2010). “4D seismic monitoring of CO2 sequestration”. *The Leading Edge* 29.2, pp. 150–155.

Luo, Y., Li, H., Xu, B., and Xu, G. D. (2010). “Spectral finite element method modeling of ultrasonic guided waves propagation in layered viscoelastic film/substrate materials”. *Journal of Applied Physics* 108.12.

Ma, X. and Zoback, M. (2018). “Static and Dynamic Response of Bakken Cores to Cyclic Hydrostatic Loading”. *Rock Mechanics and Rock Engineering*.

Martin III, R. and Haupt, R. (1994). "Static and dynamic elastic moduli in granite: The effect of strain amplitude". *ARMA North America Rock Mechanics Symposium*, ARMA–1994–0473.

Mavko, G. M. (1979). "Frictional attenuation: An inherent amplitude dependence". *Journal of Geophysical Research: Solid Earth* 84.B9, pp. 4769–4775.

Mavko, G. M. and Nur, A. (1979). "Wave attenuation in partially saturated rocks". *Geophysics* 44.2, pp. 161–178.

Mohammadpour, A., Paluszny, A., and Zimmerman, R. (2025). "A robust 3D finite element framework for monolithically coupled thermo-hydro-mechanical analysis of fracture growth with frictional contact in porous media". *Computer Methods in Applied Mechanics and Engineering* 434, p. 117557.

Morlier, P. (1971). "Description de l'etat de fissuration d'une roche a partir d'essais non-destructifs simples". *Rock mechanics* 3, pp. 125–138.

Muskhelishvili, N. (1963). "Some basic problems of the mathematical theory of elasticity". *Noordhoff, Groningen* 17404.6.2, p. 1.

Nejati, M., Paluszny, A., and Zimmerman, R. W. (2016). "A finite element framework for modeling internal frictional contact in three-dimensional fractured media using unstructured tetrahedral meshes". *Computer Methods in Applied Mechanics and Engineering* 306, pp. 123–150.

Nguyen-Van, H., Mai-Duy, N., and Tran-Cong, T. (2008). "A smoothed four-node piezoelectric element for analysis of two-dimensional smart structures". *Computer Modeling in Engineering and Sciences* 23.3, pp. 209–222.

Nowick, A. S. (2012). *Anelastic relaxation in crystalline solids*. Vol. 1. Elsevier.

Nur, A. and Simmons, G. (1969). "Stress-induced velocity anisotropy in rock: an experimental study". *Journal of Geophysical Research* 74.27, pp. 6667–6674.

O'Connell, R. J. and Budiansky, B. (1978). "Measures of dissipation in viscoelastic media". *Geophysical Research Letters* 5.1, pp. 5–8.

Otsu, N. *et al.* (1975). "A threshold selection method from gray-level histograms". *Automatica* 11.285-296, pp. 23–27.

Paluszny, A., Salimzadeh, S., and Zimmerman, R. W. (2018). "Finite-element modeling of the growth and interaction of hydraulic fractures in poroelastic rock formations". *Hydraulic Fracture Modeling*. Elsevier, pp. 1–19.

Pan, M.-J., Green, D., and Hellmann, J. (1996). "Influence of interfacial microcracks on the elastic properties of composites". *Journal of materials science* 31, pp. 3179–3184.

Pimienta, L., Fortin, J., and Guéguen, Y. (2015). "Bulk modulus dispersion and attenuation in sandstones". *GEOPHYSICS* 80.2, pp. D111–D127.

Pimienta, L., Fortin, J., and Guéguen, Y. (2017). "New method for measuring compressibility and poroelasticity coefficients in porous and permeable rocks: compressibility coefficients in rocks". en. *Journal of Geophysical Research: Solid Earth* 122.4, pp. 2670–2689.

Pimienta, L., Schubnel, A., Violay, M., Fortin, J., Guéguen, Y., and Lyon-Caen, H. (2018). "Anomalous Vp/Vs ratios at seismic frequencies might evidence highly damaged rocks in subduction zones". *Geophysical Research Letters* 45.22, pp. 12–210.

Prager, W. (1955). "The Theory of Plasticity: A Survey of Recent Achievements". *Proceedings of the Institution of Mechanical Engineers* 169.1, pp. 41–57.

Prassianakis, I. and Prassianakis, N. (2004). "Ultrasonic testing of non-metallic materials: concrete and marble". *Theoretical and Applied Fracture Mechanics* 42.2, pp. 191–198.

Raphanel, J. L., Ravichandran, G., and Leroy, Y. M. (2004). "Three-dimensional rate-dependent crystal plasticity based on Runge–Kutta algorithms for update and consistent linearization". *International Journal of Solids and Structures* 41.22-23, pp. 5995–6021.

Rice, J. R. and Cleary, M. P. (1976). "Some basic stress diffusion solutions for fluid-saturated elastic porous media with compressible constituents". *Reviews of Geophysics* 14.2, pp. 227–241.

Rice, J. R. (1977). "Pore pressure effects in inelastic constitutive relations for fissured rock masses". *In Advances in Civil Engineering Through Engineering Mechanics (Proceedings of 2nd ASCE Engineering Mechanics Division Specialty Conference, Raleigh, N.C.*, pp. 295–297.

Roberts, S., Husmeier, D., Rezek, I., and Penny, W. (1998). "Bayesian approaches to Gaussian mixture modeling". *IEEE Transactions on Pattern Analysis and Machine Intelligence* 20.11, pp. 1133–1142.

Sarout, J. (2006). "Propriétés physiques et anisotropie des roches argileuses: Modélisation micromécanique et expériences triaxiales". PhD thesis. Paris 11.

Sarout, J. and Guéguen, Y. (2008). "Anisotropy of elastic wave velocities in deformed shales: Part 1—Experimental results". *Geophysics* 73.5, pp. D75–D89.

Senetakis, K., Coop, M. R., and Todisco, M. C. (2013). "The inter-particle coefficient of friction at the contacts of Leighton Buzzard sand quartz minerals". *Soils and Foundations* 53.5, pp. 746–755.

Seriani, G. and Oliveira, S. (2020). "Numerical modeling of mechanical wave propagation". *La Rivista del Nuovo Cimento* 43.9, pp. 459–514.

Shiyekar, S. and Kant, T. (2011). "Higher order shear deformation effects on analysis of laminates with piezoelectric fibre reinforced composite actuators". *Composite Structures* 93.12, pp. 3252–3261.

Simo, J. C. and Taylor, R. L. (1985). "Consistent tangent operators for rate-independent elastoplasticity". *Computer Methods in Applied Mechanics and Engineering* 48.1, pp. 101–118.

Solodov, I. Y. (1998). "Ultrasonics of non-linear contacts: propagation, reflection and NDE-applications". *Ultrasonics* 36.1-5, pp. 383–390.

Stewart, R. R., Toksoz, M. N., and Timur, A. (1983). "Strain dependent attenuation: observations and a proposed mechanism". *Journal of Geophysical Research: Solid Earth* 88.B1, pp. 546–554.

Sun, Y., Carcione, J. M., and Gurevich, B. (2020). "Squirt-flow seismic dispersion models: a comparison". *Geophysical Journal International* 222.3, pp. 2068–2082.

Tarokh, A. and Makhnenko, R. (2019). "Remarks on the solid and bulk responses of fluid-filled porous rock". *Geophysics*.

Tisato, N. and Madonna, C. (2012). "Attenuation at low seismic frequencies in partially saturated rocks: Measurements and description of a new apparatus". *Journal of Applied Geophysics* 86, pp. 44–53.

Tutuncu, A. N. and Sharma, M. M. (1992). "The influence of fluids on grain contact stiffness and frame moduli in sedimentary rocks". *Geophysics* 57.12, pp. 1571–1582.

Vasquez, G. F., Morschbacher, M. J., and Justen, J. C. R. (2019). "Experimental efforts to access 4D feasibility and interpretation issues of Brazilian presalt carbonate reservoirs". *Interpretation* 7.4, SH1–SH18.

Viesca, R. C., Templeton, E. L., and Rice, J. R. (2008). "Off-fault plasticity and earthquake rupture dynamics: 2. Effects of fluid saturation". *Journal of Geophysical Research: Solid Earth* 113.B9.

Walsh, J. B. (1965). "The effect of cracks on the uniaxial elastic compression of rocks". en. *Journal of Geophysical Research (1896-1977)* 70.2, pp. 399–411.

Wang, L., Rybacki, E., Bonnelye, A., Bohnhoff, M., and Dresen, G. (2021). "Experimental investigation on static and dynamic bulk moduli of dry and fluid-saturated porous sandstones". *Rock Mechanics and Rock Engineering* 54.1, pp. 129–148.

Yaghmaie, R. and Ghosh, S. (2018). "Computational modeling of finite deformation piezoelectric material behavior coupling transient electrical and mechanical fields". *Journal of Computational Physics* 373, pp. 148–170.

Yang, J. (2018). *An introduction to the theory of piezoelectricity*. second. Springer.

Yurikov, A., Nourifard, N., Pervukhina, M., and Lebedev, M. (2019). "Laboratory ultrasonic measurements: shear transducers for compressional waves". *The Leading Edge* 38.5, pp. 392–399.

Zhang, J., Zhang, B., and Fan, J. (2003). "A coupled electromechanical analysis of a piezoelectric layer bonded to an elastic substrate: Part I, development of governing equations". *International Journal of Solids and Structures* 40.24, pp. 6781–6797.

Zhou, C., Xie, H., Zhu, J., Wang, Z., Li, C., and Wang, F. (2022). "Mechanical and fracture behaviors of brittle material with a circular inclusion: insight from infilling composition". *Rock Mechanics and Rock Engineering* 55.6, pp. 3331–3352.

Zhou, W., Li, H., and Yuan, F.-G. (2015). "Fundamental understanding of wave generation and reception using d36 type piezoelectric transducers". *Ultrasonics* 57, pp. 135–143.

Zimmerman, R. W., Somerton, W. H., and King, M. S. (1986). "Compressibility of porous rocks". *Journal of Geophysical Research: Solid Earth* 91.B12, pp. 12765–12777.

Zimmerman, R. W. (1990). *Compressibility of sandstones*. Elsevier.

Zimmerman, R. (2000). "Coupling in poroelasticity and thermoelasticity". *International Journal of Rock Mechanics and Mining Sciences* 37, pp. 79–87.

Appendix A

Experimental Study of Hysteresis in Hydrostatic Tests

A.1 Introduction

This section discusses rock behaviour at the microscale, where the presence of cracks plays an important role. The main reason is that pores are very stiff compared to cracks; hence, the rock material response is often controlled by the opening, closing, and friction along cracks. First, the results of the laboratory experiments on sandstone, showing energy dissipation within the rock's elastic range under a hydrostatic pressure, in both dry and saturated conditions, are presented. The raw data were collected by Dr. Lucas Pimienta of the Université Fédérale de Lausanne (Switzerland), at the Ecole Normale Supérieure (ENS), Paris, and in the context of my PhD, I was personally in charge of the data treatment (filtering, visualisation, machine learning) and interpretation. This analysis is followed by some relevant theories on the mechanics of microcracked porous materials to support the discussion of the experimental results, based on the assumption that cracks cause the dissipation of energy that is observed experimentally.

Rocks behave as elastic materials, meaning that they are able to store and dispense elastic energy up to a maximum amount. Beyond a certain energy threshold, they exhibit inelastic behaviour by dissipating energy. However, it has been evidenced that rock samples dissipate energy even within their presumed elastic range. One way to examine the amount of energy dissipated is to analyse the stress-strain curve, which is linear in the case of pure elasticity. The stress-strain curve is obtained by performing loading-unloading cycles on the rock sample. Energy dissipation in uniaxial experiments has been thoroughly studied recently under dry conditions for non-linear elasticity (David *et al.*, 2012), and fluid-saturated conditions for frequency effects (Borgomano *et al.*, 2017).

In this section, experiments were done by following a new protocol (Pimienta *et al.*, 2017) to analyse the effects of small cyclic variations of hydrostatic stress on the measured elastic properties of rocks.

A.2 Experimental setup and methods

A.2.1 Data acquisition and processing

The laboratory experiments involved a clean 13% porosity Fontainebleau sandstone (99.9% quartz), quite isotropic and permeable, and with a dry bulk modulus of 4 GPa. A battery of tests was executed using the same protocol and machinery as presented by Pimienta *et al.* (2015). The tests were conducted on a dry and water-saturated sample, whose pore pressure was controlled externally by pumps.

The dry sample was submitted to a series of slow hydrostatic loading cycles. At selected confining pressures, the load was oscillated between various amplitudes. The same tests were done on the saturated sample, with the exception that the pore-fluid pressure could be controlled. For the saturated experiments, a doublet of dead volumes ($V_D = 6.6$ mL total, nearly half of the sample's pore volume) remained connected to the sample, even after closing the valves. For this reason, the saturated sample was not in a purely undrained regime, since the compressibility of the fluid outside the specimen was also at play. Depending on the experiment, the fluid mass was kept constant (using dead volumes), the confining pressure was kept constant, and the oscillations happened at the fluid level. However, the raw data was not directly exploitable because of the nature of the experiment, which deals with micro deformations sensitive to the ambient temperature and surrounding vibrations. To reduce any potential bias in strain measurements, we took the average strain of all the strain gauges into account. Our focus in this study was on the volumetric strain, denoted as ϵ_v. This was calculated by adding the average axial strain and twice the average radial strain ($\epsilon_v = \epsilon_{ax} + 2\epsilon_{rad}$). Additionally, we examined the bulk modulus, denoted as K, which is obtained by taking the average slope of the stress-strain curve. Specifically, we calculate K as $\Delta P_c / \Delta \epsilon_v$. Keeping the oscillations' amplitude constant was sometimes challenging, resulting in a drift of the mean confining pressure. To solve this problem, we systematically filtered the strain and stress data in the Fourier domain by removing the frequencies lower than the peak amplitude. This is schematised in Fig.A.1, representing the stress-strain loops before and after processing.

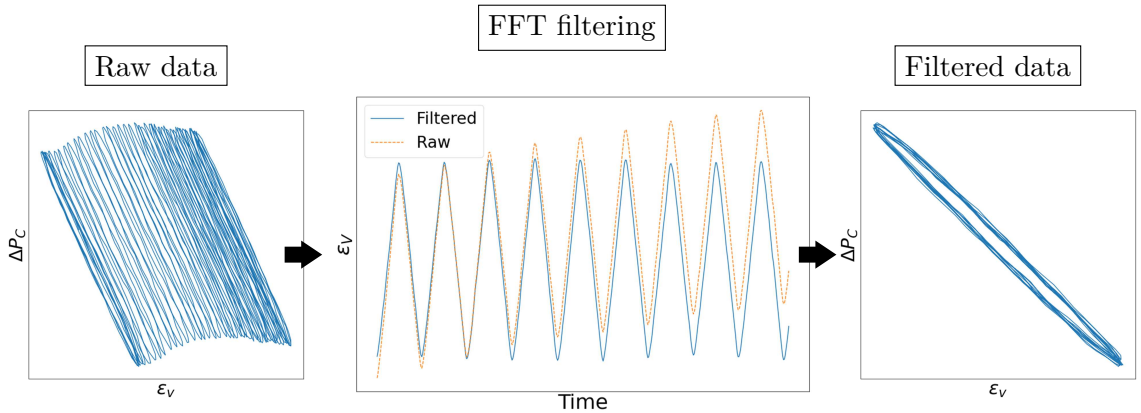


Figure (A.1) FFT processing of raw data to remove drifting effect for stress and strain. In the Fourier domain, the frequencies were lower than the peak amplitude in the strain and stress data. This process removed the drifting effect observed in the raw data.

Estimation of the attenuation factor Q^{-1}

The goal of these experiments was to reveal the hysteresis in the stress-strain relation of a rock under hydrostatic stress. The hysteresis was a proxy for the energy dissipated by the sample, and is conventionally represented by the attenuation factor, Q^{-1}. This attenuation factor was calculated using two methods: the Fast Fourier Transform method (FFT), which evaluates the phase shift between stress and deformation, and the ellipse method, which relates the area of the hysteresis loop to the average energy stored in the sample (O'Connell *et al.*, 1978).

In the FFT method, we picked the phase of the stress and strain signals in the Fourier domain before calculating the difference $\Delta\phi$ between the two phases. The phase shift, if any, would correspond to a delay in the strain response of the rock, characteristic of energy dissipation. The attenuation factor was given by

$$Q^{-1} = \tan(\Delta\phi)\,. \tag{A.1}$$

The ellipse method stems from the direct definition of the attenuation factor, which is the ratio of the dissipated energy ΔE and the average energy V stored by the rock:

$$Q^{-1} = \frac{\Delta E}{4\pi V}\,. \tag{A.2}$$

In practical terms, ΔE is the area of the stress-strain loop, and V is the area between the loop and the oscillation axis $\Delta P_c = 0$ MPa. See Fig. A.2, in which both areas were computed incrementally, following Tisato *et al.* (2012).

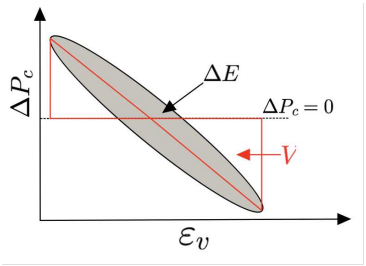


Figure (A.2) Schematic representation of the dissipated energy ΔE (area of the stress-strain loop) and the average stored energy V (area delimited in red), used to calculate Q^{-1} via the ellipse method.

Bayesian Gaussian Mixture (BGM) model

To estimate the various slopes of the stress-strain curve in a single cycle, a machine learning method that automatically clusters data points by linear affinity was employed. The Bayesian Gaussian Mixture (BGM) model used a multi-Gaussian distribution number k, which represents the number of clusters in the data. The parameter k was set to four, since four obvious clusters were usually observed. The BGM method uses a system of prior and conjugate prior precisions to distinguish the various clusters. Firstly, it assumes that a random subset of the data follows a single Gaussian distribution, parametrised by mean and precision, with a precision of 1. In this first assumption, the mean is unknown, and a conjugate prior, a second assumption based

on an additional Gaussian distribution, is needed. In the second assumption, the mean is set to 0 and the precision to 1. Once a conjugate prior has been set, a new precision for the subset is calculated with no assumption and the result of a posterior distribution is obtained. This operation is repeated over the rest of the data, as explained by (Roberts *et al.*, 1998). In the end, the data are clustered in thin ellipsoids according to the density of strain and stress components of each point. Then, a linear regression on each cluster provides a slope corresponding to the bulk modulus.

A.3 Experimental results

In this section, the results from the hydrostatic loading of the dry sample are presented first, with an analysis of the influence of small variations of the confining pressure on the dissipation of energy in dry conditions. Then, the same analysis of the data from the hydrostatic loading of the saturated sample under semi-drained conditions is performed; the fluid can be drained to a dead volume but can be locally undrained depending on the stress amplitude. Finally, the results of the BGM clustering method, which allows the identification of slope variations within the stress-strain curves, are showcased.

A.3.1 Hydrostatic loading of dry sample

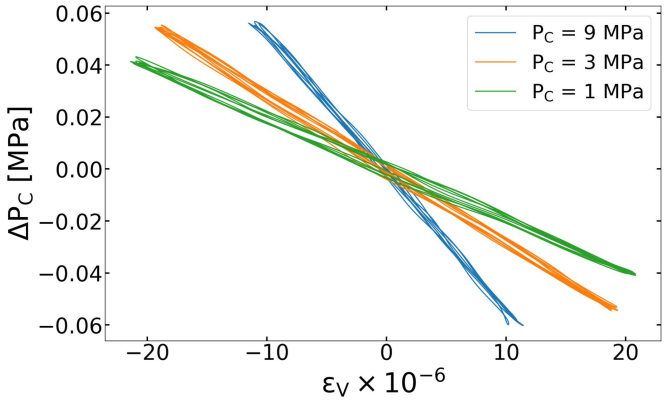
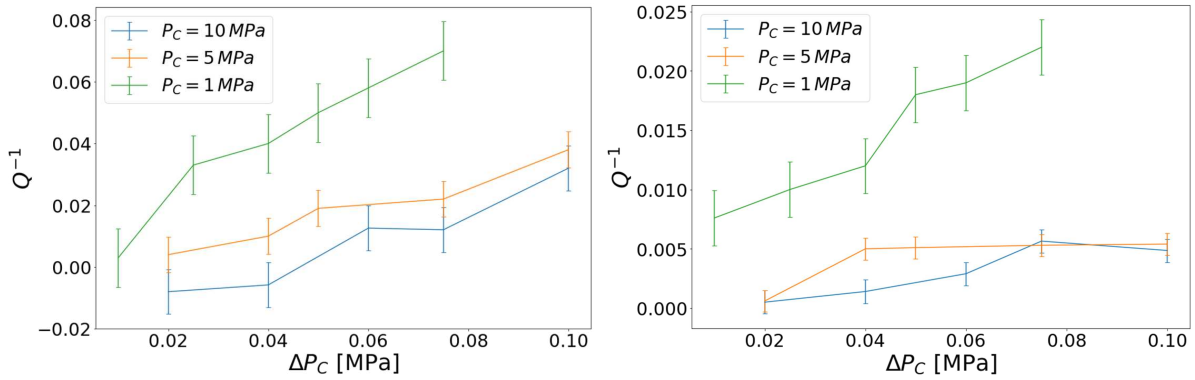


Figure (A.3) Stress-strain curve when oscillating the confining pressure by $\Delta P_c \sim 0.052$ MPa, at $P_c = 1, 3, 9$ MPa during hydrostatic loading of dry sample. There is an apparent hysteresis at $P_c = 1$ and 3 MPa.

To study the impact of a slight change in the hydrostatic confining pressure (P_c) on the stress-strain relationship of the dry sample, the hydrostatic load was varied at different values of P_c (1, 3, and 9 MPa) while maintaining the same amplitude ($\Delta P_c = 0.052$ MPa). As shown in Fig. A.3, $P_c = 9$ MPa, the stress-strain curve is linear over a repeated loading-unloading cycle, meaning the deformation is purely elastic, and no energy dissipation occurs. At lower confining pressures ($P_c = 1$ and 3 MPa), the stress-strain curve resembles a loop, the loop area being slightly bigger at $P_c = 1$ MPa compared to 3 MPa. In other words, for an oscillation amplitude $\Delta P_c = 0.052$ MPa, there appears to be energy dissipation if the confining pressure is less than 3 MPa.

Different oscillation amplitudes were applied to investigate the impact of varying amplitudes of



(a) (b)

Figure (A.4) The attenuation factor Q^{-1}, calculated via the FFT method **(a)**, and ellipse method **(b)** as a function of the oscillation amplitude ΔP_c, at hydrostatic confining pressures $P_c = 1, 5$ and 10 MPa, in the dry experiment.

ΔP_c. The results in Fig. A.5 indicate that at a confining pressure of 1 MPa, a narrow hysteresis loop can be detected for oscillations of 0.01 MPa (Fig. A.5a). Still, this loop falls within the margin of error of the method. The same applies to the curves corresponding to $\Delta P_c = 5$ and 10 MPa, where the process reaches its limits, and interpretations become uncertain. However, for $\Delta P_c = 0.1$ MPa (Fig. A.5c), the hysteresis loops at $P_c = 1$ and 5 MPa are well-defined. It can be observed that there is no hysteresis at $P_c = 10$ MPa.

The average slopes of the curves, which correspond to the measured bulk moduli, vary with the confining pressure. As can be expected, the rock is more compressible at lower confining pressures compared to high pressures, because more cracks areclosed at higher pressures. This is why the slopes of the green curves are less steep than those of the orange one, which is, in turn, shallower than those of the blue one. To conclude, under dry conditions, there is a dissipation of energy at lower confining pressures and larger oscillation amplitudes. The amount of energy that is dissipated was quantified and associated with the Q^{-1} factor. For example, using the FFT method, we observed that at a given confining pressure, Q^{-1} indeed increased with ΔP_c (Fig. A.4.a). At $P_c = 1$ MPa, Q^{-1} significantly increased when the oscillation amplitude was increased to 0.025 MPa, from 0.01 MPa (150% increase). Then Q^{-1} increased steadily to reach its maximum value, 0.07, at ΔP_c =0.075 MPa. At a higher confining pressure P_c =5 MPa, the Q^{-1} factor was about one-third of that calculated at $P_c = 1$ MPa for similar values of ΔP_c. Nevertheless, the trend remained the same as Q^{-1} kept increasing with ΔP_c. It is the smallest at a confining pressure of 10 MPa and exudes the same trend. In addition, these trends are also backed by the Q^{-1} values obtained using the ellipse method (Fig. A.4.b). The ellipse method, which is highly sensitive to the quality of the data filtering, seemed to be less accurate than the FFT method for those minimal Q^{-1} values. Nonetheless, the two methods converge at higher Q^{-1} values, as shown further down in the saturated experiments.

With regards to the evolution of the bulk modulus as a function of ΔP_c, we can observe, in Fig A.6.a, that under dry conditions, the measured bulk decreases at larger ΔP_c for a hydrostatic confining pressure of 1 MPa; from $K = 2.22$ GPa at $\Delta P_c = 0.01$ MPa, it falls to $K = 2.18$ GPa

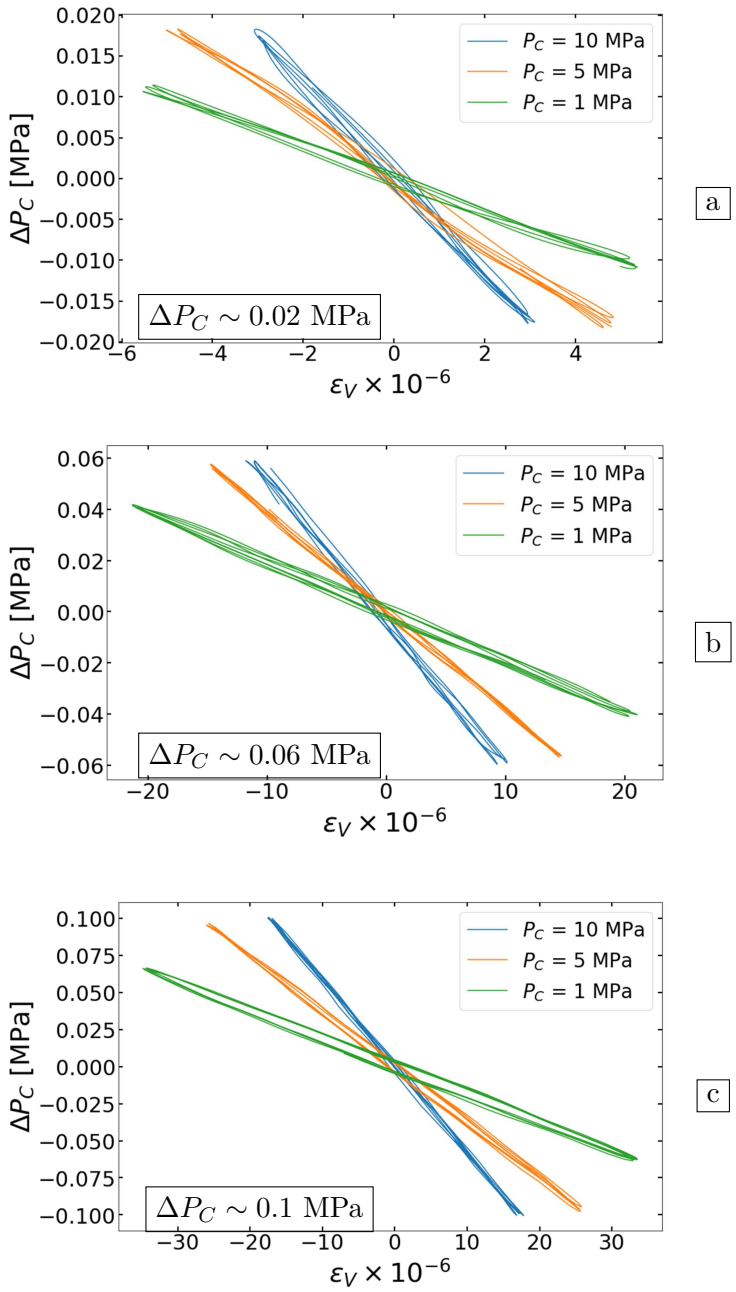
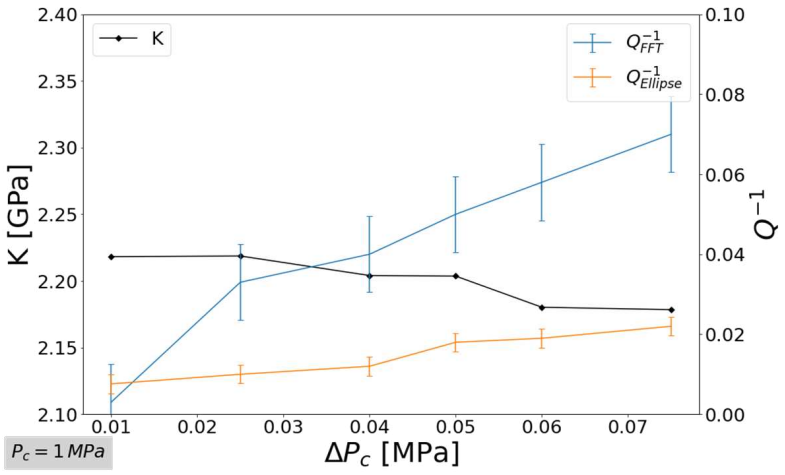
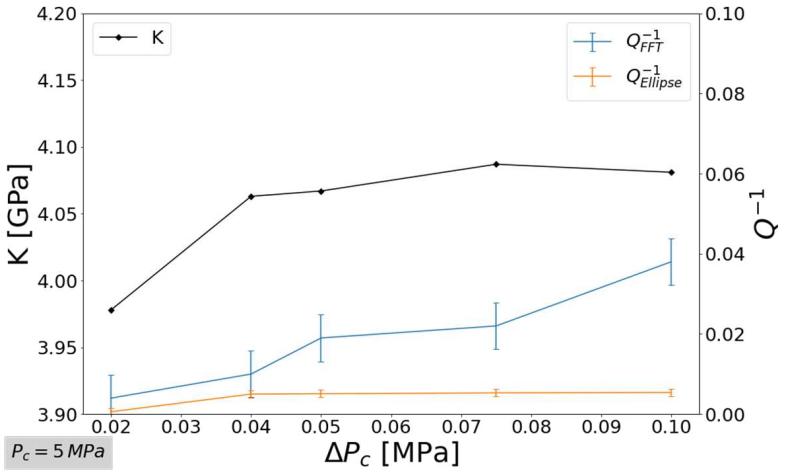


Figure (A.5) Stress-strain loops/curves at different oscillation amplitudes of confining pressure ΔP_c MPa, over hydrostatic pressures $P_c = 1, 5, 10$ MPa on the dry sample. **(a)** At $\Delta P_c \sim 0.02$ MPa, there is almost no hysteresis for any confining pressure, supported by the Q^{-1} values presented in A.4. **(b)** At $\Delta P_c \sim 0.02$ MPa, there is a visible hysteresis at $P_c = 1$ MPa, but no visible one a $P_c = 5$ and 10 MPa. **(b)** At $\Delta P_c \sim 0.1$ MPa, there are definite hysteresis loops at $P_c = 1$ and 5 MPa, with the loop area at $P_c = 1$ MPa larger than the one at 5 MPa, still there is no visible hysteresis at $P_c = 10$ MPa.

at $\Delta P_c = 0.075$ GPa. This corresponds to a 1.8% decrease of the bulk modulus, and concurs with the observed small but increasing attenuation factor. At larger confining pressures, $P_c = 5$ MPa, the variations of K are even smaller. The bulk modulus K tends to oscillate over 4.06 MPa, with no clear trends. That is to say that the energy dissipated at $P_c = 5$ MPa for various ΔP_c, under dry conditions, is too small to have any tangible repercussion on the measured bulk modulus.



(a)



(b)

Figure (A.6) Bulk modulus (black curve) as a function of the amplitude of the oscillations of the confining pressure, and the corresponding Q^{-1} (calculated via the FFT in blue and Ellipse method in orange), on the dry sample for: **(a)**– a confining pressure $P_c = 1$ MPa, **(b)**– a confining pressure $P_c = 5$ MPa. At $P_c = 1$ MPa, the K value slightly decreases at higher amplitudes of ΔP_c At $P_c = 5$ MPa, there is a small jump in K for an increase of ΔP_c from 0.02 to 0.04 MPa, and then K remains relatively unchanged.

A.3.2 Hydrostatic loading of water-saturated sample

The data from the hydrostatic cycles on the water-saturated sample show a stress-strain hysteresis loop for an effective pressure P_{eff} as large as 5 MPa, at oscillation amplitudes as small as 0.1 MPa (Fig.A.7). In these cycles, the quantity of fluid was fixed, and two closed dead volumes were used to allow for some drainage. Once the dead volume was full, variations of pore-fluid pressure were observed as a response to the oscillating confining pressure.

The values of the attenuation factor on the bulk modulus Q_K^{-1} are displayed in Fig. A.8 at $P_{eff} = 1$ and 5 MPa, at various oscillation amplitudes. At both effective pressures, the average bulk modulus decreased with higher oscillation amplitudes. At the same time, the attenuation factor between the bulk modulus measured during loading, and the one measured in the unloading phase, tended to decrease at higher oscillation amplitudes. The dependence of

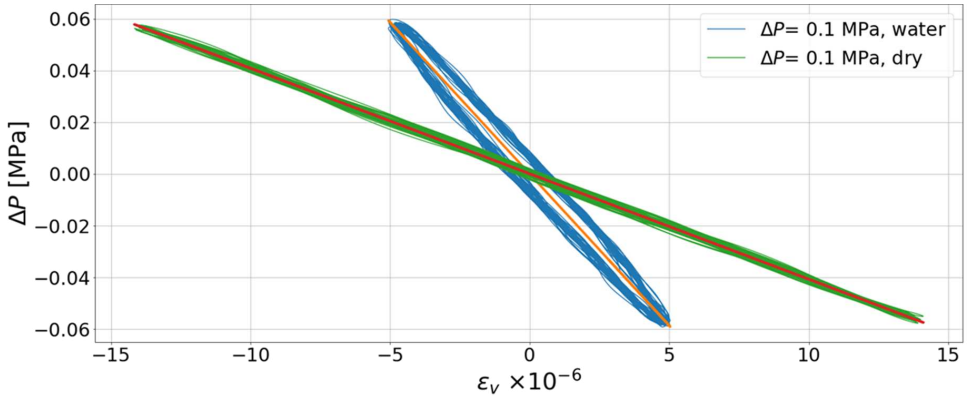
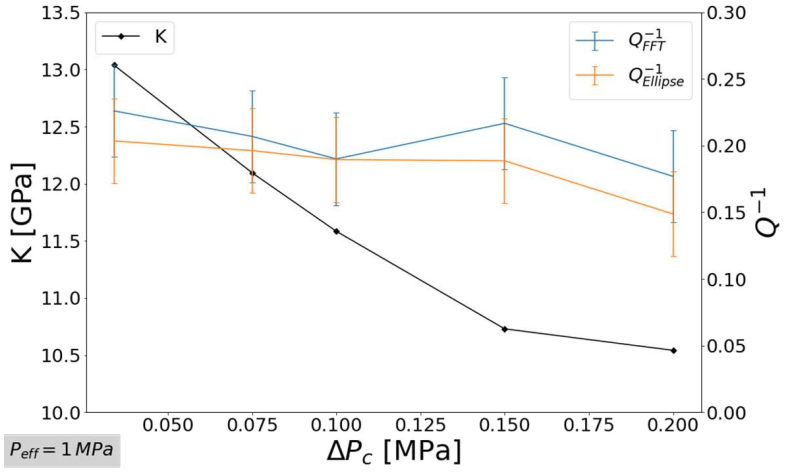
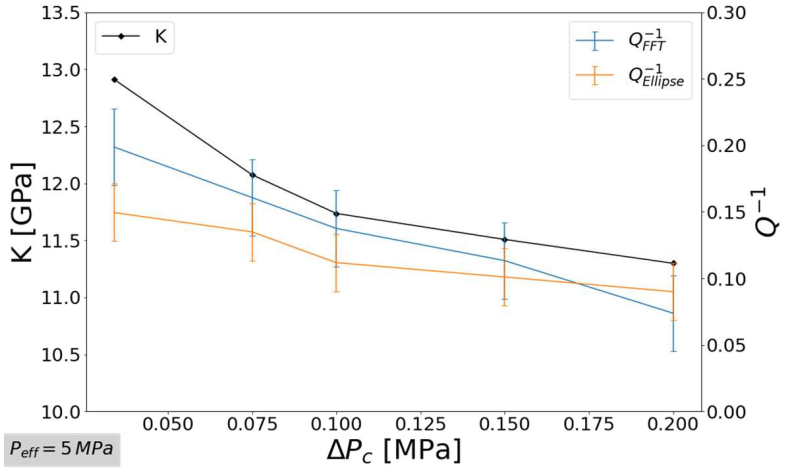


Figure (A.7) Stress-strain loops at $P_{eff} = 5$ MPa (confining pressure of 7 MPa and pore pressure of 2 MPa), and $\Delta P_c = 0.1$ MPa for the dry (green) and water-saturated sample (blue). There is no hysteresis in the dry case, and the measured bulk modulus is smaller than in the saturated case.



(a)



(b)

Figure (A.8) Bulk modulus (black curve) as a function of the amplitude of the oscillations of the confining pressure, and the corresponding Q^{-1} (calculated via the FFT in blue and Ellipse method in orange), on the saturated sample for **(a)**– an effective pressure $P_{eff} = 1$ MPa, **(b)**– an effective pressure $P_{eff} = 5$ MPa. At $P_{eff} = 1$ MPa, ΔP_c has a much greater effect on the K measurements than at $P_{eff} = 5$ MPa The K value decreases at higher amplitudes of ΔP_c.

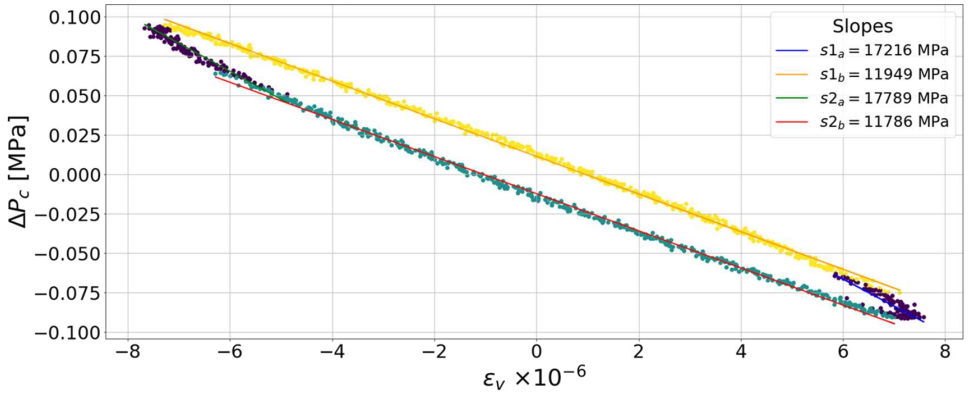


Figure (A.9) Stress-strain loop and K values (slopes) at different stages of hydrostatic loading cycles on the saturated sample, at $P_{eff} = 1$ MPa and $\Delta P_c = 0.1$ MPa. Four clusters (two in the loading and two in the unloading phase) of data following a linear trend were identified through a spectral clustering of the data points. A linear regression on the data of each cluster provided four slopes: s1a, s1b, s2a, and s2b. At the start of the loading phase, the bulk is $s1a = 17.2$ GPa, which decreases to $s1b = 11.9$ GPa further in the loading. At the beginning of the unloading phase, the bulk is $s2a = 17.8$ GPa, which decreases to $s2b = 11.9$ GPa further during the unloading.

the bulk modulus to ΔP_c is thus two-fold; first, higher ΔP_c values lead to lower bulk estimates (the converse also holds); second, there is less dissipation at higher ΔP_c values for a given P_{eff}.

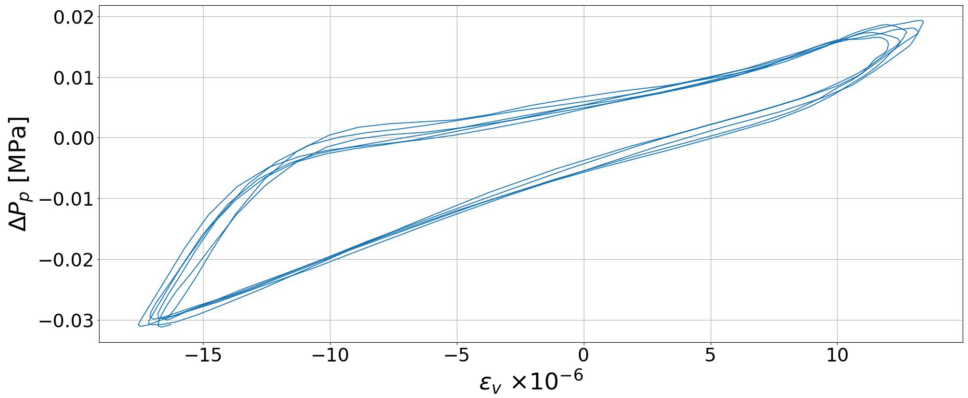


Figure (A.10) Stress-strain loop of the hydrostatic loading of the saturated sample in a semi-undrained regime, for an oscillating pore pressure $\Delta P_p = 0.025$ MPa, at $P_{eff} = 5$ MPa ($P_c = 7$ MPa and $P_p = 2$ MPa).

This amplitude effect was noticeably more significant in the saturated experiment compared to the dry one, in which ΔP_c had only a marginal impact at P_{eff}=1 MPa (Fig. A.6 and A.8). In the saturated experiment, a 75% increase of ΔP_c (from 0.05 to 0.2 MPa) resulted in a 19% decrease of the K measured (from 13 GPa to 10.5 GPa at P_{eff} =1 MPa, and from 12.9 GPa to 11.3 GPa at $P_{eff} = 5$ MPa).

In addition to the K estimates obtained from a linear regression on the data, evaluating K at different stages told a more complex story of the energy dissipation within the rock. In a loading cycle, four data clusters following the same linear trend were generally identified (Fig. A.9). The slopes of these linear trends represent different K values; two slopes ($s1_a = 17.2$

GPa and $s1_b = 11.9$ GPa) were identified in the loading phase, and two others ($s2_a = 17.8$ GPa and $s2_b = 11.8$ GPa). The slopes $s1_b$ and $s2_b$ were almost identical, whereas $s1_a$ and $s2_a$ were always a little more distinct. In fact, the main difference between the loading and unloading stages seemed to materialise at the beginning of each phase; at the commencement of the loading, the sample was stiffer, as more stress was required to deform it, while at the beginning of the unloading, the sample appeared to be slightly more elastic since it recovered its shape more easily. This means that the mechanism responsible for the hysteresis is activated at the beginning of each phase and answers differently to elastic compression (loading) than tension (unloading). This means that the mechanism associated with the hysteresis acts differently depending on the type of stress, whether a confining or a pore-fluid over-pressure.

The difference between the hysteresis loops of the dry and saturated experiments poses questions about the role of the fluid. The pore fluid pressure was oscillated at an amplitude ΔP_p while the confining stress was kept constant to investigate the fluid's impact further. The resulting stress-strain loop had a very different allure than the previous experiment. For instance, Fig. A.10 shows the stress-strain loop for $\Delta P_p = 0.025$ MPa, at $P_{eff} = 5$ MPa; four stages were also distinguished, but there was no semblance of symmetry between the loading (increasing P_P) and unloading (decreasing P_P). At the beginning of each phase, we also noted the difference in slopes (bulk moduli), yet in this case, the significant difference in bulk modulus was observed later in the phase.

Appendix B

Microcrack Mechanics

B.1 Elasticity solution

The elasticity solution is fundamental to this contribution, and the porous, homogeneous material composing the shell is linearly elastic, isotropic with equivalent properties $(\kappa^*, G^*, \alpha^*)$. The initial state corresponds to a pressure set to p_{f0}, isotropic stress equal to $-p_{f0}$, and is associated with zero deformation and displacement.

The solution is found with the displacement method. The displacement is radial, and thus of the type $\underline{u}(r) = u(r)\underline{e}_r$ with the scalar function $u(r)$ of the radial position with respect to the centre of the pore as the only unknown. The only non-zero linearized strain components are:

$$\epsilon_r = u_{,r}\,, \quad \epsilon_\theta = \epsilon_\varphi = \frac{u}{r}\,, \tag{B.1}$$

with a comma stranding for the partial derivative for the variable that follows. The volumetric strain is the sum of these three components: $\epsilon_v = u_{,r} + 2\frac{u}{r}$. The poroelasticity constitutive relations for an isotropic medium are now applied, and the stress field in terms of the displacement function or its gradient and the fluid pressure reads:

$$\begin{aligned} \sigma_r + p_{f0} &= (\kappa^* - \frac{2G^*}{3})\epsilon_v + 2G^* u_{,r} - \alpha^*(p_f - p_{f0})\,, \\ \sigma_\theta + p_{f0} = \sigma_\varphi + p_{f0} &= (\kappa^* - \frac{2G^*}{3})\epsilon_v + 2G^* \frac{u}{r} - \alpha^*(p_f - p_{f0})\,. \end{aligned} \tag{B.2}$$

This stress field satisfies point-wise mechanical equilibrium, which, because of the problem symmetry, is expressed by the single equation:

$$\sigma_{r,r} + \frac{1}{r}(2\sigma_r - \sigma_\theta - \sigma_\varphi) = 0\,. \tag{B.3}$$

Insert now the expressions in (B.2) in this equilibrium equation to obtain a second-order differential equation for the unknown function $u(r)$. The solution is found by integration, and reads:

$$u(r) = Ar + \frac{B}{r^2}\,, \tag{B.4}$$

for two constants A and B. The stress components in terms of these constants read:

$$\sigma_r + p_{f0} = 3\kappa^* A - 4G^* \frac{B}{r^3} - \alpha^*(p_f - p_{f0})\,, \quad \sigma_\theta + p_{f0} = \sigma_\varphi + p_{f0} = 3\kappa^* A + 2G^* \frac{B}{r^3} - \alpha^*(p_f - p_{f0})\,. \tag{B.5}$$

The constants are found by requiring that the remote stress is the hydrostatic pressure σ_H (positive in compression) while the radial stress at the pore surface is minus the fluid pressure p_f:

$$A3\kappa* = -(p_f - p_{f0})(1-\alpha^*) - \frac{(\sigma_H - p_f)}{1-\phi}\,, \quad B = -\frac{(\sigma_H - p_f)}{4G^*}\frac{R_P^3}{1-\phi}\,. \tag{B.6}$$

The stress fields finally read:

$$\sigma_r = -p_f - \frac{(\sigma_H - p_f)}{1-\phi}\left(1 - (\frac{R_P}{r})^3\right)\,, \quad \sigma_\theta = \sigma_\varphi = -p_f - \frac{(\sigma_H - p_f)}{1-\phi}\left(1 + \frac{1}{2}(\frac{R_P}{r})^3\right)\,. \tag{B.7}$$

. The effective properties of the spherical assemblage defined in (2.24) are in terms of the assemblage volumetric strain, θ, which is equal to $3u_r(R_S)/R_S$ for small deformations. This volume change for the assemblage is found by combining (B.4) and (B.6):

$$\theta = -(1-\alpha^*)\frac{p_f - p_{f0}}{\kappa^*} - \frac{(\sigma_H - p_f)}{1-\phi}\frac{4G^* + 3\kappa^*\phi}{4G^*\kappa^*} \quad . \tag{B.8}$$

This relation between volume change and pressure and remote stress σ_H provides the effective medium properties as defined in eq. (2.24) and presented in (2.26).

B.2 Effective properties of an elastic medium with isotropic circular cracks

The stress-strain relation eq. (2.1) with the introduction of the crack compliance tensor in eq. (2.2) reads:

$$\underline{\underline{\dot{\epsilon}}} = \mathbb{C} : (\underline{\underline{\dot{\sigma}}} + \alpha\dot{p}_f\underline{\underline{\delta}}) + \frac{c\gamma\pi}{2l}\Big\{\underline{\underline{N}}\cdot(\underline{\underline{\dot{\sigma}}} + \dot{p}_f\underline{\underline{\delta}}) + (\underline{\underline{\dot{\sigma}}} + \dot{p}_f\underline{\underline{\delta}})\cdot\underline{\underline{N}} - \nu\mathbb{N} : (\underline{\underline{\dot{\sigma}}} + \dot{p}_f\underline{\underline{\delta}})\Big\} \quad , \tag{B.9}$$

$$\text{with} \quad \underline{\underline{N}} = \int_{\mathcal{H}} \underline{n}\otimes\underline{n}\, d\mathcal{H} \quad \text{and} \quad \mathbb{N} = \int_{\mathcal{H}} \underline{n}\otimes\underline{n}\otimes\underline{n}\otimes\underline{n}\, d\mathcal{H}\,,$$

the normal $\underline{n}$ being defined by:

$$\underline{n} = \cos\beta\underline{e}_r + \sin\beta(\sin\beta'\underline{e}_\varphi + \cos\beta'\underline{e}_\theta)\,, \tag{B.10}$$

in terms of the polar angles (β, β'). In eq. (B.9), Biot's effective stress is introduced for the matrix response, whereas the Terzaghi effective stress is proposed for the crack response. The second-order $\underline{\underline{N}}$ is isotropic so proportional to the identity tensor $\underline{\underline{\delta}}$ with a proportionality factor

of $2\pi/3$ found as follows:

$$\begin{aligned}\underline{\underline{N}}\cdot\underline{e}_r &= \int_{\mathcal{H}}\underline{n}\cos\beta\, d\mathcal{H}\\ &= \int_{\beta=0}^{\pi/2}\int_{\beta'=0}^{2\pi}\Big[\cos^2\beta\underline{e}_r+\sin\beta\cos\beta(\cos\beta'\underline{e}_\theta+\sin\beta'\underline{e}_\varphi)\Big]\sin\beta d\beta' d\beta\\ &= \frac{2\pi}{3}\underline{e}_r\,.\end{aligned}\tag{B.11}$$

The fourth-order tensor $\mathbb{N}$ is also isotropic and has thus the following spectral decomposition:

$$\mathbb{N}=3k\mathbb{J}+2g\mathbb{K}\,,\tag{B.12}$$

in which k and g are two unknowns and the orthogonal tensors $\mathbb{J}$ and $\mathbb{K}$ defined by $\mathbb{J}=1/3\underline{\underline{\delta}}\otimes\underline{\underline{\delta}}$ and $\mathbb{K}=\mathbb{I}_s-\mathbb{J}$ with $\mathbb{I}_s$ standing for the symmetric, fourth-order identity tensor. The first constant k introduced in (B.12) is found by using the orthogonality property $\mathbb{N}:\mathbb{J}=3k\mathbb{J}$ which, using the definition in (B.9b):

$$\mathbb{N}:\mathbb{J}=\frac{1}{3}\int_{\mathcal{H}}\underline{n}\otimes\underline{n}\,\underline{n}\cdot\underline{n}\,d\mathcal{H}\otimes\underline{\underline{\delta}}=\frac{2\pi}{9}\underline{\underline{\delta}}\otimes\underline{\underline{\delta}}=\frac{2\pi}{3}\mathbb{J}\Rightarrow 3k=\frac{2\pi}{3}\,.\tag{B.13}$$

The second constant g in eq. (B.12) is found by considering another symmetry property of $\mathbb{N}$, which is that all indices of its components in a Cartesian coordinate system can be permuted. The components of the isotropic tensor $\mathbb{N}$ must have equal weight, such as in the expression

$$\delta_{ij}\delta_{kl}+\delta_{ik}\delta_{jl}+\delta_{il}\delta_{jk}\tag{B.14}$$

, which are the components of the tensor:

$$5\mathbb{J}+2\mathbb{K}\,.\tag{B.15}$$

The ratio 5/2 between the scalars multiplying the two orthogonal tensors above is respected in (B.12) if $g=3k/5$ provides the value of the second unknown scalar $2g=4\pi/15$. The expressions for the tensor $\underline{\underline{N}}$ and $\mathbb{N}$ are now inserted back into eq. (B.9) to obtain the effective moduli κ^* and G^* and the effective Biot's coefficient α^*:

$$\dot{\underline{\underline{\epsilon}}}=\Big[\frac{1}{3\kappa^*}\mathbb{J}+\frac{1}{2G^*}\mathbb{K}\Big]:(\dot{\underline{\underline{\sigma}}}+\alpha^*\dot{p}_f\underline{\underline{\delta}})\tag{B.16}$$

$$\text{with}\quad \frac{1}{3\kappa^*}=\frac{1}{3\kappa}+\frac{c\pi^2\gamma}{3l}(2-\nu)\quad,\quad \frac{1}{2G^*}=\frac{1}{2G}+\frac{2c\pi^2\gamma}{3l}(1-\frac{\nu}{5})\,,$$

$$\text{and}\quad \alpha^*=1-(1-\alpha)\frac{\kappa^*}{\kappa}\,.$$

B.3 Finite-element solution

The starting point of the finite-element method is the theorem of virtual work, which equates internal and external virtual works and reads as follows in 3D:

$$\int_\Omega \underline{\underline{\sigma}}_{n+1} : \underline{\underline{\tilde{\epsilon}}}\, dV = \int_{\partial\Omega^T} \underline{T}^d_{n+1} \cdot \underline{\tilde{u}} dS \tag{B.17}$$

in which Ω and $\partial\Omega^T$ are the assemblage domain and the part of its boundary where forces are prescribed. A superposed tilde in eq. (B.17) denotes the virtual strain and displacement. Time has been discretised, and the theorem is written at the end of the increment $n+1$. The three objectives are to reduce this equation to the 1D setting appropriate for our spherically symmetric problem, introduce the finite-element discretization, and discuss the time discretisation.

The domain is limited to the extent of the matrix since the fluid is always in equilibrium within the pore. It is discretised in the radial direction with a series of finite elements. Spectral elements have been selected because of the interesting property that nodal points and the Lobatto quadrature points coincide. Each nodal point represents the shell's REV, which is an effective medium made of the matrix + cracks. The shape function $N_a(r)$ of any node a has the properties that $N_a(r_b) = \delta_{ab}$ at any node positioned at r_b. The radial displacement over any element is interpolated by the sum $u(r) = \sum_a^N N_a(r)$, the total number of nodes per element being N. The strain components computed within each element are the radial and twice the hoop strain. They comprise the column vector $\{\epsilon\}$. This vector is obtained by the operation:

$$\{\epsilon\} = [B]\{u\}\,, \quad \text{with} \quad [B] = \left[\ldots \left| \begin{matrix} N_{a,r}(r_b) \\ \frac{2}{r_b}\delta_{ab} \end{matrix} \right| \ldots \right]\,, \tag{B.18}$$

in which $[B]$ is the classical B-operator (illustrated above at node b for a varying between 1 and N) and $\{u\}$ is the column vector containing the N nodal radial displacements of the element. Note that the virtual displacement and strain introduced in (B.17) have similar interpolations.

The stress at time t_{n+1} introduced in eq. (B.17) is found from the update algorithm discussed in Appendix B.4 for open cracks and in Appendix B.5 for the sliding cracks. These updates correspond to a generic relation of the type:

$$\{\sigma\}_{n+1} = \{\sigma\}_n + [\mathfrak{C}^{ec}]^{-1}\{\Delta\epsilon\} - \alpha\Delta p_f\{1\}\,, \tag{B.19}$$

in which the stress vector increment $\{\Delta\sigma\}$ and the unit vector $\{1\}$ have for components $\Delta\sigma_r, \Delta\sigma_\theta$ and $1, 1$, respectively. This equation is non-linear since the crack compliances, corresponding to the matrix $[\mathfrak{C}^{ec}]$, are a function of the stresses at the end of the time step. This equation is now inserted in the theorem of virtual work in (B.17), and the contribution of a single element Ω^e to the global system of equations resulting from the finite-element discretization reads:

$$\int_{\Omega_e} {}^t[B]\{\sigma\}_{n+1}\, r^2 dr \; = T^d_{n+1} r^2|_{\partial\Omega^T_e}\,. \tag{B.20}$$

Note that the applied force T^d_{n+1} on the element boundary $\partial\Omega^T_e$ is the remote stress $-\sigma_{H\,n+1}$ on

the external radius R_S (last node of the last element for a mesh constructed from the internal to the external radii) and the pore pressure $+p_{f\,n+1}$ at the pore wall (first node of the first element). Note also that eq. (B.20) is non-linear and is solved by a Newton-Raphson search to satisfy equilibrium at the end of the time step t_{n+1}. The stress at iteration $(k+1)$ of the $n+1$ increment, $\{\sigma\}_{n+1}^{(k+1)}$ is the sum of the stress at previous iteration $\{\sigma\}_{n+1}^{(k)}$ plus a perturbation $\{\delta\sigma\}$. This stress perturbation is related to the perturbation in strain $\{\delta\epsilon\}$ obtained by the linearisation of the constitutive relations in (B.19):

$$\{\delta\sigma\} = [\mathbb{C}^{ec}]^{-1}\{\delta\epsilon\}\,. \tag{B.21}$$

The perturbation in strain is related to the displacement perturbation $\{\delta u\}$ by the B-operator introduced in (B.18) so that the linearised set of equations to solve at each iteration is:

$$\int_{\Omega_e} {}^t[B][\mathbb{C}^{ec}]^{-1}[B]\, r^2 dr\, \{\delta u\} \;= T^d_{n+1} r^2|_{\partial\Omega^T} - \int_{\Omega_e} {}^t[B]\{\sigma\}^{(k)}_{n+1} r^2 dr\,. \tag{B.22}$$

Note that the stiffness used in (B.22) and introduced in (B.21) should result from a consistent linearisation of (B.19). It is preferred here to keep with the inverse of the compliance set-up at the end of the update, at the risk of not obtaining a quadratic convergence rate. The number of iterations remains small (2 to 5) with a convergence tolerance of 10^{-7}. The linearised strain algorithm solved at each node is given in eq. (2.1) for chapter 2 and in eq. (3.6) and eq. (3.7) for chapter 3.

B.4 Numerical algorithm for cracks aperture update

This appendix concerns the numerical algorithm used to capture the evolution of the apertures of the isotropic distribution of cracks. The starting point is again the stress-strain relation in (2.1) with the introduction of the crack compliance tensor in (2.2):

$$\dot{\underline{\underline{\epsilon}}} = \mathbb{C}\colon(\dot{\underline{\underline{\sigma}}} + \alpha\dot{p}_f\underline{\underline{\delta}}) + \frac{c\gamma\pi}{2l}\Big\{\underline{\underline{N}}_O\cdot(\dot{\underline{\underline{\sigma}}} + \dot{p}_f\underline{\underline{\delta}}) + (\dot{\underline{\underline{\sigma}}} + \dot{p}_f\underline{\underline{\delta}})\cdot\underline{\underline{N}}_O - \nu\mathbb{N}_O : (\dot{\underline{\underline{\sigma}}} + \dot{p}_f\underline{\underline{\delta}})\Big\} \quad , \tag{B.23}$$

$$\text{with} \quad \underline{\underline{N}}_O = \int_{\mathcal{H}_\mathcal{O}} \underline{n}\otimes\underline{n}\, d\mathcal{H} \quad \text{and} \quad \mathbb{N}_O = \int_{\mathcal{H}_\mathcal{O}} \underline{n}\otimes\underline{n}\otimes\underline{n}\otimes\underline{n}\, d\mathcal{H}\,,$$

The integration range is now limited to the part of the hemisphere $\mathcal{H}_\mathcal{O}$ corresponding to open cracks. The first cracks to close as the remote loading increases are those aligned with the radial direction. The last ones to close are those perpendicular to the radial direction. Consequently, the integration in terms of the two polar angles defined in Figure 2.3 corresponds to the range $\{\beta, \beta'\} = [0;\beta_c]\times[0;2\pi]$ with β_c corresponding to the condition of crack closure in (2.4):

$$\cos^2\beta_c\,(\sigma_r + p_f) + \sin^2\beta_c\,(\sigma_\theta + p_f) = -\sigma_C \quad \text{with}\,\beta_c \in [0;\frac{\pi}{2}]\,. \tag{B.24}$$

The quadrature in β' is always from 0 to 2π because of the problem's spherical symmetry. The result of the computation of these two quadratures proposed in a matrix notation reads:

$$\begin{Bmatrix} \dot{\epsilon}_r \\ 2\dot{\epsilon}_\theta \end{Bmatrix} = \frac{1}{9G\kappa} \begin{bmatrix} G+3\kappa & 2G-3\kappa \\ 2G-3\kappa & 4G+3\kappa \end{bmatrix} \begin{Bmatrix} \dot{\sigma}_r + \alpha\dot{p}_f \\ \dot{\sigma}_\theta + \alpha\dot{p}_f \end{Bmatrix} + \frac{c\gamma\pi^2}{l} \times \tag{B.25}$$

$$\begin{bmatrix} \frac{2}{3}(1-\cos^3\beta_c) - \frac{\nu}{5}(1-\cos^5\beta_c) & -\frac{\nu}{5}[\frac{2}{3} - \frac{5}{3}\cos^3\beta_c + \cos^5\beta_c] \\ -\frac{\nu}{5}[\frac{2}{3} - \frac{5}{3}\cos^3\beta_c + \cos^5\beta_c] & \frac{4}{3} + \frac{2}{3}\cos^3\beta_c - 2\cos\beta_c + \\ & \frac{\nu}{5}[\cos^5\beta_c - \frac{10}{3}\cos^3\beta_c + 5\cos\beta_c - \frac{8}{3}] \end{bmatrix} \begin{Bmatrix} \dot{\sigma}_r + \dot{p}_f \\ \dot{\sigma}_\theta + \dot{p}_f \end{Bmatrix}.$$

There are two ways to check the components of the second matrix in (B.25). First, if all cracks are closed ($\beta_c = 0$), the components are all equal to zero. Second and less trivial, if all cracks are open ($\beta_c = \pi/2$), the system in (B.25) is then consistent with the findings in Appendix B.2.

Time is now discretised, and eq. (B.25) is written at the end of increment $n+1$ at which the strain vector and the fluid pressure are proposed during an incremental Newton-Raphson search for mechanical equilibrium:

$$\begin{Bmatrix} \Delta\epsilon_r \\ 2\Delta\epsilon_\theta \end{Bmatrix} + \frac{1-\alpha}{3\kappa}\Delta p_f \begin{Bmatrix} 1 \\ 2 \end{Bmatrix} = \begin{bmatrix} \\ \mathbb{C}^{ec}\left(\beta_c(t_{n+1})\right) \\ \\ \end{bmatrix} \begin{Bmatrix} \Delta\sigma_r + \Delta p_f \\ \Delta\sigma_\theta + \Delta p_f \end{Bmatrix}, \tag{B.26}$$

in which the components of the matrix $\mathbb{C}^{ec}$ are the sums of the components of the two matrices found in (B.25). The difficulty for solving (B.26) to obtain the stress state at time t_{n+1} is that these components are functions of the angle β_c defined in (B.24), which, in turn, is a function of the stress. This implicit system is solved with a fixed-point iterative process. A tolerance on the stress norm variation is set to 10^{-7} to define convergence.

B.5 Numerical algorithm for frictional cracks update

The objective is to complement the algorithm presented in Appendix B.4 to account for the displacement by slip over the closed cracks.

The resolved shear stress defined in eq. (2.6) is related to the specific stress state of this problem:

$$\underline{\tau} = (\sigma_r - \sigma_\theta)\sin\beta\cos\beta\,\underline{p} \quad \text{with} \quad \underline{p} = \sin\beta\underline{e}_r - \cos\beta(\cos\beta'\underline{e}_\theta + \sin\beta'\underline{e}_\varphi)\,, \tag{B.27}$$

in terms of the unit vector $\underline{p}$, perpendicular to the normal direction $\underline{n}$, and defined by the two polar angles β and β' introduced in Figure 2.2. The displacement jump across a given crack defined in (2.7) is proportional to the backstress rate $\dot{\underline{\omega}}$. This vector is now defined in terms of its component and the unit vector $\underline{p}$: $\dot{\underline{\omega}} = \dot{\omega}\underline{p}$ where ω is a function of the first polar angle β and not of the second β' because of the problem's symmetry. This rate $\dot{\underline{\omega}}$ should also be oriented along the unit vector $\underline{m}$ defined in (2.8) by the normalisation of the vector $\underline{\tau} - \underline{\omega} = ((\sigma_r - \sigma_\theta)\sin\beta\cos\beta - \omega)\underline{p}$. We thus have $s = \underline{m}\cdot\underline{p}$ which is the sign of the scalar

$(\sigma_r - \sigma_\theta)\sin\beta\cos\beta - \omega$. The direction of the vector $\underline{\dot{\omega}}$ being now defined the positive rate $\dot{\lambda} = s\dot{\omega}$ is obtained from the consistency of the condition (2.9) during continuous slip:

$$\dot{\lambda} = s(\dot{\sigma}_r - \dot{\sigma}_\theta)\sin\beta\cos\beta + \mu(\dot{\sigma}_r\cos^2\beta + \dot{\sigma}_\theta\sin^2\beta + \dot{p}_f)\,. \tag{B.28}$$

The strain rate due to the slipping cracks according to (2.1) with (B.28) is then:

$$\frac{c\gamma\pi}{2l}\int_{\mathcal{H}_\mathcal{S}}(\underline{n}\otimes\underline{p}+\underline{p}\otimes\underline{n})\Big((\dot{\sigma}_r - \dot{\sigma}_\theta)\sin\beta\cos\beta + s\mu(\dot{\sigma}_r\cos^2\beta + \dot{\sigma}_\theta\sin^2\beta + \dot{p}_f)\Big)\,\chi(\dot{\lambda})d\mathcal{H}\,, \tag{B.29}$$

in which the quadrature is over $\mathcal{H}_\mathcal{S}$, the part of the hemisphere where cracks are closed and the slip condition is respected (χ is the Heaviside function). In other words, eq. (B.29) applies to the closed cracks and only if the scalar in (B.28) is positive. Note that this scalar is independent of the second polar angle β' and that the quadrature in (B.29) can be reduced to the first polar angle. The strain rate vector due to slip then reads:

$$\begin{Bmatrix}\dot{\epsilon}^s_r\\ \\ 2\dot{\epsilon}^s_\theta\end{Bmatrix} = \frac{2c\gamma\pi^2}{l}\int_{\beta_c}^{\pi/2}\chi(\dot{\lambda})\begin{bmatrix}\cos\beta(\sin\beta+\mu s\cos\beta) & -\sin\beta(\cos\beta-\mu s\sin\beta)\\ \\ -\cos\beta(\sin\beta+\mu s\cos\beta) & +\sin\beta(\cos\beta-\mu s\sin\beta)\end{bmatrix} \times\sin^2\beta\cos\beta d\beta\begin{Bmatrix}\dot{\sigma}_r+\dot{p}_f\\ \\ \dot{\sigma}_\theta+\dot{p}_f\end{Bmatrix}, \tag{B.30}$$

using a matrix notation. Further analytical developments are challenging for an arbitrary loading because the backstress varies with β and is not defined by macro-scale variables. It is thus preferred, for the sake of simplicity, to propose the following numerical quadrature of (B.30): divide the range of β, which is $[0;\pi/2]$, in k intervals. For each i^{th} interval, consider the orientation $\beta = (i-1/2)\pi/(2k)$ and if the closing condition is respected and the slip criterion exceeded, check the sign of $\dot{\lambda}$ in (B.28). If the sign is positive, add the contribution of the left-hand side of (B.30) to the matrix $\mathbb{C}^{ec}$ defined in eq. (B.26) in Appendix B.4. Note that the resulting matrix is then non-symmetric. Note also that this angular discretisation implies that k internal variables are introduced to keep track of the distribution of the backstress magnitude over the hemisphere.

The numerical algorithm to integrate in time these constitutive relations has its technical difficulties due to the risk of numerical fluctuation between slip and no-slip conditions in some orientations if an implicit update is chosen as described briefly in Appendix B.4. This is mainly because the stress point is initially close to the tip of the Coulomb cone in the space spanned by the normal stress and resolved shear stress (see Appendix B.6 for further discussion). This problem, which is known in computational crystal plasticity (Raphanel *et al.*, 2004), was solved by these authors by proposing a high-order explicit integration scheme. The same idea is proposed here, and the strain increment over the time step Δt is subdivided into m intervals to permit the application of an Adams-Bashforth scheme. The search for equilibrium at the end of the time step $t_{n+1} = t_n + \Delta t$ requires a numerical tangent ideally resulting from a consistent linearization of the update algorithm (Simo *et al.*, 1985) to warrant a quadratic rate of conver-

gence. Still, it is proposed to avoid the linearisation and to take for numerical tangent the sum of the continuum tangents at every intermediate step, weighted by the integration scalars of the Adams-Bashforth scheme. Order m of 3 to 5 were tested, and the sub-quadratic convergence rate was indeed noticed. The order $m = 3$ is used for all numerical results presented here.

B.6 Kinematic hardening

The two objectives of this Appendix are, first, to present the motivation for the introduction of kinematic hardening from a fracture mechanics point of view, and second, to follow a cyclic loading for a single family of cracks with azimuthal symmetry. The stress loading is bi-axial and inspired by the state of stress close to the pore based on a linear elastic response as presented in Appendix B.1 with eq. (B.7), setting the radius to the pore radius. The stress of state beyond the hydrostatic initial condition is indeed bi-axial:

$$\sigma_r = -p_f\,, \quad \sigma_\theta = \sigma_\varphi = -p_f - \Sigma \quad \text{with} \quad \Sigma = \frac{3(\sigma_H - p_f)}{2(1-\phi)}\,, \tag{B.31}$$

keeping the fluid pressure constant.

B.6.1 Kinematic hardening and fracture mechanics

The effect of cracks under uniaxial loading has been demonstrated by many contributions since the seminal work of Walsh (1965). One of the key ideas in that paper has been the stress conditions for the reverse slipping of the cracks at the start of the unloading phase: sliding to occur requires a reduction in the sum of the resolved shear stress plus the frictional shear stresses, $\Delta\tau + \Delta\tau_f$ twice as large as the maximum frictional stress τ_f^{max}:

$$\Delta\tau + \Delta\tau_f > 2\tau_f^{max}\,, \tag{B.32}$$

using Walsh (1965)'s notation. The resolved shear stress increment has the same definition as in this contribution (eq. 2.6) while the frictional shear stress increment is $\mu(\Delta\sigma_n + \Delta p_f)$ in our setting. The maximum frictional stress is reached prior to the reverse loading and then reads $\mu(\sigma_n + \sigma_C + p_f)^{max}$.

The explanation of this slip condition is not trivial, and some clarifications are now proposed using the arguments outlined by Andrieux *et al.* (1986) and based on the work of Muskhelishvili (1963). For a 2D crack in an infinite medium, the normal stress on the crack's surface is uniform and equal to the normal stress based on the remote stress tensor, as defined in eq. (2.4). As the crack closes, there is already a tangential displacement jump b_t, and the associated shear stress denoted ω equals this jump divided by the crack compliance γ introduced in eq. (2.2). Based on the remote stress tensor, the resolved shear stress τ is also equal to ω at closure. The frictional forces to induce slip upon loading beyond closure are thus the normal stress and the difference between τ and ω, the latter being first defined by the elasticity problem up to closure. The yield criterion (2.6) is constructed based on these two forces and reminds one of a kinematic hardening plasticity law, although the back-stress, ω, has a life before crack closure.

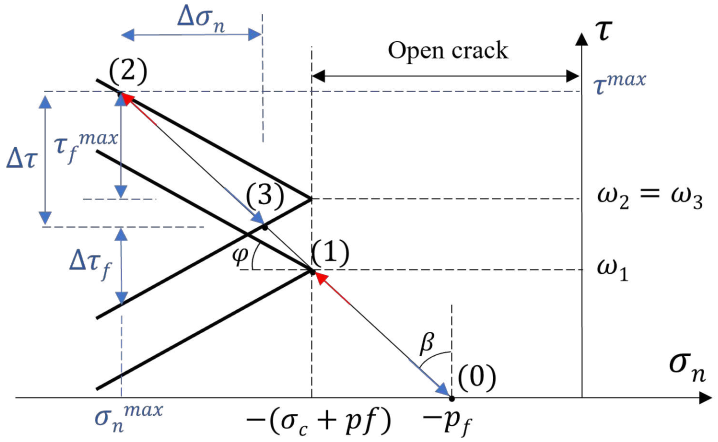


Figure (B.1) Evolution of the position of the elasticity domain in the stress space during a bi-axial loading cycle typical to the region close to the pore and for a crack family oriented by the first polar angle β. From the initial stress point (0) to (1), the crack is open and is closed up to (2) during loading. During the unloading phase, the crack sticks between (2) and (3). Reverse-slip occurs between (3) and up to the crack reopening at (1).

Its graphical representation in Figure B.1 depicts the evolution in the stress space during a cyclic compression for a crack having the first polar angle β. In the loading phase, the crack remains open from the initial stress point (0) to point (1), after which it is closed. Note that at closure, the stress point is exactly at the apex of the Coulomb criterion. The crack sticks or slips if the condition $\varphi + \beta \geq \pi/2$ is met. If slip occurs, it does so immediately after crack closure. The back stress keeps evolving based on the rate of tangential displacement jump across the crack surfaces divided by the elasticity compliance, eq. (2.7). This displacement jump amplitude is governed by the consistency condition on the yield criterion, equations (2.8) and (2.9). The yield surface is thus continuously translated upward until the maximum load is reached at point (2) in Figure B.1. In the subsequent unloading phase, the crack experiences sticking between points (2) and (3), and the back stress does not change since the tangential displacement jump is constant. Then reverse-slipping occurs between point (3) and the crack's reopening point (1). Note that the final slip during unloading is again at the apex of the yield criterion. The reasoning based on 2D elasticity solutions is applied to 3D in this contribution without further justification.

The remainder of this Appendix is devoted to the evolution of the straining during the cyclic loading in a REV close to a spherical pore, as depicted above. The analysis is done for a single family of cracks with azimuthal symmetry to link with earlier work by David *et al.* (2012).

B.6.2 A single family with azimuthal symmetry

The stress-strain relation for a single family is still provided by eq. (2.1) if the integrant is modified to include the distribution function $c^*\delta(\beta - \beta^*)/(2\pi \sin\beta)$ in which c^* is the crack density in the direction β^* orienting the crack family of interest and $\delta(\beta - \beta^*)$ the classical Dirac function. The strain-stress relation then simplifies to:

$$\underline{\underline{\dot{\epsilon}}} = \mathbb{C} : (\underline{\underline{\dot{\sigma}}} + \alpha \dot{p}_f \underline{\underline{\delta}}) + \frac{c^*}{4l} \int_{\beta'=0}^{2\pi} \left(\underline{\dot{b}}(\underline{n}^*) \otimes \underline{n}^* + \underline{n}^* \otimes \underline{\dot{b}}(\underline{n}^*) \right) d\beta' \,, \tag{B.33}$$

in which the normal $\underline{n}^*$ is oriented by β^* and the second polar angle β' in the range $[0; 2\pi]$.

The loading due to the remote stress in (B.31) leads to straining $(\epsilon_r, 2\epsilon_\theta)$ with the open crack contribution in (B.33) reading

$$\frac{c^*\gamma\pi}{l}\begin{bmatrix}\cos^2\beta^*(1-\frac{\nu}{2}\cos^2\beta^*) & -\frac{\nu}{2}\cos^2\beta^*\sin^2\beta^* \\ -\frac{\nu}{2}\cos^2\beta^*\sin^2\beta^* & \sin^2\beta^*(1-\frac{\nu}{2}\sin^2\beta^*)\end{bmatrix}\begin{Bmatrix}\dot\sigma_r+\dot p_f \\ \dot\sigma_\theta+\dot p_f\end{Bmatrix}, \tag{B.34}$$

using a matrix notation. The back-stress evolution before closure is dictated by the resolved shear stress $\underline{w} = \underline{\tau} = (\sigma_r - \sigma_\theta)\cos\beta^*\sin\beta^*\underline{p}^*$ in which the vector $\underline{p}*$ is orthogonal to $\underline{n}^*$ and defined in eq. (B.27) of Appendix B.5 for the polar angles (β^*, β'). The contribution of (B.34) ceases once the crack family is closed, and this happens when the remote loading is equal to $\sigma_H = 2(1-\phi)\sigma_C/(3\sin^2\beta^*) + p_f$. In Figure B.1, this loading path from the initial condition (0) brings us to the stress point (1), which is at the tip of the Coulomb cone. In summary, at crack closure:

$$\tau_{(1)} = \omega_{(1)} = \Sigma_{(1)}\sin\beta^*\cos\beta^*, \quad \sigma_{n(1)} = -p_f - \Sigma_{(1)}\sin^2\beta^* \quad \text{with} \quad \Sigma_{(1)} = \sigma_C\sin^{-2}\beta^*, \tag{B.35}$$
$$\epsilon_{\theta(1)} = -\frac{1}{2}\Big(\frac{4G+3\kappa}{9G\kappa} + \frac{c^*\gamma\pi}{l}\sin^2\beta^*(1-\frac{\nu}{2}\sin^2\beta^*)\Big)\Sigma_{(1)}.$$

The case of interest is now $\varphi + \beta^* \geq \pi/2$ since slipping occurs immediately upon further loading after closure. From Appendix B.5, the crack family contribution to the straining is then:

$$\frac{c^*\gamma\pi}{l}\begin{bmatrix}\cos\beta^*(\sin\beta^*+\mu s\cos\beta^*) & -\sin\beta^*(\cos\beta^*-\mu s\sin\beta^*) \\ -\cos\beta^*(\sin\beta^*+\mu s\cos\beta^*) & \sin\beta^*(\cos\beta^*-\mu s\sin\beta^*)\end{bmatrix}\begin{Bmatrix}\dot\sigma_r+\dot p_f \\ \dot\sigma_\theta+\dot p_f\end{Bmatrix}, \tag{B.36}$$

with $s = 1$ during loading. The conditions at the end of this loading are then

$$\omega_{(2)} = \Sigma_{(2)}\sin\beta^*(\cos\beta^* + \mu\sin\beta^*) - \mu\Sigma_{(1)})\sin^2\beta^*, \tag{B.37}$$
$$\epsilon_{\theta(2)} - \epsilon_{\theta(1)} = -\frac{1}{2}\Big(\frac{4G+3\kappa}{9G\kappa} + \frac{c^*\gamma\pi}{l}\sin\beta^*(\cos\beta^* - \mu\sin\beta^*)\Big)(\Sigma_{(2)} - \Sigma_{(1)}),$$

having used eq. (2.9) to follow the evolution of the backstress. The unloading occurs with stick conditions, and the conditions at the start of reverse sliding are:

$$\omega_{(3)} = \omega_{(2)}, \quad \Sigma_{(3)} = (\Sigma_{(2)} - 2\Sigma_{(1)})\frac{\mu\sin\beta^*}{\cos\beta^* + \mu\sin\beta^*}, \tag{B.38}$$
$$\epsilon_{\theta(3)} - \epsilon_{\theta(2)} = -\frac{1}{2}\frac{4G+3\kappa}{9G\kappa}(\Sigma_{(3)} - \Sigma_{(2)}).$$

Reverse slip occurs upon further unloading and implies that $s = -1$ in eq. (B.36). It also means that the stress conditions are back at point (1) at the final unloading, closing the hysteresis loop.

Figure B.2 shows the deformation during the cyclic loading for various values of the frictional angle, and under dry conditions for the sake of simplicity. The cracks have the orientation angle

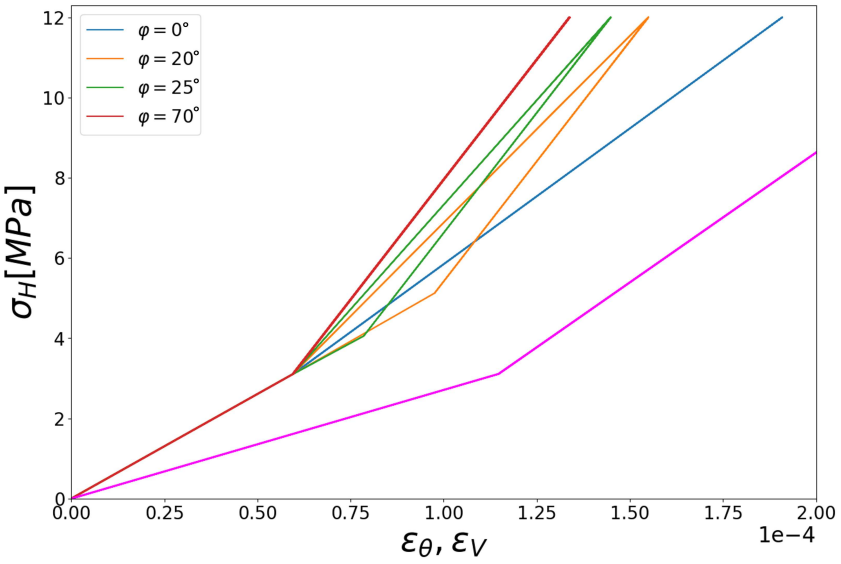


Figure (B.2) Remote stress σ_H versus hoop strain ϵ_θ and volumetric strain ϵ_V (magenta line) for a single family of cracks ($\beta^* = \pi/3$) and for various values of crack friction angle φ (in degrees) for dry conditions. The hysteresis in ϵ_θ is a function of the crack friction, and the maximum effect is attained for an intermediate value of the friction angle. There is no hysteresis in volumetric strain by construction.

$\beta^* = \pi/3$ so that the cracks are slipping unless the friction angle φ is larger than $\pi/6$ (stick condition $\varphi + \beta^* \geq \pi/2$). The closure stress is $\sigma_C = 4$ MPa, and the crack density is $c^* = 0.6$. The porosity of the specimen is set to $\phi = 0.125$, whereas the matrix elastic properties are $E = 95.46$ GPa and $\nu = 0.07$, corresponding to quartz. The loading cycle consists of a loading phase, with σ_H varying from 0 MPa to 12 MPa, and an unloading back to initial conditions. The four stress-strain curves σ_H vs ϵ_θ are multi-linear and characterised by four values for the slope E_θ defined with:

$$
\begin{aligned}
\dot{\sigma}_H &= -E_\theta \dot{\epsilon}_\theta \quad \text{with} \\
\frac{1}{E_\theta} &= \frac{4G + 3\kappa}{12G\kappa(1-\phi)} \quad \text{closed and sticking cracks}\,, \\
\frac{1}{E_\theta} &= \frac{4G + 3\kappa}{12G\kappa(1-\phi)} + \frac{3c^*\gamma\pi}{4l(1-\phi)} \frac{\sin\beta^*}{\cos\varphi} \cos(\beta^* + s\varphi) \quad \text{closed and slipping cracks}\,, \\
\frac{1}{E_\theta} &= \frac{4G + 3\kappa}{12G\kappa(1-\phi)} + \frac{3c^*\gamma\pi}{4l(1-\phi)} \sin^2\beta^* (1 - \frac{\nu}{2}\sin^2\beta^*) \quad \text{open cracks}\,.
\end{aligned}
\tag{B.39}
$$

Crack closure occurs at σ_H approximately equal to 3.1 MPa, and the stress-strain curve is independent of friction for lower values. If there is no friction ($\varphi = 0$), the cracks slip since $\varphi + \beta^* \leq \pi/2$. In addition, E_θ is the same during the loading and unloading stages as seen in eq. (B.39)c ($\varphi = 0$). There is also no sticking phase since the yield surface cone is closed, and reverse slipping happens at the very start of the unloading, Figure B.1. On the contrary, if $\varphi = 20°$ and $\varphi = 25°$, the cracks first slip in the loading stage since $\varphi + \beta^* \leq \pi/2$ but stick at the beginning of the unloading. The sticking modulus E_θ is the same for both values of φ as it is independent of friction. Also, the sticking phase is longer at $\varphi = 25°$ compared to $\varphi = 20°$ because, as shown in Figure B.1, in the former, the yield surface cone has an angle larger than in the latter, meaning that a greater decrease of stress is required to reverse slip. Note that, in

the slipping phases, E_θ loading is greater at $\varphi = 25°$ than at $\varphi = 20°$, whereas it is the opposite during the unloading, in agreement with eq. (B.39)c. Finally, if $\varphi = 70°$, the cracks always stick since $\varphi + \beta^* \geq \pi/2$.

One last point to note is that regardless of the value of the crack's friction coefficient, the volumetric strain versus the stress curve shows no hysteresis (magenta line). That is because crack slipping induces no volumetric change within the REV. Its modulus κ^* is thus constant regardless of the crack slipping. However, crack slipping reduces the equivalent shear modulus G^* of the REV and, therefore, does lead to hysteresis in the volumetric macro response of the assemblage as revealed by the classical relation (2.26).

B.7 Spherical Assembly effective properties for slipping cracks

The objective is to derive an analytical solution for the bulk modulus, Biot coefficient, and the pore volume fraction rate of the assemblage if all cracks are closed and slipping. For closed and sticking cracks and for open cracks, the solution is presented in the main text, relying on Appendices B.1 and B.2. The analytical expression of the bulk modulus in the general case of a distribution of cracks, either open, closed, or sticking or slipping, is challenging to derive since the material moduli are heterogeneous within the shell. There is a particular case for which homogeneity is conserved in terms of moduli, and it corresponds to a distribution of closed and slipping cracks at all radii of the hollow sphere.

The starting point is again the definition of the stress-strain relation in eq. (2.1) with the crack strain rate defined in (B.30) with β_c set to zero since all cracks are closed. The quadrature is exact, and the strain-stress rate relation is simplified to:

$$\begin{Bmatrix} \dot{\epsilon}_r \\ 2\dot{\epsilon}_\theta \end{Bmatrix} = \frac{1}{9G\kappa} \begin{bmatrix} G+3\kappa & 2G-3\kappa \\ 2G-3\kappa & 4G+3\kappa \end{bmatrix} \begin{Bmatrix} \dot{\sigma}_r + \alpha\dot{p}_f \\ \dot{\sigma}_\theta + \alpha\dot{p}_f \end{Bmatrix} + \frac{4c\gamma\pi^2}{15l} \begin{bmatrix} 1+\mu s & -(1-\frac{3}{2}\mu s) \\ -(1+\mu s) & 1-\frac{3}{2}\mu s \end{bmatrix} \begin{Bmatrix} \dot{\sigma}_r + \dot{p}_f \\ \dot{\sigma}_\theta + \dot{p}_f \end{Bmatrix}. \tag{B.40}$$

This system of equations is now inverted to express the stress rates in relation to the strain and the pressure rates:

$$\begin{Bmatrix} \dot{\sigma}_r \\ \\ \dot{\sigma}_\theta \end{Bmatrix} = \frac{1}{D}\begin{bmatrix} 4G+3\kappa+9G\kappa\Gamma(1-\frac{3}{2}\mu s) & -2G+3\kappa+9G\kappa\Gamma(1-\frac{3}{2}\mu s) \\ \\ -2G+3\kappa+9G\kappa\Gamma(1+\mu s) & G+3\kappa+9G\kappa\Gamma(1+\mu s) \end{bmatrix} \tag{B.41}$$

$$\times \left(\begin{Bmatrix} \dot{\epsilon}_r \\ \\ 2\dot{\epsilon}_\theta \end{Bmatrix} - \begin{Bmatrix} \frac{\alpha}{3\kappa}+\Gamma\frac{5}{2}\mu s \\ \\ \frac{2\alpha}{3\kappa}-\Gamma\frac{5}{2}\mu s \end{Bmatrix} \dot{p}_f \right),$$

$$\text{with} \quad D = 3[1+\Gamma G(3+\frac{1}{2}\mu s)] \quad \text{and} \quad \Gamma = \frac{4c\gamma\pi^2}{15l}\,. \tag{B.42}$$

Note that the matrix components on the right-hand side of this equation are denoted A_{ij}/D with $i,j = r$ or θ in what follows.

Introduce these expressions into the equilibrium equations in (B.3) and obtain:

$$[4G+3\kappa+9G\kappa\Gamma(1-\frac{3}{2}\mu s)]r\frac{\partial^2\dot{u}}{\partial r^2} + 2[4G+3\kappa+9G\kappa\Gamma(1-4\mu s)]\frac{\partial\dot{u}}{\partial r} \tag{B.43}$$
$$-2[4G+3\kappa+9G\kappa\Gamma(1+\frac{7}{2}\mu s)]\frac{\dot{u}}{r} = 45G\Gamma\mu s(1-\alpha)\dot{p}_f\,.$$

The homogeneous part of this differential equation is a second-order Cauchy-Euler equation, which is solved with the trial function $(r/R_S)^m$, and the exponent m is the solution of the second-order polynomial

$$m^2 + m\frac{4G+3\kappa+9G\kappa\Gamma(1-\frac{13}{2}\mu s)}{4G+3\kappa+9G\kappa\Gamma(1-\frac{3}{2}\mu s)} - 2\frac{4G+3\kappa+9G\kappa\Gamma(1+\frac{7}{2}\mu s)}{4G+3\kappa+9G\kappa\Gamma(1-\frac{3}{2}\mu s)} = 0\,. \tag{B.44}$$

The unexpected finding is that one of the two roots of this polynomial is the scalar -2 for all friction values, so that the two roots read:

$$m_1 = \frac{4G+3\kappa+9G\kappa\Gamma(1+\frac{7}{2}\mu s)}{4G+3\kappa+9G\kappa\Gamma(1-\frac{3}{2}\mu s)}\,, \qquad m_2 = -2\,. \tag{B.45}$$

Note that the first root is close to 1, and the set $(1,-2)$ corresponds to the two powers of the displacement polynomial found for an isotropic, elastic solid, as seen in Appendix B.1. The final expression for the displacement rate is:

$$\dot{u}(r) = C_1 R_S(\frac{r}{R_S})^{m_1} + C_2 R_S(\frac{r}{R_S})^{-2} - r\frac{1}{3}(1-\alpha)\frac{\dot{p}_f}{\kappa}\,, \tag{B.46}$$

for two dimensionless constants C_1 and C_2 which are obtained from the stress-boundary conditions as follows.

The first of the three steps to find these constants is to express the stress rate in eq. (B.42) in

terms of the two unknowns:

$$\begin{Bmatrix} \dot\sigma_r + \dot p_f \\ \\ \dot\sigma_\theta + \dot p_f \end{Bmatrix} = \frac{C_1}{D}\left(\frac{r}{R_S}\right)^{m_1-1}\begin{Bmatrix} A_{rr}m_1 + 2A_{r\theta} \\ \\ A_{\theta r}m_1 + 2A_{\theta\theta} \end{Bmatrix} + \frac{2C_2}{D}\left(\frac{r}{R_S}\right)^{-3}\begin{Bmatrix} -A_{rr} + A_{r\theta} \\ \\ -A_{\theta r} + A_{\theta\theta} \end{Bmatrix}. \tag{B.47}$$

The second step sees the application of the stress boundary conditions $\dot\sigma_r|_{R_P} = -\dot p_f$ and $\dot\sigma_r|_{R_S} = -\dot\sigma_H$ at the pore radius and the external radius, respectively. These two conditions, combined with the first equation in (B.47), provide a system of two equations for the unknown scalars:

$$\begin{Bmatrix} 0 \\ \\ -\dot\sigma_H + \dot p_f \end{Bmatrix} = \frac{1}{D}\begin{bmatrix} (A_{rr}m_1 + 2A_{r\theta})\phi^{\frac{1}{3}(m_1-1)} & 2(-A_{rr} + A_{r\theta})\phi^{-1} \\ \\ A_{rr}m_1 + 2A_{r\theta} & 2(-A_{rr} + A_{r\theta}) \end{bmatrix}\begin{Bmatrix} C_1 \\ \\ C_2 \end{Bmatrix}. \tag{B.48}$$

The third and final step consists of inverting this system to determine the two constants:

$$\begin{Bmatrix} C_1 \\ \\ C_2 \end{Bmatrix} = (-\dot\sigma_H + \dot p_f)\begin{Bmatrix} \tilde C_1 \\ \\ \tilde C_2 \end{Bmatrix} \quad \text{with} \quad \begin{Bmatrix} \tilde C_1 \\ \\ \tilde C_2 \end{Bmatrix} = \frac{D}{D'}\begin{Bmatrix} 2(A_{rr} - A_{r\theta})\phi^{-1} \\ \\ (A_{rr}m_1 + 2A_{r\theta})\phi^{\frac{1}{3}(m_1-1)} \end{Bmatrix} \tag{B.49}$$
$$\text{and} \quad D' = -2(A_{rr}m_1 + 2A_{r\theta})(A_{rr} - A_{r\theta})(\phi^{\frac{1}{3}(m_1-1)} - \phi^{-1}),$$

having introduced two constants $\tilde C_1$ and $\tilde C_2$ which have dimension of one over stress.

The solution for the displacement being determined, the rate of volume change $\dot\theta = 3\dot u(R_S)/R_S$ is now expressed in terms of the pressure and hydrostatic rate of changes thanks to (B.46) and (B.49) providing the final expression:

$$\dot\sigma_H = -\bar\kappa_s\,\dot\theta + \bar\alpha_s\dot p_f \tag{B.50}$$
$$\text{with} \quad \bar\kappa_s = \frac{1}{3(\tilde C_1 + \tilde C_2)} \quad \text{and} \quad \bar\alpha_s = 1 - (1-\alpha)\frac{\bar\kappa_s}{\kappa}.$$

in which the effective bulk modulus $\bar\kappa_s$ and the effective Biot coefficient $\bar\kappa_s$ are introduced. Note again that these two material parameters are defined for all cracks of the spherical assembly being in slip condition, as marked by the letter s in subscript.

Although analytical, this solution for the effective properties of the assemblage with all cracks slipping requires a numerical implementation, which can be checked in the case of zero friction. In that instance, the solutions for the two exponents m_1 and m_2 in eq. (B.44) are 1 and -2, as already pointed out above. The displacement has indeed the same structure as in eq. (B.4) of Appendix B.1 for an isotropic elastic solid. Inspection of the system (B.42) with $\mu = 0$ confirms this interpretation and reveals that the effective moduli and coefficient are:

$$\kappa^* = \kappa, \quad G^* = G/(1 + 3G\Gamma), \quad \alpha^* = \alpha \quad \text{and} \quad \bar\kappa_s = \kappa\frac{1-\phi}{1 + \frac{3\kappa}{4G}(1+3G\Gamma)\phi}. \tag{B.51}$$

Note that the results for the particular case of zero friction are easily extended to the case of a constrained fluid volume using eq. (2.20).

The rest of this Appendix is devoted to the pore volume fraction, the fluid volume within the porous medium normalized by the volume of the spherical assembly. The non-linear evolution of this pore volume fraction, accounting for the dead volume of the experiment, is discussed in detail in Section 2.2.2. The two objectives are first to concentrate on the rate form adopted for the effective properties of the spherical assemblage summarised by eq. (2.24) and second, to derive expressions for Biot's coefficient and the storage coefficient based on the second equation in (2.23). This is a check that the general structure of the constitutive relations discussed in section 2.2.3 is valid.

The fluid volume within the assemblage is due to the multi-cracked matrix composing the shell and the central pore. Since all cracks are assumed closed, the matrix pore volume change is still given by eq. (2.10) with $\dot{\epsilon}_{vC}$ set to zero. The pore volume fraction of the matrix is thus:

$$\dot{v} = \alpha C_1(2+m_1)(\frac{r}{R_S})^{m_1-1} + \dot{p}_f(R_{pM} - \alpha(1-\alpha)\frac{1}{\kappa}) \,, \tag{B.52}$$

having made use of the displacement in (B.46) to deduce the local volume change. Integrate this contribution over the shell and normalize by the volume of the assemblage to obtain the contribution to the assemblage pore volume change:

$$\alpha C_1 3(1-\phi^{\frac{m_1+2}{3}}) + \dot{p}_f(R_{pM} - \alpha(1-\alpha)\frac{1}{\kappa})(1-\phi) \,. \tag{B.53}$$

The second contribution is due to the central pore, and its contribution to the assemblage after normalization is $\phi\dot{u}(R_P)/R_P$ or based on the displacement field in eq. (B.46):

$$3[C_1\phi^{\frac{m_1+2}{3}} + C_2] - \phi(1-\alpha)\frac{\dot{p}_f}{\kappa} \,. \tag{B.54}$$

The sum of these two contributions (B.53 and B.54) is the pore volume fraction rate of the assemblage. It remains to replace the constants C_1 and C_2 by the expressions in eq. (B.49), which are functions of the remote stress and fluid pressure rate. The former is eliminated thanks to the first equation in eq. (2.24), so that the effective parameters are finally obtained:

$$\begin{aligned} \bar{\alpha}_s &= \frac{\tilde{C}_1[\phi^{\frac{m_1+2}{3}} + \alpha(1-\phi^{\frac{m_1+2}{3}})] + \tilde{C}_2}{\tilde{C}_1 + \tilde{C}_2} \,, \\ \bar{R}_{ps} &= R_{pM}(1-\phi) - \frac{1-\alpha}{\kappa}(\phi + \alpha(1-\phi)) \\ &\quad +3(1-\bar{\alpha}_s)\left(\tilde{C}_1[\alpha(1-\phi^{\frac{m_1+2}{3}}) + \phi^{\frac{m_1+2}{3}}] + \tilde{C}_2\right) \,. \end{aligned} \tag{B.55}$$

The comparison between (B.50) and the first equation above is now necessary to confirm the symmetry argument discussed in section 2.2.3. Introduce the definition of $\bar{\kappa}_s$ in (B.50) to eliminate the sum $\tilde{C}_1 + \tilde{C}_2$ while making sure that only $\tilde{C}_1$ remains in the expression. Use the definition of that constant in (B.49) and conclude that the two expressions (B.50) and (B.55) for Biot's coefficient are indeed equivalent. A non-trivial check of our derivation, but also a confirmation, albeit not a proof of the statement made in section 2.2.3.

B.8 Elastic effective compressibility of composite sphere model

The elasticity solution, when all cracks are open or closed, and sticking is fundamental to this study. The shell is made of a material that contains microcracks but is homogeneous and possesses linearly elastic and isotropic properties with equivalent values (κ^*, G^*, B^*). These isotropic elastic moduli are calculated for non-interacting penny-shaped cracks and are given by

$$\frac{1}{3\kappa^*} = \frac{1}{3\kappa} + \frac{c\pi^2\gamma}{3l}(2-\nu) \quad , \quad \frac{1}{2G^*} = \frac{1}{2G} + \frac{2c\pi^2\gamma}{3l}(1-\frac{\nu}{5}) \, , \text{and} \quad B^* = 1-(1-B)\frac{\kappa^*}{\kappa} \, . \tag{B.56}$$

The initial state of the shell is characterized by a fluid pressure set to p_{f0}. This isotropic confining stress is equal to the fluid pressure and is associated with zero deformation and displacement. The solution to this linear elasticity problem for small perturbations is classical and documented above. The main result is that the spherical assemblage volume change θ (equal to $3u_r(R_S)/R_S$ where $u_r(R_S)$ is the radial displacement at the external radius of the assemblage) is related to the fluid pressure and the confining pressure by

$$\theta = -\left[(1-B^*)\frac{1}{\kappa^*} - \frac{1}{1-\phi}\frac{4G^*+3\kappa^*\phi}{4G^*\kappa^*}\right](p_f - p_{f0}) - \frac{1}{1-\phi}\frac{4G^*+3\kappa^*\phi}{4G^*\kappa^*}(\sigma_H - p_{f0}) \, , \tag{B.57}$$

where σ_H is the remote hydrostatic stress. This analytical solution provides the effective properties:

$$\bar{\kappa} = \kappa^* \frac{1-\phi}{1+\phi\frac{3\kappa^*}{4G^*}} \, , \quad \bar{B} = 1-(1-B^*)\frac{\bar{\kappa}}{\kappa^*} \, , \tag{B.58}$$

and the compressibility moduli

$$C_{bc} \equiv \frac{\partial\theta}{\partial\sigma_H}|_{p_f} = \frac{1}{\bar{\kappa}} \, , \quad C_{bp} \equiv \frac{\partial\theta}{\partial p_f}|_{\sigma_H} = \frac{\bar{B}}{\bar{\kappa}} \, . \tag{B.59}$$

We thus have the classical results that $C_{bp} = \bar{B}C_{bc}$ and $C_{bc} > C_{bp}$ since the effective Biot coefficient in eq. (B.58) is less than one.

B.9 Comparison with Biot-Gassmann

The prediction of the undrained bulk modulus, in practice, is often based on the classical relation of Biot-Gassmann, which reads

$$\bar{\kappa}_u = \bar{\kappa} + \frac{\left(1-\frac{\bar{\kappa}}{\kappa}\right)^2}{\frac{\phi}{\kappa_f} + \frac{1-\phi}{\kappa} - \frac{\bar{\kappa}}{\kappa^2}} \, , \tag{B.60}$$

and requires the introduction of the skeleton κ and the fluid bulk modulus κ_f, as well as the porosity ϕ considered here to be the poral porosity. It applies to linear poro-elasticity only. The simplest proof of this relation relies on two thought experiments. The first experiment consists of a REV submitted to a hydrostatic loading under undrained conditions, and the second

experiment is a drained experiment with the same hydrostatic loading and a fluid pressure adjusted, such that the overall volume changes in the two experiments are identical. The comparison of the two experiments yields Skempton's coefficient, while the description of the fluid mass, introducing the fluid's incompressibility and porosity, leads to this famous relation. It is important to note that, in this reasoning, the microstructure is represented by a rock skeleton. This skeleton responds linearly and elastically, without any secondary porosity. Additionally, we assume a loading condition where each grain experiences a hydrostatic remote load equal to the fluid pressure. As a result, the internal stress within each grain is purely spherical.

The first comparison between Biot-Gassmann predictions and the numerical results is presented in Figure B.3. The drained and the undrained bulk modulus are the red and green curves, respectively, also found in Figure 2.8a (orange and black curves) in the main text. They show two plateaus, the first for low and the second for large confining pressure. The transition between the two plateaus is dependent on the fluid's draining regime. The blue curve is the undrained bulk modulus predictions based on equation B.60 and the drained results. Comparing the blue and green curves, it is seen that the lower plateau is well captured up to numerical accuracy while the upper plateau is overestimated by approximately 0.2 %. This difference is most likely due to the different activities of the distributed cracks under either drained or undrained conditions. What cannot be captured by equation B.60 is, of course, the transition from the lower to the upper plateau.

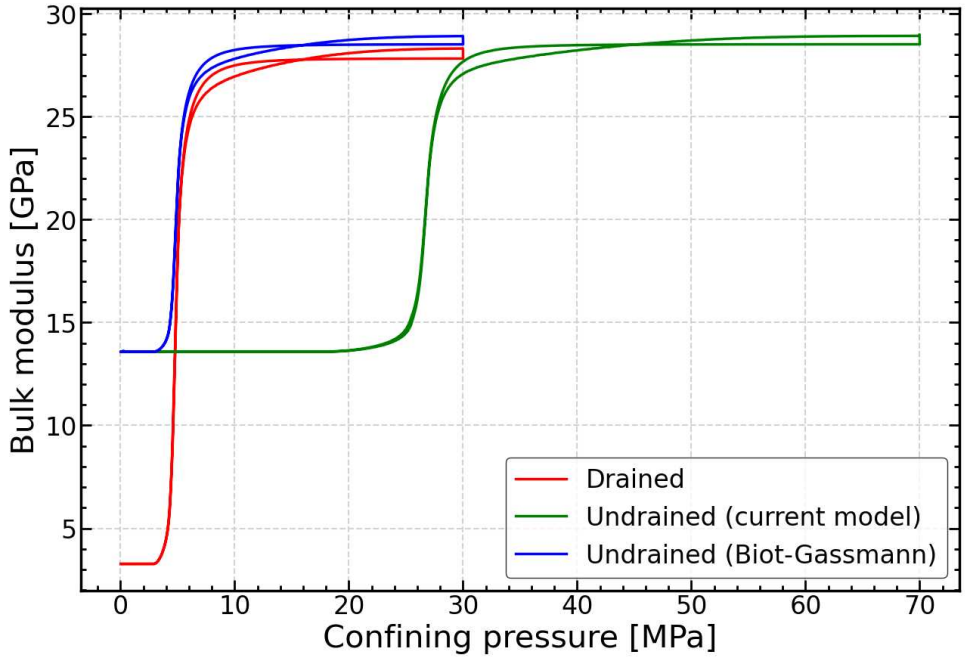


Figure (B.3) Predictions with Biot-Gassmann of the undrained bulk modulus from the poral porosity and the drained modulus and comparison with the numerical undrained modulus. The elastic material composing the pore shell is purely elastic, setting $\alpha = 0$ (indicating the absence of microporosity).

It should be mentioned that this comparison is done assuming the pervasively cracked material composing the shell around the pore to be purely elastic and not porous (Biot coefficient and porosity set to zero). The second comparison of the prediction resulting from the application of Biot-Gassmann is presented in Figure B.4 and corresponds to the case when this material is as-

sumed to be also poro-elastic with a Biot coefficient α set to 0.8. It is seen that Biot-Gassmann's predictions are underestimating the numerical predictions (green curve) by approximately 30 %.

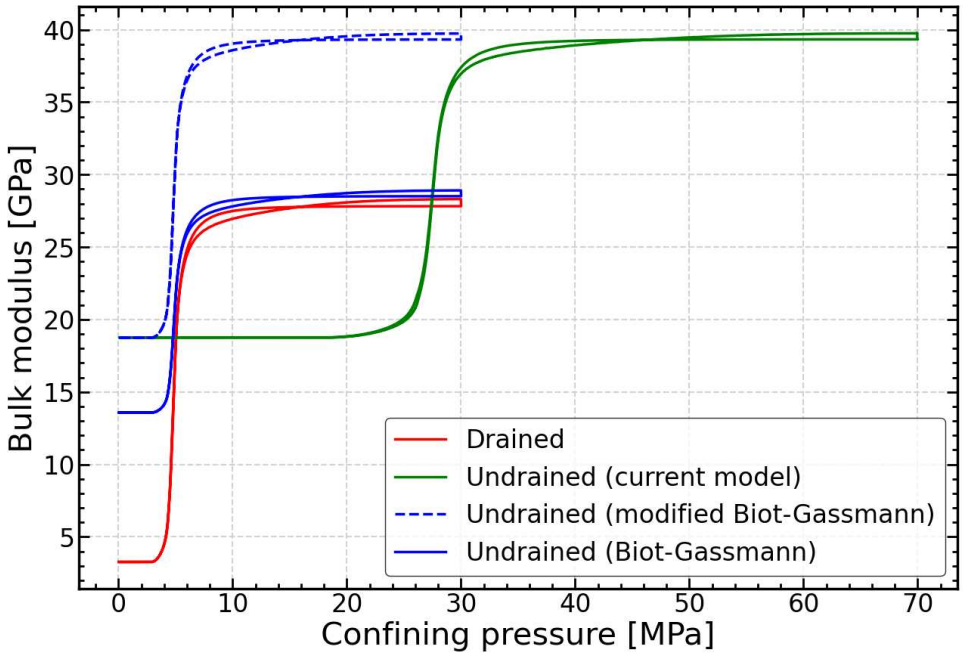


Figure (B.4) Predictions for the undrained bulk modulus when $\alpha = 0.8$ (indicating some microporosity within the matrix).

This difference can only be explained by the fact that the derivation of Biot-Gassmann relies on the granular microstructure to be purely elastic and not poro-elastic, as mentioned earlier. It is interesting to pursue this reasoning and to rewrite equation B.60 in terms of the macro-scale Biot coefficient $\bar{\alpha}$

$$\bar{\kappa}_u = \bar{\kappa} + \frac{\bar{\alpha}^2}{\dfrac{\phi}{\kappa_f} + \dfrac{(1-\phi)(1-\bar{\alpha})}{\bar{\kappa}} - \dfrac{(1-\bar{\alpha})^2}{\bar{\kappa}}} \quad \text{with} \quad \bar{\alpha} = 1 - (1-\alpha)\frac{\bar{\kappa}}{\kappa}\,, \tag{B.61}$$

eliminating the skeleton's bulk modulus. In the same equation, it is proposed to substitute the relation obtained in equation (2.28) for the macro-scale Biot's coefficient, which accounts for the micro-scale porosity. This ad-hoc modification is plotted in Figure B.4 as a dashed blue curve. The comparison between this modified Biot-Gassmann predictions and the numerical results is now excellent: the two plateaus are well captured, exactly for the lower and with an accuracy again of less then a percent for the upper plateau. It remains to encourage a line of action where this modified relation could be proved (or disproved) mathematically. A reasoning based on the two thought experiments discussed in the introduction is certainly one way to proceed.

B.10 Morlier's crack density inversion

Suppose we assume that the non-linearity of the elastic response of a rock is only due to the closing of microcracks. In that case, we can estimate the crack density parameter c directly from the stress-strain curve. Let us consider that all cracks have platelet or penny shapes, similar to

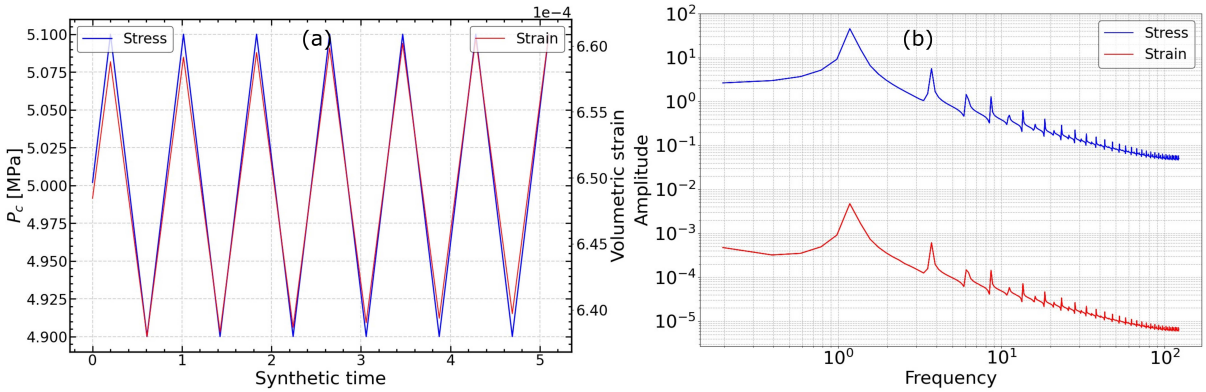


Figure (B.5) The Fourier transform is performed on the simulated stress and strain signals from (a) to (b). Then the bulk modulus is calculated from the ratio of the maximum peak amplitudes in the stress and strain spectra. The bulk modulus is equal to 9.62 GPa.

those used in the non-interacting penny-shaped crack models in Chapter 2 and Kachanov, 1992. Each crack's initial volume equals $2\pi l^3\alpha$, with a radius l and aspect ratio α. When a homogeneous elastic body of volume V_b and bulk modulus K is subjected to a hydrostatic confining pressure P, the amount of elastic energy stored is equal to $P^2V_b/2\kappa$. If microcracks/defects are added inside that body, the total elastic strain energy Σ will also include the elastic strain contribution due to the closing of those cracks $\Delta\Sigma$ (Eshelby, 1957; Zimmerman, 1990). The effective bulk modulus $\bar{\kappa}$ is then defined as:

$$\Sigma = \frac{P^2V_b}{2\bar{\kappa}} = \frac{P^2V_b}{2\kappa} + \Delta\Sigma\,, \tag{B.62}$$

corresponding to eq. (11.1) of Zimmerman (1990). The crack's stain contribution is given by:

$$\Delta\Sigma \;=\; \frac{8\bar{c}_{op}(1-\nu^2)}{9(1-2\nu)}\frac{P^2V_b}{\bar{\kappa}}\,, \tag{B.63}$$

The derivation of this equation is detailed in chapters 11 and 12 of Zimmerman, 1990. By substituting eq.(B.63) into B.62, we obtain the open-crack density as the confining pressure increases in eq.(3.8).

B.11 Influence of the sinusoidality of the loading path

The Fourier transform method utilised for estimating the bulk modulus during forced oscillations can be sensitive to the sinusoidal nature of these oscillations. In this brief analysis, we compare two types of oscillation signals: a triangular function and a step function. The Fourier transform is applied to both stress and strain oscillations to determine the signal amplitudes. Subsequently, the bulk modulus is calculated by taking the ratio of the maximum peak amplitudes in the stress and strain spectra.

Figures B.5 and B.6 illustrate the application of the Fourier transform method to triangle and step oscillations, respectively. The triangle function produces a bulk modulus of 9.62 GPa, while the step function results in a bulk modulus of 9.60 GPa. This indicates a small discrepancy of

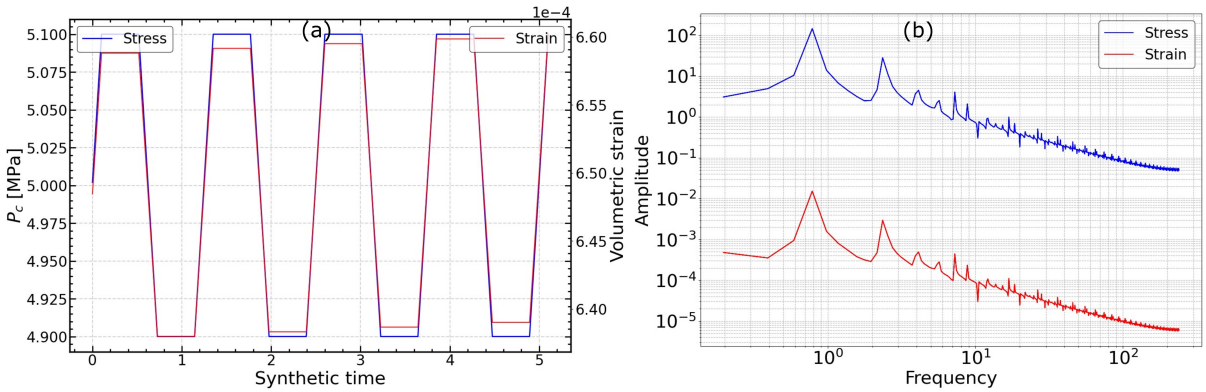


Figure (B.6) The Fourier transform is performed on the simulated stress and strain signals from (a) to (b). Then the bulk modulus is calculated from the ratio of the maximum peak amplitudes in the stress and strain spectra. The bulk modulus is equal to 9.60 GPa.

0.2% between the two types of oscillation signals.

Appendix C

Wave Propagation

C.1 Bubnov-Galerkin method

The objective is to propose a numerical approach for the receiver which is less CPU-intensive than the spectral element approach. The starting point is to consider an approximation of the potential

$$\varphi(\underline{x}) \simeq \sum_{i=1}^{m} A_i \phi_i(\underline{\xi}) \,, \tag{C.1}$$

in which A_i is the amplitude of one of the m^{th} modes ϕ_i. The coordinate vector $\underline{\xi}$ is defined in the computational domain Λ_R and is mapped from the physical domain Ω_R for either S-type or P-type receivers, as illustrated in Figure 4.6, by $\underline{\xi} = \underline{\underline{F}} \cdot (\underline{x} - \underline{x}_c)$ in which $\underline{x}_c$ is the central point of the receiver. The mapping tensor is

$$\begin{aligned} \text{S wave}: \quad & \underline{\underline{F}} = \frac{2}{l_1} \underline{\xi}_1 \otimes \underline{e}_1 + \frac{2}{l_2} \underline{\xi}_2 \otimes \underline{e}_2 \,, \\ \text{P wave}: \quad & \underline{\underline{F}} = \frac{2}{l_2} \underline{\xi}_1 \otimes \underline{e}_2 - \frac{2}{l1} \underline{\xi}_2 \otimes \underline{e}_1 \,, \end{aligned} \tag{C.2}$$

introducing the orthogonal bases $(\underline{\xi}_1, \underline{\xi}_2)$ and $(\underline{e}_1, \underline{e}_2)$ in the computational and physical domain, respectively. The modes $\phi(\underline{\xi})$ introduced in (C.1) will be given explicitly later on, and their only properties to be mentioned for the moment are that they account for the voltage boundary conditions on the two electrodes presented by the solid vertical lines in the computational domain. On the right electrode ($\xi_1 = +1$), the modes are zero, and on the left electrode ($\xi_1 = -1$), the potential is uniform and thus independent of the second coordinate. This uniform value is the problem unknown since it corresponds to the voltage to be measured.

The basic idea of the Bubnov-Galerkin method is to enforce an orthogonality condition between each of the modes ϕ_i and the residual of the Gauss equation, in the absence of any charge, defined in (4.2)

$$\int_{\Omega_R} \phi_i(\underline{\xi}) \nabla \cdot \underline{D} dV = 0 \quad \forall\, i \in \{1, ...m\} \,. \tag{C.3}$$

Integration by parts and application of the divergence theorem with the boundary conditions

defined in (4.4) results in

$$\int_{\Omega_R} \nabla_\xi \phi_i(\underline{\xi}) \underline{\underline{F}} \cdot \underline{D}\, dV = 0 \quad \forall\, i \in \{1, ...m\}\,, \tag{C.4}$$

having accounted for the change of variables between the physical and the computational domains thanks to the transformation gradient $\underline{\underline{F}}$. Introduce now the second constitutive relation in (4.1) with the relation (4.3) between electric field and potential, as well as the approximation (C.1), and obtain the linear system

$$\int_{\Omega_R} \nabla_\xi \phi_i(\underline{\xi}) \cdot (\underline{\underline{F}} \cdot \underline{\underline{\varepsilon}} \cdot {}^t\underline{\underline{F}}) \cdot \nabla_\xi \phi_j(\underline{\xi})\, dV A_j = \int_{\Omega_R} \nabla_\xi \phi_i(\underline{\xi}) \cdot \underline{\underline{F}} \cdot \underline{\underline{e}} : \underline{\epsilon}\, dV \quad \forall\, i \in \{1, ...m\}\,, \tag{C.5}$$

for the unknown mode amplitudes A_j. The key to success with this approach is the selection of the modes $\phi_i(\underline{\xi})$. This exercise is now documented for the 1D and 2D analyses.

C.1.1 1D analysis

The 1D setting, defined by the ξ_1-axis, is the simplest and the proposed set of modes to be inserted in (C.1) reads

$$\phi_i(\xi_1) = \cos\left(\frac{\pi}{4}(2i-1)(1+\xi_1)\right)\,. \tag{C.6}$$

Each function is zero at the right electrode ($\xi_1 = +1$) and equal to one at the left electrode ($\xi_1 = -1$). The sum of the unknown $\sum_i^m A_i$, which corresponds to the interpolation (C.1) at the left electrode, is the unknown voltage. This set (C.6) of trigonometric functions has the orthogonality property that the matrix on the left-hand side of eq. (C.5) is diagonal. The inversion is thus immediate in obtaining the amplitudes.

C.1.2 2D analysis

The difficulty in multi-dimensional problems is to choose a set of functions that satisfy the boundary conditions for the potential while, hopefully, keeping the orthogonality property found for the 1D case. The following interpolation is proposed, which is equivalent to (C.1)

$$\begin{aligned}
\varphi(\xi_1,\xi_2) \;\simeq\; & \sum_{i=1}^{m} A_{1i}\phi_{1i}(\xi_1) + b(\xi_1)[A_{2i}\phi_{2i}(\xi_2) + A_{3i}\phi_{3i}(\xi_2) + A_{4i}\phi_{4i}(\xi_2)]\,, \\
\text{with} \quad & \phi_{1i}(\xi_1) = \cos\left(\frac{\pi}{4}(2i-1)(1+\xi_1)\right)\,, \\
& b(\xi_1) = \sin\left(\frac{\pi}{2}(1+\xi_1)\right)\,, \\
& \phi_{2i}(\xi_2) = \sin\left(\frac{\pi}{2}(2i-1)(1+\xi_2)\right)\,, \\
& \phi_{3i}(\xi_2) = \cos\left(\frac{\pi}{4}(2i-1)(1+\xi_2)\right)\,, \\
\text{and} \quad & \phi_{4i}(\xi_2) = \cos\left(\frac{\pi}{4}(2i-1)(1-\xi_2)\right)\,.
\end{aligned} \tag{C.7}$$

The first series $\phi_{1i}(\xi_1)$ is similar to the one proposed for the 1-D setting in (C.6) and depends only on the first coordinate. The three other series $\phi_{\alpha i}(\xi_2)\,(\alpha = 2,3,4)$ are introducing the

variation concerning the second coordinate. They are pre-multiplied by a bubble function of the first coordinate to ensure a zero contribution on the electrodes, as expected. The modes $\phi_{2i}(\xi_2)$ are zero on top and bottom of the computational domain ($\xi_2 = \pm 1$). Modes $\phi_{3i}(\xi_2)$ and $\phi_{4i}(\xi_2)$ are zero at only one of the boundaries and equal to one at the other.

The modes proposed in (C.7) satisfy the boundary conditions but do not have the orthogonality property between every mode observed in the 1D setting. The symmetric system (C.5) has to be inverted by classical Gauss elimination.

C.2 Impact of the backing material

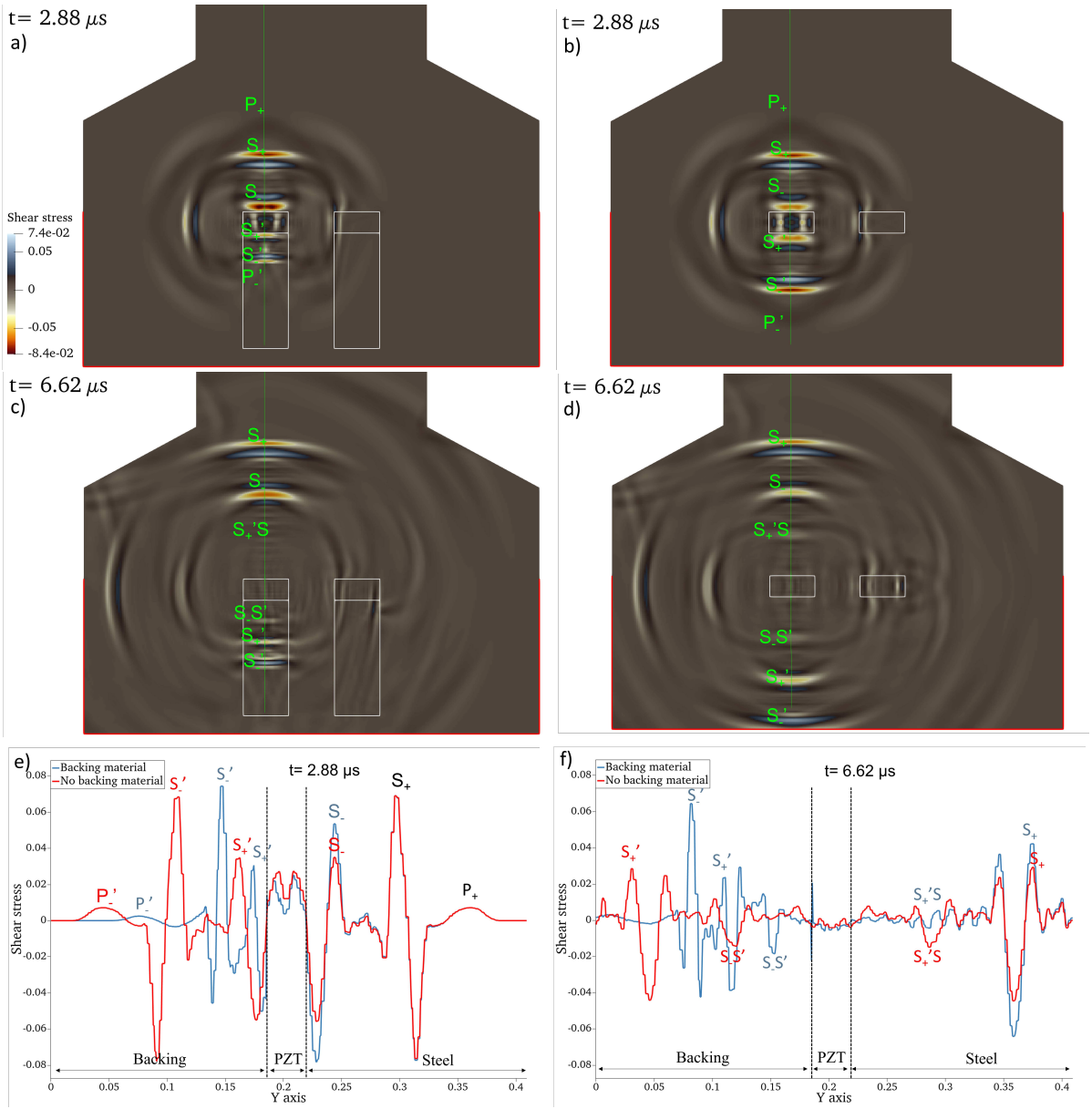


Figure (C.1) The comparison of the shear stress in the lower anvil and actuator with no damping material ((a) and (c)) and one with a backing that has the same elastic properties as the PZT ((b) and (d)). (e) and (f) represent the shear stress along the vertical green line at $t = 2.88\,\mu s$ and $t = 6.62\,\mu s$, respectively.

We conducted simulations using two materials to understand the impact of different types of damping materials on the emitted S-wave and thus complement the design of our piezoelectric proxies. First, an anisotropic backing with the same elastic properties as the PZT, and second, an isotropic material with the same properties as the anvil, as if the backing were absent. Figure C.1a and c, and Figure C.1b and d show two snapshots of the shear stress distribution for the simulation including the backing and without a backing, respectively. The snapshots are at time $t = 2.88\,\mu s$ and $t = 6.62\,\mu s$. This figure also includes plots of the shear stress along the vertical line that goes through the middle of the actuator for both simulations: the blue and red curves correspond to the anisotropic backing and the absence of backing, respectively.

At $t = 2.88\,\mu s$, the results (Figure C.1a,b and e) show that the nature of the damping material has no impact on the S-wave that has been emitted at the top of the PZT: waves labelled P_+ and S_+ are identical in both simulations. Note that the shear stress associated with P_+ results from the superposition of two P waves, one compressive and the other extensive, so that the shear stress does not vanish where they cross despite the symmetric pattern. However, S_-, which is generated at the PZT-backing interface and propagates upward, induces a 40 % smaller stress than if no backing is used. Also, waves P'_-, S'_-, and S'_+ have a smaller velocity inside the backing if its material is more compliant than the steel, with consequences on the late part of the waveform at the receiver, as it will be seen later on.

At $t = 6.62\,\mu s$ as displayed in Figure C.1 c, d, and f, the damping effect of the backing becomes more apparent. For the waves propagating upward, the main difference is S'_+S, which is an upward reflection at the lower PZT-backing interface of the S'_+. Its amplitude is significantly larger if there is no backing material because it travels unimpeded (FigureC.1 d). In the presence of backing material (FigureC.1 c), the S_-S', S'_+ and S'_- waves are slower in the backing and part of the energy reflected upward at the interface backing-anvil will affect the receiver waveform at latter times and thus will not add noise around the arrival of the main S_+ wave.

In sum, the anisotropic backing material reduces the noise in the waveform, starting from the S'_+S wave. This addition to the piezoelectric proxy will help us better match the calibration experiment.

C.3 2D validation and first convergence analysis

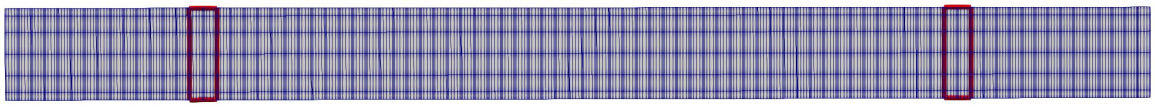


Figure (C.2) The 2D mesh, with two elements in each piezo-electric device highlighted in red, for the comparison with the exact 1D solution.

The main objective is to validate the 2D numerical development of the coupled algorithm. For this purpose, a series of 2D spectral finite element meshes, as presented in Figure C.2, are constructed, each element having 7×7 nodes. The meshes are approximately uniform in size, and the number of elements in the piezo-electric devices varies between one and thirty-two.

These meshes correspond to the 1D prototype presented in Figure 4.1 in terms of the position of the piezo-electric devices (highlighted in red) having a thickness of 3 mm (l) and separated by a rock sample of 80 mm ($2L$). The PZT's poling direction is horizontal in order to trigger P-waves that propagate horizontally. To the left of the actuator and to the right of the receiver, a steel bar has been discretised. It is important to note that special elements representing absorbing boundary conditions are placed at both ends of the assembly to prevent reflections and to simulate an infinite bar. Additionally, the nodes on the lower and upper boundaries of the mesh have their vertical displacements constrained to replicate one-dimensional propagation. Therefore, the elastic constant used in Equation 4.6 for both the rock and the steel sections is the oedometric modulus. The maximum voltage, V_0, is set to one, and the pulse has a duration, T, of one, following the shape shown in Figure 4.2.

The results presented in Figure C.3 show the voltage measured at the receiver over time. Comparing the numerical predictions to the exact solution (available up to 33.28 µs), we find that the waveform is generally well captured, even with just a single element in the piezoelectric ceramic. However, a minimum of two elements is necessary to achieve the maximum voltage at the receiver. Additionally, four elements are required to ensure the numerical predictions converge once the voltage reaches negative values.

Further attention is now given to picking the P wave, as illustrated in Figure C.3b. The dashed vertical line indicates the exact arrival time at the receiver. Picking the precise arrival time is challenging because the voltage behaves as a quadratic function of time, as shown in equation 4.40, making it tangential to the horizontal axis. The numerical predictions display a slight undulation before the exact arrival time, and the prediction based on a single element is not very effective for wave picking. To achieve accuracy in this plot, at least four elements are necessary. However, it is worth noting that the undulation remains noticeable with both four and eight elements. Only the mesh with thirty-two elements demonstrates excellent accuracy at the scale used on the vertical axis of this graph.

The main conclusion is that the 2D development has been validated by comparing its predictions to the exact solution from a 1D model. During this process, it was confirmed that wave picking, which is inherently challenging, requires a specific level of accuracy that dictates the necessary mesh resolution. The finest mesh used in this simplified scenario would be too CPU-intensive for more complex geometries. Therefore, a compromise must be reached between the accuracy of the numerical predictions and the acceptable CPU time. Additionally, the quality of the available laboratory data will be crucial in establishing this balance.

C.4 2D Convergence analysis

The 2D convergence analysis is continued here with a focus on the simplified problem described in Section 4.5. Four uniform meshes are illustrated in Figure C.4, with the number of elements in the piezoelectric devices varying between 2×2 and 4×4. Each element consists of 7×7 nodes.

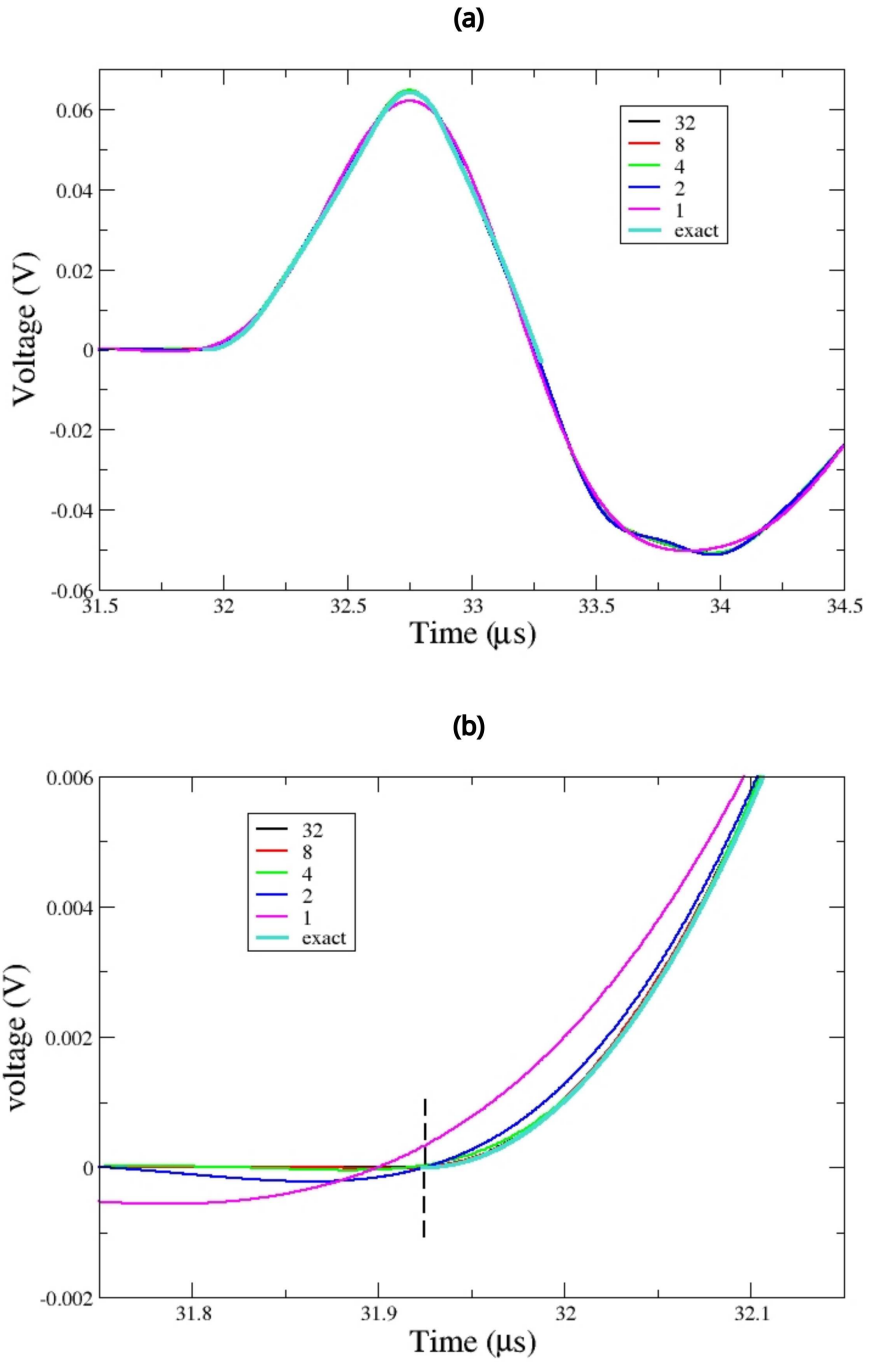


Figure (C.3) Waveforms at the receiver for different mesh resolutions (number of elements in each piezo-electric device is provided) and comparison with the exact solution in (a). The difficulty of picking the arrival of the S wave is illustrated by zooming in on the waveform in (b). The vertical dashed segment marks the exact arrival time.

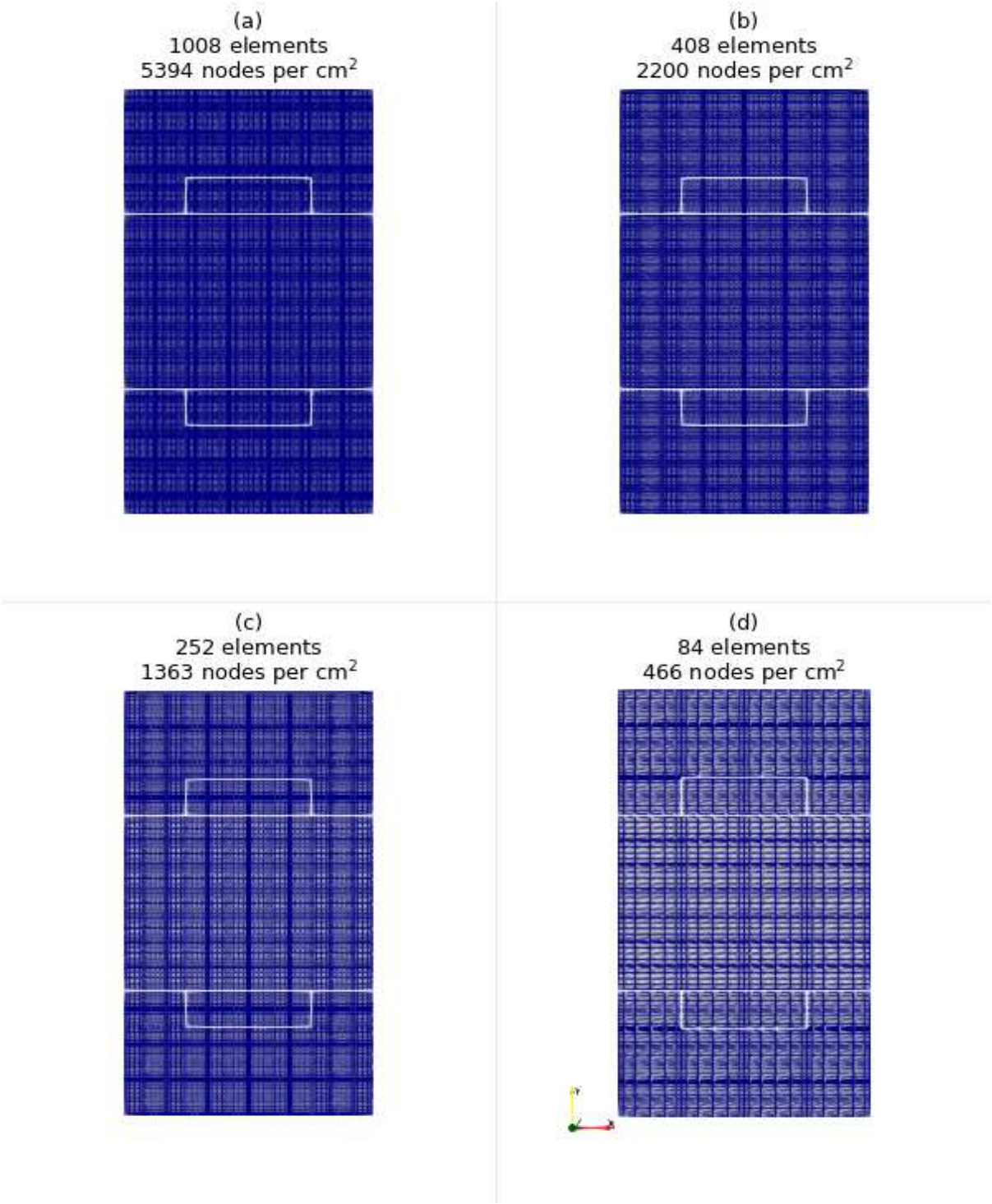


Figure (C.4) Meshes of different resolutions used for convergence analysis on the simplified problem of section 4.5.

Since the mesh is uniform, a nodal density is also proposed, ranging from 466 to 5,394 nodes per square centimetre, representing a difference of more than an order of magnitude. The material properties remain consistent with those outlined in the main text of Section 4.5. Also, this analysis focuses exclusively on S-wave emissions.

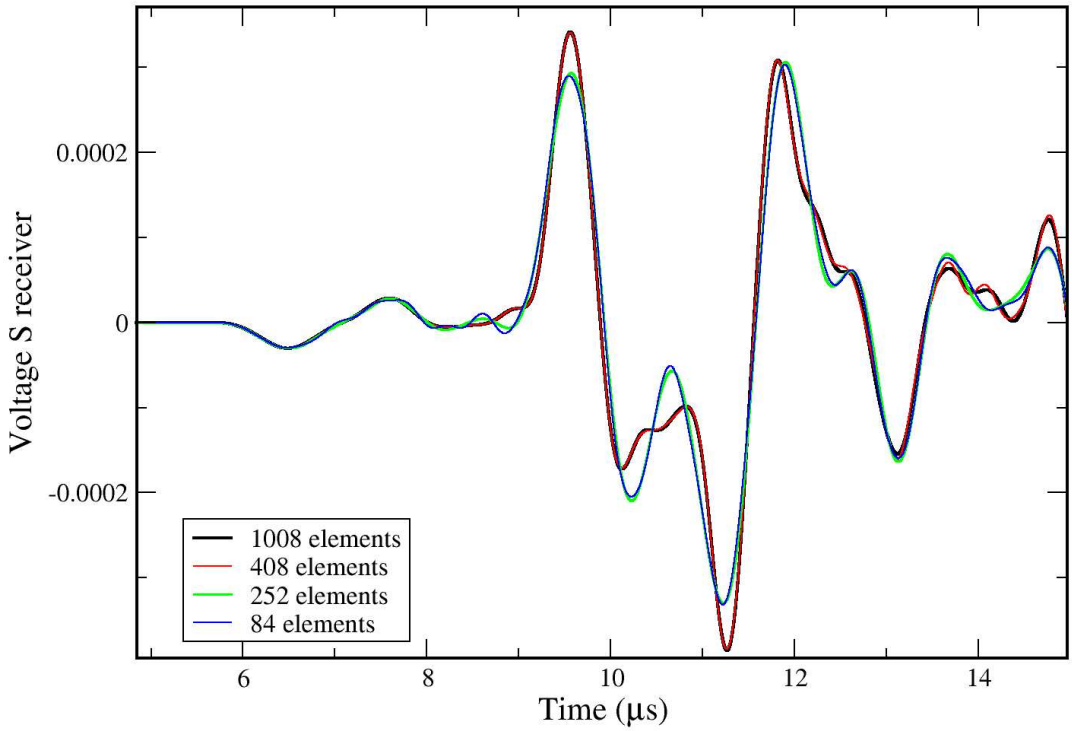


Figure (C.5) Waveforms at the receiver for different mesh resolutions presented in Figure C.4.

Results are presented in Figure C.5 for the four different meshes. It is assumed that the finest mesh provides the closest approximation to the exact solution, which is unknown here. The general waveform does not vary significantly with 408 elements. The maximum voltage is not well captured, however, for 252 elements. The waveform around the time 10.5 μs is also sensitive to the mesh size, and the use of 252 elements is not sufficient. Surprisingly, the waveform is not affected significantly by the mesh size after the time 11.9 μs.

This analysis will not delve further into the detection of the S wave, as was done in the simpler 1D problem, since it is evident that a mesh consisting of 408 elements is required for an accurate estimate. Specifically, a mesh resolution of 2200 nodes per square centimetre is recommended for optimal accuracy. However, the node density used for the full specimen analysed in sections 4.6 and 4.7 is lower, at 1209 nodes per square centimetre. This choice of mesh resolution is already underlined in Appendix C.3, where it is noted that it is influenced by the need for a realistic CPU time while still providing sufficient accuracy when compared to experimental data, as elaborated upon in the main text. This convergence analysis demonstrated that the

resolution of the mesh has only a minimal impact on the group velocity and overall pattern of the S waves.